DSPACE

https://dspace.org/

The process mineralogy of selected Southern African uranium ores

Youlton, Brandon

2015-05-06
http://hdl.handle.net/10539/17642

Downloaded from a DSpace repository. https://dspace.org/

The Process Mineralogy of Selected Southern African Uranium Ores

Brandon Youlton

0410708G

Supervised by Prof. Judith Kinnaird

A Thesis Submitted to the Faculty of Science, University of the Witwatersrand, Johannesburg, in Fulfilment of the Requirements for the Degree of Doctor of Philosophy

3 December 2014, Johannesburg

Declaration

I declare that this Thesis is my own, unaided work. It is being submitted for the Doctor of Philosophy at the University of the Witwatersrand, Johannesburg. It has not been submitted before for any degree or examination at any other University.



B. Youlton

3rd day of December 2014 in Johannesburg.

Acknowledgments

Thanks go to Judith Kinnaird for assistance in obtaining the samples used in this study, financing of the chemical analyses and for her advice and guidance. The author would also like to thank Paladin Energy for contributing most of the U ore used in this study and SGS South Africa for sponsoring instrument and batch reactor time. The advice of Johan O' Connell, Louis Coetzee and Maria Klaas is also greatly appreciated.

Abstract

During the acid leaching of uranium, gangue-reagent interactions have both negative and positive consequences. Gangue dissolution increases reagent costs, and in some cases can prevent the economic acid leaching of an ore, but can also increase uranium mineral exposure and improve recoveries. Due to rapid dissolution kinetics, the acid consumption characteristics of the various carbonate species are readily predicted, however the same is not true of silicate gangue. Due to factors including slower leach rates, incongruent dissolution, parabolic kinetics, and surface area, pH and temperature dependence, the gangue acid consumption characteristics of silicate minerals are significantly more complex. A detailed mineralogical investigation and acid leach tests were conducted on sandstone- and granite-hosted uranium ore samples. The dissolution characteristics of the more common gangue phases were determined. The study demonstrated that gangue-reagent interactions and U dissolution can be predicted from mineralogical data. A model was developed which allows for the use of mineralogical and geochemical data to predict gangue reagent consumption. The basic framework of the model is universally applicable, but may require calibration, depending on the mineral assemblage and complexity of a specific uranium deposit.

Contents

Chapter 1. Overview of the Extractive Metallurgy of Uranium 9
1.1. Uranium Deposits of Southern Africa 10
1.2. Extractive Metallurgy of Uranium 12
1.3. Process Mineralogy of Uranium Ores 14
1.4. Aims and Hypothesis 16
Chapter 2. Optical Petrography of the Sedimentary Ores 18
2.1. Introduction, Aims and Objectives 18
2.2. Methodology 19
2.3. Results 19
2.4. Discussion 27
2.5. Summary and Conclusions 29
Chapter 3. Comminution 32
3.1. Introduction, Aims and Objectives 32
3.2. Methodology 39
3.3. Results 43
3.4. Discussion 49
3.5. Summary and Conclusions 52
3.6. Recommendations 54
Chapter 4. X-ray Diffraction 55
4.1. Introduction, Aims and Objectives 55
4.2. Basic Principals and Phase Identification 55
4.3. Quantitative Analysis 58
4.4. Limits of Detection and Quantification 64
4.5. Methodology 65
4.6. Results 74
4.7. Prediction of Reagent Consumption Characteristics 85
4.8. Discussion 118
4.9. Summary and Conclusions 127

Chapter 5. Scanning Electron Microscopy and QEMSCAN Analyses 129
5.1. Introduction, Aims and Objectives 129
5.2. Methodology 135
5.3. Results 142
5.4. Discussion 174
5.5. Summary and Conclusions 176
Chapter 6. Leach Testwork 180
6.1. Introduction Aims and Objectives 180
6.2. Methodology 180
6.3. Results 183
6.4. Discussion 192
6.5. Summary and Conclusions 194
Chapter 7. Modelling of Reagent Consumption 197
7.1. Methodology 197
7.2. Results 200
7.3. Discussion and Conclusions 208
Chapter 8. Part I Conclusions 211
8.1. Key Findings 214
Chapter 9. Application to Igneous Ores 215
9.1. Aims 215
9.2. Regional Geology of Namibian Igneous-hosted Uranium Deposits 216
9.3. Rössing 219
9.4. Valencia 222
Chapter 10. Mineralogical Characterisation 225
10.1. Introduction Aims and Objectives 225
10.2. Methodology 225
10.2.1. Optical Petrography 226
10.2.2. Comminution 226
10.2.3. Chemical Analyses 228
10.2.4. X-ray Diffraction and QEMSCAN Bulk Mineralogical Analyses 228
10.2.5. Scanning Electron Microscopy 230

10.2.6. QEMSCAN Trace Mineral Search....230
10.3. Results....232
10.3.1. Optical Petrography....232
10.3.2. Comminution....242
10.3.3. Chemical Analyses....245
10.3.4. Quantitative Gangue Mineralogy....246
10.3.5. Scanning Electron Microscopy....256
10.3.6. QEMSCAN Trace Mineral Search....263
10.4. Discussion....274
10.4.1. Optical Petrography and Gangue Mineralogy....274
10.4.2. Comminution....276
10.4.3. Chemical Analyses....277
10.4.4. Scanning Electron Microscopy and QEMSCAN Trace Mineral Search 278
10.5. Summary and Conclusions....279
Chapter 11. Modelling of Acid Leach Behaviour....282
11.1. Introduction....282
11.2. Methodology....282
11.3. Results....287
11.4. Summary and Conclusions....289
Chapter 12. Acid Leach Tests....291
12.1. Introduction Aims and Objectives....291
12.2. Methodology....291
12.3. Results....293
12.3.1. Uranium Dissolution....294
12.3.2. Gangue Dissolution and Reagent Consumption....295
12.4. Discussion....300
12.5. Summary and Conclusions....303
Chapter 13. Model Calibration for Igneous Ores....305
13.1. Introduction....305
13.2. Methodology....305

13.3. Results and Discussion 306
13.3.1. Iron Oxide Dissolution 306
13.3.2. Biotite Dissolution 308
13.3.3. Manganese Demand Equation 311
13.3.4. Comparison of Measured Acid Demands with those Predicted by the Calibrated Model 312
13.4. Summary and Conclusions 313
Chapter 14. Conclusions 316
14.1. Gangue Dissolution and Reagent Consumptions 316
14.2. Uranium Dissolution 318
Chapter 15. Recommendations for Further Work 320
15.1. Grind Optimisation 321
15.2. Detection Limits of XRD 321
15.3. Extension of the Model to Witwatersrand Ores 322
References 323
Appendices 343

Chapter 1. Overview of the Extractive Metallurgy of Uranium

Uranium (U) has a number of uses ranging from the manufacture of isotopes for food irradiation and medicine, to weapons and the propulsion of ocean-going vessels; however, the main use of U is as fuel in nuclear power plants (Cole, 1998).

The nuclear industry underwent a prolonged period of stagnancy (Marcus, 2008) caused, in part, by safety concerns following accidents at Three Mile Island and Chernobyl (Cole, 1998). More recently the need to meet increasing demand for electricity, elevated fossil fuel prices and concerns relating to CO_2 emissions, have rekindled interest in nuclear power, and resulted in a 10 fold increase in the spot price of U in only 5 years (Harding, 2007). However, the effects of the 2010 tsunami, on the Fukushima power plant in Japan, have rekindled reservations relating to the use of nuclear energy and resulted in reduced spot U prices (Njini, 2012).

Nuclear power has one of the lowest life-cycle greenhouse gas emissions of any electricity generating technology (Weisser *et al.*, 2008). The use of nuclear energy also reduces particulate matter and other pollutants resulting from fossil fuels, and conserves fossil fuel resources for other (non-energy) needs (Marcus, 2008). Nuclear energy also lends itself to the generation of reliable baseload power (Weisser *et al.*, 2008), which is not as readily achieved by other alternative energy technologies (Denholm *et al.*, 2005).

The U used to supply nuclear reactors is obtained either from mining and processing of U ore, or from stockpiles. In the 1980s and 1990s significant amounts of U were derived from stockpiles, however these have been

substantially reduced, and it is expected that mining and processing will replace these stockpiles as the dominant source of U (IAEA, 2009).

The economic viability of a U deposit is determined by the value of the metal that can be recovered versus the cost associated with mining and processing. This balance, between cost and metal content, is particularly important in the post-Fukushima U market.

This project will focus on improving the accuracy with which the process characteristics of a U ore can be predicted. Special attention will be given to predicting reagent consumption, dissolution rates and percentage U dissolution during acid leaching. These factors directly affect both the metal recovery and processing costs.

1.1. Uranium Deposits of Southern Africa

In Southern Africa, uranium occurs in a number of different localities (Figure 1) including primary U, hosted in sheeted leucogranites in Namibia (Kinnaird and Nex, 2007), U and gold mineralisation in the metamorphosed sediments of the Witwatersrand Basin (McCarthy, 2006), Karoo-aged deposits within the main Karoo Basin of South Africa (Le Roux and Brynard, 1994), as well as at Kayelekera in Malawi (Bowden and Shaw, 2007), Letlhakane in Botswana (A-Cap Resources, 2009), calcrete hosted U at Trekkopje (Youlton, 2007) and Langer Heinrich in Namibia (Hartleb, 1988).

The gangue mineralogy of the Namibian sheeted leucogranites consists of quartz and feldspars (Kinnaird and Nex, 2007). These minerals are relatively inert and do not result in excessive reagent consumption, however, due to the low Fe content of the gangue it may be necessary to add Fe to achieve optimal leach

conditions (Johnson, 1990). The abrasive nature of the ore can also result in wear problems during processing (Johnson, 1990).

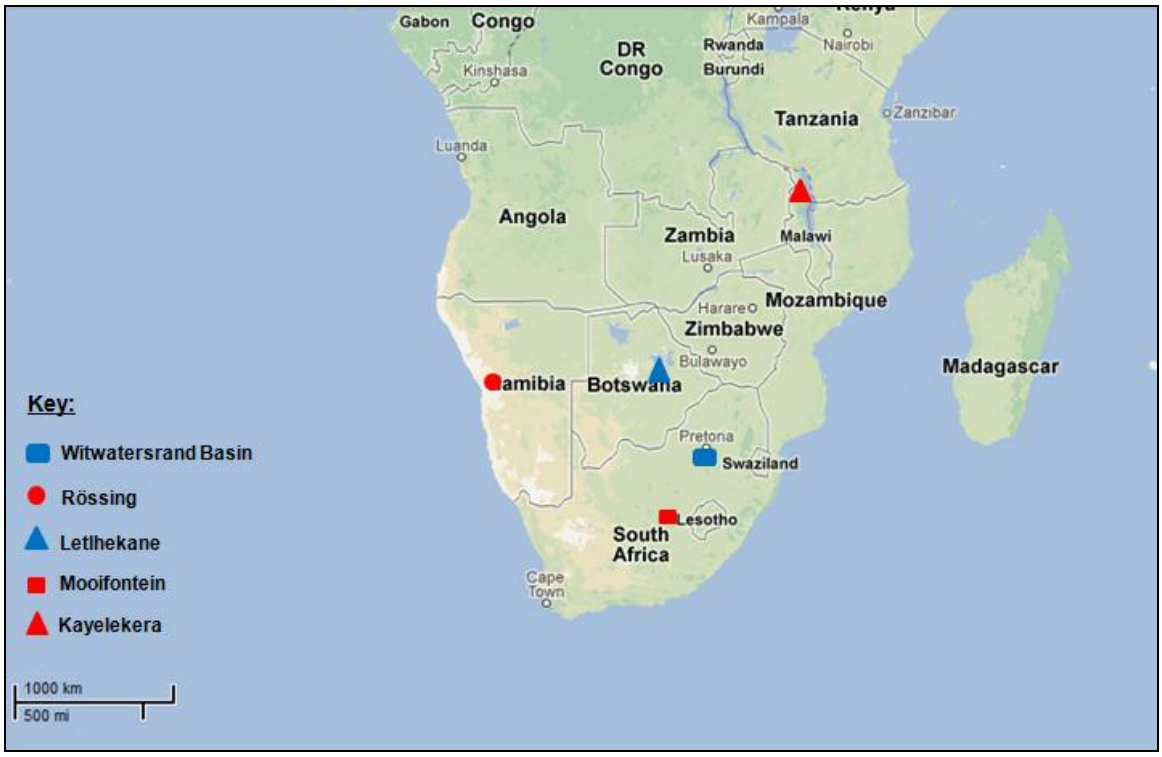

Figure 1: Google map showing the locations of selected Southern African uranium deposits. Those marked with red symbols are discussed in more detail in later chapters. The Trekkopje deposit is too close to the Rössing deposit to be shown separately at this scale.

In the Witwatersrand Basin the uranium is associated with gold mineralisation and occurs in metamorphosed conglomerates (McCarthy, 2006) which are dominated by quartz with minor to trace amounts of pyrophyllite, sericitic muscovite, chloritoid and chlorite (Phillips and Law, 1994). The sulphide mineralogy is dominated by pyrite with traces of pyrrhotite, chalcopyrite, gersdorffite, cobaltite, sphalerite and galena (Robb and Meyer, 1995). While these rocks represent a major uranium resource, the economics of mining and processing are largely controlled by the associated Au mineralisation, and one of the major advantages of U leaching is that it results in improved gold recoveries (Lottering *et al.*, 2008).

In the main Karoo basin of South Africa, U mineralisation occurs with fluvial sandstones of the Beaufort Group (Le Roux, 1993). Uranium is hosted in coffinite and uraninite, and mainly occurs at the base of thicker, more permeable palaeo-channels (Turner, 1985). Associated ore minerals include pyrite, molybdenite and arsenopyrite (Turner, 1985). There is also a weak relationship between U and calcite (which is typically present in concentrations of about 10%) (Le Roux, 1993).

The Kayelekera deposit occurs in Malawi in Karoo-aged sediments, but outside of the main Karoo Basin. The mineralisation occurs within arkosic sandstones with up to 25% muscovite and biotite, and is associated with organics, pyrite and chlorite (Bowden and Shaw, 2007). In the reduced zone coffinite dominates, with lesser uraninite, while in the oxide facies meta-autunite and boltwoodite dominate, with minor uranophane (Bowden and Shaw, 2007). In spite of the high concentrations of acid-consuming muscovite and biotite, the Kayelekera deposit is processed by acid leach (Paladin Energy, 2010).

In the calcrete-hosted U deposits of Namibia, carnotite occurs within palaeo-channel sediments (Hartleb, 1988). The gangue consists of quartz, feldspar, mica, palygorskite, smectite and calcite (Youlton, 2007). Calcite concentrations are significantly higher than the Karoo deposits and are typically about 17% (calculated from data presented by Youlton [2007]). Because of the high concentrations of reactive gangue, both Langer Heinrich (Venter and Boylett, 2009) and Trekkopje (Faurie, 2010) use an alkali leach.

1.2. Extractive Metallurgy of Uranium

The hydrometallurgical extraction of uranium is conventionally achieved by either acid or alkali (carbonate) leach (Abhilash *et al.*, 2009). Acid leaches are typically preferred to alkali methods, as they frequently offer more rapid dissolution

kinetics and are able to leach more efficiently at coarser grinds (Lunt et al, 2007). Carbonate leaches are used where the reactivity of the gangue prevents acid leaching, and also result in more selective dissolution of the uranium (Merrit, 1971; Lunt et al, 2007).

Conventional U leaching involves a process of ore size reduction (comminution), acid or alkali leaching, solid liquid separation, purification and concentration (typically by ion exchange or solvent extraction) and precipitation (Guettaf *et al.*, 2009).

The purpose of comminution is to expose the U minerals to the leach solution. The optimal grind is sufficiently fine to expose the uranium minerals without over grinding (which increases costs and may cause high pulp viscosities) (IAEA, 1990).

After comminution, the ore is leached. Sulphuric acid is typically used to achieve the low pH required for acid leaching (Ho and Quan, 2007). During acid leaching hexavalent U minerals tend to dissolve readily, while tetravalent U minerals require oxidation to the hexavalent state prior to dissolution (Lunt et al, 2007). In the processing of the Witwatersrand ores of South Africa MnO_2, in the form of pyrolusite, is the preferred oxidant (Lottering *et al.*, 2008). At Olympic Dam sodium chlorate is used (Miki and Nicol, 2009). Other oxidants include SO_2/O_2 (Ho and Quan, 2007), hydrogen peroxide and oxygen (Venter and Boylett, 2009). It has been found that these oxidising agents do not act on the U minerals directly, but instead serve to oxidise iron to the Fe^{3+} state, which in turn oxidises the U (Lottering *et al.*, 2008).

1.3. Process Mineralogy of Uranium Ores

The bulk composition of the rock, especially gangue mineralogy, controls the consumption of sulphuric acid and oxidiser, as well as the potential for Fe^{3+} generation (Merritt, 1971; Ho and Quan, 2007 and Lottering *et al.*, 2008). Gangue minerals which may occur in U deposits include quartz, feldspars, carbonates, muscovite, biotite, chlorite, pyrophyllite, clays, iron oxides and hydroxides, sulphides, sulphates and phosphates (Hartleb, 1988; Nex *et al.*, 2001; Kinnaird and Nex, 2007; Lottering *et al.*, 2008).

Quartz and feldspar are relatively inert, while carbonates are highly acid consuming (Merritt, 1971 and IAEA, 1980). Although not as reactive as the carbonates, the phyllosilicates (chlorite, biotite, muscovite and clay minerals) and phosphates are also acid consuming (IAEA, 1980) and can even remove dissolved U from solution (Fuller *et al.*, 2002). Sulphide minerals increase consumption of both acid and oxidiser (Merritt, 1971; IAEA, 1980). While the iron oxide/hydroxide phases consume acid, they also contribute Fe to the solution which plays a significant role in U oxidation (Merritt, 1971 and IAEA, 1980).

Increasing reagent consumption is not the only potentially deleterious effect that gangue minerals can have. Certain minerals, especially phosphates are able to absorb dissolved U from solution.

In spite of the role of gangue mineralogy in controlling reagent consumption, it has thus far not been possible to use mineralogical data to predict reagent consumption. There are two reasons why this has not been achieved:

The IAEA (1980) state that it is not possible to explicitly predict the behaviour of certain gangue phases, especially the silicates and sulphides. If this is true then it would not be possible to make predictions relating to reagent consumption from

quantitative mineralogical data alone. However, recent attempts to better understand the role of various minerals (including the silicates and sulphides) in acid mine drainage have produced valuable data regarding the behaviour of these phases under acidic oxidising conditions (for example Lowson, *et al.*, 2005; Danielle *et al.*, 2008 and McKibben *et al.,* 2008). The availability of these data may make it possible to use quantitative mineralogy to accurately predict reagent consumption.

The second difficulty relates to the limitations of readily available mineralogical instruments, and was encountered by Reynolds *et al.* (2010) when attempting to make use of X-ray diffraction (XRD) to characterise uranium ore. They found that standard XRD techniques gave inconclusive results and found it necessary to use, far less readily available, synchrotron technology to achieve acceptable results.

Reynolds *et al.* (2010) suggested that the poor quality of their XRD data may be due to the high concentrations of Fe in the sample. The fluorescence of Fe (in response to Cu Kα irradiation) may be the cause of the high degree of noise in the resulting diffractograms, which obscured the minor and trace phases. However it may be possible to characterise U ores by standard XRD because not all U ores contain such high concentrations of Fe, and if an ore is Fe-rich, it is possible to prevent fluorescence by using Co Kα radiation in preference to Cu.

Gangue is not the only mineralogical factor which influences the leach response of a U ore. The nature of the U species also plays a significant role. This is illustrated by the Rössing U deposit in Namibia. At this deposit, the U hosted in uraninite is recovered by acid leach (Johnson, 1990). However, in a particular area within the Rössing deposit, known as the SH area, the U cannot be recovered because it is hosted in the refractory mineral betafite (Kinnaird and Nex, 2007). Lottering *et al.* (2008) observed a similar phenomenon in the U-

bearing ores of the Witwatersrand. They found that the presence of brannerite in these ores made it very difficult to achieve U dissolutions in excess of 90%.

These two examples illustrate the importance of U mineral speciation in controlling the extent of U dissolution in a particular ore. QEMSCAN (previously known as QEM.SEM) technology is able to quantitatively determine metal speciation of a sample as well as determining the size distribution and liberation characteristics (Coetzee *et al.*, 2011). Most published QEMSCAN work relates to its use in Au mineralogy (for example Goodall *et al.*, 2005 and Coetzee *et al.*, 2011), however the same techniques can also be applied to U (Youlton, 2007).

1.4. Aims and Hypothesis

The project will focus on improving the accuracy with which the metallurgical response of ores can be predicted based on mineralogical data, and will centre around two aims:

1. Develop an equation that allows for the use of quantitative XRD data to predict reagent consumption in the acid leaching of selected Southern African ores, for a given set of conditions.
2. Contribute to the understanding of the relationship between U mineral characteristics and the percentage of U dissolution that can be achieved by acid leach.

The pursuit of these aims will make it possible to test the following hypothesis:

The limitations of conventional mineralogical techniques (Reynolds et al, 2010), and the complexity of the mineralogy (IAEA, 1980), are such that it is not possible to use XRD and QEMSCAN to accurately predict the metallurgical response of Southern African U ores.

This study consists of two parts. Part I will make use of sedimentary U ores and will mainly focus on gangue mineral dissolution and reagent consumption. Part II will make use of igneous ores and will mainly focus on the prediction of U dissolution from mineralogical data. However, while these are the primary focuses of the two parts, Part I will also consider the effect of gangue dissolution on U dissolution, and Part II will test the method developed to predict reagent consumptions that was developed in Part I. Part I consists of Chapters 2 to 8, Part II consists of Chapters 9 to 14.

Part I: Sedimentary Ores

Chapter 2. Optical Petrography of the Sedimentary Ores

2.1. Introduction, Aims and Objectives

Two Karoo-aged deposits, Kayelekera and Mooifontein (marked in red in Figure 1), have been selected for this part of the study. These deposits were selected because, of the Southern African deposits that are processed by acid leaching; those of Karoo age contain the highest concentrations of reactive gangue. For this reason, a study of the effects of gangue mineralogy on reagent consumption would be most valuable for these deposits. Also, the complex mineralogy of the selected samples is a realistic test of whether the metallurgical response of ores can be predicted from mineralogical data.

A series of techniques have been used to achieve the aims. These include optical mineralogy, X-ray diffraction (XRD), scanning electron microscopy (SEM), QEMSCAN and batch acid leach tests. This chapter details the optical petrographic analyses of the samples.

The purpose of the optical petrography was to characterise the gangue minerals as they occur in the head sample prior to crushing. These data will be used to better understand the lithologies that occur at Mooifontein and Kayelekera, and will contribute to an understanding of their behaviour during comminution and leaching.

This section consists of a qualitative/semi-quantitative assessment of the ore. No attempt has been made to correct the data for stereological bias, because it is quicker and more accurate to use QEMSCAN data for stereological determinations. However, the qualitative/semi-quantitative data provided here

serves as a means of checking the quantitative data presented in the following chapters.

2.2. Methodology

The samples as they were received from the Mooifontein prospect and Kayelekera mine were composites, consisting of rock ranging from fist size to 45 cm in diameter. The Mooifontein sample (abbreviated to Mooi) had a mass of ~28 kg. Three samples were obtained from the Kayelekera mine. These represented reduced arkose ore (RAO) with a mass of ~4 kg, oxidised arkose ore (OAO) with ~8 kg mass and mudstone ore (MSO) with ~3 kg mass.

Because of the large amount of material in the Mooifontein sample, it was possible to divide the sample into higher and lower grade material using a scintillometer. After which, representative portions of each sample were selected. These were used to produce polished thin sections from each sample. In the case of the Mooi sample thin sections were prepared from both the higher and lower grade portions. Thereafter the higher and lower grade portions were recombined. Due to the friable nature of Karoo ores, it was necessary to resin impregnate the samples prior to thin section preparation.

The polished thin sections were examined under reflected and transmitted light using a Nikon petrographic microscope with the facility to collect photomicrographs.

2.3. Results

The samples are described in the tables that follow in terms of mineralogy, textures and alteration/metamorphism. No attempt was made to characterise the uranium mineralogy of the samples, because this would be more accurately and quantitatively analysed by SEM and QEMSCAN.

Table 1: Petrographic description of the Mooifontein sample

Lithology: Very fine arkose
Most of the rock consists of very fine subangular sand grains. These consist of quartz, plagioclase and K-feldspar (mostly microcline). Irregular bodies of medium sand occur within the very fine sandstone. Granite lithic fragments are very rare and were only observed in the medium sand. This texture can be seen in the scan of the thin section shown in the bottom right corner of this table (which is continued on the following page) A second thin section with black carbon grains is also shown. The degree of cementation is variable and some portions of the rock have significant amounts of calcite cement, while others are very poorly cemented. Plagioclase grains show partial replacement by zeolite, sericite and less commonly calcite, while K-feldspar is partially replaced by sericite. Detrital biotite and muscovite occur throughout the rock. Many of the biotite grains are extensively replaced by chlorite. Discrete chlorite grains (with no biotite) are also present. It is not clear whether these are detrital, or represent the complete (possibly in-situ) replacement of original biotite. The rock is both texturally and mineralogically immature. Sulphides are rare and only pyrite and chalcopyrite were present. These grains are typically anhedral, however a single euhedral pyrite grain was observed. Sulphides do not typically show an association with any particular mineral. However, rare very fine pyrite occurs as disseminations within carbon grains. Carbon is most abundant in the more uranium-rich portions of the sample, and most grains contain no pyrite.
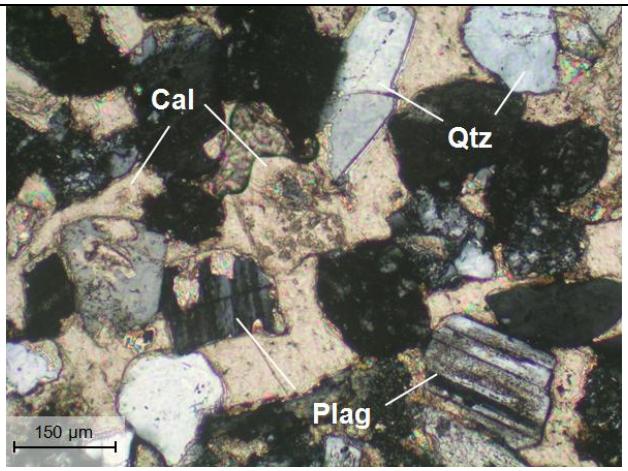 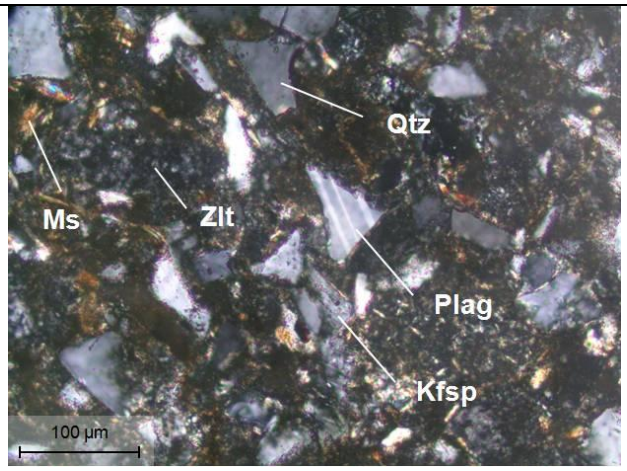 *Quartz (Qtz) and plagioclase (Plag) cemented by calcite (Cal) (left). Poorly cemented finer quartz, plagioclase, K-feldspar (Kfsp) and muscovite (Ms) is more typical of the bulk of the sample. Some feldspar grains that are more altered and some of the plagioclase grains appear to have been altered to zeolite (Zlt) (right).*
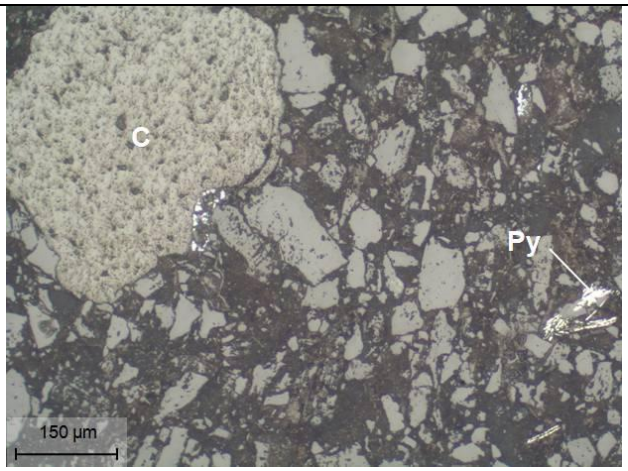 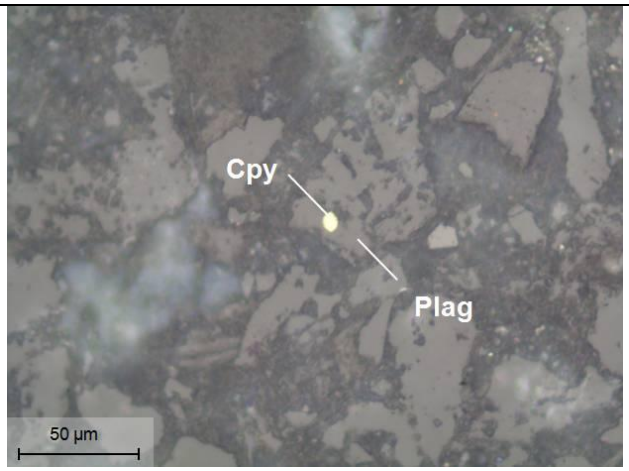 *Carbon (C) and elongate pyrite (Py) (left). Chalcopyrite (Cpy) in a plagioclase (Plag) grain (right).*

Table 1 Cont.: Petrographic description of the Mooifontein sample

Mineral assemblage and approx. quantity (%)		**Mineral description, alteration and mineralisation**	
Quartz	Major	*Angular to subrounded (typically subangular). Mostly between 0.03 and 0.25 mm in size, however in coarser portions of the sample grains may reach 0.4 mm.*	
Plagioclase	Major	*Similar size, texture and distribution to quartz. Many grains show partial alteration to zeolite, sericite and less commonly and calcite.*	
K-feldspar	Major	*Mostly microcline. Similar size, texture and distribution to quartz. Many grains are partially altered to sericite.*	
Calcite	Major	*Occurs as cement between detrital grains and in some cases as a replacement of plagioclase. Calcite distribution is variable and some portions of the rock are well cemented, while others are not.*	
Zeolite	Minor	*Alteration product of plagioclase.*	
Chlorite	Minor	*Very fine to 0.3 mm grains. It is not clear whether these are detrital, or the product of in-situ biotite replacement. However, several biotite grains show partial replacement by chlorite.*	
Muscovite	Minor	*Approximately equal amounts of detrital muscovite and sericitic material replacing feldspar. Detrital grains are between 0.01 and 0.2 mm in size.*	
Biotite	Trace	*Detrital grains up to 0.3 mm in size. Many grains are extensively replaced by chlorite.*	
Carbon	Trace	*0.05 to 0.5 mm angular to subrounded most abundant in higher grade portions of the composite sample.*	
Rutile	Trace	*0.02 to 0.05 mm and angular.*	
Pyrite	Trace	*0.001 to 0.16 mm, mostly anhedral to elongate, however one euhedral grain was observed. Pyrite generally shows no consistent association with other minerals; however associations with carbon were observed (where the pyrite occurs finely disseminated through the carbon.*	
Chalcopyrite	Trace	*Anhedral grains 0.02 to 0.03 mm in size.*	
Alt/Met minerals:		*Zeolite, chlorite, sericitic muscovite and calcite. It is not clear whether the chlorite is detrital or the product of in-situ biotite replacement. Some of the calcite is a replacement of plagioclase, but most occurs as cement.*	
Texture and structure:		*Most of the rock consists of variably cemented very fine arkosic sandstone, however irregular masses of medium arkosic sand are also present. Granitic lithic fragments are very rare and appear to only occur in the medium arkosic sand.*	
Veining:		*No veining was observed.*	

Table 2: Petrographic description of the reduced arkose ore sample from Kayelekera

Lithology: Carbonaceous medium arkose
This composite consists of arkosic rocks of several sizes. Most consist of medium sand, however, some consist of granule and even pebble size grains. Plagioclase and quartz are the major components of the rocks, but minor amounts of K-feldspar are also present. These grains are bound by a phyllosilicate cement consisting of chlorite and smectite. Fine carbon occurs throughout and causes the dark coloration of the rock. Pyrite is the dominant sulphide and is often associated with the carbon. Very rare grains of chalcopyrite were also observed. Lithic fragments occur almost exclusively in the coarser rocks. These consist mainly of granite fragments. The fragments are subrounded and have an interlocking texture typical of granites, however, rare myrmekitic intergrowths were also observed. In addition to the igneous lithic fragments, rare metamorphic fragments were observed. These consist mainly of deformed quartzite. The rock is both texturally and mineralogically immature.
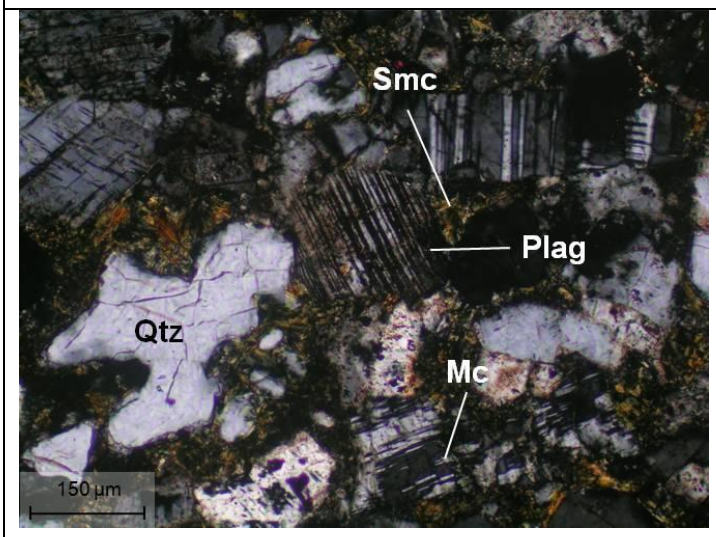 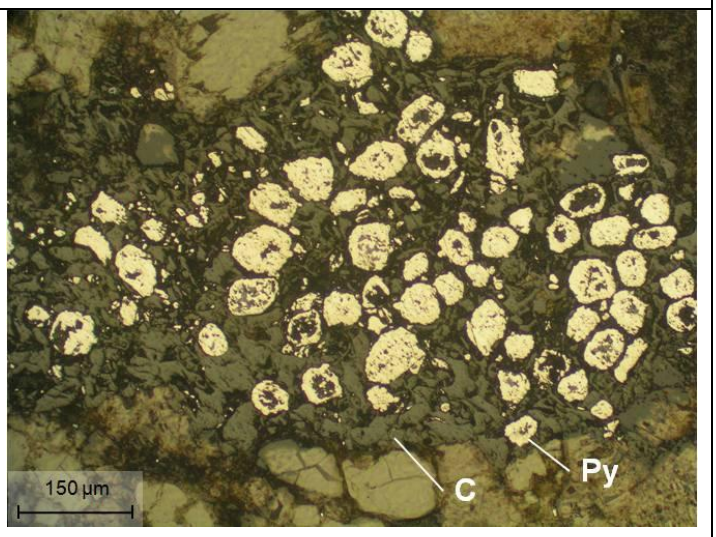
Plagioclase (Plag), quartz (Qtz) and microcline (Mc) cemented by smectite (Smc) (left). Anhedral pyrite (Py) associated with carbon (C) (right).
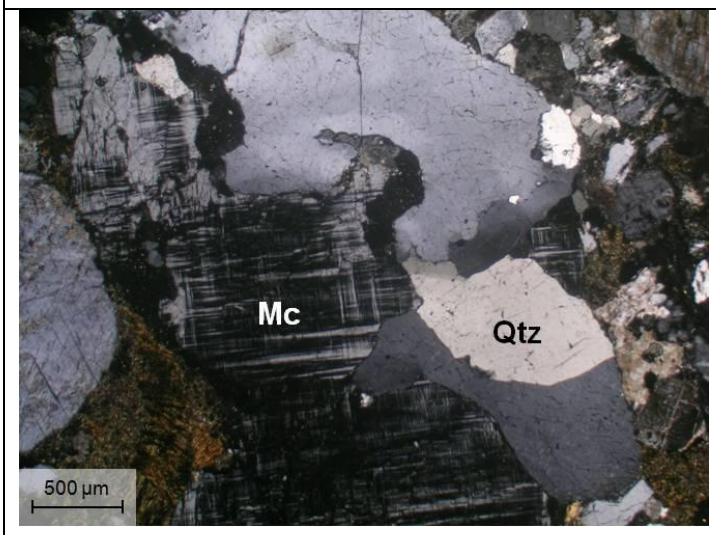 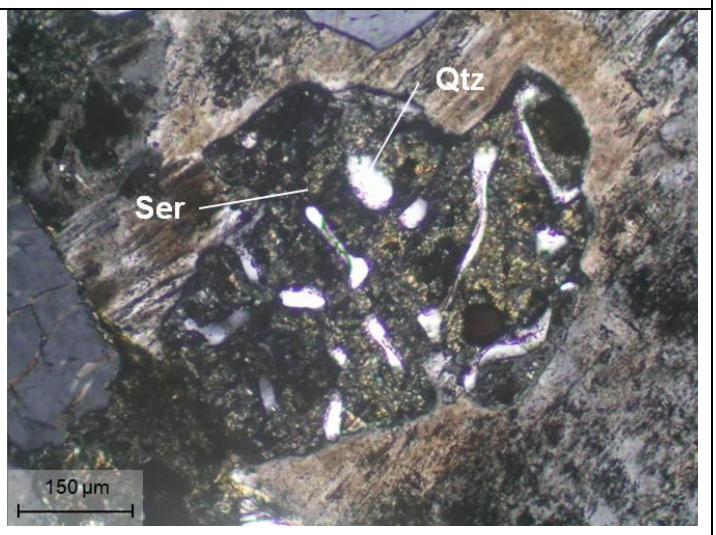
Interlocking quartz (Qtz) and microcline (Mc) in a granite lithic fragment (left). Myrmekitic intergrowths between quartz and feldspar, where the feldspar has since been altered to sericite (Ser) (right).

Table 2 Cont.: Petrographic description of the reduced arkose ore Sample

Mineral assemblage and approx. quantity (%)		Mineral description, alteration and mineralisation	
Plagioclase	Major	*Angular to subrounded grains, typically 0.05 to 0.35 mm in size. However, in coarser rocks, grains may reach 9 mm in size. Most grains are fairly fresh, but some have been saussuritised. May occur in lithic fragments, but these are very rare.*	
Quartz	Major	*Angular to subrounded grains typically 0.03 to 0.4 mm in size. However, in coarser rocks quartz may reach 6.5 mm.*	
K-feldspar	Minor	*Mostly microcline occurring in 0.08 to 0.3 mm angular to subrounded grains, which may reach 2.6 mm in coarser rocks. Some grains show alteration to sericite.*	
Chlorite	Minor	*Very fine to 0.210 mm grains (typically 0.08 mm) occurring with smectite as cement between grains of plagioclase, quartz, K-feldspar and less commonly lithic fragments. Some grains appear to be a replacement of biotite.*	
Smectite	Minor	*Very fine to 0.06 mm grains occurring with chlorite as cement between quartz, feldspars and lithic fragments.*	
Carbon	Trace	*0.01 to 1.2 mm grains occurring throughout the sample.*	
Pyrite	Trace	*0.002-0.1 mm anhedral grains. Many are associated with carbon.*	
Muscovite	Trace	*Typically very fine to 0.25 mm, however rare grains reach 0.5 mm. Also sericitic alteration of feldspars.*	
Zircon	Trace	*Well rounded grains between 0.07 and 0.2 mm in size. Some grains are zoned.*	
Rutile	Trace	*0.07 to 0.42 mm angular grains. These appear altered to leucoxene along their periphery.*	
Leucoxene	Trace	*Alteration product of rutile.*	
Chalcopyrite	Trace	*Very rare, 0.01 mm anhedral grains.*	
Alt/Met minerals:		*Sericite, chlorite and leucoxene.*	
Texture and structure:		*Angular to subrounded grains of plagioclase, quartz, K-feldspar and lithic fragments cemented by chlorite and smectite. Rare lithic fragments are also present. These are mainly granite fragments, which occur almost exclusively in the coarser-grained rocks and may reach 6.2 mm in size. The lithic fragments show interlocking textures typical of granites, but rare myrmekitic textures were also observed. In addition to igneous lithics, rare metamorphic lithics also occur in coarser rocks within the composite. These are mainly of deformed quartzite.*	
Veining:		*No veining was observed.*	

Table 3: Petrographic description of the oxidised arkose ore sample from Kayelekera

Lithology: Very coarse arkose

An oxidised arkose dominated by very coarse, anhedral to subhedral sand grains. These consist of quartz, plagioclase, K-feldspar and lithic fragments. The lithic fragments are mainly granitic with similar proportions of quartz, plagioclase and K-feldspar to those seen in the rock as a whole. In addition to the granitic lithic fragments, rare quartzite fragments were also observed. These consist of almost pure quartz. While the quartz in some fragments is polygonal, it also occurs as deformed grains. The quartz, plagioclase, K-feldspar and lithic fragments are cemented by smectite, calcite and, very rarely, quartz. The rock is not strongly altered, but minor alteration of feldspar to sericite, as well as the formation of jarosite and limonite has occurred.

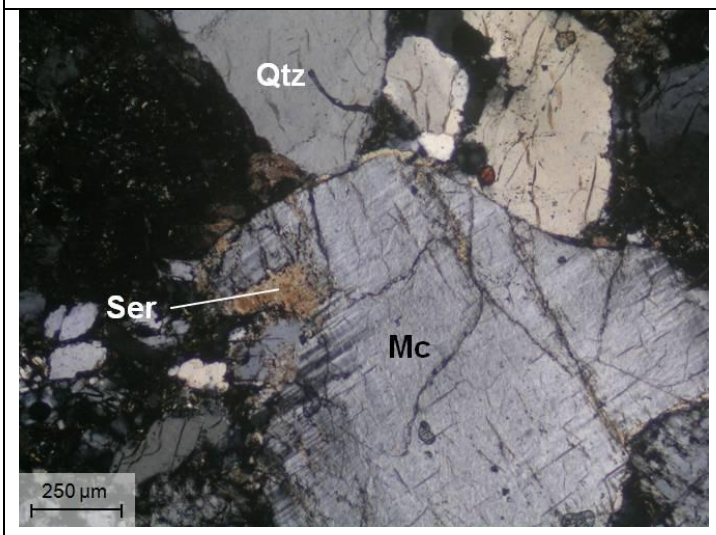

Cross Polarised Light 5x 904

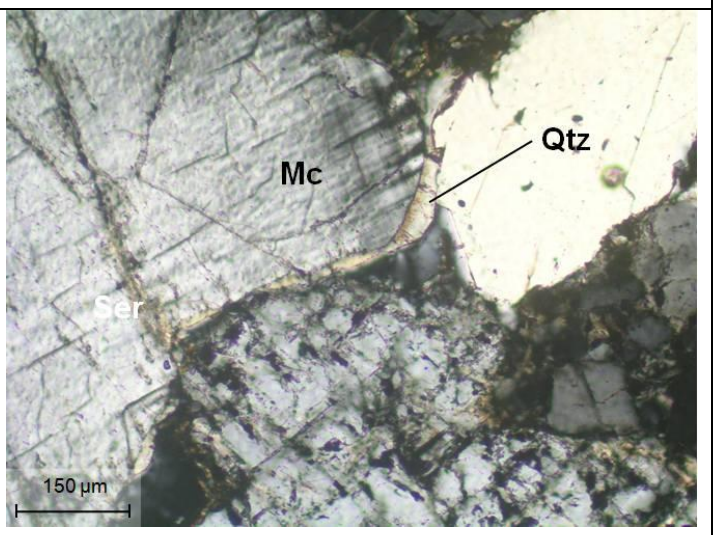

Cross Polarised Light 10 x 905

Quartz (Qtz) and microcline (Mc). The microcline is slightly altered to sericite (Ser) and the sericite is limonite stained (left). Microcline with quartz cement (right).

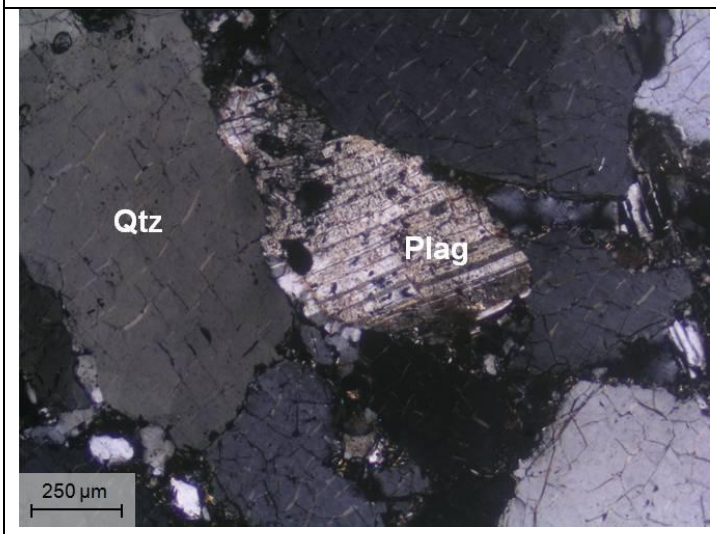

Cross Polarised Light 5x 906

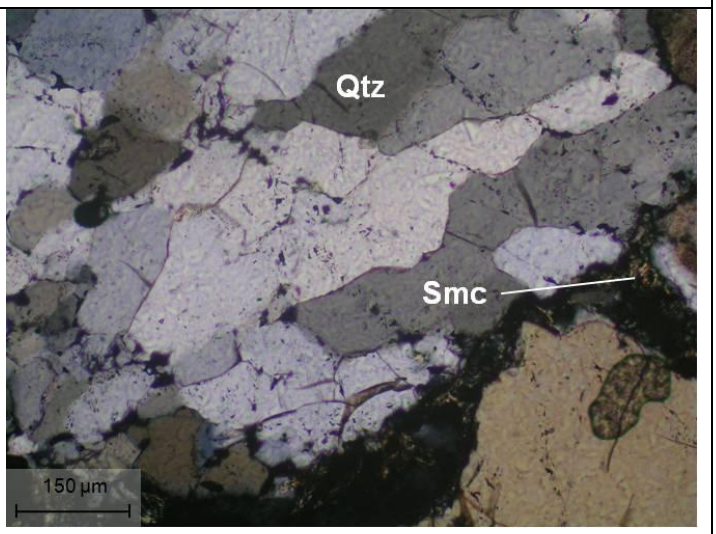

Cross Polarised Light 10x 907

Plagioclase (Plag) and quartz (Qtz) grains (left). Deformed quartz in a quartzite lithic fragment. The fragment is cemented by smeticite (Smc) (right).

Table 3: Petrographic description of the oxidised arkose ore sample

Mineral assemblage and approx. quantity (%)		**Mineral description, alteration and mineralisation**	
Quartz	Major	*0.08 to 3.4 mm (typically 1.4 mm), angular to subrounded detrital grains and a component of rare granite and quartzite lithic fragments. Also occurs as cement in some of the rocks in the composite.*	
Plagioclase	Major	*0.16 to 3 mm (typically 1.6 mm), angular to subrounded detrital grains and a component of rare granite lithic fragments.*	
K-feldspar	Minor	*Mostly microcline occurring as 0.15 to 2.8 mm (typically 2 mm), angular to subrounded grains and as a component of rare granite lithic fragments.*	
Smectite	Trace	*Very fine to 0.3 mm material occurring between quartz, plagioclase and K-feldspar grains. May be acting as cement.*	
Calcite	Trace	*Appears to occur as cement between grains of quartz and feldspar.*	
Muscovite	Trace	*Rare, up to 0.7 mm detrital grains and very fine sericitic alteration of feldspars.*	
Jarosite	Trace	*Not seen in thin section, however, earthy masses of yellow jarosite were seen in hand specimen. These were handpicked from the sample and identified by XRD.*	
Limonite	Trace	*Occurs as staining on other grains and is the cause of the brown coloration.*	
Monazite	Trace	*Subrounded to rounded grains. May reach 0.5 mm in size.*	
Alt/Met minerals:		*Muscovite, jarosite and limonite.*	
Texture and structure:		*The sample is dominated by very coarse sand grains consisting of quartz, plagioclase and K-feldspar, with rare lithic fragments. These grains are angular to subrounded and cemented by calcite and smectite and in some rocks quartz. Most of the lithic fragments are granitic, with a similar proportion of quartz, plagioclase and K-feldspar as seen in the rock as a whole, however quartzite fragments are also present. These fragments consist almost entirely of quartz. In some fragments the quartz is polygonal, while in other quartz grains have been deformed.*	
Veining:		*None observed.*	

Table 4: Petrographic description of the mudstone ore sample from Kayelekera

Lithology: Mineralised mudstone

The rock is dominated by illite-smectite which occurs as fine randomly-orientated grains. Quartz, plagioclase and K-feldspar grains are angular and distributed throughout. Fine carbon is also present. Although U minerals have generally been ignored for the purposes of the optical petrography, one of the fractures contains meta-autunite mineralisation. This mineralisation is sufficiently coarse to be seen in the thin section shown to the bottom right of this table.

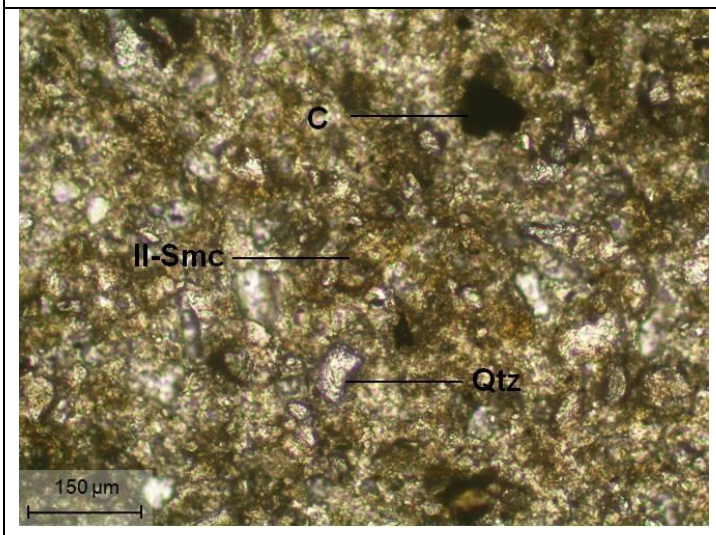

Plane Polarised Light 10x 908

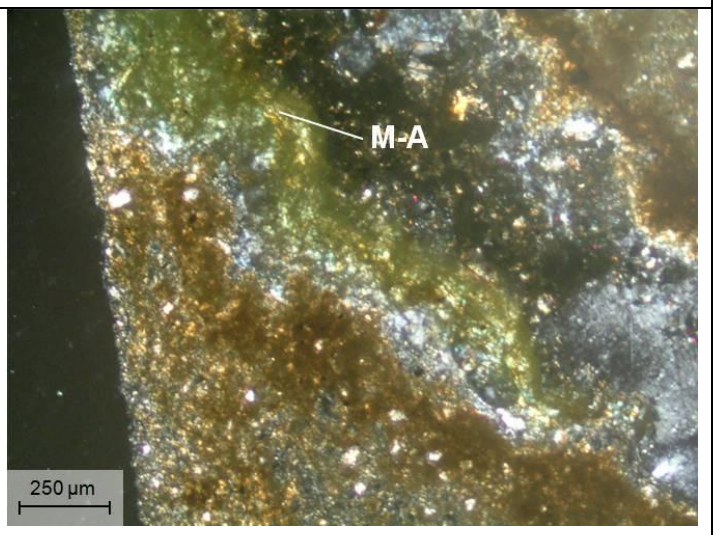

Cross Polarised Light 5x 910

Angular quartz (Qtz) in a groundmass of very fine illite-smectite (Il-Smc). A carbon (C) gain is also shown (left). Meta-autunite (M-A) occurring on the edge of a limonite stained fracture (right).

Mineral assemblage and approx. quantity (%)		**Mineral description, alteration and mineralisation**	
Illite-smectite	Major	*Randomly orientated grains typically very fine-grained, however, rare grains may reach 0.12 mm in size.*	
Quartz	Major	*0.005 to 0.07 mm angular grains occur throughout.*	
Plagioclase	Major	*Similar size and distribution to quartz.*	
K-feldspar	Major	*Similar size and distribution to quartz.*	
Carbon	Trace	*0.01 to 0.13 mm randomly orientated grains of organic carbon.*	
Limonite	Trace	*Staining mostly associated with fractures.*	
Meta-autunite	Trace	*Very fine to 0.2 mm grains occurring along a fracture.*	
Alt/Met minerals:		*Limonite*	
Alt/Met style:		*Limonite staining along the edges of fractures.*	
Texture and structure:		*Fine angular grains of quartz, plagioclase and K-feldspar distributed through a matrix of very fine randomly-orientated illite-smectite.*	
Veining:		*No true veins were observed, however a 1.4 mm wide fracture preserves meta-autunite mineralisation.*	

2.4. Discussion

Petrology

The Mooifontein (Mooi) sample is an arkosic sandstone. The silicate mineralogy, and presence of rare granitic lithic fragments, indicates that the rock had a granitic provenance. The alteration/metamorphic assemblage is indicative of retrograde zeolite facies metamorphism of detrital (originally igneous) grains as well as exposure to surficial conditions. The apparent association between carbon and U may have genetic implications.

Carbon is also present in the reduced arkose ore from Kayelekera (RAO). It is not clear whether the carbon is of bacterial or plant origin, however le Roux (1993) suggested that in the main Karoo basin bacteria consumed detrital organic matter and produced hydrogen sulphide as a by-product. The hydrogen sulphide aided in sulphide formation and also provided the reducing environment required to precipitate U from solution. It is possible that a similar process to that described by le Roux (1993) took place at Mooifontein and Kayelekera, and that this accounts for the apparent association between carbon and U.

Due to the small sample size (one sample from each lithology), it is difficult to be certain whether any conclusions made from examining these samples can be extrapolated to the deposit as a whole. However, in these samples the oxidised arkose ore (OAO) is significantly coarser than the RAO. It is clearly oxidised (as its name suggests), but contains jarosite. Jarosite is not a particularly common mineral, but is sometimes formed from the oxidation of sulphides (Jin-yan *et al.*, 2009 and Norlund *et al.*, 2010). It is possible that the OAO was once more reduced and contained sulphides. When the rock was exposed to oxidising conditions, the sulphides oxidised to from jarosite. It is therefore possible that, similar to the RAO, the uranium in this lithology precipitated in response to the

reducing conditions of the rock (even though the rock now represents oxidised material).

Both the RAO and mudstone ore (MSO) have significantly higher grade than the OAO. The RAO has a grade of 2369 ppm U_3O_8, MSO 1635 ppm U_3O_8, while OAO only has a grade of 387 ppm U_3O_8 (see Chapter 3 on comminution for more detail regarding grade). During the oxidation of the OAO it is possible that some U dissolved and this may account for the difference in grade between the Kayelekera samples.

RAO and OAO both contain granite and quartzite lithic fragments. These fragments suggest that the detrital material was sourced from a granitic provenance which also contained a small amount of quartzitic material. It is possible that these granites also represent the source of the U.

A number of different cements are present in the samples. Mooi is calcite cemented, while the Kayelekera RAO has phyllosilicate cement and OAO shows three different cement types. The dominant types are smectite and calcite, however rare grains are cemented by quartz. While silica cement is rare, its presence indicates that silica-saturated solutions passed through the rock.

Predicted Comminution Characteristics

Comminution is the process of reducing the particle size of an ore, typically by means of crushing and milling (Wills and Napier-Munn, 2006). The strength of a rock is its ability to survive applied forces (for example during comminution) without fracture or failure, and is determined by the nature of the constituent minerals and their cement (Olaleye, 2010). With the exception of rare silica cement in the OAO, the rocks in this study were all cemented by soft minerals (smectite, calcite or both). However, the sand grains (quartz, plagioclase and microcline) do not consist of soft minerals. Because of the softness of the cement,

and hardness of the detrital grains, it is expected that these rocks will mill rapidly, provided the desired grind is coarser than the average size of the sand grains. If the desired grind is smaller than the average size of the sand grains, it will be necessary to mill the harder quartz, plagioclase and microcline, and will result in slower milling rates and increase wear on comminution equipment.

2.5. Summary and Conclusions

Thin sections were prepared from the Mooi, and Kayelekera RAO, OAO and MSO samples. Since the samples are composites it was necessary to prepare a number of thin sections from each sample in order to ensure that the descriptions were an accurate representation of the whole composite. The thin sections were examined using a petrographic microscope under transmitted and reflected light.

Mooi is a very fine arkosic sandstone, with sand grains between 0.03 and 0.25 mm in size. The sand grains consist of quartz, plagioclase and K-feldspar with calcite cement. The presence of zeolite suggests that the rock has undergone zeolite facies metamorphism. Based on hand specimen examination and scintillometer measurements, there appears to be an association between uranium and carbon.

RAO is a medium arkosic sandstone with sand grains consisting of plagioclase and quartz, with minor K-feldspar. The sand has a grain size of between 0.03 and 0.4 mm and is cemented by chlorite and smectite. Trace amounts of carbon are present and there is an association between carbon and pyrite.

OAO is a very coarse arkosic sandstone with sand grains of quartz, plagioclase and K-feldspar typically 1.6 mm in size. These are mainly cemented by smectite and calcite, however very rare quartz cement was also observed.

MSO is a mudstone consisting of illite-smectite as well as very fine quartz, plagioclase and K-feldspar. Trace amounts of carbon are also present and the rock preserves meta-autunite mineralisation that can be seen in hand specimen.

All of the arkosic samples contain rare granite lithic fragments. These (as well as the overall compositions of the rocks) suggest that the detrital material was sourced from a granitic provenance. It is possible that these rocks also served as a source of the uranium.

The reduced nature of most of the samples suggests that redox reactions played a role in the precipitation of U from aqueous solution and may be a major factor in the formation of the mineralisation. Organic carbon occurs in Mooi, RAO and MSO and in RAO there is an association between carbon and pyrite. Le Roux (1993) suggested that in the main Karoo basin bacteria fed off of detrital organic matter and produced hydrogen sulphide as a by-product. The hydrogen sulphide aided in sulphide formation and also provided the reducing environment required to precipitate U from solution. It is possible that a similar process to that described by le Roux (1993) took place at Mooifontein and Kayelekera, and that this accounts for the apparent association between carbon and U and carbon and pyrite.

OAO at first appears to be the exception, as this rock is mineralised, but not reduced. However, there are indications that the rock once contained sulphides, which may suggest that the rock was originally reduced, and has since been oxidised. If this is the case, then reduction may also have controlled U precipitation in this sample. Subsequent oxidation with associated partial dissolution of U may account for the lower grade of this sample when compared to the other Kayelekera samples.

Because the arkosic samples consist of hard sand grains cemented by soft minerals, it is likely that the rocks will mill rapidly provided the desired grind is

coarser than the average size of the sand grains. For this reason it is expected that for a given grind the Mooi sample will mill most rapidly, followed by RAO. Since OAO is significantly coarser than the other arkose samples, it is expected that this sample will mill more slowly, especially if the grind is finer than 1.6 mm. Predicting of the comminution response of MSO was not as simple as the arkose samples.

Chapter 3. Comminution

3.1. Introduction, Aims and Objectives

The purpose of the comminution was to homogenize the samples and produce material of the appropriate particle size and degree of liberation, for the testwork which was to follow.

Crushing

Comminution (or the reduction of ore particle size) is performed for two main reasons. The first is to homogenise material (typically for laboratory testwork) while the second is to liberate the economic mineral (or minerals) from the gangue (Wills and Napier-Munn, 2006). This is achieved by crushing and milling.

During crushing, fracture usually occurs in response to stress applied as the ore is “nipped” between the plates of the crusher (Briggs and Bearman, 1996) or in response to impact (Wills and Napier-Munn, 2006) in the case of impact crushers.

When an ore particle is compressed between the plates of a crusher an area of tensile stress develops within the rock (Figure 2). Existing flaws amplify the stress and the rock fails along the largest flaw (Briggs and Bearman, 1996). Because a crack may be stopped when it reached a crystal boundary, or when it encounters another crack, fine-grained rocks tend to be tougher than coarser rocks (Wills and Napier-Munn, 2006).

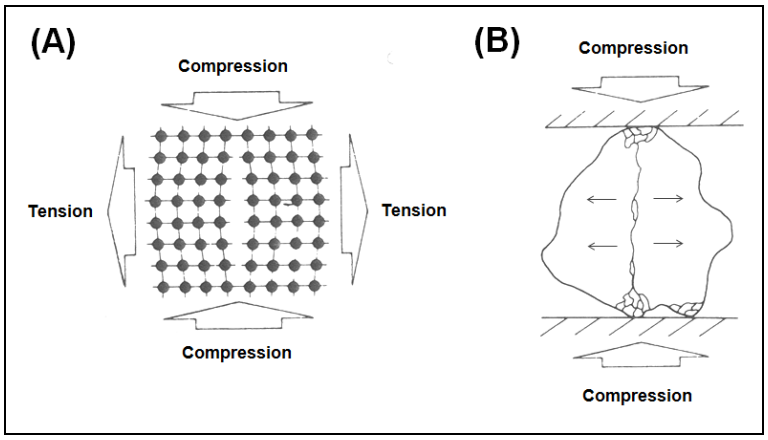

Figure 2: Response of a crystal (A) and rock (B) to compressive forces applied during crushing (Wills and Napier-Munn, 2006).

There are a number of different crusher types, these include the jaw crusher, impact crusher, roll crusher and cone crusher.

The jaw crusher consists of two plates. Typically, one is fixed while the other is attached to an eccentric. As the eccentric rotates one plate moves towards and away from the other. The ore is fed into the crusher and repeatedly nipped and released as it moves down between the crusher plates (Wills and Napier-Munn, 2006). Jaw crushers are designed for heavy duty and continuous operation with long machine life (Olaleye, 2010). Figure 3 illustrates the operation of a jaw crusher.

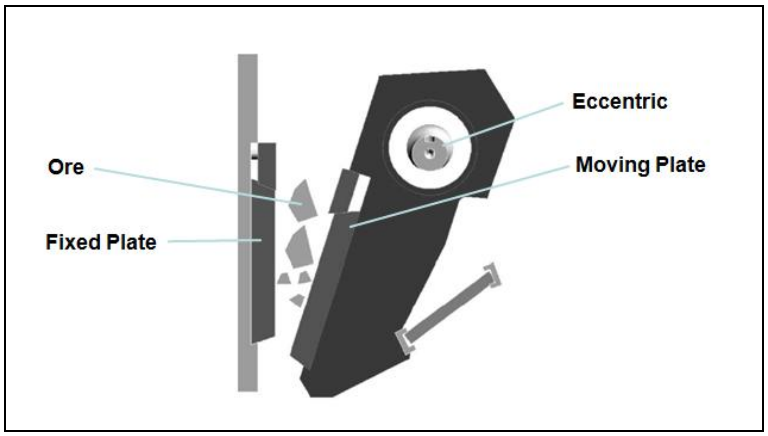

Figure 3: Schematic diagram of a jaw crusher (Lindqvist and Evertsson, 2003).

In impact crushers, breakage is achieved by propelling rock fragments into a hard surface by means of a spinning disk (Briggs and Bearman, 1996) (Figure 4). These crushers are preferred for the production of aggregate (Bengtsson and Evertsson, 2006). This is because the impact crusher exploits existing weakness in the material, while creating significantly less weakness and retained stress in the resulting crushed material (when compared to crushers in which the rock is pinned between two rigid surfaces), and therefore yield a stronger product (Briggs and Bearman, 1996).

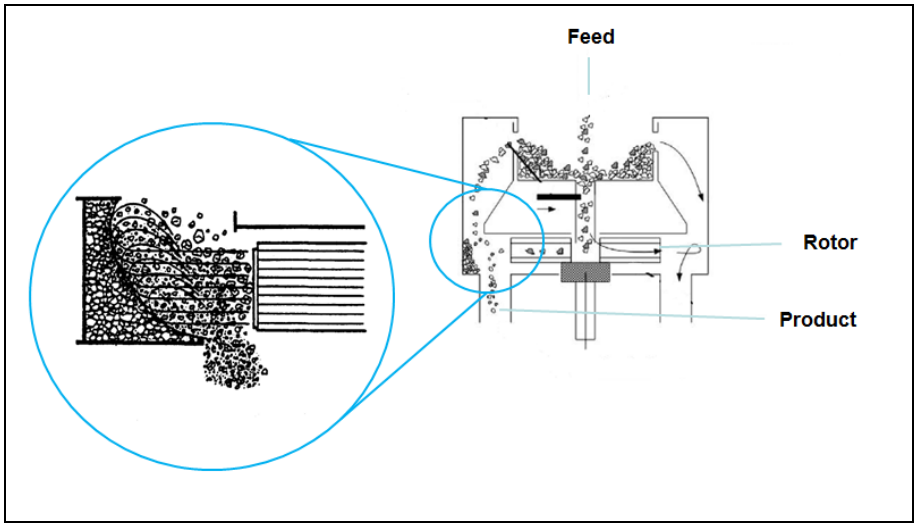

Figure 4: Schematic diagram of an impact crusher (Briggs and Bearman, 1996 and Bengtsson and Eversson, 2008).

Roll crushers typically consist of two horizontal cylinders, although non-cylindrical roll crushers have also been developed (Vellertri and Weedon, 2001). These cylinders revolve towards each other. The rock to be crushed is fed between the cylinders. As the rock passes between the cylinders, they apply a crushing force which results in size reduction (Wills and Napier-Munn, 2006).

Although roll crushers are able to handle wet, sticky, friable and frozen ores, and are the most energy efficient of the crushers (Wills and Napier-Munn, 2006 and Vellertri and Weedon, 2001), there are significant disadvantages associated with their use. These include high wear rates, and relatively low reduction ratios (~3:1),

although some success has been achieved in increasing these reduction ratios by the use of non-cylindrical configurations (Vellertri and Weedon, 2001).

Because of these limitations, cone crushers are often preferred to roll crushers (Wills and Napier-Munn, 2006). Cone crushers consist of a moving mantle within an immobile concave (Figure 5). The mantle is attached to an upper (concentric) bearing and a lower (eccentric) bearing. Rotation of the eccentric causes oscillation of the mantle, which results in the crushing of rock between the mantle and concave (Lindqvist and Evertsson, 2003). The close side setting (CSS) is the shortest distance between the mantle and the concave (Lindqvist and Evertsson, 2006). This distance can be adjusted by either a hydraulic mechanism or a thread, which make it possible to change the position of either the mantle or concave depending on the crusher type (Hulthén and Evertsson, 2011).

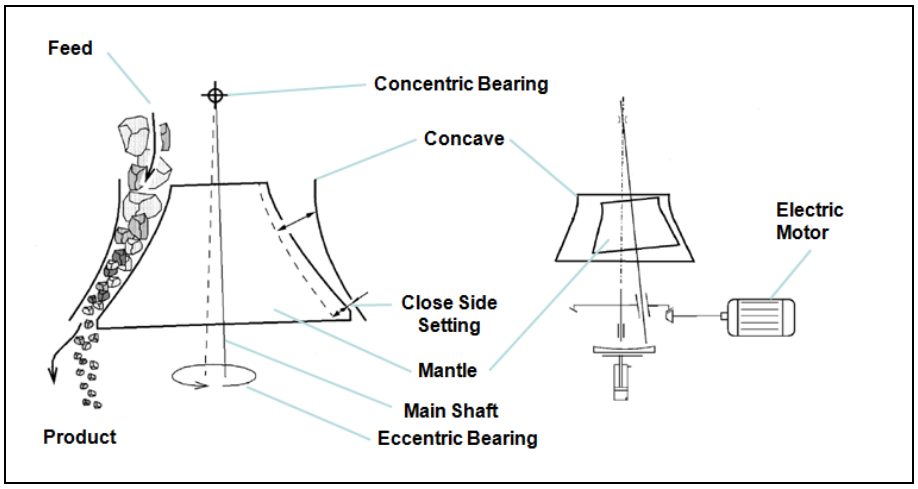

Figure 5: Schematic diagrams of a cone crusher (Lindqvist and Evertsson, 2006).

It is usually not possible to achieve the desired particle size in a single crushing stage. There are two different approaches to crushing circuits, open circuit and closed circuit, where closed circuit offers greater control over the particle size of the resulting product (Wills and Napier-Munn, 2006). Open and closed circuit configurations are illustrated in Figure 6.

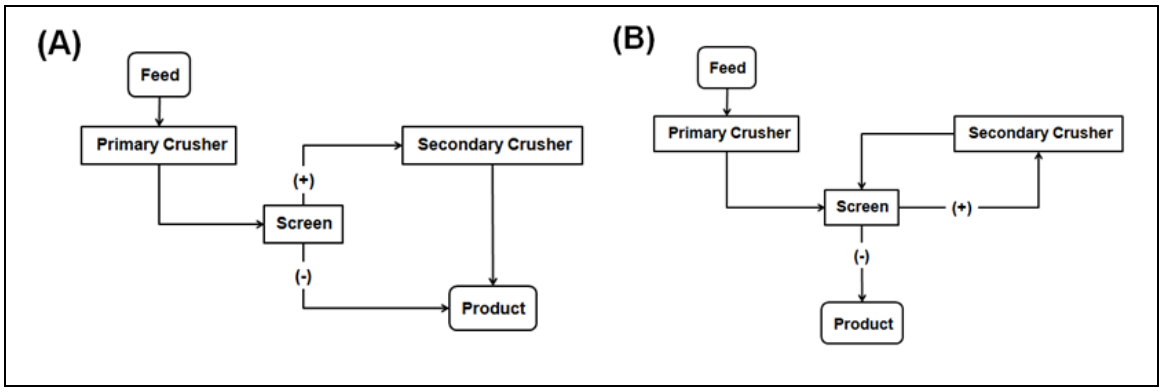

Figure 6: Open (A) and closed (B) circuit crushing configurations (Wills and Napier-Munn, 2006).

Because of the robust nature of jaw crushers, they are typically used as primary crushers (Olaleye, 2010). The choice of secondary crusher differs with application.

Milling

The main reason for milling is to achieve the degree of exposure of the ore minerals necessary for later processing steps. Undergrinding results in incomplete mineral liberation, while overgrinding wastes energy (Wills and Napier-Munn, 2006). Comminution consumes large amounts of energy. It has been estimated that as much as 4% of global electricity production is used in comminution (Fuerstenau *et al.*, 1999). Optimising mill efficiency can therefore have significant cost benefits.

There are a number of different mill types. These include ball mills (Kotake *et al.*, 2004), rod mills (Rogovin, *et al.*, 1988), roll mills (Fuerstenau *et al.*, 1999), semi-autogenous grinding (SAG) mills (Michaux and Djordjevic, 2005) and fully autogenous grinding (FAG) mills (Loveday, 2004). With the exception of the roll mill, these are all considered tumbling mills. Tumbling mills consist of horizontal rotating cylinders. These cylinders enclose the grinding medium (for example balls or rods) and the ore. Together the ore and medium make up the mill charge (Wills and Napier-Munn, 2006).

In addition to costs associated with energy consumption, the consumption of grinding medium also contributes to the cost of running a mill. Ball and rod mills consume between 0.1 and 1 kg of the grinding medium per ton of ore (Wills and Napier-Munn, 2006). However, not all mills are fully reliant on the action of rods or balls. FAG mills rely on the ore itself to act as the grinding medium, while SAG mills only contain a small amount of medium (usually balls), which serve to aid grinding (Wills and Napier-Munn, 2006).

SAG and FAG mills have gained in popularity because they offer reduced capital costs, even though they are typically less energy efficient than ball or rod mills (Johnson, *et al.*, 1994). However, SAG and FAG mill circuits are higher risk than ball and rod mills, mainly because they are more sensitive to changes in ore characteristics (Bradford *et al.*, 1998). For this reason autogenous methods have been avoided in the present study.

Cilliers *et al.* (1994) determined the motion of an individual rod within a rod mill by placing a light emitting diode within the end of a rod. This was viewed through 20 mm glass that was used to close one of the mill ends. The position of the rod was recorded at intervals of 1/25 of a second. The results of their investigation are illustrated in Figure 7.

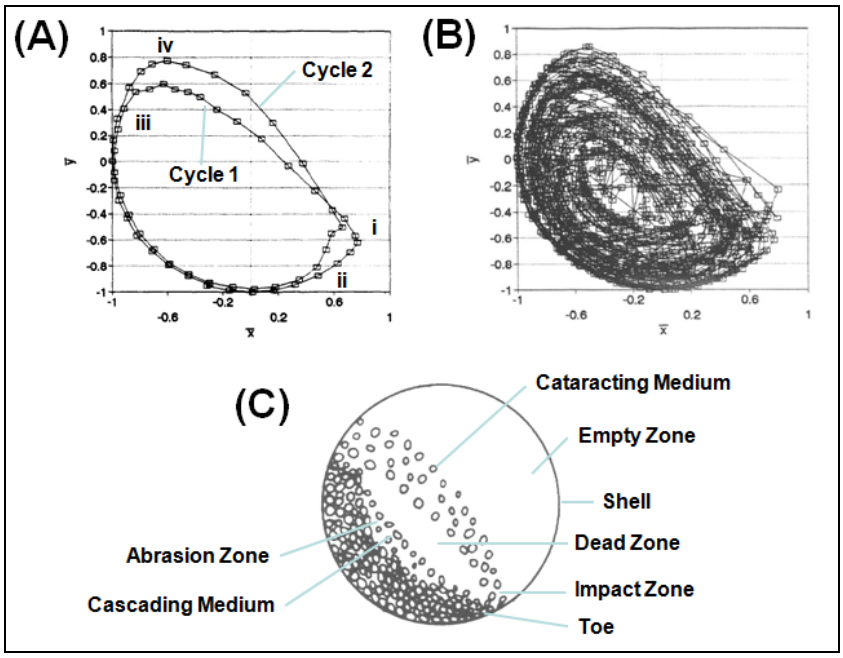

Figure 7: Movement of an individual rod within a rod mill. (A) shows the first two cycles, (B) shows a large number of cycles (Cilliers *et al.*, 1994). (C) is a schematic representation of the motion of grinding medium within a tumbling mill after Wills and Napier-Munn (2006). At point i the rod has essentially no velocity. Between i and ii the rod enters the toe and accelerates to match the speed of the mill shell. From ii to iii the rotation of the mill imparts gravitational potential energy to the rod. From iii to iv the rod leaves the circular path of the mill shell and from iv the rod accelerates as it descends down to point i (Cilliers *et al.*, 1994). Depending on how the medium (rod or balls) descend they are considered to either cataract or cascade. Cataracting medium results in breakage by impact while cascading medium causes breakage by abrasion (Wills and Napier-Munn, 2006).

In a tumbling mill, size reduction is widely thought to be the result of particles being nipped between the grinding medium (balls or rods), however there is evidence to indicate that grinding motions resulting from load and shear stresses also play a significant role (Cleary and Morrison, 2011). Therefore particle size reduction is the result of either impact or abrasion. Cataracting medium results in impact breakage, while cascading medium tends to reduce particle size by abrasion (Wills and Napier-Munn, 2006). Impact breakage is considered to be the more energy efficient breakage mechanism (Johnson, *et al.*, 1994).

The relative proportion of cataracting and cascading medium is determined by the mill speed, with cascading occurring at lower speeds and cataracting at higher speed. If the speed is increased further, a speed is reached when centrifugal forces prevent the charge from falling, and the charge maintains a

fairly constant position relative to the shell. This is known as the critical speed and can be determined by Equation 1 (Wills and Napier-Munn, 2006).

$$Nc = \frac{42.3}{(D - d)^{1/2}}$$

Equation 1

Where Nc is the critical speed (in rpm), D is the mill diameter (in metres) and d is the rod or ball diameter (in metres).

Ball mills typically operate at 70-80% of the critical speed, while rod mills operate at lower speeds (50 to 65% of the critical speed) (Wills and Napier-Munn, 2006).

3.2. Methodology

The crushing and milling methodology is illustrated in Figure 8.

Crushing

The particle size of the “as received” samples was too large to be accommodated by the laboratory scale jaw crusher. The samples were therefore manually broken using a hammer and thick steel plate. The resulting material was then sufficiently fine to be crushed by the jaw crusher.

Multiple crushing stages were used to achieve a size of 100% passing 3 mm. The jaw crusher was used as the primary crusher because of its robust nature, and to maintain consistency with typical plant practice (Olaleye, 2010). Cone crushers (with two different close side settings) were used for the secondary and tertiary crushing. These were chosen over impact crushers because of the more pervasive damage they cause to the resulting particles (Briggs and Bearman,

1996). A closed crushing circuit was used to control the particle size to the maximum extent possible.

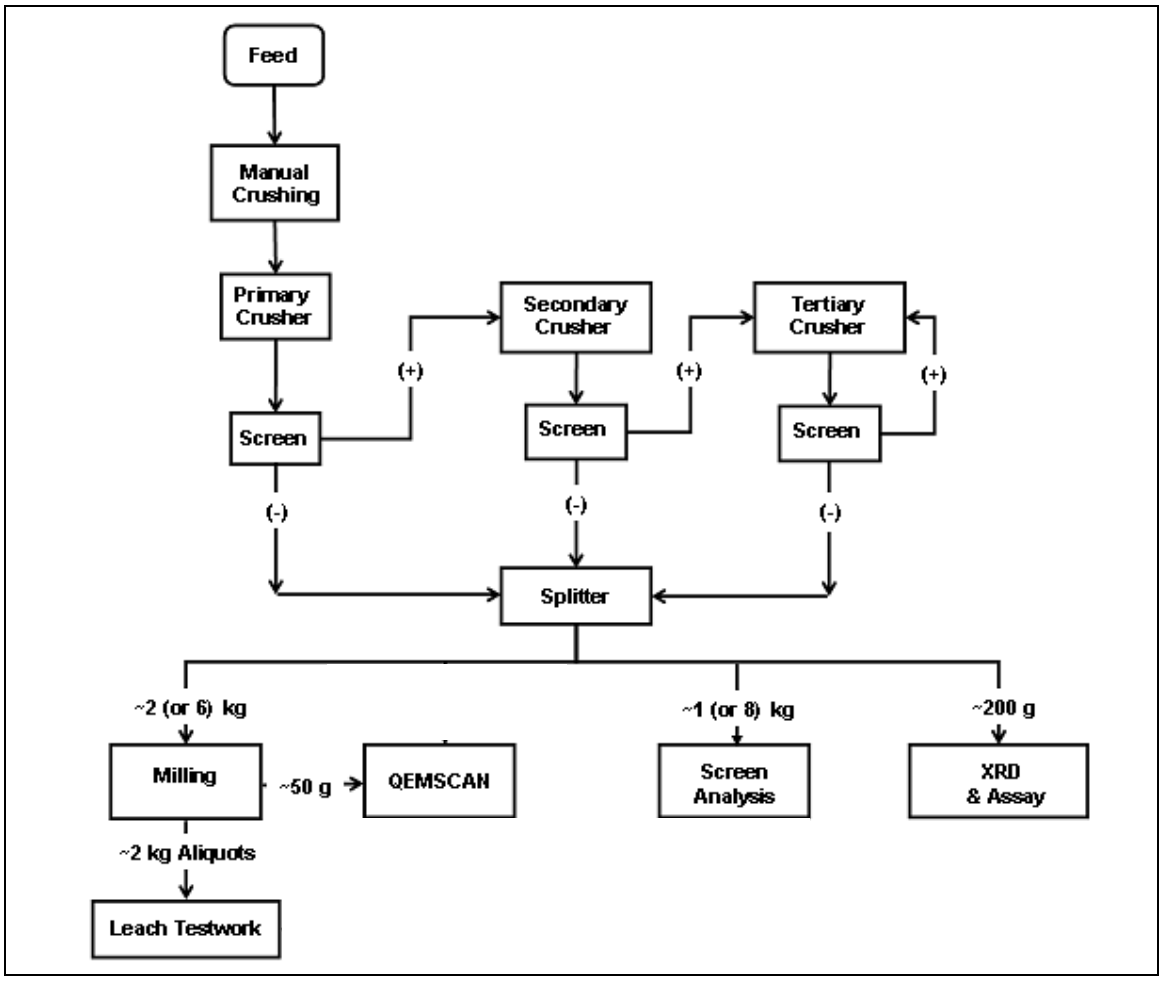

Figure 8: Flow diagram illustrating the crushing, milling and screening procedure. Because of the additional material, it was possible to use larger masses for the Mooi sample than the Kayelekera samples. The masses of the Mooi sample are given in brackets.

The crushed material was then split into a number of different aliquots. Initial splitting made use of a riffle splitter, which reduced the masses of the subsamples to a size that could be handled by a rotary splitter. All subsequent splitting was done using a rotary splitter.

An aliquot was split off and pulverized for XRD and geochemical analysis. Aliquots were also split off for QEMSCAN analysis, screen analysis, and milling. While the XRD, major element geochemical analysis and QEMSCAN analyses

are discussed in later chapters, the screen analysis and milling are discussed below.

Screen Analysis

One kilogram aliquots of the Kayelekera samples, and an 8 kg aliquot of the Mooi sample were screened into 6 fractions (-3 mm/+850 µm, -850/+425 µm, -425/+212 µm, -212/+106 µm, -106/+53 µm and -53 µm). These sizes were selected such that each screen size is typically half the size of the previous screen.

Milling

Approximately 1 kg aliquots were milled using a laboratory-scale rod mill. The rod mill was chosen in preference to the ball mill because it tends to produce a narrower range in size distribution (Wills and Napier-Munn, 2006). The mill case had a diameter of 245 mm, a length of 300 mm and weighed 13.22 kg. The rods were 285 mm in length and had three different diameters. Seven rods had a 13.5 mm diameter, 11 rods had a 15 mm diameter, and 16 rods had an 18.5 mm diameter. The rods had a combined mass of 16.14 kg.

Using the above configuration Equation 1 gives a critical speed of 88.5 rpm. A speed of ~45 rpm was used for the milling tests. This is ~51% of the critical speed and falls within the usual range (50 to 65 rpm) in which rod mills are usually operated (Wills and Napier-Munn, 2006).

A grind of 80% passing 212 µm was chosen based on screen analyses of the crushed material. It was decided that this grind would result in acceptable levels of exposure of uranium minerals, without requiring excessive grinding of the ore.

In order to achieve the desired grind, it was necessary to mill a subsample for a short period and then screen it to determine the proportion of -212 µm material. Great care and long screening times were necessary for the MSO sample because of the tendency to form agglomerates that would not pass easily through the screen.

Initially the full 1 kg subsample was screened, but it was found that screening ~100 g of material gave results that compared very well with those obtained by screening of the entire subsample. Thereafter only ~100 g of material was screened after each period of milling. After screening and weighing, the material was then returned to the mill for the next phase of milling.

Because 2 kg of milled material was required for each of the Kayelekera samples, and 6 kg from the Mooi sample, it was not possible to mill the full amount of material at once. Therefore a milling curve was produced by plotting the percentage passing 212 µm as a function of time. The curve made it possible to determine the exact amount of time needed to achieve the desired grind for a particular sample. The curve was produced from the first subsample of each of the samples, and subsequent subsamples could then be milled to the desired grind without the need for repeated screening and milling.

Due to the large amount of Mooi material available, it was possible to grind material from this sample to two different sizes. In addition to the 212 µm aliquots, a 2 kg aliquot of Mooi material was ground to 80% passing 75 µm. This is also known as a P_{80} of 75 µm. This finer grind was included to provide information on the effect of grind on reagent consumption and U dissolution, but would also illustrate the relationship between rock texture and milling hardness at a second (finer) grind.

3.3. Results

Crushing and Screen Analysis

The results of the screen analysis are given in Table 5 and presented graphically in Figure 9. There appears to be a bimodal distribution in the Mooi sample. In the coarser fractions the grade and distribution follow the mass of the sample, but there is also a slight upgrade in the fine fraction. Although there is an upgrade, it only accounts for a small amount of the uranium distribution.

The RAO and OAO from Kayelekera were both upgraded in the fine fractions.

The MSO sample was downgraded in the +850 µm fraction, with corresponding upgrades in the finer fractions. However, the intermediate fractions are higher grade than the fine fractions.

Table 5: Results of the screen analysis showing the proportion of the sample mass, as well as the uranium grade and distribution across the size fractions

Mooifontein				
Screen Fraction	**Mass**		**U_3O_8**	
(µm)	**(g)**	**(%)**	**Grade (ppm)**	**Distribution (%)**
-3000/+850	2475.44	31.40	272	34.2
-850/+425	1423.64	18.06	272	19.7
-425/+212	1060.14	13.45	261	14.0
-212/+106	1199.44	15.22	169	10.3
-106/+53	754.22	9.57	223	8.5
-53	969.52	12.30	272	13.4
Total	**7882.4**	**100.0**	**250***	**100**
Kayelekera Reduced Arkose Ore				
Screen Fraction	**Mass**		**U_3O_8**	
(µm)	**(g)**	**(%)**	**Grade (ppm)**	**Distribution (%)**
-3000/+850	196.83	22.40	1835	17.3
-850/+425	227.25	25.86	1794	19.6
-425/+212	174	19.80	1976	16.5
-212/+106	118.14	13.44	2465	14.0
-106/+53	70.14	7.98	3211	10.8
-53	92.41	10.52	4903	21.8
Total	**878.77**	**100.0**	**2369***	**100**
Kayelekera Oxidised Arkose Ore				
Screen Fraction	**Mass**		**U_3O_8**	
(µm)	**(g)**	**(%)**	**Grade (ppm)**	**Distribution (%)**
-3000/+850	335.78	36.25	198	18.5
-850/+425	253.65	27.38	252	17.8
-425/+212	151.48	16.35	364	15.4
-212/+106	85.64	9.24	600	14.3
-106/+53	46.95	5.07	807	10.6
-53	52.91	5.71	1583	23.3
Total	**926.4**	**100**	**387***	**100**
Kayelekera Mudstone Ore				
Screen Fraction	**Mass**		**U_3O_8**	
(µm)	**(g)**	**(%)**	**Grade (ppm)**	**Distribution (%)**
-3000/+850	383.18	44.56	642	17.5
-850/+425	186.71	21.71	2113	28.1
-425/+212	109.88	12.78	2962	23.2
-212/+106	75.49	8.78	2779	14.9
-106/+53	49.53	5.76	2501	8.8
-53	55.09	6.41	1925	7.5
Total	**859.9**	**100**	**1635***	**100**

*Weighted mean of the screen fractions.

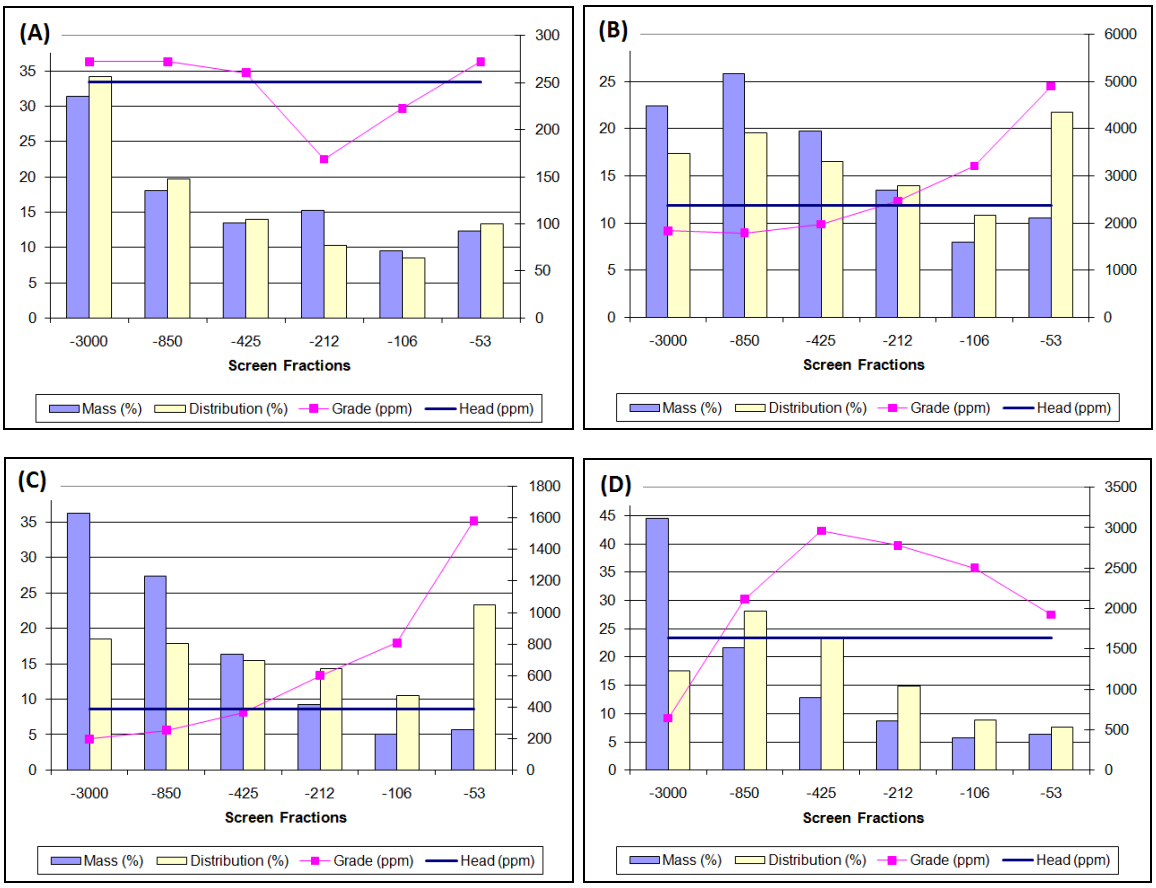

Figure 9: Graphical representation of the results of the screen analysis. Sample mass, uranium grade and distribution data for the Mooi (A) sample and Kayelekera RAO (B), OAO (C) and MSO (D) samples are show for each screen fractoin. The masses represent the mass distribution of each of the screen fractions, the grades are the uranium grade in ppm U_3O_8 and the distributions are the proportion of the total uranium hosted by each fraction.

Milling

The results of the 212 µm milling tests are given in Table 6, and presented graphically in Figure 10. During these tests the Mooi sample milled the quickest, followed by the Kayelekera RAO, while the OAO and MSO took significantly longer to achieve the desired grind.

Table 6: Percent of the sample milled to passing 212 µm after various milling intervals

Mooifontein		Reduced Arkose Ore	
Time (min)	**Passing 212 µm (%)**	**Time (min)**	**Passing 212 µm (%)**
0.00	37.08	0.00	31.94
2.00	55.09	2.00	50.09
4.00	67.99	3.63	61.77
6.00	77.86	6.63	74.00
8.00	88.01	9.13	84.35
6.42*	**80.00**	**8.08***	**80.00**
Oxidised Arkose Ore		**Mudstone Ore**	
Time (min)	**Passing 212 µm (%)**	**Time (min)**	**Passing 212 µm (%)**
0.00	20.02	0.00	20.95
2.00	33.88	2.00	34.28
4.00	42.63	5.58	45.63
7.00	53.42	17.20	75.42
20.00	87.79	20.20	82.41
17.05*	**80.00**	**19.17***	**80.00**

* Calculated time required to reach 80% passing 212 µm.

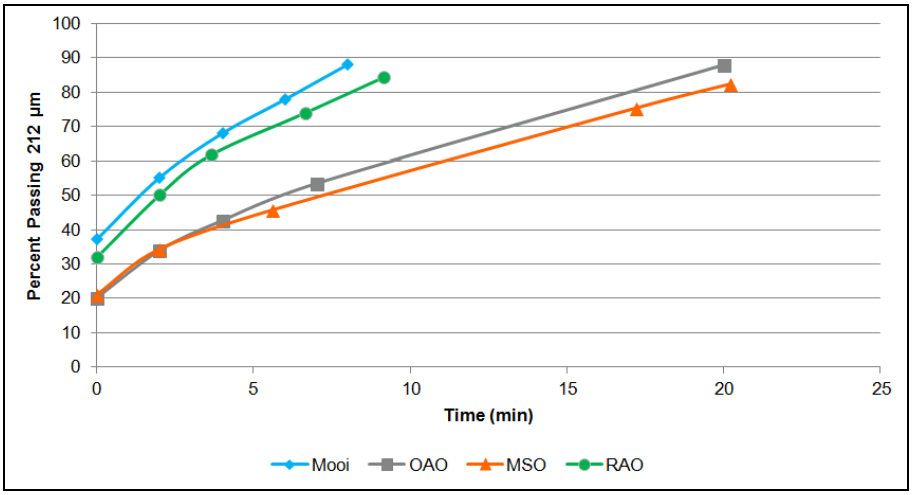

Figure 10: Milling curves illustrating the size reduction of each of the samples as a function of time.

After the initial 2 minute interval the MSO began to form agglomerates. These consisted of lumps of very fine milled material. These agglomerates were loose in the ore, but also adhered to the rods and mill casing. This resulted in

difficulties in removing the ore from the mill, and in screening the material to produce the milling curve. It was necessary to screen the MSO samples for at least twice as long as Mooi or RAO. It was also necessary to manually break agglomerates during the screening to ensure that finer particles could pass through the screen.

The results of milling Mooi to a P_{80} of 75 µm are given in Table 7. The milling of this sample required much longer milling times and produced a much flatter milling curve (Figure 11) than was seen in any of the 212 µm milling tests.

Table 7: Percent of the Mooi sample passing 75 µm after various milling intervals

Time (Min)	Passing 75 µm (%)
0.00	16.75
10.00	31.80
42.00	82.08
40.67*	80.00

* Calculated time required to reach 80% passing 75 µm.

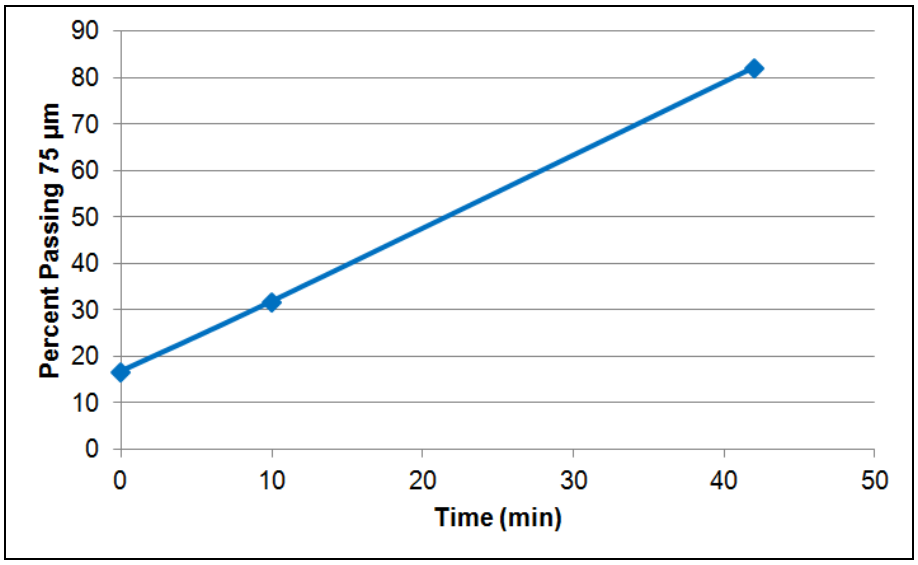

Figure 11: Milling curve used to determine the time needed to grind Mooi to a P_{80} of 75 µm.

Ideally, in order to quantitatively determine the rate of milling, the derivative of the milling curve with respect to time should be determined. This would yield the instantaneous rate of size reduction (in units of percent passing 212 (or 75) µm per minute). However, while it was reasonably easy to fit quadratic functions to the curves of the arkosic samples, an acceptable fit was not found for the MSO. Therefore instead of using a more desirable instantaneous rate, it was necessary to determine average milling rates between individual data points. This produced very acceptable results for the first milling interval, since each of the samples 212 µm had the same (2 minute) milling interval. Since later intervals varied in duration, it was more difficult to accurately compare these. However, as can be seen from Figure 10, the milling curves tend to be flat during the last milling interval. Because the curves are flat, an average gradient is a fair approximation of the instantaneous gradient, and this makes it possible to quantitatively compare the milling rates for this interval. Table 8 lists the average gradient of the milling curves in the first and last milling intervals.

The rates of size reduction of the 75 µm milling were very different from those seen in the 212 µm milling tests. The comparison between the tests at the different grinds is complicated by the differences in the durations of the milling intervals, however, it can be seen that the 75 µm milling produced a much flatter curve (Figure 11) with very similar initial and final rates. In contrast to the 212 µm milling tests, the last milling interval had a slightly faster rate than the initial interval (however, the difference is slight and may be due to experimental error).

Table 8: Comparison of the rates of size reduction during the initial and final milling periods

-	Grind	First Interval	Last Interval
Units	**µm**	**% Passing Desired Size/min**	
Mooi	**212**	9.00	5.07
Mooi	**75**	1.50	1.57
RAO	**212**	9.08	4.14
OAO	**212**	6.93	2.64
MSO	**212**	6.67	2.33

3.4. Discussion

Crushing and Screen Analysis

In the Mooi sample there appears to be a bimodal distribution. In the coarser fractions the U grade and distribution follow the mass of the sample (i.e. the majority of the U occurs in the fractions which also host the majority of the sample mass). This suggests that the U has not been liberated from the gangue and therefore the U distribution is controlled by the size of the associated gangue. There is also a slight upgrade in the fine fraction. This upgrade is probably due to liberated uranium mineral grains that were concentrated in the fine fractions. However, although there is an upgrade, it only accounts for a small amount of the contained uranium.

RAO and OAO were both upgraded in the fine fractions. This suggests that the material represented by these samples is amenable to upgrade by size classification. It also suggests that the uranium minerals are likely to be reasonably well liberated even though the samples have a fairly coarse particle size distribution (100% -3 mm).

MSO was downgraded in the +850 µm fraction, with corresponding upgrades in the finer fractions. However, the intermediate fractions were higher grade than the fine fractions. This suggests that the uranium is either poorly liberated or occurs in fairly coarse grains. Visual inspection of the sample prior to crushing found bright green grains of a uranium mineral (identified as meta-autunite by XRD). Many of these were several millimetres in size, suggesting that the grade and distribution characteristics of this sample were caused by coarse grain size, rather than poor liberation.

Milling

The gradient of the 212 µm milling curves (Figure 10) indicate the rate at which the size of the sample was reduced. Each of the curves shows an initial rapid rate of size reduction, followed by a flattening of the curve. It is likely that this initial rapid size reduction occurred because of breakage along particular zones of weakness. These probably represent residual damage from the crusher, as well as poorly cemented clastic material. As these zones of weakness became less abundant, most of the size reduction was achieved by breaking of intact cement, or the clastic grains. Since these were significantly tougher than the damaged, or poorly cemented material, the rate of milling decreased.

The RAO had the highest initial milling rate, and the second highest final milling rate. These high milling rates are likely to be due to the nature of the cement in this sample. Since the clastic grains are cemented by smectite and chlorite, milling proceeded rapidly.

The Mooi sample had very similar milling characteristics to the RAO sample. However, there was a smaller reduction from the initial to the final milling rate. This is probably due to the fine grain-size of the quartz and feldspar (typically less than 250 µm). Therefore breakage along the weaker carbonate cement would result in most grains achieving a size that would pass through the 212 µm screen.

The OAO had the lowest initial and final milling rates of the arkose samples. Although some of the rocks in this sample showed silica cement, this cement is very rare and most of the sample is cemented by smectite. The large size of the quartz, plagioclase and K-feldspar was the reason for the low milling rates. Because the average sand size (about 1.6 mm) is significantly coarser than the desired grind, it was necessary to mill the sand grains, rather than breaking the softer cement (as occurred in Mooi and RAO).

Although the MSO contains a higher proportion of softer minerals than the arkosic samples, and a finer grain size, it had similar milling characteristics to the OAO sample. It is likely that the reason for the low milling rate was that agglomerates had began to form, and that significant amounts of energy were consumed in the breaking up of agglomerates, rather than in producing particle size reduction.

The 75 µm of Mooi was characterised by a very flat milling curve and longer milling times. This was because many of the sand grains were coarser than 75 µm. It was therefore necessary to break the quartz, plagioclase and K-feldspar rather than the softer calcite cement.

Assuming that the power consumption of the mill is fairly constant, then the energy consumption in achieving the desired grind is proportional to time. This is a fairly reasonable assumption because all the tests made use of the same mill, with the same charge of rods and very similar masses of ore (~1 kg). The only major difference between each of the milling tests would therefore be the nature of the ore. Since the ore only accounted for ~3.3% of the combined mass of the mill and ore (~1 kg ore versus 16.14 kg rods and 13.22 kg mill casing), it is unlikely that small differences in the nature of the ore would result in significant changes in the power consumption of the mill. The only possible exception may be the MSO sample, where the sticky nature of the ore may have stabilised the rod pile, and allowed the individual rods to achieve a greater height (and therefore consume greater energy) than would be possible without the stabilising effect of the ore. Therefore the mill may have consumed slightly more energy per unit time when milling the MSO sample. However for the sake of comparison, it was assumed that this effect is small.

Therefore assuming constant power consumption by the mill, the Mooi sample required the least energy to mill to a P_{80} of 212 µm. By comparison with the Mooi

sample the RAO sample used 1.26 times as much energy, the OAO sample consumed 2.66 times as much energy and the MSO sample consumed 2.99 times as much energy.

Milling Mooi to a P_{80} of 75 µm required 6.33 times as much energy as milling to 212 µm. Due to this significant increase in energy consumption (and associated wear of equipment), it would be important to determine if the benefits of using such a fine grind would justify the costs.

3.5. Summary and Conclusions

Due to the coarse size of the rocks in each of the composites, it was necessary to manually crush the rock prior to mechanical crushing. A three stage closed crushing circuit was used to reduce the particle size to 100% passing 3 mm. The primary crusher was a laboratory scale jaw crusher, while the secondary and tertiary crushers were cone crushers with different CSS settings.

An aliquot of each sample was screened in to 6 fractions and the fractions were assayed for U and Th content. The Mooi sample had a bimodal U distribution. In the coarser fractions the U distribution follows the mass of the sample, but with a slight upgrade in the fine fraction. This suggests that the U was only partially liberated, with the coarser fractions containing locked U and the slight upgrade in the fines due to liberated grains.

Both RAO and OAO were upgraded in the fine fractions, suggesting that the U in these samples was fairly well liberated (even at this coarse particle size). This suggests that these rocks could be amenable to upgrade by size classification (although a finer grind will be necessary).

MSO had the highest grades in the intermediate fractions. Rather than being the result of incomplete liberation, the U distribution was due to the unusually large size of meta-autunite grains in this sample.

One kilogram aliquots of each sample were milled in a laboratory scale rod mill to produce material for the leach tests and QEMSCAN analyses. The rod mill was run at 51% of the critical speed. The desired grind was 80% passing 212 µm. Milling curves, which record the particle size reduction as a function of time, were also produced during the milling tests.

Each of the curves shows an initial more rapid rate of size reduction, followed by a flattening of the curve. It is likely that this initial rapid size reduction occurred because of breakage along particular zones of weakness. These probably represent residual damage from the crusher, as well as poorly cemented clastic material. As these zones of weakness became less abundant, the rate of milling decreased and the curves became more flat.

Since both the Mooi and Kayelekera RAO samples have soft cement (calcite and phyllosilicate respectively) and sand grains that are finer than the desired grind, these samples milled quickly. The MSO milled slowly due to the formation of agglomerates. Significant amounts of energy were spent breaking these agglomerates, rather than reducing the size of the ore particles.

The OAO also milled slowly even though this sample has similar cement to the other arkose samples. The reason for the low milling rate was the size of the quartz, plagioclase and K-feldspar sand. Since these grains were significantly coarser than the desired grind, it was necessary to break the sand grains, rather than causing breakage along the softer cement.

Assuming fairly constant energy consumption by the mill, Mooi had the lowest power consumption, while RAO used 1.26 times as much energy, the OAO

sample consumed 2.66 times as much energy and the MSO sample consumed 2.99 times as much energy.

It may be possible to save energy in the milling of MSO material either by using a coarser grind, or by milling MSO with arkosic material. Since the meta-autunite in this sample is particularly coarse, a coarser grind would still allow for acceptable liberation. Alternatively milling MSO with arkosic material may reduce the tendency to produce agglomerates and could improve milling rates.

Milling of Mooi to a P_{80} of 75 µm required 6.33 times as much energy as milling to 212 µm, even though 75 is not a third as fine as 212 µm. This significant change in energy requirements is due to the size of the sand grains in Mooi. Because 212 µm is coarser than many of the sand grains, it was not necessary to break the harder detrital grains to reach this grind. However, 75 µm is finer than the detrital grains and required the breaking of quartz, plagioclase and K-feldspar, rather than the softer cement.

3.6. Recommendations

Additional tests are recommended to determine the optimal grind for leaching of material from Mooifontein and Kayelekera. These tests could involve crushing a set of bulk samples, then splitting these into a number of aliquots. These aliquots could then be milled to various particle sizes and either examined by QEMSCAN, or acid leached, to determine the effect of grind on U exposure. Blending of mudstone and arkosic ore should also be investigated, in order to determine if this would result in a reduction in the time taken to mill the mudstone. The analysis of the results of these tests should also consider the increase in energy and reagent costs associated with using a finer grind.

Chapter 4. X-ray Diffraction

4.1. Introduction, Aims and Objectives

The purposes of the XRD analyses were to determine the compositions of each sample, especially with respect to deleterious gangue minerals. These data were then use to predict the reagent consumption characteristics of each sample and to determine the detection limit of XRD for these deleterious phases.

Three groups of analyses were performed. These included (1) analyses of the head samples, (2) detailed analysis of the clay fraction of each sample, (3) analyses for detection limit determination.

4.2. Basic Principals and Phase Identification

A beam of X-rays striking an atom may be either absorbed (resulting in the ejection of electrons) or scattered (Warren, 1990). X-ray scattering allows for XRD analyses.

Scattered X-rays can interact either constructively or destructively. The Bragg equation (Equation 2) describes the conditions for constructive interference of X-rays scattered from the regular lattice of a crystal (Figure 12) (Nesse, 2000).

$$n\lambda = 2d \sin\theta$$

Equation 2

Where n is an integer, λ is the wavelength, d is the spacing between planes of atoms within the crystal lattice and θ is the acute angle between the incident ray and plane of atoms.

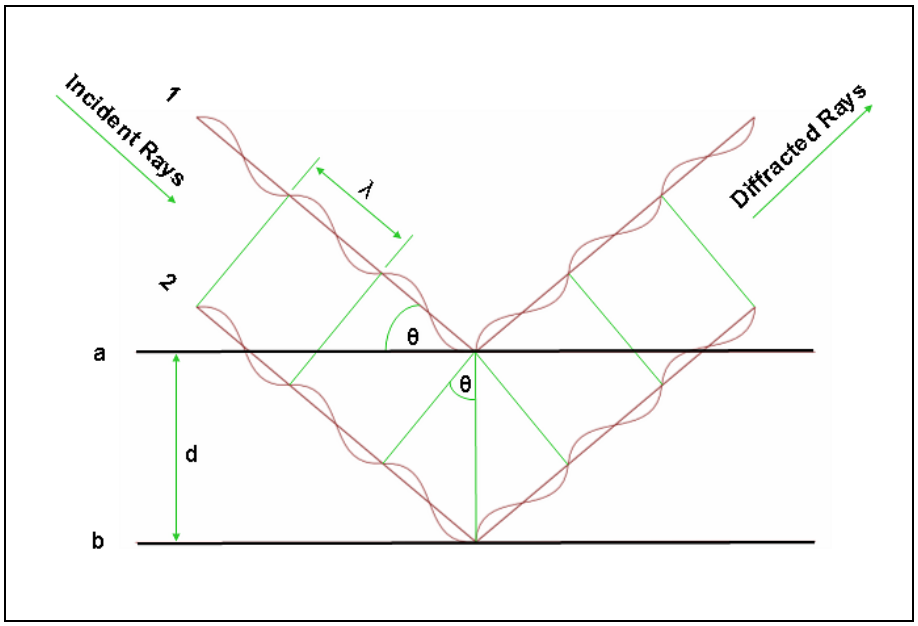

Figure 12. X-rays diffracted from the regular lattice of a perfect crystal, illustrating the conditions described by the Bragg equation. Where λ is the wavelength of rays 1 and 2, d is the spacing between planes (a and b) within the crystal lattice and θ is the acute angle between the incident ray and planes a and b. After Nesse (2000).

In the XRD analysis of powders, the sample consists of a very large number of extremely small crystallites. These are assumed to be randomly orientated (Valvoda, 1987). This random orientation theoretically makes it possible to present all possible planes of the constituent crystallites at the surface of a single sample. These planes will diffract X-rays when the Bragg criterion is met.

An X-ray diffractometer consists of an X-ray tube, a mask to constrain the wavelength of the X-rays, slits to convert the divergent beam (generated by the tube) to an almost parallel beam, a sample holder (typically with the ability to spin the sample), and a detector which measures the intensity of the diffracted ray. The source, detector or (more commonly) both are able to move along a curved path.

The diffractometer measures the angle between the source and detector, and generates a plot of diffracted X-ray intensity (in counts or counts per second) as a function of the angle θ (as in Figure 12), or more commonly 2θ which more

easily expresses the orientation between the source and detector. It is also possible to convert the plot to show intensity as a function of d-spacing by using the Bragg equation (Equation 2) to convert θ to the lattice d-spacing. Figure 13 shows plots (diffractograms) of diffracted X-ray intensity as a function of 2θ (A) and d-spacing (B).

Minerals are identified using XRD by comparing a measured pattern, collected from a powder sample, to patterns collected from pure minerals (or theoretical patterns generated from known crystal structure data). Figure 13 shows a measured pattern (in red) collected from a quartz sample, which is being compared to the peak positions and intensities of a reference pattern (black).

The assumption that crystallites within a powder sample are randomly orientated is often not valid (Zolotoyabko, 2009). This is especially true of platy and rod-like crystallites (Dollase, 1986). Such non-random distributions of crystallites within samples are referred to as preferred orientation. Due to preferred orientation, peaks associated with specific diffraction planes are exaggerated at the expense of peaks produced from other planes.

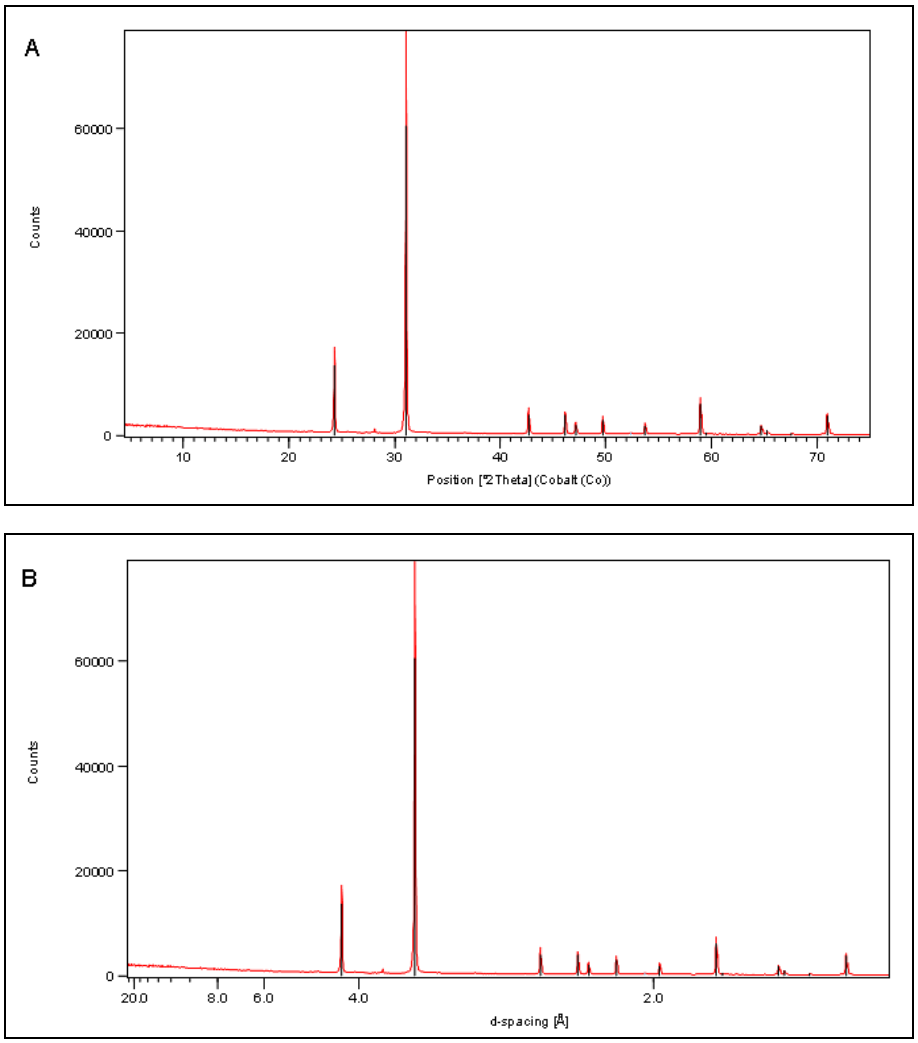

Figure 13. X-ray diffractograms measured from a quartz sample. The red line shows the measured pattern. The black lines show the positions of the peaks in the reference pattern. (A) shows the X axis expressed in degrees 2θ for Co-Kα radiation, and (B) show the X axis converted to d-spacing. While the 2θ axis is linear, d-spacing is not.

4.3. Quantitative Analysis

Once the phases in a powder sample have been identified, the next step is to determine their abundances. There are a number of methods used for quantitative XRD analysis. If the compositions of the phases are known, and XRF elemental data are available, it is occasionally possible to calculate mineral abundances using a method similar to the CIPW norm. However, instead of calculating the specific list of igneous minerals for a CIPW norm, the phases that were identified in the XRD analyses are used. The main limitation of this method

is that it requires that a certain number of minerals contain unique elements in order for the calculation to be possible. This method is also hampered by compositional variation resulting from solid solution.

Other quantitative methods rely on the relationship between mineral abundance and peak intensity (Chipera and Bish, 2002). The relationship between concentration and peak intensity as given by Brandt and Kinneging (2005) is shown below in Equation 3.

$$C_i = I_i B_i \mu$$

Equation 3

Where C_i is the concentration of phase i, I_i is the peak intensity, B_i is the calibration constant and μ is the sample mass absorption coefficient.

If standards with known concentrations of the mineral (or minerals) of interest are available, it is possible to produce a plot of C_i as a function of the product of I_i and μ. This produces a straight line with a slope of B_i. The resulting straight line can be used as a calibration curve to determine the concentration of the phase of interest in a sample.

It is necessary to know the mass absorption coefficient of the sample before it is possible to obtain accurate results. The value of the mass absorption coefficient can be determined using Equation 4.

$$\mu = \Sigma w_i \mu_i$$

Equation 4

Where w_i and μ_i are the weight proportion and mass absorption coefficient of each of the constituent minerals respectively (Ruis, 1987).

A complication develops because it is necessary to know μ in order to determine the mineral composition of a sample, and it is necessary to know the composition

of the sample in order to determine μ. Therefore the value of μ is often determined by an iterative process. The value of μ can also be found using the least-squares procedure of Rius (1987).

An alternative method of calculating the mass absorption coefficient of a sample is to let w_i and μ_i, in Equation 4, represent the weight proportion and mass absorption coefficients of the elements present in the powder sample (Shiraki and Holmen, 2002). Using this method it is possible to determine μ from XRF major element data.

The most wide spread application of the calibration curve method, is in the XRD analysis of dust filter samples for respirable crystalline silica [for example Zhuang *et al.* (2001) and Shiraki and Holmen (2002)]. In the analysis of these samples, the layer of dust on the surface of the filter is considered to be thin enough that the absorption effects are negligible. For this reason the mass absorption coefficient is ignored, and the peak intensity is directly proportional to the concentration of crystalline silica (MDHS 101, 2005). In cases where the layer of dust is to too thick for this assumption to be valid, the method of Shiraki and Holmen (2002) can be applied.

The need for pure standards for each mineral of interest, and difficulties of establishing and maintaining reliable calibration curves, limit the applicability of this method. The method is also severely hampered by instances of line overlap (Bish and Howard, 1988). For this reason several standardless methods have been developed. Of these the Rietveld method is most well known (Brandt and Kinneging, 2005).

The Rietveld refinement method was developed by Hugo Rietveld for use in obtaining crystal structure information from neutron diffraction data (Rietveld, 1969). The following is a brief summary of his methodology:

First the background of the diffraction pattern is determined. This makes it possible to separate the noise associated with the analysis, from the diffraction data. The position of each peak in the pattern is related to the crystal structure of the analyte using and the Bragg equation. A Gaussian curve is then fitted to each Bragg peak. The actual position of the Bragg peak may vary slightly because of zero error in the counter.

The width of each peak is determined using the Caglioti (Caglioti *et al.*, 1958) equation (Equation 5).

$$H_k^2 = U \tan^2\theta_k + V \tan\theta_k + W$$

Equation 5

Where H_k is the halfwidth, and U, V and W are the refined halfwidth parameters. The effect of W is the same for all peaks independent of their position, while the U and V terms make it possible to account for systematic variations in halfwidths as a function of angular peak position (represented by the angle θ).

Rietveld (1969) used Equation 6 to correct for preferred orientation of crystallites. However many modern diffraction programs prefer the March-Dollase equation (Equation 7) (Dollase, 1986 and Zolotoyabko, 2009).

$$I_{corr} = I_{obs} \exp(-G\alpha^2)$$

Equation 6

Where I_{corr} is the corrected peak intensity, I_{obs} is the observed peak intensity, G is the preferred orientation parameter and α is the acute angle between the normal to the crystallites and the scattering vector.

$$W = (r^2 \cos^2\alpha + r^{-1} \sin 2\alpha)^{-3/2}$$

Equation 7

Where W is used to correct for preferred orientation (much like the "exp $(-G\alpha^2)$" in Equation 6), r is the refined parameter and α has the same meaning as in Equation 6.

Rietveld suggested that it may be possible to extend his method to XRD data, but anticipated difficulties because XRD peaks do not show the nearly Gaussian shape seen in neutron diffraction peaks.

Applications of Rietveld refinement to XRD patterns make use of both Gaussian and Lorentzian functions in order to model the shapes of XRD peaks (Wiles and Young, 1981). The Voigt function serve as a means of combining the Gaussian and Lorentzian peak profiles (Petrov, 2007) and this combination is used to model the diffraction peak. Due to the complexity of the true Voigt function, it is often desirable to simplify the Voigt function (Olivero and Longbothum, 1977) and many Rietveld refinement programs offer a Pseudo-Voigt profile function.

Workers such as Wiles and Young (1981), and Bish and Howard (1988) developed methods of using Rietveld Refinement for quantitative analysis of XRD data. These methods are very similar to those in which diffraction patterns of pure phases are used to determine the abundance of the same phases in a mixture. The abundances are determined by varying the scale factors of each of the component patterns until they match the measured pattern. However, in order to eliminate the need to collect patterns from pure phases, these methods use Rietveld refinement to obtain a theoretical pattern (by using the crystal structures of the phases). A comparison of the resulting theoretical pattern and the measured pattern serves as a means of assessing the reliability of the refinement.

There are a number of means of comparing the theoretical and measured patterns. These include visual inspection of the two patterns, difference plots (where the theoretical pattern is subtracted from the measured pattern) and R values. There are three different R factors. These are given in Equations 8-10 after Wiles and Young (1981). Of the three, Wiles and Young (1981) considered the Weighted R_{wp} (Equation 10) to be the most significant.

$$R_B = \frac{\Sigma \mid I_{k(o)} - I_{k(c)} \mid}{\Sigma I_{k(o)}}$$

Equation 8

$$R_p = \frac{\Sigma \mid y_{i(o)} - y_{i(c)} \mid}{\Sigma y_{i(o)}}$$

Equation 9

$$R_{wp} = \frac{\Sigma w_i [y_{i(o)} - y_{i(c)}]^2}{\Sigma wi [y_{i(o)}]^2}$$

Equation 10

Where R_B is the Bragg R factor, R_p is the pattern R factor and R_{wp} is the weighted profile R factor, $y_{i(o)}$ and $y_{i(c)}$ are the observed and calculated intensities respectively, and $I_{k(o)}$ and $I_{k(c)}$ are obtained by assigning the observed intensities to the Bragg intensities (Wiles and Young, 1981). The Bragg intensity is a measure of the goodness-of-fit of a single phase, while the other two R factors apply to the whole pattern. Values of R_p less than 10 and, R_{wp} values less than 15 are tolerable, but the lower these values the better the fit (Verryn, 2010).

Figure 14 shows a measured quartz pattern (top red), the theoretical pattern (blue) and the difference plot (bottom red). The theoretical peak does not reach the full height of the main quartz peak in the measured pattern. This is seen as a pronounced peak in the difference plot below. This refinement had an R_p of 11.38 and an R_{wp} of 14.51. These indicate that the theoretical pattern is not a particularly good fit to the measured pattern.

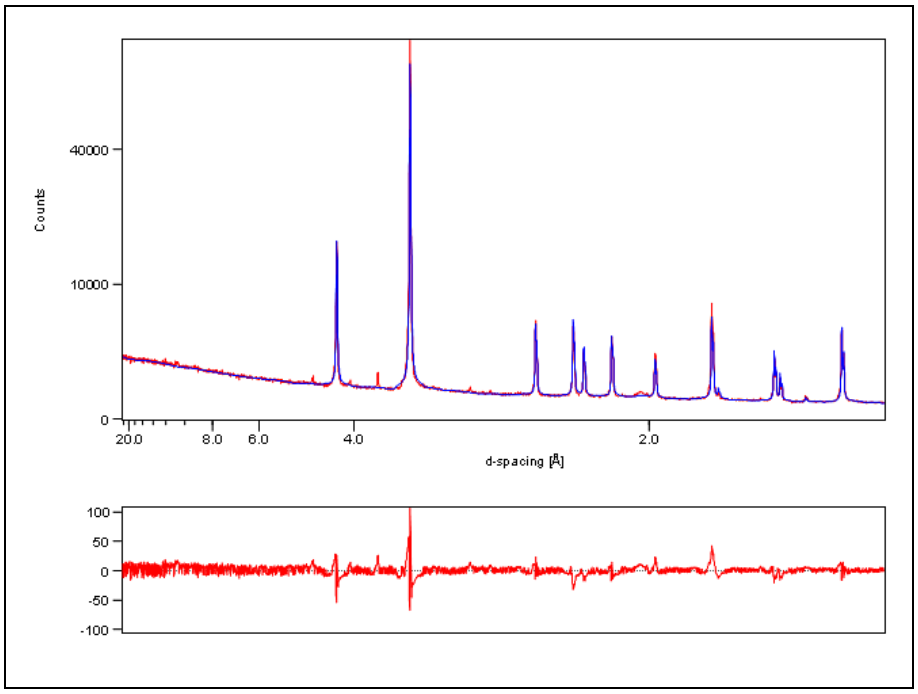

Figure 14. A refined pattern for α-quartz. The upper red profile is the measured pattern, the blue profile is the theoretical pattern and the lower red profile is the difference plot. The theoretical pattern does not reach the full height of the main quartz peak in the measured pattern. This is seen as a pronounced peak in the difference plot at 3.34 Å d-spacing. The R_p value for this refinement was 11.38, with an R_{wp} of 14.51. These values, as well as the graphical representations, indicate that the theoretical profile is acceptable, but not a particularly good fit to the measured data.

The major advantages of the Rietveld method of quantification are that it uses the whole pattern, is able to handle reasonable amounts of preferred orientation and peak overlap, and lends itself to the analysis of trace phases in complex mixtures (Bish and Howard, 1988).

4.4. Limits of Detection and Quantification

The International Union of Pure and Applied Chemistry defines the detection limit as that concentration of analyte which can be distinguished from background with a given level of certainty (usually 95%) Currie (1995). The calibration curve method most easily lends itself to the determination of instrumental limits of detection. The limit of detection can be taken as three times the standard deviation of a blank (MDHS 101, 2005), or could more accurately be calculated using Equation 11 (after Currie, 1995).

$$L_D = \delta_{\alpha,\beta,v}\,\sigma_0 \approx 2t_{1-\alpha,v}\,\sigma_0$$

Equation 11

Where L_D is the detection limit, t is the Student's t value for an α value of 0.05 and v degrees of freedom, and σ_0 is the population standard deviation, which may be approximated by s_0 (the standard deviation obtained by repeated measurements of a blank). For $\alpha = \beta = 0.05$ and $v \geq 25$, t approximates δ to within 1% (Currie, 1995).

In a similar way the limit of quantification is calculated using Equation 12.

$$L_Q = 10\,s_0$$

Equation 12

Where L_Q is the limit of quantification (or the lowest concentration that can be quantified with an acceptable level of certainty) and S_0 is the standard deviation obtained by repeated measurements of a blank (MDHS 101, 2005).

4.5. Methodology

All XRD analyses were performed using a Panalytical X'pert Pro diffractometer. The diffractometer parameters and settings are listed in Table 9.

Table 9: X-ray diffractometer parameters and settings used in this study

Parameter	Description
Radiation	Co-Kα
Incident Beam Radius	240 mm
Diffracted Beam Radius	240 mm
Mask	20 mm
Tension	40 kV
Current	40 mA
Filter	Iron
Incident Beam Soller Slit	0.04 Rad
Divergence Slit	Automatic
Irradiated Length	12 mm
Anti-scatter Slit	Fixed (2°)
Diffracted Beam Soller Slit	0.04 Rad
Detector	X'celerator
Detector Mode	Scanning

Three groups of analyses were performed. These included (1) analyses of the head samples, (2) detailed analysis of the clay fraction of each sample, and (3) analyses for detection limit determination.

Clay Fraction Analysis

Certain clay minerals present major obstacles to economic processing of ores (McFarlane *et al.*, 2005). For this reason the clay fraction of each sample was studied in detail. A 10 to 20 g aliquot of the -1.7 mm material from each head sample was placed in a 100 ml table vial. Fifty millilitres of ethanol was added to each vial. The vials were sealed and the clay fraction dispersed through the ethanol using ultrasound (Ehrmann, 2001) for 10 min. Thereafter the sample (and ethanol) was poured into a centrifuge tube. An additional 40 ml of ethanol was used to wash out the tablet vial to ensure that the entire sample was recovered.

Ethanol was used in preference to distilled water because it was found to result in lower amounts of precipitated material, and therefore a purer clay product.

Ethanol also evaporates more rapidly than water reducing the time taken to prepare samples.

Clay analyses by XRD are typically conducted on the -2 µm fraction of a sample (Jaboyedoff *et al.* 2001). By a combination of Stoke's law and Equation 13 (Serway and Faughn, 2003), it was found that centrifugation for about 6 minutes 49 seconds at a speed of 500 rpm, would cause the +2 µm fraction to settle out, while leaving -2 µm material in suspension. Faster speeds would have resulted in more rapid settling, however the errors introduced during initial acceleration and final deceleration of the centrifuge were considered unacceptable at these higher speeds.

$$a = v^2 / r$$

Equation 13

Where a is the acceleration, v is the velocity and r is the radius.

After centrifugation the overlying 70 ml of ethanol (which contained the -2 µm material) was drained off using a syringe. A glass slide was placed at the bottom of a 200 ml glass beaker. The suspension was poured into the beaker and the beaker (with glass slide and suspension) was placed in an oven at 60° C (Ehrmann, 2001). The ethanol was evaporated off and the clays formed an orientated layer on the surface of the slide. The percentage clay fraction contained in each sample was determined gravimetrically.

The orientated slides were analysed by XRD. The scan parameters used in these analyses are presented in Table 10.

Table 10: Scan settings for clay analyses by X-ray diffraction

Parameter	Description
Start Angle	4.000°
End Angle	80.003°
Step Size	0.0167113°
Time per Step	50.165 sec
Number of Steps	4548
Total Time	30 min 49 sec
Stage	Flat Bracket

After analysis, the samples were glycolated (Środoń, 1980) by exposure to ethylene glycol vapour, at a temperature of 60° C (Ehrmann, 2001), overnight. Glycolation causes the smectite structure to swell which aids in the accurate identification of clay minerals (Moore and Reynolds, 1989). After glycolation the samples were reanalysed by XRD using the settings in Table 10.

The diffractograms were processed using HighScore Plus software and phases were quantified by Rietveld Refinement using HighScore Plus and the PanICSD database. Due to the orientated nature of the samples, preferred orientation featured prominently in the later stages of these refinements.

Head Analysis

X-ray diffraction was used to quantitatively determine the major mineral compositions of each head sample. These were used to predict the influence of gangue mineralogy on reagent consumption. The leach residues were also analysed by XRD, however those analyses are discussed as part of the leach testwork.

The head sample analyses were performed on micronized powder samples. A 3 g sample mass was used for each analysis. These samples were miconised in ethanol, using a Mcrone micronising mill, for a period of three minutes in order to achieve the crystallite size recommended by McCusker *et al.* (1999). After

miconising the samples were dried in an oven at 60° C to remove the ethanol. The powder was deagglomerated and back loaded for XRD analysis.

The scan settings used for the XRD analyses of the head samples and screen fractions are given in Table 11. The scan times were shorter than those used for the clay analyses because there was significantly more sample material used for each analysis.

Table 11: Scan settings used in the XRD analyses of the head samples and screen fractions

Parameter	Description
Start Angle	4.500°
End Angle	75.005°
Step Size	0.0167113°
Time per Step	29.845 sec
Number of Steps	4219
Total Time	17 min 4 sec
Stage	Spinner PW3064
Stage Rotation Speed	1 rev/sec

The diffractograms were processed using HighScore Plus. Once the phases had been identified, they were quantified by Rietveld Refinement using HighScore Plus and the PanICSD database.

In addition to the XRD analyses, the head samples were analysed by XRF to determine their major element composition. The XRF data was used in combination with the Rietveld Refinement, to aid in the mineral quantification. The XRF data was also used to calculate MAC values for use in the preparation of calibration curves to determine detection limits.

Using their known gangue mineral compositions, an attempt was made to use the XRD data to predict the reagent consumption characteristics of each sample.

Detection Limits

In order to determine if conventional XRD is suitable for use in identifying and quantifying deleterious gangue, it was necessary to determine the lowest concentrations of these minerals that could be detected in the samples.

Ten aliquots of each of the Mooifontein (Mooi), Reduced Arkose Ore (RAO) and Mudstone Ore (MSO) head samples were diluted with known amounts of pure vein quartz. The dilutions are presented in Table 12. Because the concentrations of each mineral in the head samples had already been determined, it was possible to calculate the concentration of these minerals in each of the diluted samples.

The samples were micronized and analysed by XRD using the same method and settings used for the head samples. The peak intensities of main peaks of quartz, plagioclase, K-feldspar, calcite, muscovite, and laumontite were measured from the Mooifontein head sample and dilutions. Pyrite peak intensities were measured from the Reduced Arkose Ore head sample and dilutions, and smectite peak intensities were measured from the Mudstone Ore head and dilutions.

Because of concerns regarding preferred orientation of muscovite and laumontite, the intensities of both their main peaks, and a second peak were measured. The second peaks needed to be clean (showing no overlap with peaks from other minerals) and should be produced from a different diffraction plane from the main peak. All crystal structure data that follows was obtained from the PDF2 reference databases for patterns 01-086-1385 (muscovite) and 01-073-1933 (laumontite). The main muscovite peak occurs at ~10 Å d-spacing and is a 001 reflection. The next most intense peak, which met the selection criteria, was found at 4.45 Å d-spacing and is a -111 reflection. The main laumontite peak

occurs at 9.46 Å and is a 011 reflection. The next most intense peak that met the selection criteria was found at 6.84 Å and is a 020 reflection.

Table 12: Proportions of sample and vein quartz used to prepare the diluted samples for determination of detection limits

Component	Head Sample	Vein Quartz
Units	(%)	(%)
Mooi Head	100.00	0.00
Mooi 90	90.00	10.00
Mooi 80	80.38	19.62
Mooi 70	70.03	29.97
Mooi 60	60.07	39.93
Mooi 50	50.03	49.97
Mooi 40	40.06	59.94
Mooi 30	29.99	70.01
Mooi 20	20.03	79.97
Mooi 10	10.15	89.85
RAO Head	100.00	0.00
RAO 90	90.00	10.00
RAO 80	79.97	20.03
RAO 70	70.04	29.96
RAO 60	59.97	40.03
RAO 50	49.97	50.03
RAO 40	40.01	59.99
RAO 30	30.00	70.00
RAO 20	20.10	79.90
RAO 10	9.98	90.02
MSO Head	100.00	0.00
MSO 90	89.96	10.04
MSO 80	78.54	21.46
MSO 70	69.78	30.22
MSO 60	66.83	33.17
MSO 50	49.97	50.03
MSO 40	39.97	60.03
MSO 30	29.97	70.03
MSO 20	19.95	80.05
MSO 10	9.90	90.10

Table 13 presents the unit cell parameters for muscovite and laumontite that were used in correcting for preferred orientation and Table 14 presents the peak data. Using these data it was possible to plot the poles to each of the diffracting

planes onto a stereonet (Figure 15). These poles were used to determine the angles (α) needed for the March-Dollase (Dollase, 1986) correction. The angle between the muscovite 002 and -111 poles was 81°, and the angle between the laumontite 011 and 020 poles was 48°. A simultaneous equation (Equation 14) was set up to solve for r in the March-dollase (Dollase, 1986) equation. Once r had been determined for muscovite and laumontite in each of the diffractograms, W was calculated using Equation 14. W was then used to correct the intensity of the main peak of each phase for preferred orientation using the March-Dollase (Dollase, 1986) equation (Equation 7).

Table 13: Unit cell parameters used for muscovite and laumontite

Parameter	Muscovite	Laumontite
a (Å)	5.18	7.57
b (Å)	8.99	14.75
c (Å)	20.07	13.10
α (degrees)	90.0	90.0
β (degrees)	95.8	90.0
γ (degrees)	90.0	112.0

Table 14: Peak data used in the March-Dollase (Dollase, 1986) corrections

Mineral -	Peak Position (Å)	Relative Intensity* (%)	Diffracting Plane (Miller Index)
Muscovite	~10.00	100.0	002
Muscovite	4.45	72.2	-111
Laumontite	9.46	100.0	011
Laumontite	6.84	34.1	020

*The relative intensity is calculated as the intensity of a particular peak, divided by the intensity of the main peak of that phase. This results in 100% relative intensities for the main peaks of each phase.

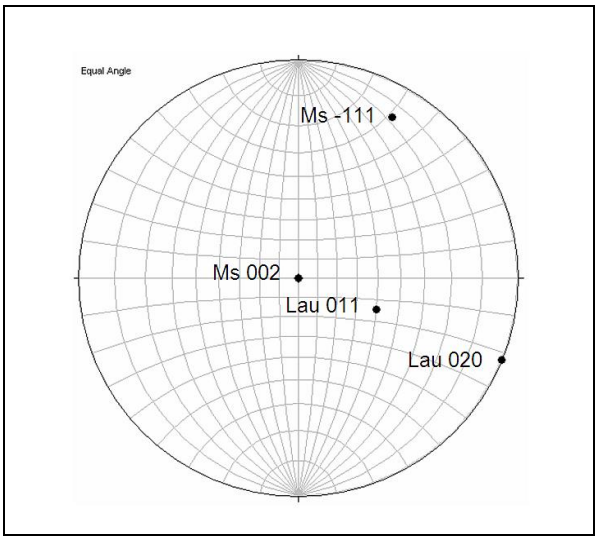

Figure 15: Stereonet (plotted using Stereowin software) showing the poles to the diffracting planes listed in Table 14. Using these poles it was possible to calculate the angles (α) needed for the March-Dollase correction (Equation 7). The angle between the muscovite 002 and -111 poles was 81°, and the angle between the laumontite 011 and 020 poles was 48°.

$$r = \left(\frac{\frac{\sin^2\alpha_b}{(100\, I_{obs(b)} / y)^{2/3}} - \frac{\sin^2\alpha_a}{(100\, I_{obs(a)} / x)^{2/3}}}{\frac{\cos^2\alpha_a}{(100\, I_{obs(a)} / x)^{2/3}} - \frac{\cos^2\alpha_b}{(100\, I_{obs(b)} / y)^{2/3}}} \right)^{1/3}$$

Equation 14

Where r is the refined parameter in the March-Dollase equation (Dollase, 1986), I_{obs} is the observed intensity of a particular peak, x is the relative intensity (Table 14) of peak a, y is the relative intensity of peak b and α has the same meaning as in Equation 6.

Calibration curves were produced for plagioclase, K-feldspar, calcite, muscovite, laumontite, pyrite and smectite using the peak intensity data (or corrected peak intensity data in the case of muscovite and laumontite) and the mineral abundance data from head samples and dilutions.

In order to determine the standard deviation of the background (needed to determine the detection limits by Equation 11, and the limit of quantification by Equation 12) a blank was prepared and analysed by XRD.

The blank was prepared by treating the Mooifontein head sample with 30% HCl solution to dissolve out the reactive minerals. HCl was used in preference to H_2SO_4 because H_2SO_4 has a tendency to convert calcite to gypsum. The gypsum forms impermeable coatings on the calcite and prevents complete dissolution of the calcite (Danielle *et al.*, 2008).

The blank was analysed 30 times using the same settings that were used for the head samples and dilutions. Background measurements were made for the same six angular positions for each of the 30 diffractograms. The standard deviation for each angular position was then calculated. These standard deviations were used (together with the calibration curves) to determine the lower detection limit and lower limit of quantification for plagioclase, K-feldspar, calcite, muscovite, laumontite, pyrite and smectite.

Because quartz was used to produce the dilutions, it was not possible to produce a calibration curve for quartz that would cover the concentration range near the lower detection limit. For this reason it was not possible to determine the lower detection limit.

4.6. Results

Clay Fraction Mineralogy

The masses of the -2 µm fractions extracted from each of the samples are given in Table 15. Comparison of these masses with the major mineralogy shows a correlation between smectite content in the head sample and the amount of -2 µm extracted from each sample.

Table 15: Weight percent clay fraction (-2 µm material) in each sample

Sample	-2 µm (Mass %)
Mooi	0.09
RAO	0.45
OAO	0.15
MSO	0.65

The results of the XRD analyses are given in Table 16 and the diffractograms of the clay fractions (before and after glycolation) are given in Figure 16 to Figure 19. Smectite occurs in all of the Kayelekera samples but not in Mooi.

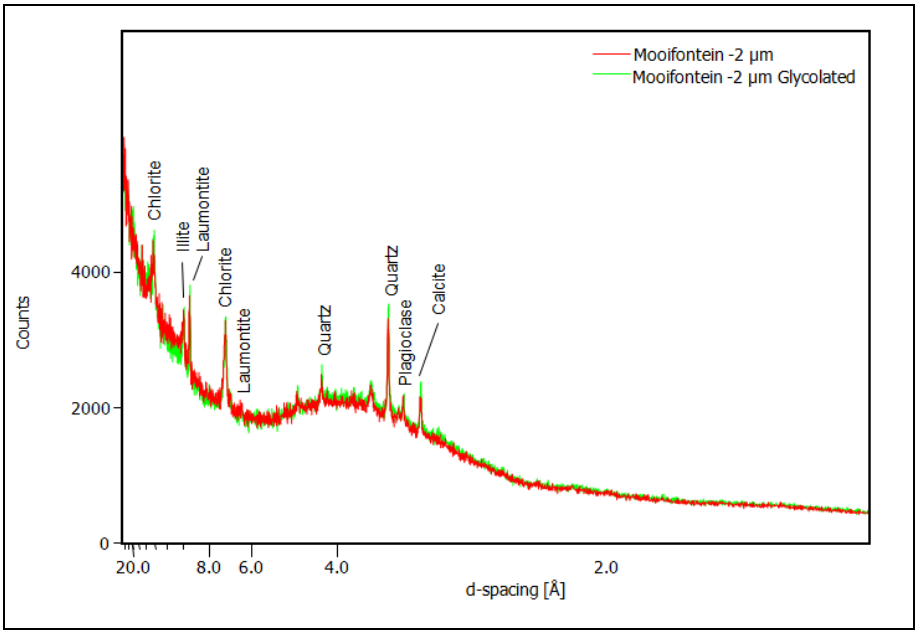

Figure 16: X-ray diffractogram of the clay fraction of Mooi. There was no change in peak positions in response to glycolation indicating that the sample does not contain smectite.

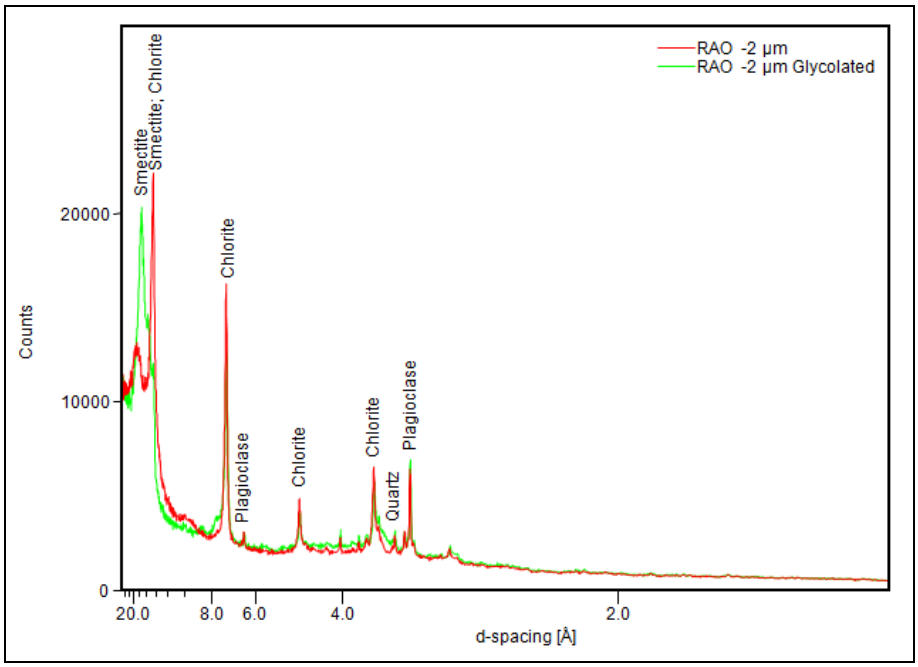

Figure 17: X-ray diffractograms of the clay fraction of RAO. The smectite peak shifted in response to glycolation.

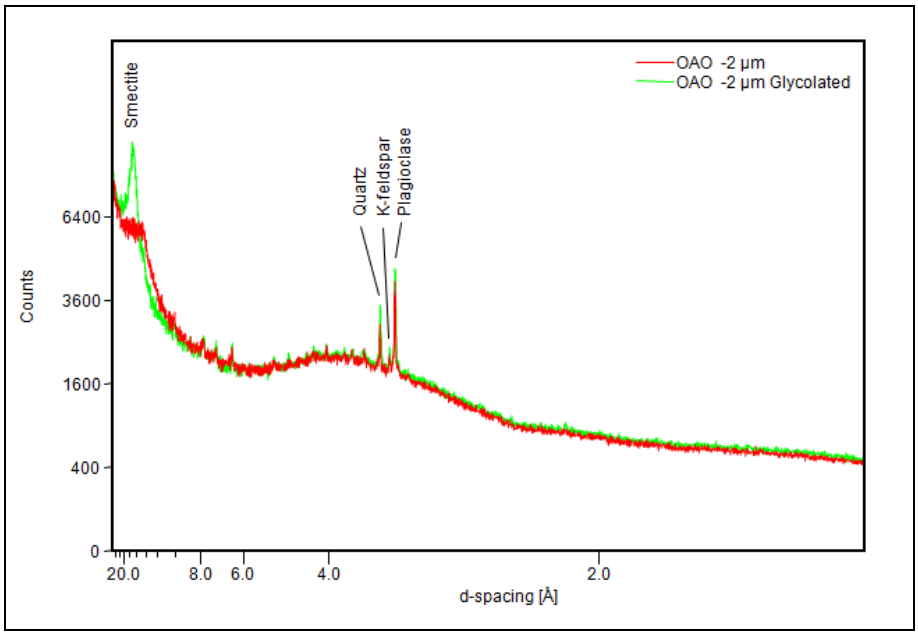

Figure 18: X-ray diffractograms of the clay fraction of OAO. Note the shift in the smectite peak in response to glycolation.

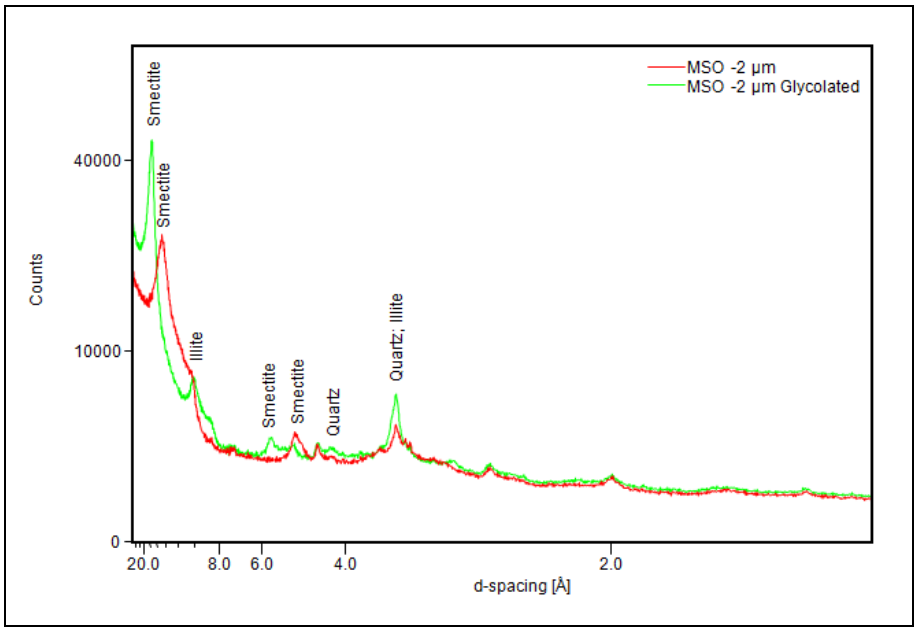

Figure 19:X-ray diffractogram of the clay fraction of the MSO sample. There was a significant shift in the smectite peak in response to glycolation.

Table 16: Rietveld refinement parameters and mineral abundances in the clay fractions

Rietveld Results	Units	Mooi	RAO	OAO	MSO
Weighted R Profile	-	3.54	14.53*	4.60	9.17
R Profile	-	2.98	11.07*	4.45	6.73
Quartz	(%)	38.1	1.7	10.1	29.0
Plagioclase	(%)	23.4	35.2	49.0	-
K-feldspar	(%)	-	-	3.4	-
Laumontite	(%)	13.5	-	-	-
Chlorite	(%)	3.3	13.4	-	-
Calcite	(%)	17.4	-	-	-
Illite	(%)	4.3	-	-	4.0
Smectite	(%)	-	49.7	37.5	67.0

*High R values are due to difficulties in resolving the overlap between chlorite and smectite. Chlorite may be underestimated.

The illite crystallinity (typically considered to be a function of the extent of development of the crystallites) was determined from the Kübler Index, which is the full width at half maximum of the first (~10Å) illite peak (Kübler and Jayboyedoff, 2000). The boundaries between poor, moderate and well crystalline illite were selected such that the range represented by poor crystallinity (broad XRD peaks) corresponds to diagenesis, and moderate crystallinity (marked by XRD peaks with intermediate widths) corresponds to deep diagenesis/incipient

metamorphism as given by Jayboyedoff *et al.* (2001). The crystallinity data for illite and smectite are given in Table 17. However the absolute Kübler Index should be treated with caution since the data was collected on an uncalibrated diffractometer. For this reason the crystallinity has only been expressed in a qualitative sense (poor, moderate or well crystalline).

Table 17: Crystallinity data for smectite and illite

Phyllosilicate	Parameter	Mooi	RAO	OAO	MSO
Smectite	Integrated peak width (Δ° 2θ, Co Kα)	-	1.094	1.139	0.854
	Crystallinity (Ehrmann, 2001)	-	Well Cryst	Well Cryst	Well Cryst
Illite	FWHM (° 2θ, Cu Kα)*	0.287	-	-	0.701
	Crystallinity (Jayboyedoff *et al.*, 2001)	Moderate	-	-	Poor

*Calculated from Co Kα data.
**Well crystalline minerals are considered to have well developed crystallites.
***Poorly crystalline minerals are considered to have poorly developed (very fine) crystallites.

Head Samples

As a means of assessing the quality of the XRD quantification, elemental abundances were calculated from the XRD data and compared with the XRF. The mineral chemistries that were used in the calculation were taken from the ideal formulae of the minerals aided by semi-quantitative EDX analysis to resolve difficulties with solid solution. The results of this comparison are presented in Table 18. These two data sets compare well, suggesting that the XRD data can be considered reliable.

The results of the XRD analysis are given in Table 19. Mooi, RAO and OAO consist of subequal amounts of quartz and plagioclase with lesser K-feldspar. Mooi also contains calcite, laumontite, chlorite and muscovite. RAO also contains chlorite and pyrite. RAO and OAO contain smectite, but the highest smectite concentrations occur in MSO. The dominant phase in MSO is illite, with lesser plagioclase and minor K-feldspar and quartz.

Table 18: Comparison of measured elemental abundances with values calculated from the XRD data

Sample	Mooi		RAO	
Units	Mass %	Mass %	Mass %	Mass %
Oxide	XRD	Chem	XRD	Chem
SiO_2	64.74	65.10	70.00	66.80
Al_2O_3	10.82	11.80	12.65	11.80
CaO	8.06	7.04	0.81	0.77
MgO	0.93	0.68	1.77	1.44
Fe_2O_3	2.76	2.44	5.75	6.95
K_2O	2.54	2.22	1.58	1.51
Na_2O	2.80	2.44	4.42	4.22
S	-	-	0.83	0.62
Sample	**OAO**		**MSO**	
Units	Mass %	Mass %	Mass %	Mass %
Oxide	XRD	Chem	XRD	Chem
SiO_2	81.64	80.70	53.10	52.48
Al_2O_3	9.46	9.71	21.79	19.75
CaO	0.25	0.23	1.26	0.84
MgO	0.36	0.11	2.13	1.65
Fe_2O_3	1.34	1.87	4.49	4.95
K_2O	1.10	1.05	4.88	3.67
Na_2O	4.59	4.19	1.36	1.11

Table 19: Major mineralogy, of each head sample, as determined by XRD

Sample	Mooi Head	RAO	OAO	MSO
Units	Mass %	Mass %	Mass %	Mass %
Quartz	32.0	31.2	49.5	7.6
Plagioclase	25.5	40.9	39.9	16.6
K-feldspar	13.6	9.4	5.7	7.9
Muscovite	2.1	-	-	-
Chlorite	6.8	8.7	-	-
Illite	-	-	-	48.7
Smectite	-	8.2	3.4	19.2
Laumontite	8.1	-	-	-
Calcite	12.0	-	-	-
Pyrite	-	1.6	-	-
Jarosite	-	-	1.5	-
Total	100.0	100.0	100.0	100.0

Screening of Mooi has resulted in a degree of mineral segregation. Plagioclase and K-feldspar have been enriched in the -425/+212 µm fraction, while laumontite and calcite have been slightly depleted. The -106 µm fraction shows

the opposite trend, with plagioclase and K-feldspar slightly depleted and laumontite and calcite slightly enriched.

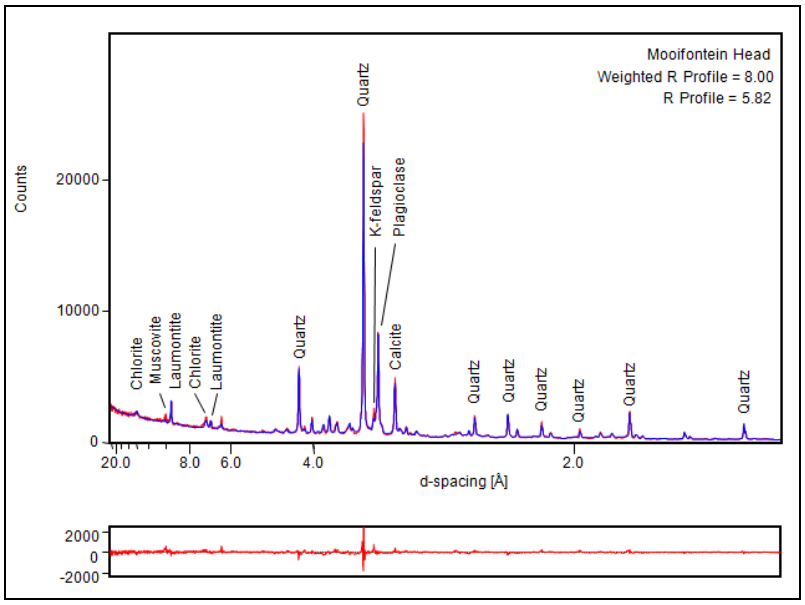

Figure 20: X-ray diffractogram of the Mooi head sample. The red pattern is the measured pattern, the blue pattern is the calculated plot resulting from the Rietveld refinement and the lower red pattern is the difference between the measured and calculated pattern.

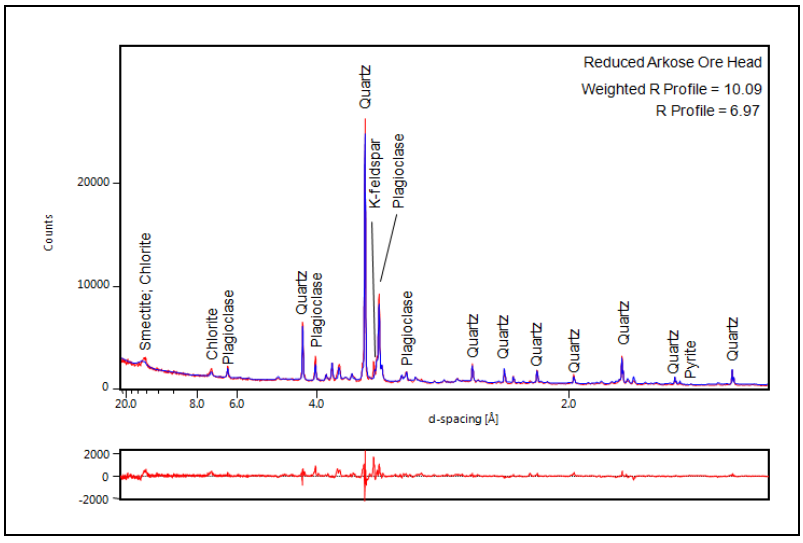

Figure 21: X-ray diffractogram of the RAO. The red pattern is the measured pattern, the blue pattern is the calculated plot resulting from the Rietveld refinement and the lower red pattern is the difference between the measured and calculated pattern.

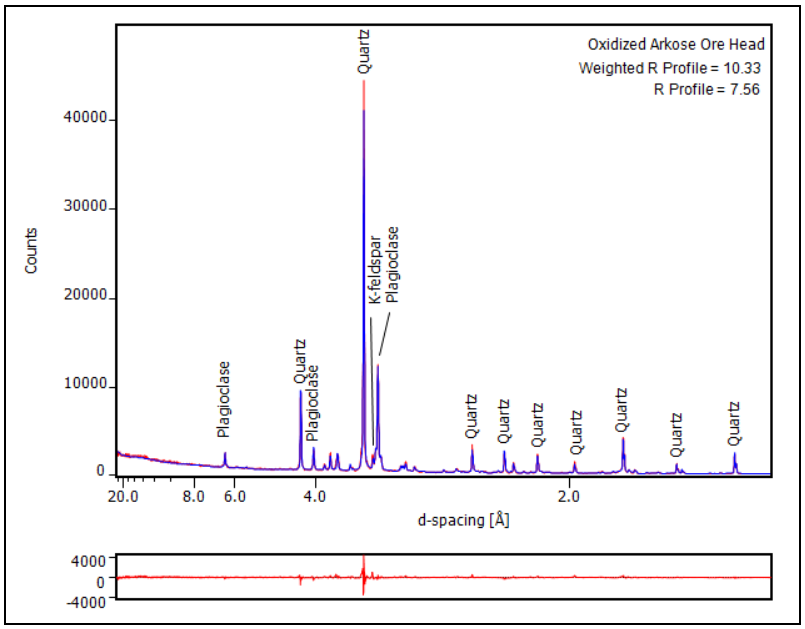

Figure 22: X-ray diffractogram of the OAO. The red pattern is the measured pattern, the blue pattern is the calculated plot resulting from the Rietveld refinement and the lower red pattern is the difference between the measured and calculated pattern.

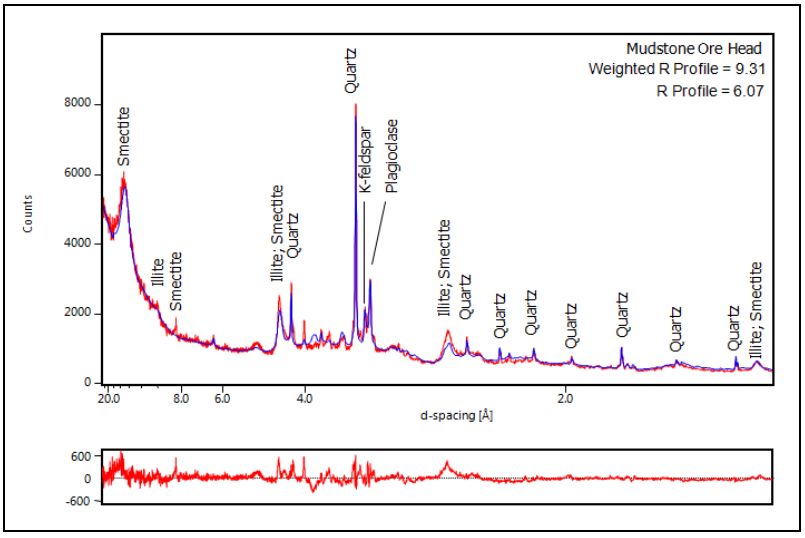

Figure 23: X-ray diffractogram of the MSO. The red pattern is the measured pattern, the blue pattern is the calculated plot resulting from the Rietveld refinement and the lower red pattern is the difference between the measured and calculated pattern.

Detection Limits

A total of 180 data points were used to determine the background noise in the XRD pattern of the acid treated Mooi blank (Appendix A includes a list of these data points). It was found that there is a relationship between the angular position

of the peak and the standard deviation of the background noise (Figure 24). If the angular position is expressed in 2Θ, then there is an exponential decrease in noise with increase in angle (Figure 24A). However if the angular position is expressed in d-spacing, the relationship becomes linear (Figure 24B). This linear relationship can be expressed by Equation 15.

$$y = 5.8188x + 1.2803$$

Equation 15

Where x is the angular position, in d-spacing, and y is the standard deviation of the background noise at that angular position. Because of this relationship, it is possible to calculate the standard deviation of the background noise for any angular position within an XRD pattern.

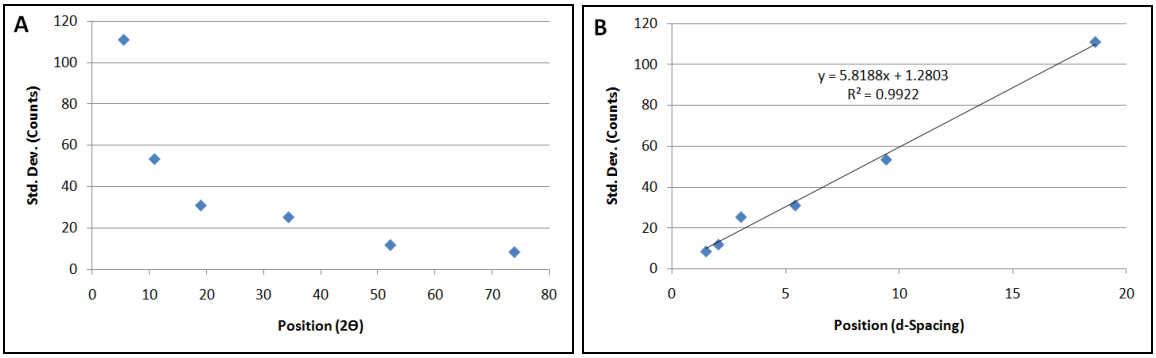

Figure 24: Relationship between angular position and the standard deviation of the background noise. There is an exponential decrease in noise with increasing angle (2Θ). However the relationship between noise and position (expressed as d-spacing) is linear.

Once the background noise was determined, calibration curves were produced for each mineral. These curves are illustrated in Figure 25 and the gradient, y-intercept and R^2 values are summarized in Table 20. The R^2 value is a measure of the degree of correlation. Perfect positive correlation gives an R^2 value of 1. The calibration curves have R^2 values between 0.92 and 0.99 indicating strong positive correlation.

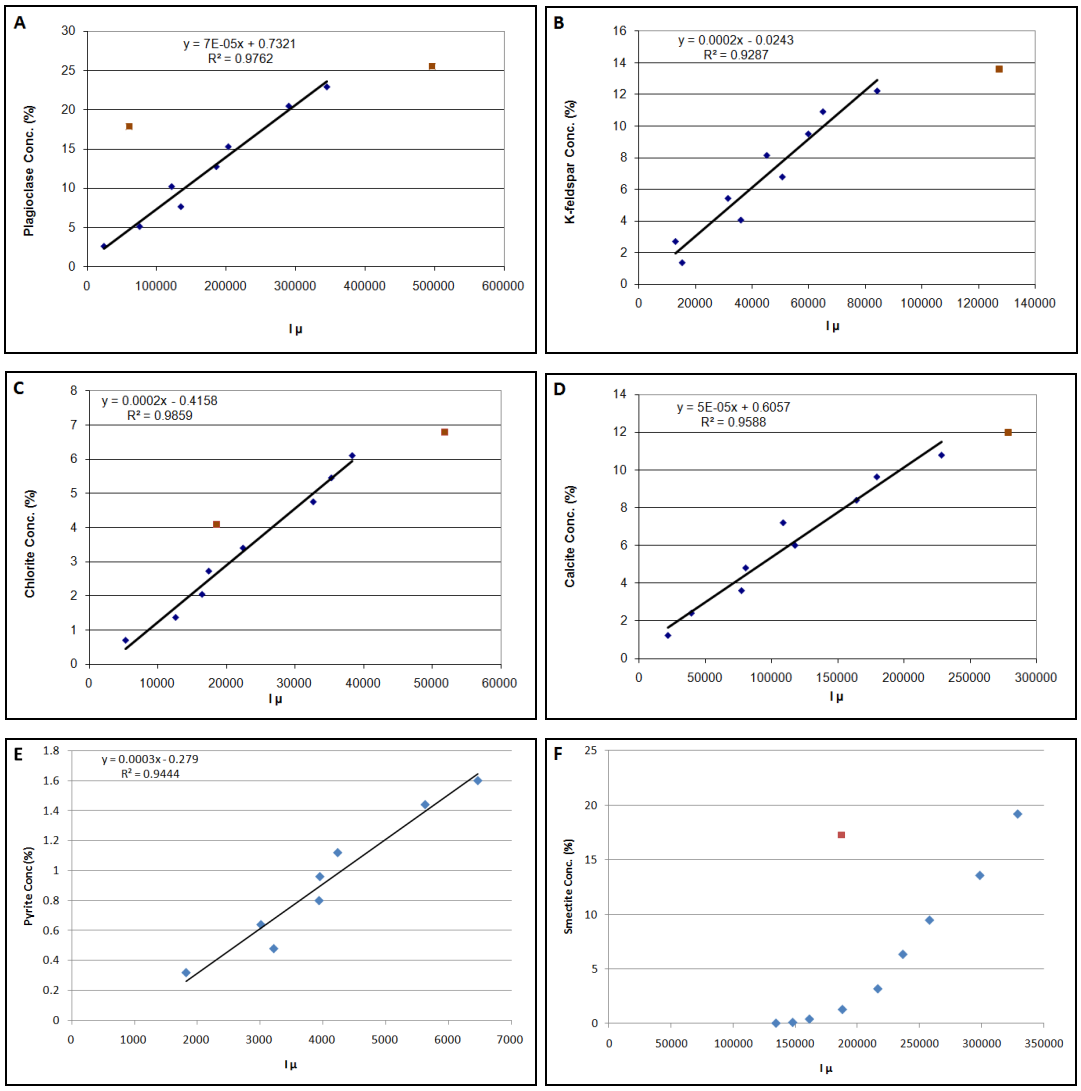

Figure 25: Calibration curves for plagioclase (A), K-feldspar (B), chlorite (C), calcite (D), pyrite (E), and smectite (F). Data points are shown in blue and outliers are in brown. Most minerals have a linear relationship between Iμ and concentration, but smectite has a quadratic relationship.

There is some scatter in the curves. This results from a number of factors including preferred orientation and instrumental error (both in the balance used to weight the dilutions and the diffractometer). However an additional source of scatter is the complex nature of the mixtures that were used to prepare the calibration standards. The standards were not simple binary mixtures of the analyte (for example calcite) and vein quartz, but were complex mixtures consisting of between 5 and 7 different minerals. These complex mixtures make the standards similar to real samples, but also result in minor variations in

mineral abundances in the aliquots that were used to produce the dilutions (even though the aliquots were derived from pulverized sample).

The use of Equation 14 made it possible to improve the calibration curves of muscovite and laumontite (Figure 26). The March-Dollase correction (Dollase, 1986) made 8% and 15% improvements in the muscovite and laumontite curves respectively.

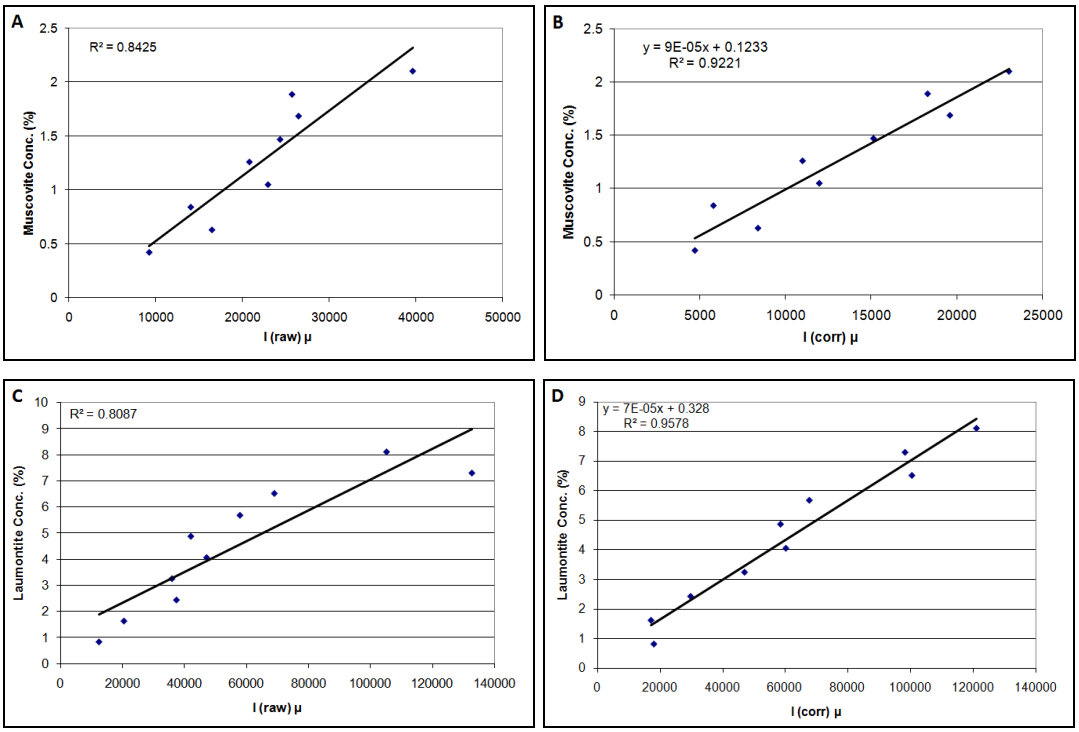

Figure 26: Calibration curves for muscovite (A and B) and laumontite (C and D). In each case the graph to the left shows the raw data and the one to the right shows the preferred orientation corrected data. The March-Dollase (Dollase, 1986) correction resulted in an 8% improvement in the muscovite curve and a 15% improvement in the laumontite curve.

Table 20: Variables used to express the linear relationship between the product of the peak intensity and mass absorption coefficient with the concentration of selected minerals, R^2 values reflect the degree of scatter

Parameter	Gradient	y-intercept	R^2
Units	**Mass % Counts^{-1}**	**Mass %**	**-**
Plagioclase	6.6×10^{-5}	0.73	0.98
K-feldspar	1.5×10^{-4}	-0.02	0.93
Muscovite	8.8×10^{-5}	0.12	0.92
Chlorite	1.7×10^{-4}	-0.42	0.99
Laumontite	6.0×10^{-5}	0.33	0.96
Calcite	4.8×10^{-5}	0.61	0.96
Pyrite	3.0×10^{-4}	-0.28	0.94

By substituting the position of the main peak of each mineral in to Equation 15 the standard deviation of the blank was determined. These data were then substituted into Equation 11 to determine the limit of detection (L_D) and Equation 12 for the limit of quantification (L_Q). The limits of detection and quantification are presented in Table 21.

Table 21: Lower limits of concentration at which selected minerals can be detected (L_D) and quantified (L_Q) by XRD

Parameter	Peak Position	Std. Dev.	L_D	L_D	L_Q	L_Q
Units	**Å d-Spacing**	**Counts**	**Counts**	**Mass %**	**Counts**	**Mass %**
Muscovite	9.95	59.2	201	0.98	592	2.89
Laumontite	9.44	56.2	191	0.64	562	1.87
Chlorite	7.06	42.4	144	1.36	424	3.99
K-feldspar	3.24	20.1	68	0.57	201	1.67
Plagioclase	3.19	19.8	67	0.25	198	0.73
Calcite	3.03	18.9	64	0.17	189	0.50
Pyrite	1.63	10.8	37	0.61	108	1.79

4.7. Prediction of Reagent Consumption Characteristics

The bulk composition of the rock, especially gangue mineralogy, controls the consumption of sulphuric acid and oxidiser, as well as the potential for Fe^{3+} generation (Merritt, 1971; Ho and Quan, 2007 and Lottering *et al.*, 2008).

In order to predict reagent consumption it is necessary to specify the leach conditions (Table 22).

Table 22: Summary of the leach conditions used in the batch acid leach tests

Leach Test	Sample	Grind	pH	Eh (SCE)	Temperature	Time
-	-	P_{80} µm	-	mV	°C	Hours*
A	Mooi Head	212	1.0	-500	35 -40	24 (+1)
B	Mooi Head	212	1.5	-450	35 -40	24 (+1)
C	Mooi Head	75	1.5	-450	35 -40	24 (+1)
D	Mooi Head	212	2.0	-400	35 -40	24 (+1)
E	RAO	212	1.5	-450	35 -40	24 (+1)
F	OAO	212	1.5	-450	35 -40	24 (+1)
G	MSO	212	1.5	-450	35 -40	24 (+1)

*The additional hour is for preconditioning prior to addition of the oxidiser. Therefore the material will be exposed to acid at the specified pH for a total of 25 hours, but only exposed to oxidiser for 24 hours.

Quartz and feldspar are relatively inert, while carbonates are highly acid consuming (Merritt, 1971 and IAEA, 1980). Although not as reactive as the carbonates, the phyllosilicates (chlorite, muscovite and clay minerals) are also acid consumers (IAEA, 1980).

Calcite

Calcite (occurring in the Mooi head sample in concentrations of 12.0%) was the only carbonate detected in the samples. The acid dissolution of calcite follows Equation 16 (Venter and Boylett, 2009).

$$CaCO_3 + H_2SO_4 \rightarrow CaSO_4 + CO_2\uparrow + H_2O$$

Equation 16

However, the rate of calcite dissolution (and therefore acid consumption) depends on a number of factors. The rate of H^+ diffusion is significant because the rate of Equation 16 is thought to be sufficiently rapid that it consumes H^+ faster than it can diffuse through the solution.

It may therefore be possible to have lower acid consumption than would be expected if complete dissolution of calcite were to occur. However, Danielle *et al.* (2008) worked on anoxic limestone drainages, used in the treatment of acid mine drainage. Unlike anoxic limestone drainages, uranium leach tests are carried out under stirred/agitated conditions (IAEA, 1990). It is likely that the agitation will result in sufficient abrasion to breach gypsum coatings. Stirring/agitation will also increase the rate of H^+ delivery as the system will make use of both convection and diffusion. For these reasons it is considered likely that complete dissolution of the calcite in Mooi will occur, resulting in maximum calcite acid consumption. The predicted calcite acid consumptions for the Mooi leach tests are presented in Table 23.

Table 23: Predicted calcite dissolution and acid consumption for the Mooi sample at various pH conditions and at two grinds (80% passing 212 and 80% passing 75 μm)

pH	Sample	Dissolution			H_2SO_4 Consumption	
-	-	mol/ton	kg/ton	% of Contained Calcite	Mol/ton	kg/ton
1.0	Mooi -212	1199	120	100	1199	118
1.5	Mooi Head -212	1199	120	100	1199	118
2.0	Mooi Head -212	1199	120	100	1199	118
1.5	Mooi -75	1199	120	100	1199	118

Laumontite

Laumontite occurs in the Mooi samples. An equation for the acid dissolution of laumontite was not found in the literature; however, by analogy with the acid dissolution of other silicate minerals, it is thought that laumontite dissolves according to Equation 17. It is possible that the overall equation given in Equation 17 occurs in two steps, the removal of Ca (Step 1) followed by the dissolution of Al (Step 2).

$$CaAl_2Si_4O_{12}.4H_2O + 8H^+ \rightarrow Ca^{2+} + 2Al^{3+} + 4H_4SiO_4$$

Equation 17

The rate of laumontite dissolution is also significant when determining the extent of laumontite acid consumption. If laumontite dissolves completely within the duration of the leach, it will consume the maximum amount of acid. However, if the rate of dissolution is sufficiently slow, it is possible that laumontite acid consumption may be lower than that which would be calculated from Equation 17 and the 8.1% laumontite content of Mooi Head sample. A rate equation for the acid dissolution of laumontite, at the appropriate pH was also not found in the literature. Dyer *et al.* (1991) claim that laumontite shows favourable stability under acidic conditions. However during the preparation of the blank, for use in determination of L_D and L_Q, complete dissolution of laumontite was observed.

Since the blank was prepared using higher H^+ activities than those used in U leaching, it is likely that only partial dissolution will occur. Although Dyer *et al.* (1991) considered the acid dissolution of laumontite to be negligible; they did suggest that replacement of Ca by H_3O^+ may have occurred during their study. If this is the case, it is likely that Ca removal (Step 1) will be significantly more complete than Al dissolution (Step 2). Since Ca removal consumes 25% of the acid in Equation 17, and some dissolution of Al is expected, it is estimated that laumontite acid consumption will be ~40% at the conditions of Leach 1, ~35% at the conditions of Leach 2 and ~30% at the conditions of Leach 3.

Table 24: Predicted laumontite dissolution and acid consumption for the Mooi sample at various pH conditions and at two grinds (80% passing 212 and 80% passing 75 μm)

pH	Sample	Dissolution	H_2SO_4 Consumption	
-	-	% of contained Laumontite	mol	kg/ton
1.0	Mooi -212	40	551	54
1.5	Mooi Head -212	35	482	47
2.0	Mooi Head -212	30	413	41
1.5	Mooi -75	35	482	47

Chlorite

The rapid dissolution rate of calcite, and the shortage of kinetic data for laumontite, has resulted in reasonably simple predictions of their dissolution characteristics. Several factors influence the dissolution characteristics of minerals. Only some of these factors were briefly considered for calcite and laumontite. The following factors influence the rate of mineral dissolution: mineral composition, time, temperature, pH, surface area and incongruent dissolution (Ross, 1969, Brantley and Conrad, 2008, Lüttge and Arvidson, 2008, and Brantley, 2008).

Since minerals dissolve at a finite rate, the extent of dissolution is a function of time. However, the rate of dissolution can also vary with time. Generally two phases are seen during dissolution, (1) an initial more rapid rate which gradually slows to (2) steady-state dissolution (Brantley, 2008). The U leach tests typically include the initial phase of rapid dissolution, but (depending on the constituent minerals and conditions of the leach) may not necessarily reach steady-state dissolution.

The rate of mineral dissolution is considered to vary with temperature according to the Arrhenius equation (Brantley and Conrad, 2008).

$$k = A \exp(-E_a/RT)$$

Equation 18

Where k is the rate constant at a given temperature, A is the pre-exponential factor, E_a is the activation energy, R is the ideal gas constant and T is the absolute temperature (Brantley and Conrad, 2008). Using the Arrhenius equation it is possible to adapt kinetic data collected at one temperature to a more desirable temperature (Brandt *et al.*, 2003), in this case 35°C.

Except in cases where dissolution is diffusion controlled, as Danielle *et al.* (2008) suggested was the case with calcite, mineral dissolution rates are directly proportional to surface area. Therefore rates are typically normalised to the

surface area of the mineral (Lüttge and Arvidson, 2008). Many workers (including Lowson (2005), Brandt *et al.* (2003) and Knauss and Wolery (1989)) favour the BET (Brunauer, Emmett and Teller, 1938) method of surface area determination. This method allows for surface area determination by measuring the adsorption of an inert gas onto the surface of the analyte.

Incongruent dissolution describes the case where elemental release rates are not proportional to the stoichiometry of the mineral (Brantley, 2008). The preferential release of Ca from laumontite (Dyer *et al.*, 1991) would therefore be a case of incongruent dissolution.

Due to the extensive work on the acid dissolution of chlorite (especially by Lowson *et al.* (2005) and Brandt *et al.* (2003)), it was possible to make detailed predictions regarding the dissolution of this mineral. Lowson *et al.* (2005) worked on steady state dissolution and considered a wide range of pH conditions. The relationship between pH and dissolution rate is shown in Figure 27 (A), and there is a steady increase in dissolution rate with decreasing pH.

Lowson *et al.* (2005) reported congruent dissolution once steady state conditions had been reached. However, Ross (1969) and Brandt *et al.* (2003) have shown that dissolution is incongruent prior to steady state conditions (less than ~48 hours), with the rate of dissolution decreasing in the following order: Al, Mg, Fe, Si. Figure 27 (B) shows initial and steady state dissolution rates for each element.

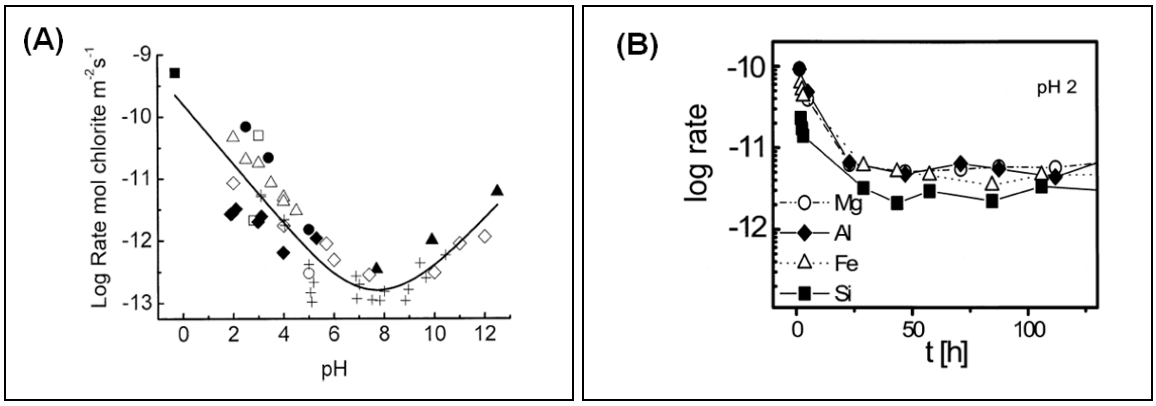

Figure 27: The relationship between pH and dissolution rate (A) (Lowson *et al.*, 2005 and the references therein) and the decrease in dissolution rate from initial to steady state (B) (Brandt *et al.*, 2003).

Lowson *et al.* (2005) gave an ideal equation for the dissolution of chlorite. This equation has been adapted slightly (Equation 19) to more closely correspond with the composition of the chlorite in the present study.

$$(Mg_{3.75}Fe_{6.25}Al_2)(Si_6Al_2O_{20})(OH)_{16} + 32H^+ \rightarrow$$
$$3.75Mg^{2+} + 6.25Fe^{2+} + 4Al^{3+}\ 6H_4SiO_4 + 12H_2O$$

Equation 19

The activation energy (60 kJ/mol), surface area (1.1 m^2/g) and the rate data from Brandt *et al.* (2003) and Lowson *et al.* (2005) were used as input data. It was assumed that the decay from initial to steady state conditions could be modelled by an exponential function (Equation 20, adapted from Serway and Faughn (2003)). This equation appears to fit the Brandt *et al.* (2003) data quite well.

$$R = R_0\, e^{-\lambda t}$$

Equation 20

Where R_0 is the initial rate, R is the rate at time t and λ is the decay constant. Equation 20 gives the surface area normalised, instantaneous rate of release for pre-steady state dissolution. Values used in this study for the initial rates and decay constants of selected silicate minerals are given in Appendix A.

Since the ore will be exposed to acid for 25 hours, the entire leach will take place before steady state conditions are reached. In order to use Equation 20 to determine the amount of each element released, the total chlorite dissolution and the amount of sulphuric acid consumed, it was necessary to consider the surface area and chlorite content of the samples. This could then be integrated from 0 to 90 000 s (25 hours) in order to determine the total amount of each element dissolved from the chlorite during the leach test (Equation 21). Since 10^4, the initial surface area, and initial chlorite concentration are all constant, Equation 21 simplifies to Equation 22 for a 25 hour leach.

The results of these calculations are given in Table 25 (with additional data in Appendix A). Between ~1 and ~4.8% of the chlorite contained in each sample is expected to dissolve, with the lowest dissolutions at the highest pH, and highest dissolution at the finest grind. While these values represent only a small proportion of the total contained chlorite, they can result in acid consumptions of up to ~10.6 kg/ton of ore. However, as can be seen from Equation 19, the dissolution of chlorite contributes Fe to the solution which plays a significant role in U oxidation (Merritt, 1971 and IAEA, 1980).

$$E_T = \int_0^{90\,000} (10^4 \times A \times C_c . R_0 . e^{-\lambda t})\, dt$$

Equation 21

$$E_T = 10^4 \times A \times Cc \times R_0 \frac{(e^{-90\,000\lambda} - 1)}{-\lambda}$$

Equation 22

Where E_T is the total amount (in mole/ton of ore treated) of a particular element released during the leach, A is the initial surface area (in m^2/g), C_c is the chlorite concentration (in percent) and the 10^4 is a conversion factor to convert from mol/g to mol/ton. The reason the conversion factor is 10^4 rather than 10^6 is because the chlorite concentration is expressed as a percentage and the factor also serves to convert the percentage to a more convenient value.

Table 25: Chlorite dissolution data calculated to reflect the variation in the rate of release of each element resulting from incongruent dissolution

Mooi Head	**Dissolution**		**H_2SO_4 Consumption**	
pH = 1.0	**mol/ton**	**% of Contained Chlorite**	**mol/ton**	**kg/ton**
Si	3.72	0.15	-	-
Al	17.14	0.68	25.70	2.52
Mg	17.07	0.61	17.07	1.67
Fe	12.12	1.00	12.12	1.19
Total	**-**	**2.44**	**54.89**	**5.39**
Mooi Head	**Dissolution**		**H_2SO_4 Consumption**	
pH = 1.5	**mol/ton**	**% of Contained Chlorite**	**mol/ton**	**kg/ton**
Si	2.60	0.11	-	-
Al	11.98	0.48	17.97	1.76
Mg	11.93	0.43	11.93	1.17
Fe	8.47	0.70	8.47	0.83
Total	**-**	**1.71**	**38.37**	**3.76**
Mooi Head	**Dissolution**		**H_2SO_4 Consumption**	
pH = 2.0	**mol/ton**	**% of Contained Chlorite**	**mol/ton**	**kg/ton**
Si	1.48	0.06	-	-
Al	6.82	0.27	10.23	1.00
Mg	6.80	0.24	6.80	0.67
Fe	4.83	0.40	4.83	0.47
Total	**-**	**0.97**	**21.85**	**2.14**
Mooi -75	**Dissolution**		**H_2SO_4 Consumption**	
pH = 1.5	**mol/ton**	**% of Contained Chlorite**	**mol/ton**	**kg/ton**
Si	7.33	0.30	-	-
Al	33.76	1.34	50.64	4.97
Mg	33.63	1.20	33.63	3.30
Fe	23.88	1.96	23.88	2.34
Total	**-**	**4.81**	**108.14**	**10.61**
RAO	**Dissolution**		**H_2SO_4 Consumption**	
pH = 1.5	**mol/ton**	**% of Contained Chlorite**	**mol/ton**	**kg/ton**
Si	3.33	0.11	-	-
Al	15.33	0.48	22.99	2.26
Mg	15.27	0.43	15.27	1.50
Fe	10.84	0.70	10.84	1.06
Total	**-**	**1.71**	**49.10**	**4.82**

Muscovite

Muscovite occurs in the Mooi head sample. The dissolution of this mineral tends to be congruent during steady-state dissolution (Knauss and Wolery, 1989), but K is released at a very slightly higher rate than other cations during the initial stage (Kalinowski and Schweda, 1996). Oelkers *et al.* (2008) found that dissolution reaches steady-state from between 2 hours and 7 days.

Oelkers *et al.* (2008) focussed on steady-state dissolution, but Knauss and Wolery (1989) provided rates as a function of both pH and time. Since Knauss and Wolery (1989) worked at a temperature of 70°C, it was necessary to adapt their rates to the conditions of the leach, using the Arrhenius equation (Equation 18) and an activation energy of 58.2 kJ/mol (Oelkers *et al.*, 2008). However this resulted in only a very slight decrease in the dissolution rate.

Working with muscovite of a similar average size to that of Mooi head sample Knauss and Wolery (1989) determined a BET surface area of 2.38 m^2g^{-1}. Assuming an inverse relationship between grain size and surface area (which holds for a spherical model), the surface area of Mooi -75 µm was estimated to be 6.74 m^2g^{-1}.

Muscovite dissolves in acid solution according to Equation 23 (Knauss and Wolery, 1989 and Oelkers *et al.*, 2008).

$$KAl_2(Si_3AlO_{10})(OH)_2 + 10H^+ \rightarrow K^+ + 3Al^{3+} + 3Si(OH)_4$$

Equation 23

Using surface area, temperature, pH, time and Equation 23 the muscovite dissolution characteristics for the Mooi leaches were predicted (Table 26). These results suggest that muscovite dissolution would be negligible under the

conditions of the leach tests, and that the sulphuric acid consumption from muscovite dissolution would only be several g/ton rather than kg/ton.

Table 26: Predicted muscovite dissolution and acid consumption

pH	Sample	Dissolution			H_2SO_4 Consumption	
-	-	mol/ton	g/ton	% of Contained Muscovite	Mol/ton	g/ton
1.0	Mooi -212	3.4×10^{-5}	1.4×10^{-2}	6.7×10^{-5}	1.7×10^{-4}	1.7×10^{-2}
1.5	Mooi Head -212	2.0×10^{-5}	8.0×10^{-3}	3.8×10^{-6}	1.0×10^{-4}	1.0×10^{-2}
2	Mooi Head -212	6.7×10^{-6}	3.7×10^{-3}	1.8×10^{-7}	3.4×10^{-5}	3.3×10^{-3}
1.5	Mooi -75	1.9×10^{-4}	7.6×10^{-2}	3.6×10^{-4}	9.5×10^{-4}	9.3×10^{-2}

Smectite

Smectite occurs in all of the Kayelekera samples in concentrations of between 3.4% (OAO) and 19.2% (MSO). Deer *et al.* (1993) described the structure and composition of smectite as follows: Smectite is a phyllosilicate consisting of a tetrahedral layer containing mainly Si (with minor Al substitution), and an octahedral layer which may contain Al, Mg, or Fe. The specific ions occurring in the octahedral layer are a major factor in determining the specific type of smectite, however extensive solid solution exists between the end member varieties. In addition to the tetrahedral and octahedral sites, smectite hosts exchangeable interlayer cations. These are typically Ca or Na, but other elements (including Mg) can occur in these sites.

Under acidic conditions smectite undergoes an initial phase of highly incongruent dissolution, associated with rapid release of interlayer Ca, Na and Mg by ion exchange (Metz *et al.*, 2005). It also appears that the octahedral layers of the smectite are dissolved in preference to the tetrahedral layers (Zysset and Schindler, 1996 and Shaw *et al.*, 2009). Equation 24 is an equation for the complete acid dissolution of smectite and is based on the equations of Amram and Ganor (2005) and Metz *et al.* (2005). However, it has been adapted slightly

to correspond more closely to the smectite composition estimated by SEM-EDS (Chapter 5).

$$(Ca_{0.22}Mg_{2.18})(Mg_{0.7}Fe_{2.3}Al)(Al_{1.8}Si_{6.2})O_{20}(OH)_4 + 19.2H^+ + 0.8H_2O \rightarrow$$
$$0.22Ca^{2+} + 2.88Mg^{2+} + 2.3Fe^{2+} + 2.8Al^{3+} + 6.2H_4SiO_4$$

Equation 24

Under conditions of constant pH, the dissolution kinetics of smectite are pseudo-first-order, with activation energies of between 71 and 89 kJ/mol (Zysset and Schindler, 1996).

Several hundred to several thousand hours are required for reactions to reach steady state conditions (Metz *et al.*, 2005), suggesting that the leach tests will be completed within the initial rapid phase.

Smectite BET surface areas range from 16 to 127 m^2/g, however there appears to be little relationship between BET surface area and reactive surface area. For this reason rates can be more accurately normalised to the smectite mass than surface area (Metz *et al.*, 2005).

Amram and Ganor (2005) derived an equation for the steady state dissolution of smectite. This is given in Equation 25.

$$\text{Rate} = 220e^{-17460/RT} \cdot \frac{3 \times 10^{-6} \times e^{10700/RT} \times a_{H+}}{1 + 3 \times 10^{-6} \times e^{10700/RT} \times a_{H+}}$$

Equation 25

Where a_{H+} is the hydrogen ion activity, T is the temperature (K) and R is the ideal gas constant [note that Amram and Ganor (2005) worked in kcal rather than kj and this should be considered in the choice of numeric value of the ideal gas constant].

While Amram and Ganor (2005) gave very detailed steady state data, they gave little information on the relationship between initial and steady state rates. This relationship was estimated from the results of Metz *et al.* (2005), illustrated in Figure 28.

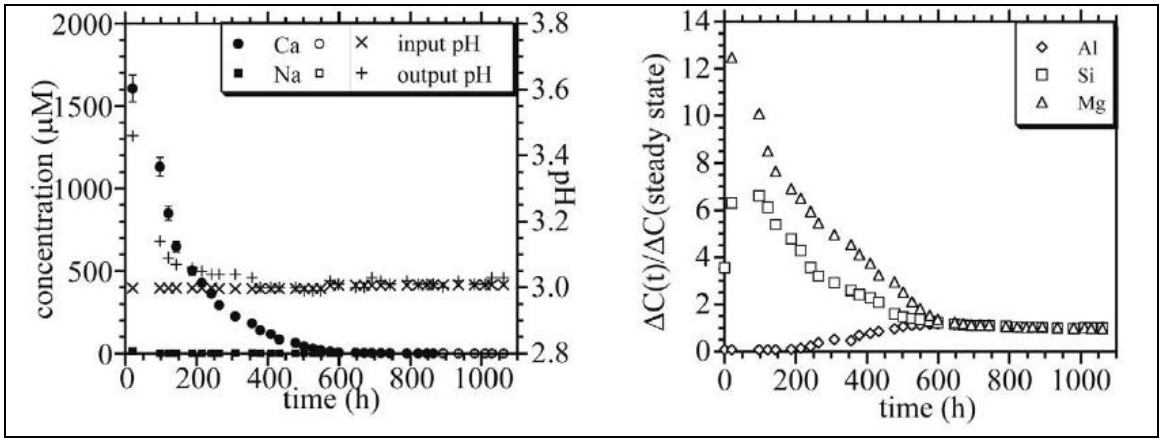

Figure 28: Ionic concentrations expressed as a function of time. The interlayer sites are represented by Ca and Na (but with Na concentrations vanishingly small). Calcium undergoes an exponential decay from initial rapid dissolution, and after ~600 hours appears to have been completely leached. Silicon and Mg also undergo exponential decay and achieve steady state conditions at ~600 hours. Aluminium shows a different trend and its rate of dissolution increased with time until steady state. After Metz *et al.* (2005)

Equation 25 was used to determine the steady state rate for each sample. This steady state rate and initial rate data, from Metz *et al.* (2005), were used to fit an exponential curve using Equation 20. The resulting data were used in a modified form of Equation 22, to determine the extent of dissolution of each element in the smectite (and the associated acid consumption). It was necessary to modify Equation 22 because the smectite rates are mass normalised rather than surface area normalised (as was the case for chlorite). A summary of the results of these calculations is given in Table 27 (with additional data in Appendix A).

Table 27: Smectite dissolution data calculated to reflect the variation in the rate of release of each element resulting from incongruent dissolution

RAO	**Dissolution**		**H_2SO_4 Consumption**	
pH = 1.5	**mol/ton**	**% of Contained Smectite**	**mol/ton**	**kg/ton**
Ca	3.26	0.16	3.26	0.32
Exchangeable Mg	32.26	0.96	32.26	3.16
Octahedral Mg	0.19	0.01	0.19	0.02
Fe	0.16	0.01	0.16	0.02
Al	0.01	0.00	0.01	0.00
Si	0.13	0.00	-	-
Total	**35.99**	**1.14**	**35.87**	**3.52**
OAO	**Dissolution**		**H_2SO_4 Consumption**	
pH = 1.5	**mol/ton**	**% of Contained Smectite**	**mol/ton**	**kg/ton**
Ca	1.35	0.16	1.35	0.13
Exchangeable Mg	13.37	0.96	13.37	1.31
Octahedral Mg	0.08	0.01	0.08	0.01
Fe	0.07	0.01	0.07	0.01
Al	0.00	0.00	0.01	0.00
Si	0.05	0.00	-	-
Total	**14.92**	**1.14**	**14.87**	**1.46**
MSO	**Dissolution**		**H_2SO_4 Consumption**	
pH = 1.5	**mol/ton**	**% of Contained Smectite**	**mol/ton**	**kg/ton**
Ca	7.62	0.16	7.62	0.75
Exchangeable Mg	75.53	0.96	75.53	7.41
Octahedral Mg	0.44	0.01	0.44	0.04
Fe	0.37	0.01	0.37	0.04
Al	0.02	0.00	0.03	0.00
Si	0.30	0.00	-	-
Total	**84.28**	**1.14**	**83.99**	**8.24**

Since the rates are normalised to the smectite mass and not surface area, all of the Kayelekera samples are expected to have the same percentage smectite dissolution. However, since the samples contain different amounts of smectite this results in acid consumptions of between ~1.5 and 8.2 kg H_2SO_4 per ton of ore processed.

Illite

The only sample to contain measurable amounts of illite was MSO the (48.7% illite). Moderately crystalline illite was also detected in the clay fraction of Mooi, however the concentration of this phase was sufficiently low, (and the crystallinity sufficiently high) that it was considered acceptable to include the dissolution of this phase in the muscovite calculations. Therefore only illite in MSO will be considered here.

Deer *et al.* (1993) described illites as clay minerals, similar in structure to the micas. They have a general formula of $K_yAl_4(Si_{8-y},Al_y)O_{20}(OH)_4$, where Ca and Na can substitute for K, and Mg and Fe can substitute for Al. Kohler *et al.* (2003) gave an equation for the acid dissolution of illite. This has been slightly adapted, to more closely correspond to the composition calculated from the semi-quantitative EDS analysis (see Chapter 5), and is given in Equation 26.

$$K_{1.26}(Mg_{0.02}Fe_{0.19}Al_{3.80})(Al_{1.26}Si_{6.75})O_{20}(OH)_4 + 16.86H^+ + 3.07H_2O \rightarrow 1.26K^+ + 0.02Mg^{2+} + 0.19Fe^{2+} + 5.06Al^{3+} + 6.75H_4SiO_4$$

Equation 26

Bibi *et al.* (2011) describe the dissolution of illite as highly incongruent in the initial phase with K and Al release in preference to Si. They suggested that dissolution follows a sequence of first dissolving interlayer K, followed by octahedral Mg, Fe and Al, with dissolution of Si as slowest, and rate limiting, step.

There is some disagreement, in the literature, as to the steady state in acid dissolution of illite. Bibi *et al.* (2011) state that illite requires 1500 to 2200 hours to reach steady state, while Kohler *et al.* (2005) argue that illite dissolution never truly reaches steady state. Although it may be important in modelling the weathering environment, the distinction is trivial in acid leaches of 25 hours duration. For durations consistent with leach tests, it is sufficient that the

dissolution rates of both authors show distinctly flat curves between 1500 and 2200 hours.

The relationship between pH, temperature and dissolution rates is illustrated in Figure 29. Lowest rates are seen at low temperature and near neutral pH, with systematic increases in rate with decreasing of increasing pH.

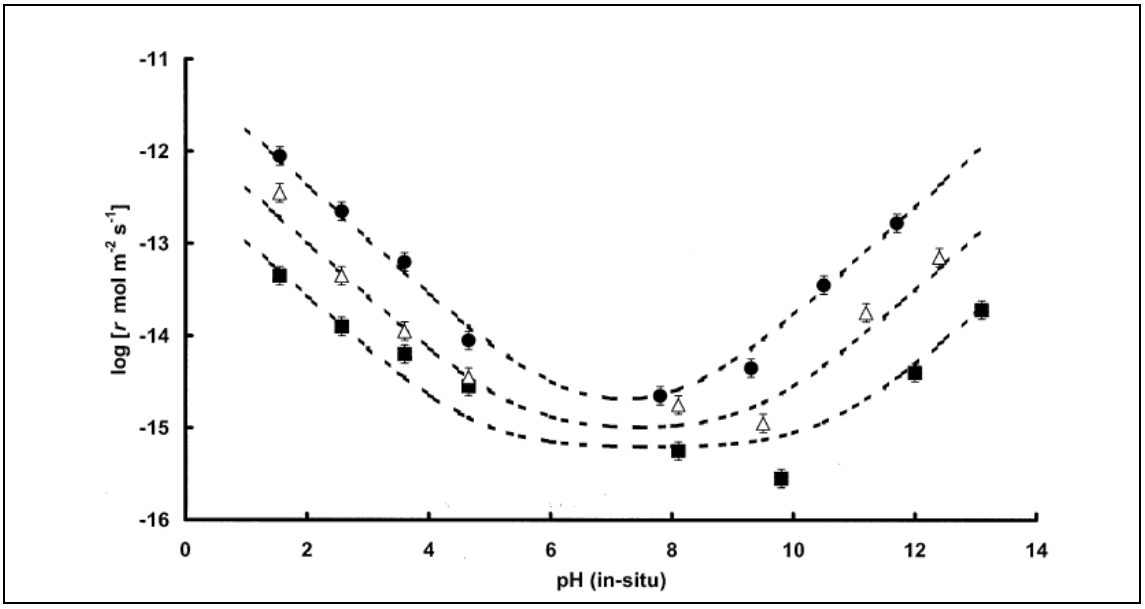

Figure 29: Dissolution rate as a function of pH and temperature. The lower curve represents rates at 5ºC, the middle curve at 25ºC and the upper curve at 50ºC (Kohler *et al.*, 2003).

In calculating the extent of dissolution, and acid consumption, a BET surface area of 42 m^2/g (Bibi *et al.*, 2011), an illite dissolution rate of 2.00×10^{-13} (based on the data of Kohler *et al.*, 2003) and the initial and steady state release ratios of Bibi *et al.* (2011) and Kohler *et al.* (2005) were used. It is expected that 0.9% of the total illite will dissolve during the leach test, resulting in an acid consumption of ~11 kg/ton (Table 28).

Table 28: Illite dissolution data of MSO

Determination	Dissolution		H_2SO_4 Consumption	
Units	**mol/ton**	**% of Contained Illite**	**mol/ton**	**kg/ton**
Si	8.6	0.05	-	-
Al	23.5	0.13	35.28	3.46
Mg	24.5	0.28	24.55	2.41
Fe	33.3	0.17	33.27	3.26
K	34.3	0.28	17.15	1.68
Total	**-**	**0.90**	**110.24**	**10.81**

Plagioclase

The members of the plagioclase group represent a solid solution series between the end members albite ($NaAlSi_3O_8$) and anorthite ($CaAl_2Si_2O_8$) (Klein, 2002). The dissolution of plagioclase follows Equation 27, which has been modified from Chen and Brantley (1996), to more closely resemble the albitic plagioclase composition in the present study.

$$Na_{0.93}Ca_{0.07}Al_{1.07}Si_{2.93}O_8 + 4.28H^+ + 3.72H_2O \rightarrow$$
$$0.93Na^+ + 0.07Ca^{2+} + 1.07Al^{3+} + 2.93H_4SiO_4$$

Equation 27

End member albite contains a continuous network of Si-O tetrahedra, while in pure anorthite, a third of the Si-O tetrahedra have been replaced by tetrahedral Al (Klein, 2002). This difference in structure is thought to contribute to the observed differences in the dissolution rates of the various plagioclase minerals. In albite the continuous network of Si-O tetrahedra result in slower dissolution rates. However, the disruption in this structure (caused by the substitution of more rapidly leaching Al) significantly increases the rate of dissolution of anorthite (Casey *et al.*, 1991). For this reason, any rate equation, used to predict the dissolution of plagioclase, must have been produced for the particular plagioclase mineral, or must consider the composition of the mineral as part of the equation.

Plagioclase occurs in all four of the samples and is present in concentrations of between 16.6% (MSO) and 40.9% (RAO). Albite can have up to 10 mole percent anorthite before being considered a different mineral (Klein, 2002). This suggests a minimum Na_2O/CaO ratio (in weight percent) of 4.97. Comparison of the major element data (Table 18) for the RAO and OAO samples shows that they meet this criterion (with values of 5.48 and 18.22 respectively). The Mooi and MSO samples do not meet this criterion. However, significant amounts of Ca occur in other minerals, and even Mooi with a ratio of 0.32, can be shown to contain albitic plagioclase after assigning an appropriate amount of Ca to calcite and laumontite. Therefore the rate equation of Chen and Brantley (1996), which was developed specifically for albite, was used in modelling the dissolution of plagioclase (Equation 28).

$$\text{Log } r = -2.71 - \frac{3410}{T} - 0.5\text{pH}$$

Equation 28

Where r is the rate of albite dissolution (in mol albite cm^{-2} s^{-1}) and T is the temperature (in Kelvin).

Chen and Brantley (1996) developed two rate equations for plagioclase dissolution (the first and simpler is given in Equation 28). Such an equation may be considered excessively simple as it does not consider the inhibitory effect of aqueous Al (Oelkers, *et al.*, 1994). The second equation of Chen and Brantley, (1996) did consider aqueous Al and should produce slightly more accurate results. However, since the accuracy of an estimation of the aqueous Al activity depends on the accuracy of the dissolution calculations, of all the aluminosilicates in each sample (including albite itself), it was considered more accurate to use the equation (Equation 28) that did not consider aqueous Al.

The dissolution of albite tends to be incongruent, in the initial phase of dissolution, with the preferential release of Al, Na and Ca (Stillings and Brantley, 1995). This

results in the formation of a leached layer which has been depleted in Al, Na and Ca (Casey *et al.*, 1991). Diffusion through this layer results in a decrease in the dissolution rate of Al, Na and Ca, resulting in congruent dissolution under steady state conditions (Brantley, 2008).

Stillings and Brantley (1995) used relative release ratios (RRRs) to express the preferential release of various cations, where the RRR is calculated according to Equation 29.

$$RRR_j = \frac{R_j}{R_{Si}}$$

Equation 29

Where R_j is the release rate of element j and R_{Si} is the release rate of Si. Although not expressly stated by Stillings and Brantley (1995), it is clear that the release rates also consider the stoichiometry of the element in the mineral since an RRR of 1 is indicative of congruent dissolution, values less than 1 indicate preferential release of Si and values greater than 1 indicate preferential release of element j.

Stillings and Brantley (1995) reported initial RRRs of 3.5 for Al, 15 for Na and 19 for Ca, all of these decay to an RRR of 1 after about 500 to 1000 hours. Silica-based dissolution rates also decrease with time as reactive sites dissolve. This decrease can result in steady state rates one tenth as fast as the initial rate (Casey *et al.*, 1991). Using these data and Equation 20 it was possible to estimate the elemental release rate as a function of time (Figure 30).

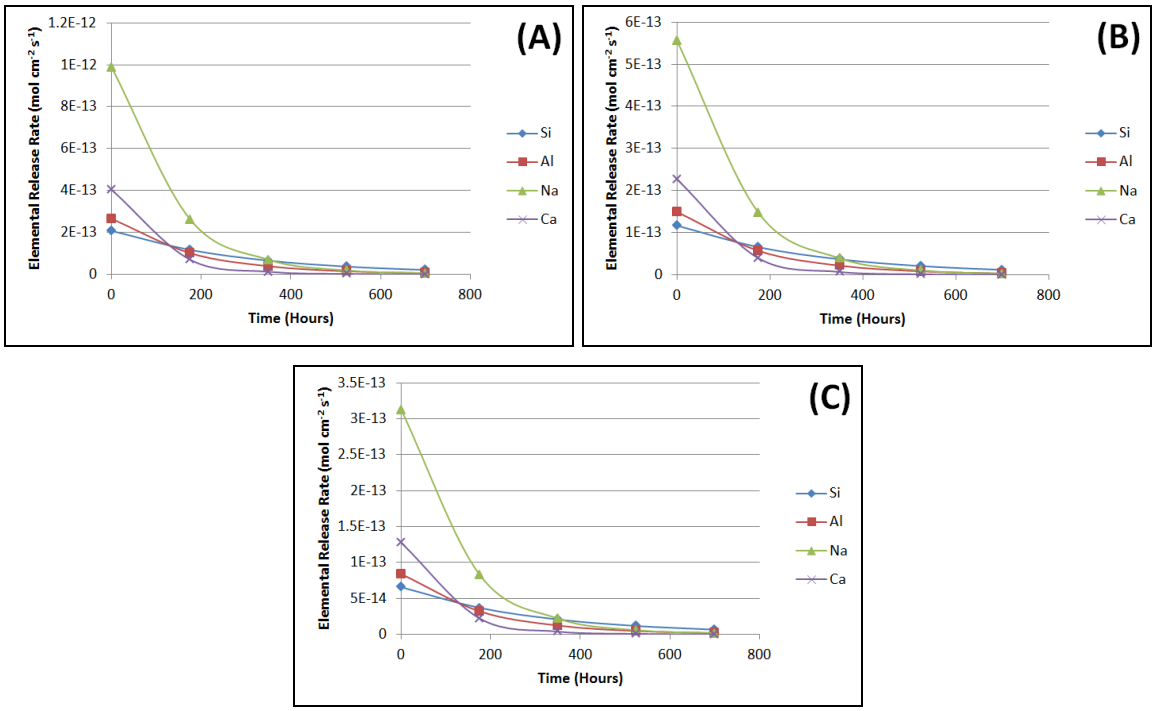

Figure 30: Elemental release rates at pH 1 (A), 1.5 (B) and 2 (C). For convenience time has been plotted in hours, however all calculations and rates were calculated per second.

In order to determine the extent of elemental dissolution (and associated acid consumption) it was necessary to estimate the surface area of the plagioclase in each sample. This proved to be more complex than for the phyllosilicates because of a widespread tendency to screen off the fine fraction of the plagioclase used in published dissolution experiments (Table 29). Therefore, while it was possible to simply select a published surface area for the phyllosilicates, it was necessary to calculate surface areas for plagioclase.

There are several methods of determining the specific surface area of a sample. These include the BET method (with involves measurements using the adsorption of an inert gas such as N_2 or Ar) and the geometric method (where a surface area is calculated from a grain size, assuming a particular particle shape) (Knauss and Wolery, 1986; Hodson, 2006). Determining a BET surface area for the plagioclase in the present study was impractical because the samples do not consist exclusively of plagioclase. This would make a geometric surface area more practical. However, because the geometric method assumes a simple

particle shape, it does not consider the effect of fractures and other surface roughness. This surface roughness can be calculated using Equation 30 (Helgeson *et al.*, 1984).

$$R = \frac{A_{ads}}{A_{geo}}$$

Equation 30

Where R is the surface roughness, A_{ads} is the BET surface area and A_{geo} is the geometric surface area.

Assuming a spherical model the geometric surface area can be calculated using Equation 31 (Tester *et al.*, 1994).

$$A_{geo} = \frac{6 \times 10\,000}{\Phi\rho}$$

Equation 31

Where A_{geo} is the specific geometric surface area (in cm^2/g), Φ is the particle diameter (in μm) and ρ is the density of the mineral (in g/cm^3).

Using Equation 31, geometric surface areas were calculated from published data. The median of the upper and lower screen sizes was used as a proxy for Φ. Equation 30 was then used to determine surface roughness (Table 29). While there was significant scatter in the data, there is a clear trend of increasing surface roughness with decreasing particle size. This may be due to an increase in the amount of surface damage and fracturing, in response to the additional grinding required to achieve the smaller particle size.

Aside from natural random variation, the scatter is likely to be due to errors in the calculation of the geometric surface area (due to the use of the median of the upper and lower screen sizes as a proxy for Φ). In samples where the mean particle size is closer to the lower screen size, the calculated geometric surface

area represents an underestimate. Where the mean particle size is closer to the upper screen size, the geometric surface area will have been overestimated because of this assumption. In order to minimize this effect, the mean of the data for each author was used instead of the raw surface roughness values (Figure 31).

Table 29: Geometric surface area and surface roughness calculated from published data

Reference	Size Range	BET Surface Area	Geometric Surface Area	Surface Roughness
-	μm	cm^2/g	cm^2/g	-
Casey and Westrich (1991)	25-75	4050	458	8.84
		1800	458	3.93
		6450	458	14.08
		5200	458	11.35
		4900	458	10.70
		2000	458	4.37
		2700	458	5.90
		4050	458	8.84
		3500	458	7.64
Knauss and Wolery (1986)	75-125	1620	229	7.07
		920	229	4.02
Stillings and Brantley (1995)	75-150	426	204	2.09
		877	204	4.31
		845	204	4.15
		952	204	4.68
Chen and Brantley (1997)	75-150	665	204	3.27

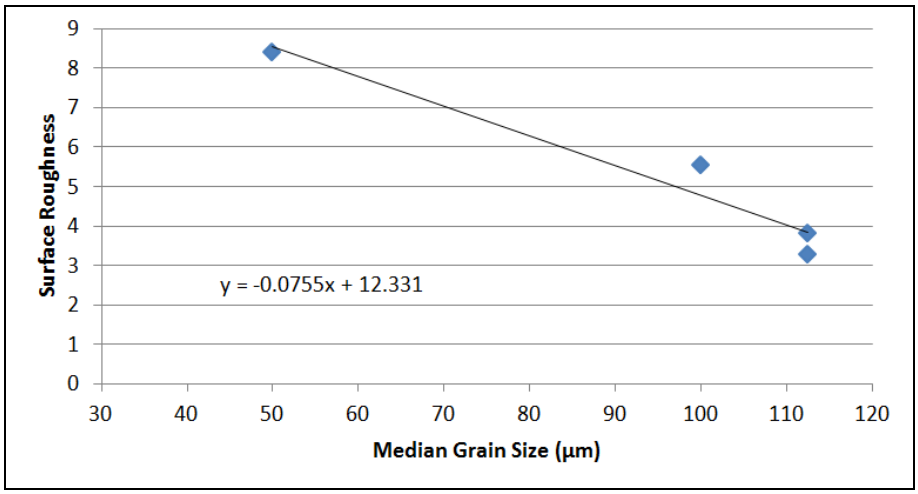

Figure 31: Average surface roughness plotted as a function of the median grain size. Note the trend towards increasing surface roughness with decreasing grain size.

By combining Equation 31 and the linear regression shown in Figure 31, it was possible to derive a geometric surface area that considers both the model (spherical) surface area and surface roughness (Equation 32). This surface area (Est SA_{ads}) is an estimate of what would be measured by the BET method.

$$\text{Est } A_{ads} = \frac{739\,860}{\Phi\rho} - \frac{4530}{\rho}$$

Equation 32

Where Est A_{ads} is the estimated BET surface area, Φ is the particle diameter (in µm) and ρ is the density of the mineral (in g/cm^3).

Particle sizes of 80% passing 212 µm and 75 µm have median grain sizes of 132.5 µm and 46.9 µm respectively. Using these median grain sizes and a density of 2.62 g/cm^3 (Klein, 2002), Equation 32 yields specific surface areas of 402 cm^2/g for the 80% passing 212 µm samples and 4292 cm^2/g for the 80% passing 75 µm sample. Using these results and Equation 22, the predicted dissolution and acid consumption characteristics of plagioclase were calculated (Table 30).

Table 30: Predicted dissolution and acid consumption characteristics of plagioclase

Mooi -212	**Dissolution**		**H_2SO_4 Consumption**	
pH 1.0	**mol/ton**	**% of Contained Plagioclase**	**mol/ton**	**kg/ton**
Si	1.84	0.02	-	-
Al	2.29	0.02	3.43	0.34
Na	8.31	0.07	4.15	0.41
Ca	3.30	0.05	3.30	0.32
Total	**-**	**0.17**	**10.88**	**1.07**
Mooi -212	**Dissolution**		**H_2SO_4 Consumption**	
pH 1.5	**mol/ton**	**% of Contained Plagioclase**	**mol/ton**	**kg/ton**
Si	1.03	0.01	-	-
Al	1.29	0.01	1.93	0.19
Na	4.67	0.04	2.34	0.23
Ca	1.85	0.03	1.85	0.18
Total	**-**	**0.10**	**6.12**	**0.60**
Mooi -212	**Dissolution**		**H_2SO_4 Consumption**	
pH 2.0	**mol/ton**	**% of Contained Plagioclase**	**mol/ton**	**kg/ton**
Si	0.58	0.01	-	-
Al	0.72	0.01	1.09	0.11
Na	2.63	0.02	1.31	0.13
Ca	1.04	0.02	1.04	0.10
Total	**-**	**0.05**	**3.44**	**0.34**
Mooi -75	**Dissolution**		**H_2SO_4 Consumption**	
pH 1.5	**mol/ton**	**% of Contained Plagioclase**	**mol/ton**	**kg/ton**
Si	11.04	0.12	-	-
Al	13.73	0.15	20.60	2.02
Na	49.88	0.45	24.94	2.45
Ca	19.80	0.31	19.80	1.94
Total	**-**	**1.03**	**65.34**	**6.41**
RAO	**Dissolution**		**H_2SO_4 Consumption**	
pH 1.5	**mol/ton**	**% of Contained Plagioclase**	**mol/ton**	**kg/ton**
Si	1.66	0.02	-	-
Al	2.06	0.02	3.09	0.30
Na	7.49	0.07	3.75	0.37
Ca	2.97	0.05	2.97	0.29
Total	**-**	**0.15**	**9.82**	**0.96**

Table 30 Continued: Predicted dissolution and acid consumption characteristics of plagioclase

OAO	Dissolution		H_2SO_4 Consumption	
pH 1.5	**mol/ton**	**% of Contained Plagioclase**	**mol/ton**	**kg/ton**
Si	1.62	0.02	-	-
Al	2.01	0.02	3.02	0.30
Na	7.31	0.07	3.66	0.36
Ca	2.90	0.05	2.90	0.28
Total	**-**	**0.15**	**9.58**	**0.94**
MSO	**Dissolution**		**H_2SO_4 Consumption**	
pH 1.5	**mol/ton**	**% of Contained Plagioclase**	**mol/ton**	**kg/ton**
Si	0.67	0.01	-	-
Al	0.84	0.01	1.26	0.12
Na	3.04	0.03	1.52	0.15
Ca	1.21	0.02	1.21	0.12
Total	**-**	**0.06**	**3.98**	**0.39**

K-feldspar

Like albite, K-feldspar is a tectosilicate. It has a chemical formula of $KAlSi_3O_8$ (Klein, 2002). The dissolution of K-feldspar follows Equation 33 (adapted from Chen and Brantley, 1997).

$$KAlSi_3O_8 + 4H^+ + 4H_2O \rightarrow K^+ + Al^{3+} + 3H_4SiO_4$$

Equation 33

As with albite, K-feldspar displays incongruent dissolution in the initial phases of dissolution and Stillings and Brantley (1995) observed initial RRRs of 4 for Al and 20 for K. The rate equation for feldspar dissolution is given in Equation 34 (Brantley, 2003).

$$r = k_H(a_{H+})^n + k_{OH}(a_{OH-})^m$$

Equation 34

Where r is the steady state dissolution rate (in mol K-feldspar/m^2/s), k_H is the acid promoted constant, k_{OH} is the alkali dissolution constant, a_{H+} is the hydrogen ion activity, a_{OH-} is the hydroxyl ion activity and the values n and m are determined by the composition of the mineral. For K-feldspar k_{H+} is between $10^{-9.9}$ and $10^{-9.4}$, k_{OH} is between $10^{-10.4}$ and $10^{-9.2}$, n is between 0.4 and 0.5 and m is between 0.3 and 0.7 (Brantley, 2003).

The values of a_{H+} and a_{OH-} can be determined using Equation 35 and Equation 36 respectively (Harris, 1999). Using the above data, and these equations, the predicted leaching and acid consumption characteristics of K-feldspar were calculated (Table 31).

$$pH = - \log a_{H+}$$

Equation 35

$$a_{H+} \times a_{OH-} = K_w$$

Equation 36

Where a is the activity of the subscripted species and K_w is the dissociation constant of water. At 35° C Kw is 2.09×10^{-14} (Harris, 1999).

Table 31: Predicted K-feldspar Dissolution and Acid Consumption Characteristics

Mooi -212	**Dissolution**		**H_2SO_4 Consumption**	
pH 1	**mol/ton**	**% of Contained K-feldspar**	**mol/ton**	**kg/ton**
Si	2.25	0.05	-	-
Al	2.94	0.06	4.41	0.43
K	14.31	0.41	7.15	0.70
Total	**-**	**0.52**	**11.56**	**1.13**
Mooi -212	**Dissolution**		**H_2SO_4 Consumption**	
pH 1.5	**mol/ton**	**% of Contained K-feldspar**	**mol/ton**	**kg/ton**
Si	1.42	0.03	-	-
Al	1.85	0.04	2.78	0.27
K	9.03	0.26	4.52	0.44
Total	**-**	**0.33**	**7.30**	**0.72**
Mooi -212	**Dissolution**		**H_2SO_4 Consumption**	
pH 2	**mol/ton**	**% of Contained K-feldspar**	**mol/ton**	**kg/ton**
Si	0.90	0.02	-	-
Al	1.17	0.02	1.76	0.17
K	5.71	0.16	2.85	0.28
Total	**-**	**0.21**	**4.61**	**0.45**
Mooi -75	**Dissolution**		**H_2SO_4 Consumption**	
pH 1.5	**mol/ton**	**% of Contained K-feldspar**	**mol/ton**	**kg/ton**
Si	15.19	0.31	-	-
Al	19.80	0.39	29.70	2.91
K	96.45	2.77	48.22	4.73
Total	**-**	**3.48**	**77.92**	**7.64**

Table 31 Continued: Predicted K-feldspar Dissolution and Acid Consumption Characteristics

RAO	Dissolution		H_2SO_4 Consumption	
pH 1.5	**mol/ton**	**% of Contained K-feldspar**	**mol/ton**	**kg/ton**
Si	0.98	0.02	-	-
Al	1.28	0.03	1.92	0.19
K	6.24	0.18	3.12	0.31
Total	**-**	**0.23**	**5.04**	**0.49**
OAO	**Dissolution**		**H_2SO_4 Consumption**	
pH 1.5	**mol/ton**	**% of Contained K-feldspar**	**mol/ton**	**kg/ton**
Si	0.60	0.01	-	-
Al	0.78	0.02	1.17	0.11
K	3.79	0.11	1.89	0.19
Total	**-**	**0.14**	**3.06**	**0.30**
MSO	**Dissolution**		**H_2SO_4 Consumption**	
pH 1.5	**mol/ton**	**% of Contained K-feldspar**	**mol/ton**	**kg/ton**
Si	0.83	0.02	-	-
Al	1.08	0.02	1.62	0.16
K	5.25	0.15	2.62	0.26
Total	**-**	**0.19**	**4.24**	**0.42**

Quartz

Quartz occurs in all of the samples in concentrations of between 7.6% (MSO) and 49.5% (OAO). The dissolution of quartz under acidic to neutral conditions follows Equation 37 (Blum *et al.*, 1990). From this equation it can be seen that the dissolution of quartz is not acid-consuming. For this reason no attempt was made to model the dissolution of quartz.

$$SiO_2 + 2H_2O \rightarrow H_4SiO_4\ (aq)$$

Equation 37

Jarosite

Jarosite was only detected in the OAO sample where it is present in a concentration of 1.5%. The dissolution of jarosite follows Equation 38 (Baron and Palmer, 1996), which shows that the dissolution of jarosite is acid consuming. However, based on the results of Smith *et al.* (2005), who worked at similar conditions to a U leach test, it appears that jarosite dissolution will be minimal within 24 hours.

$$KFe_3(SO_4)_2(OH)_6 + 6H^+ \rightarrow K^+ + 3Fe^{3+} + 2SO_4^{2-} + 6H_2O$$

Equation 38

The slow kinetics and low concentration of jarosite suggest that the dissolution of this phase will not have a major influence on the leach (except for contributing a small amount of additional Fe to solution).

Pyrite

Pyrite was detected in the RAO sample in a concentration of 1.6%. The dissolution of pyrite in the presence of Fe^{3+} follows Equation 39 (Wiersma and Rimstidt, 1984). This equation shows that pyrite dissolution consumes Fe^{3+}. As shown by Equation 40 (Lottering *et al.*, 2008), the concentration of Fe^{3+} in solution is maintained by the addition of MnO_2, which in turn consumes acid. Therefore, the dissolution of pyrite results in the consumption of both acid and MnO_2. Combining Equation 39 with Equation 40 and cancelling spectator ions results in Equation 41.

$$FeS_2 + 14Fe^{3+} + 8H_2O \rightarrow 15Fe^{2+} + 2SO_4^{2-} + 16H^+$$

Equation 39

$$2Fe^{2+} + MnO_2 + 4H^+ \rightarrow 2Fe^{3+} + Mn^{2+} + 2H_2O$$

Equation 40

$$FeS_2 + 7MnO_2 + 12H^+ \rightarrow Fe^{2+} + 2SO_4^{2-} + 7Mn^{2+} + 6H_2O$$

Equation 41

Under conditions of pH and temperature typical of a U leach, McKibben and Barnes (1986) found that the initial rate of pyrite oxidation is related to the abundance of Fe^{3+} and H^+. Equation 42 is adapted from the equation of McKibben and Barnes (1986) to give rates in seconds rather than minutes.

$$r = 10^{-11.52} (M_{Fe3+})^{0.5} (M_{H+})^{-0.5}$$

Equation 42

Where r is the rate of pyrite dissolution (in mol/cm^2/s) and M_j represents the concentration of the respective Fe species (in mol/L or M).

In a U leach the redox potential is mainly dependant on Fe speciation according to Equation 43 (Ring, 1980). Therefore at a redox potential of -450 mV and assuming a total Fe concentration of 2 g/L (Ring, 1980), the leach solution could be expected to have an Fe^{3+} concentration of 31.5 mM. Using this value and an H^+ concentration determined using Equation 35, the initial rate of pyrite dissolution is expected to be 9.54 x 10^{-14} mol/cm^2/s.

$$E_c = -397 - 0.1984\ T \log [Fe^{3+}]/[Fe^{2+}]$$

Equation 43

Where Ec is the redox potential relative to a saturated calomel electrode and $[Fe^x]$ is the molar concentration of the relevant Fe species.

Using the petrographic data (Chapter 2) and Equation 31, the specific pyrite surface area is estimated to be 235 cm^2/g. It is therefore estimated that pyrite dissolution will consume ~19 g/ton of H_2SO_4 and ~20 g/ton MnO_2.

Manganese Dioxide

Manganese dioxide is added to the leach to maintain the redox potential. Lottering *et al.* (2008) used between 2 and 4 kg/ton MnO_2 for their leach tests. Based on these values it is estimated that the 400 mV test will consume 2 kg/ton, the 450 mV test 4 kg/ton and the 500 mV test 6 kg/ton. The RAO leach is also expected to consume 6 kg/ton although this test will be run at 450 mV. Pyrite in RAO will result in a small increase in MnO_2 consumption; however, the preservation of pyrite is an indication that the rock as a whole is significantly more reducing than the other samples in this study.

Based on Equation 40 and these estimated MnO_2 requirement, the quantities of reagent required to maintain the redox potential were calculated (Table 32).

Table 32: Estimated Quantities of MnO_2 and H_2SO_4 Required for Eh Control

Leach Test	Eh (SCE)	MnO_2		H_2SO_4	
-	mV	Mol/ton	kg/ton	Mol/ton	kg/ton
A	-500	69.02	6.00	138.03	13.54
B	-450	46.01	4.00	92.02	9.03
C	-400	23.01	2.00	46.01	4.51
D	-450	46.01	4.00	92.02	9.03
E	-450	46.01	4.00	92.02	9.03
F	-450	46.01	4.00	92.02	9.03
G	-450	46.01	4.00	92.02	9.03

Free Acid

In this case free acid concentration refers to the acid that remains in solution to maintain the low pH needed for U dissolution. Equation 35 gives the relationship between H^+ activity and pH and Equation 44 gives the relationship between activity and concentration (Harris, 1999).

$$A_c = [C]\ \gamma_c$$

Equation 44

Where A_c is the activity of ion C, [C] is the concentration (in mol/L) of C and γ_c is the activity coefficient.

The extended Debye-Hückel method (Equation 45) is typically used to determine the activity coefficient for solutions with an ionic strength less than 0.1 mol/L (Harris, 1999). The ionic strength is calculated using Equation 46 (Messnaoui and Bounahmidi, 2006).

$$\log \gamma = \frac{-0.51\ z_i^2\ (I)^{0.5}}{1 + [\alpha\ (I^{0.5})/305]}$$

Equation 45

$$I = 0.5\ \Sigma\ c_i\ z_i^2$$

Equation 46

Where γ is the activity coefficient, z_i is the charge of the ion, α is hydrated radius of the ion in pm, c_i is the concentration of ion i and I is the ionic strength.

As can be seen from Equation 46 the presence of any charged species (ions or complexes) in solution contributes to the ionic strength, which influences the activity coefficient of H^+ and therefore influences the amount of free acid required to achieve the desired pH. Using the dissolution data estimated for each mineral in each sample it is possible to estimate the solution composition.

However, the limitation of the extended Debye-Hückel equation to low ionic strength solutions makes it unsuitable for determining activity coefficients in U leach solutions. A number of other methods are available. These include the Davies equation and the Pitzer equation. The Pitzer equation provides more accurate activity coefficients, but is significantly more complex. The Davies equation is slightly less accurate but does not involve the complexity of the Pitzer equation (Samson *et al.*, 1999). Due to the approximate nature of the input data

(based on solution compositions estimated from mineral dissolution data) it was decided that the slight improvement in accuracy did not justify the complexity of the Pitzer equation. Therefore the form of the Davies equation given by White (in Press) was used (Equation 47).

$$\log \gamma_i = -Az^2[-bI + \sqrt{I}/(1+\sqrt{I})]$$

Equation 47

At 35°C, A is 0.5190 and b is 0.3 (White, in Press). Other variables are the same as in Equation 45.

The presence of Ca^{2+} and SO_4^{2-} ions in solution contributes to the ionic strength. However, their concentration in solution is influenced by two reactions. The first involves the formation of gypsum (Danielle *et al.*, 2008) which removes both Ca^{2+} and SO_4^{2-} from solution in equal molar quantities. The second involves the formation of ion pairs in solution (Reardon and Langmuir, 1976). While these ions remain in solution, their effective concentration is reduced (White, in Press).

$$Ksp_{gypsum} = A_{Ca^{2+}} \times A_{SO4^{2-}}$$

Equation 48

$$K_{CaSO4^\circ} = \frac{A_{Ca^{2+}} \times A_{SO4^{2-}}}{A_{CaSO4^\circ}}$$

Equation 49

Where Ksp_{gypsum} is the solubility product constant of gypsum, A_i is the activity of the respective species (equal to the product of the activity constant and the concentration) and K_{CaSO4° is the equilibrium constant for the formation of calcium sulphate ion pairs. Typical values for Ksp_{gypsum} range from $10^{-4.59}$ to $10^{-4.35}$ while K_{CaSO4° has a value of $10^{-2.31}$ (Reardon and Langmuir, 1976 and Messnaoui and Bounahmidi, 2006).

Substituting Equation 48 into Equation 49 shows that at equilibrium the concentration of calcium sulphate ion pairs is a function of Ksp_{gypsum}, $K_{CaSO4^\circ}$and the activity coefficient of the ion pair (Equation 50).

$$[CaSO4°] = \frac{Ksp_{gypsum}}{\gamma_{CaSO4°} \times K_{CaSO4°}}$$

Equation 50

For low ionic strength solutions $\gamma_{CaSO4°}$ is close to 1, but at higher ionic strengths can be as low as 0.02 (Reardon and Langmuir, 1976). Therefore, depending on the ionic strength of the solution, there could be between 366 and 18 240 ppm Ca^{2+} which is in solution, but bound up in ion pairs.

In addition to complexities resulting from gypsum precipitation and ion pair formation, modelling of the system required consideration of the dissociation of H_2SO_4. The first dissociation (Equation 51) has a sufficiently high equilibrium constant that it can be considered to proceed to completion, while the second dissociation (Equation 52) has an equilibrium constant of 1.2×10^{-2} (Brown *et al.*, 2003).

$$H_2SO_4 = H^+ + HSO_4^-$$

Equation 51

$$HSO_4^- = H^+ + SO_4^{2-}$$

Equation 52

Because of all of these factors (especially the interdependence of H^+ activity and ionic strength), an iterative approach was used to estimate the H^+ activity coefficient. It was first assumed that all activity coefficients were unity. The ionic strength was then calculated using the mineral dissolutions as input data, and satisfying equilibria given in Equation 48 to Equation 50. Equation 46 was then used to estimate the ionic strength. In the second iteration the Davies equation (Equation 47) was used to estimate the activity coefficient of each element component, except $CaSO_4°$ which was estimated using data from Reardon and Langmuir (1976). These steps were repeated with each iteration. The model achieved an acceptable level of stability after three to four iterations (Appendix A).

Based on this model it is estimated that it will require between ~7 and ~37 kg of acid per ton of ore to maintain the desired pH (Table 33). These values are significantly higher than would be expected if only the activity coefficients of H^+ were considered, however as shown by Equation 52, not all of the H in solution is present as free acid. This is exacerbated by the high acid consumption of some of the samples. As the acid is consumed, H^+ is removed from the system. This causes SO_4^{2-} to build up in the system and forces Equation 52 to the left, removing more acid from solution. The only major exception is the dissolution of Ca^{2+} which also removes SO_4^{2-} from solution.

Table 33: Sulphuric acid required to maintain the desired pH

Leach Test	Sample	Grind	pH	H_2SO_4
-	-	P_{80} µm	-	kg/ton
A	Mooi Head	212	1.0	36.19
B	Mooi Head	212	1.5	21.20
C	Mooi Head	212	2.0	7.98
D	Mooi Head	75	1.5	29.17
E	RAO	212	1.5	10.58
F	OAO	212	1.5	6.51
G	MSO	212	1.5	7.51

4.8. Discussion

Clay Fraction Mineralogy

The presence of zeolite in the Mooi sample suggests that the rock has undergone very low grade (zeolite facies) metamorphism. However, since it was possible to identify the zeolite as laumontite it is possible to more accurately constrain the metamorphic conditions indicated by this assemblage. Laumontite is stable in the temperature range of 110° to 300° C (Miyashiro and Shido, 1970 and Weisenberger and Selbekk, 2009), which constrains the present metamorphic assemblage of Mooi to within that range.

Absolute illite crystallinity was not determined; however it was possible to determine illite crystallinity in a qualitative sense. This determination indicated that the Mooi sample had undergone higher metamorphic temperatures than the Kayelekera samples. Since Mooi had undergone very low grade metamorphism, it is likely that the Kayelekera samples had only undergone diagenesis. This is supported by the absence of illite interstratification in the smectite of the RAO and OAO. The absence of illite interstratifications in smectite is thought to correspond to temperatures of less than 110° C, although the age of the sediments and other factors can influence the interstratification and crystallinity characteristics of illite-smectite (Pollastro, 1993).

In addition to providing information on the geological history of the U deposits, the presence of smectite also has implications for U extraction. Smectite can form gels during the leaching process. These gels can contain as little as 5-7% solids (McFarlane *et al.*, 2005) and result in difficulties in separating the leach residue from the pregnant solution, preventing further processing.

Another characteristic of smectite is its ability to retain radionuclides (such as uranium) by ion exchange or surface complexation (Metz *et al.*, 2005). While this characteristic may be very desirable for environmental applications, it is deleterious under leach conditions as it may result in incomplete U recovery.

Major Mineralogy and Prediction of Reagent Consumption

XRD analyses of the head samples indicated that, with the exception of the MSO sample, these samples are all arkosic sandstones, containing between ~39% (Mooi) and ~50% (RAO) feldspar. Quartz is also a major phase and is either the most abundant, or second most abundant, gangue mineral. The Mooi sample also contains subordinate amounts of calcite and minor amounts of laumontite, chlorite and muscovite. The RAO sample contains minor amounts of chlorite, smectite and pyrite and OAO contains smectite and jarosite.

The composition of the MSO differs from the arkose samples. In this sample illite is the dominant phase with subordinate amounts of smectite and plagioclase, and minor K-feldspar and quartz.

Based on the modelling of the dissolution characteristics of each sample it appears that calcite is the most important gangue acid consumer in Mooi, followed by laumontite and then chlorite. In RAO chlorite and smectite are the dominant acid consumers, while in OAO smectite is the most significant deleterious phase. In MSO both illite and smectite are important.

It has been suggested that the feldspar are relatively inert under the conditions of a typical U leach (IAEA, 1980). The dissolution modelling suggests that while the feldspars are significantly less reactive than the carbonates and many of the phyllosilicates, the dissolution of plagioclase and K-feldspar are expected to contribute to a small amount of acid consumption.

Unlike the feldspars, quartz dissolution does not consume acid and therefore no attempt was made to model the dissolution of this phase.

The gangue mineralogy and pH of the leach are not the only factors influencing the degree of acid consumption. Due to the relationship between surface area and grind, it appears that grind may have as strong an influence on reagent consumption as pH. While the finer grind improves U mineral exposure, it also increases comminution costs and gangue acid consumption. It is therefore particularly important to determine the ideal grind for ores with high gangue acid consumptions to balance the most effective conditions for U leaching.

Acid consumption of gangue minerals can adversely affect the economics of a project by increasing processing costs. In spite of this, there is an advantage to the acid attack of gangue phases. Lottering *et al.* (2008) found that acid leaching

improves the exposure of ore minerals and can serve as a form of chemical comminution.

In addition to acid consumed by gangue phases, acid is also required to maintain the desired pH and redox potential. The choice of MnO_2 as the oxidiser and H_2SO_4 as the acid has very specific effects on the reagent consumption characteristics of the leach. Approximately 2.3 kg of H_2SO_4 are required to facilitate the dissolution of each kg of MnO_2. The use of H_2SO_4 has the advantage of contributing two moles of acidic protons per mole of H_2SO_4 added. At low SO_4^{2-} activities this is an advantage. However, when acid consumptions are very high SO_4^{2-} can build up in solution resulting in high activities (except where Ca is present in sufficient concentrations to remove the SO_4^{2-}). The first acid dissociation constant of H_2SO_4 is very large, and dissociation therefore can be considered complete, however the second dissociation constant, although large, is significantly lower (Brown *et al.*, 2003). Therefore, high SO_4^{2-} activities favour the formation of the HSO_4^- ion and remove H^+ from solution. As a result, much larger quantities of acid are required to reach the desired pH than would be expected if only the relationship between H^+ activity and pH was considered.

Considering gangue acid consumption and the amount of acid required to maintain the Eh and pH, it is possible to make a crude assessment of the economics of acid leaching these ores. Assuming prices of 52.00 $/lb for U_3O_8 (spot price, UxC, 2012) and 0.09 $/lb for H_2SO_4 (Gonzalez *et al.*, 2011) the acid required to leach Mooi would cost almost half of the value of the contained U. However, 0.09 $/lb for H_2SO_4 is probably a very conservative estimate and depending on the specifics of the project (including location) the acid costs could be significantly higher. This suggests that acid leaching of Mooi will not be economic.

In contrast with the poor economics of acid leaching Mooi, the higher grade and lower reagent consumption of RAO, OAO and MSO suggest that they could be

economically processed by acid leach (depending on other mining and processing costs).

The use of XRD for gangue characterisation in U ores has two main advantages. The first is the accurate characterisation of phyllosilicates, which can be benign or deleterious depending on the type. The second advantage is that XRD is time and cost effective. Modern XRD analyses are significantly more rapid than either optical petrography or automated SEM analyses. It also costs between a quarter and half of the price of these other methods. Therefore XRD could be of particular value in producing rapid cost effective analyses for exploration programs. Alternatively XRD could be used to rapidly identify areas of concern within a project, which could later be investigated by slower, more expensive techniques.

The major limitation of XRD data in modelling gangue acid consumption is the lack of textural data. The dissolution of most minerals (especially silicates) is strongly dependant on surface area. This data cannot be obtained by XRD. However, this limitation can be partially mitigated by using the grind to estimate mineral surface areas.

As a means of checking the validity of the equations used to model the dissolution characteristics of the various gangue minerals, the pregnant solutions from the leach tests will be assayed for Si, Al, Mg, Fe, Mn, K and Na (Chapter 6). Distinguishing the dissolution characteristics of the various minerals could potentially be complicated by the presence of the same elements in more than one mineral (e.g. K in both muscovite and K-feldspar or Ca in laumontite and calcite). XRD analyses of the residues will therefore be necessary to determine the extent of dissolution of certain minerals as a function of time.

Detection and Quantification Limits

The limits of detection and quantification were determined for 7 different gangue minerals. The limits of detection range from 0.17% for calcite to 1.36% for chlorite. These minerals also represent the highest and lowest limits of quantification, with values of 0.50% and 3.99% respectively. The particularly low detection limit of calcite is advantageous because of the high gangue acid consumption and rapid dissolution kinetics of this phase. However, the high detection limit of chlorite is unfortunate as in many of the samples chlorite was the most significant silicate acid consumer.

Preferred orientation was observed in the peaks of certain minerals. This phenomenon can have an effect on the limits of detection and quantification. If the peak used in the identification and quantification (typically the main peak) is enhanced, then preferred orientation lowers the limit of detection. However, if the peak is diminished then preferred orientation raises the detection limit. In either case preferred orientation will typically raise the limit of quantification. This is because a second (typically less intense) peak is needed for the March-Dollase (Dollase, 1986) correction.

The theoretical limit of detection of a mineral is a function of the position of the main peak (in d-spacing), with lower detection limits possible for peaks of lower d-spacing, the mass absorption coefficient of the matrix and the calibration constant of the phase. The practical limit of detection is also a function of the complexity of the ore. If the gangue mineralogy is particularly complex, with many overlapping peaks, it may not be possible to identify a phase from the main peak alone. This could significantly raise the limits of detection of a particular phase.

The micas all have peaks at ~10 Å. This can result in difficulties distinguishing between the micas at low concentrations, especially in cases where multiple micas are present. The main mica peak is also strongly enhanced by preferred

orientation. This makes the identification of mica possible at very low concentrations, but necessitates the use of a second peak (in this case the one at 4.45 Å) for quantification.

The main laumontite peak does not overlap with other common minerals, but preferred orientation should be considered.

The ~7 Å chlorite peak overlaps with that of kaolinite. It is therefore necessary to use the 14 Å peak to distinguish kaolinite from chlorite. However, the 14 Å peak can overlap with smectite. In these samples glycolation was used to increase the spacing between the smectite layers and made it possible to resolve the chlorite and smectite peaks.

As chlorite is a phyllosilicate, it would be expected to show similar preferred orientation characteristics to muscovite. However, although no attempt was made to correct for preferred orientation of this phase (mostly due to the lack of a suitable second peak to use in the correction), the calibration curve showed reasonably low scatter. This suggests that, at least in these samples, chlorite is not as strongly prone to preferred orientation as muscovite.

K-feldspar is not as strongly acid consuming as chlorite and its detection at very low concentrations is therefore not as critical.

Plagioclase does not have peak overlap problems with any common minerals. This makes identification of plagioclase at low concentrations more accurate; however sediments may contain several types of plagioclase. This would not only influence the diffraction characteristics, but also the leach characteristics of the ore.

The main calcite peak overlaps with that of chalcopyrite. This overlap can be a major problem if both are present in the ore. If both phases are not present, then

the colour of the pulverized material can be used as a guide. Chalcopyrite results in a dark grey pulp, while calcite-bearing pulps tend to be lighter in colour.

Pyrite does not experience serious overlap problems making identification of pyrite at low concentrations reasonably straight forward. The identification of pyrite is also aided by the low background noise at the positions where its main peaks occur.

Having determined the limits of detection of these gangue phases in these samples, it would be desirable to be able to make predictions regarding the detection limits of these minerals in other matrices. The vast number of possible matrices would appear to make estimation of the matrix mass absorption coefficient an impossibly difficult task. However, the matrices of Southern African U ores tend to be dominated by a relatively small number of minerals. The Witwatersrand ores are dominated by quartz (Lottering *et al.*, 2008), while the granite hosted deposits of Namibia are dominated by quartz and feldspar (Kinnaird and Nex, 2007). The same is true of Karoo-aged sandstones, such as those in the present study. This suggests that an understanding of the mass absorption characteristic of quartz and the various feldspar species would allow for the estimation of the mass absorption characteristics of most Southern African U ores.

Figure 32 shows two ternary diagrams with mass absorption coefficients as a function of the concentrations of quartz and the various feldspar species. The overall form of these diagrams are based on those of Streckeisen (1976), however in this plot albite (An0-An5) was grouped with K-feldspar. As can be seen from Figure 32, the mass absorption characteristics of albite and K-feldspar are very different, and for this reason the two phases were separated.

It can be seen that, for Co-Kα radiation, the mass absorption characteristics of quartz and albite are reasonably similar, as are those of K-feldspar and anorthite.

These same trends are seen for Cu-Kα radiation, although the numerical values are lower than those of Co.

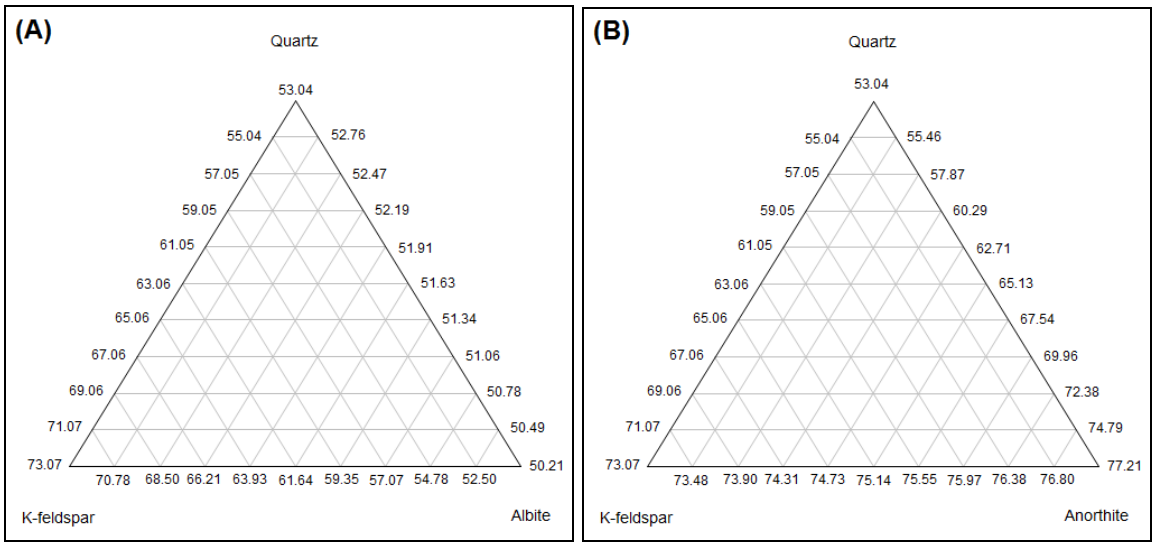

Figure 32: Mass absorption coefficients for Co-Kα radiation as a function of quartz and feldspar composition. The base ternary diagrams were generated using Geoplot software (Zhou and Li, 2006) with the mass absorption values determined using the MAC calculator function in HighScore Plus. Diagrams are based on those of Streckeisen (1976), however, because of the differences in the mass absorption coefficients of K-feldspar and albite, it was not possible to group the alkali feldspars in the lower left corners according to the Strekeisen method.

It would also be desirable to be able to estimate the detection limits of other minerals. In order to make this estimation, an estimated calibration constant is needed. It may be possible to make an estimate of this calibration constant from the reference intensity ratio (RIR) given in Equation 53 (Brandt and Kinneging, 2005).

$$\beta_i = \frac{1}{RIR_i}$$

Equation 53

Where β_i is the product of the calibration constant and the mass absorption coefficient of phase i, and RIR_i is the reference intensity ratio of the same phase.

This method would be fairly approximate as neither the mass absorption coefficient nor the calibration constant have been determined, but would allow for

a rough estimate of the detection limit in unknown samples (provided the mass absorption coefficient of the sample is not excessively large). However, further work would be required to develop and test such a method.

4.9. Summary and Conclusions

A single sample from the Mooifontein deposit and three samples from Kayelekera were examined by XRD. These analyses included detailed analysis of the clay fraction and head major mineral analyses. The results of these analyses were used to model the reagent consumption characteristics of each sample. The limits of detection and quantification of most of the gangue phases were also determined.

An attempt was made to predict the reagent consumption characteristics of the various gangue phases. The results of these calculations are likely to be somewhat approximate for two reasons:

1. Most workers studying the acid dissolution characteristics of gangue minerals focus on steady state conditions, in an attempt to model long term process such as acid mine drainage or weathering. This results in a shortage of data dealing with the initial rapid phase of dissolution and the factors controlling rates in this initial phase.

2. The role of surface area in controlling dissolution. For most applications, XRD data does not yield any textural information. It is therefore necessary to determine the surface area by some other method. In this case the P_{80}, and a small amount of optical data from Chapter 2, was used as a guide either in the selection of a specific surface area from published data, or in a geometic surface area model. Because it was not possible to directly measure the surface area, these factors will result in some degree of error.

The BET method of determining surface area is very widely used in determining dissolution rate. However, it is not readily applied to natural leach-feed material, which consists of a number of different minerals with varying surface areas. The geometric surface area is more able to handle these variations, but corrections are necessary to ensure that surface roughness is considered. While XRD data does not typically lend itself to the determination of surface area, a model was developed for the feldspars which makes it possible to obtain an estimated “BET” surface area from size data. The use of similar models, and mineralogical size data, will make it possible to more accurately estimate surface areas in leach-feed material.

Chapter 5. Scanning Electron Microscopy and QEMSCAN Analyses

5.1. Introduction, Aims and Objectives

The aims of the scanning electron microscopy (SEM) and QEMSCAN analyses were to:

1. Determine which minerals host the U mineralisation in each sample and in what proportions (this is hereafter referred to as the U deportment).
2. Determine the exposure and association characteristics of the U phases.
3. Validate the XRD gangue mineral identification and quantification.
4. Characterise the texture of the gangue phases with respect to grain size, exposure and association.

Determining the U deportment will make is possible to determine the mineralogical controls on U recovery resulting from the presence of refractory U minerals (if present). The exposure and association characteristics will be used to determine the adequacy of the grind.

Characterisation of the texture of the various gangue phases will make it possible to understand the kinetics of gangue dissolution (and therefore gangue acid consumption).

QEMSCAN

The SEM operates by scanning an electron beam over the sample and analysing the resulting interaction between the electrons and sample. These interactions result in both X-ray emissions and backscattered electrons (Reed, 2005). The X-ray emissions are characteristic of the elements that are hit by the electron beam

and the backscattered electron intensity is a function of the average atomic number of the mineral (Sutherland and Gottlieb, 1991). Therefore the combination of these two data sets makes it possible to determine the composition of a mineral, or alternatively identify a mineral based on its chemical composition.

However, the beam does not interact with an infinitely small point in the sample material, but rather with a volume of material having a finite width and extending some depth into the sample. Figure 33 (Reed, 2005) illustrates the path of an incident electron beam and the resulting points of X-ray emission. For this reason it is possible to obtain mixed spectra resulting from penetration of the beam into adjacent grains. This effect is most pronounced in very fine-grained minerals, or at the boundaries between minerals.

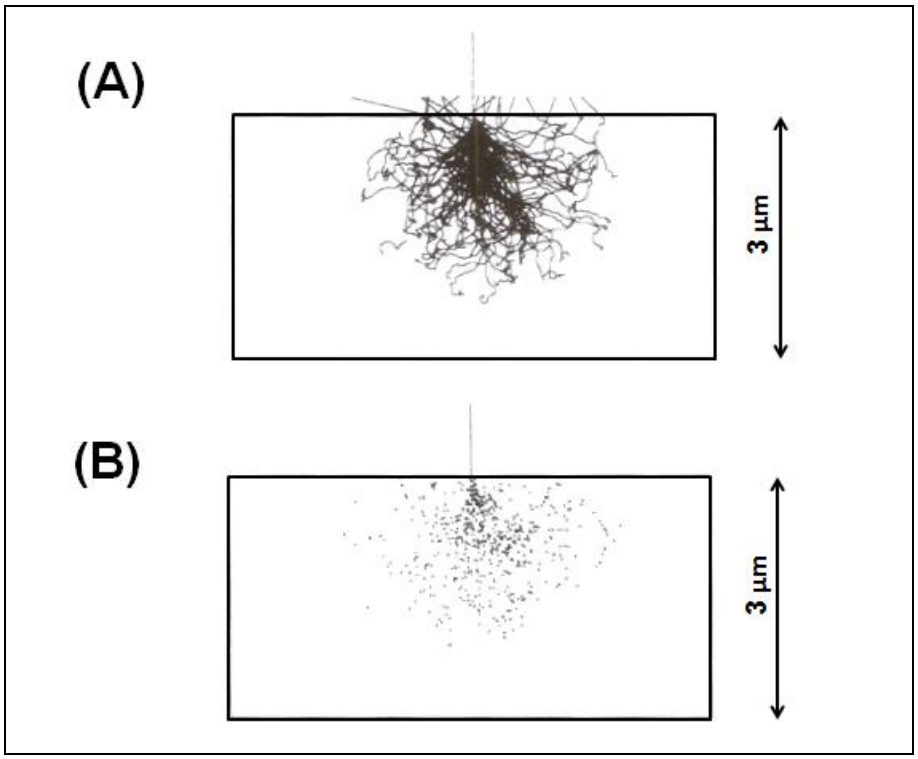

Figure 33: Monte Carlo simulation of the path followed by an electron beam (20 kV accelerating voltage) through a Si target (A) and points of X-ray emission (B) from within the sample (Reed, 2005 and the reference therein).

The automation of a SEM makes it possible to collect large amounts of data on a routine basis (Sutherland and Gottlieb, 1991) and reduces the dependence on the skill of the operator (Sutherland *et al.*, 1988). Examples of automated SEMs include the MLA and QEMSCAN (van Alphen, 2007). The QEMSCAN technology was used in the present study. As of 2011 there were 66 QEMSCANs worldwide (Pirrie and Rollinson, 2011), two of which are at SGS South Africa's Johannesburg Advanced Mineralogical Facility.

The QEMSCAN is based on QEM.SEM technology, and uses both the energy dispersive X-ray (EDX) spectrum and the backscattered electron (BSE) intensity, to create images in which the pixels represent the mineral species present in a sample (Liu *et al.*, 2005). There are four operations utilised in QEMSCAN mineralogy: The automatic mineral identification (i), production of an image of the mineralogy of the sample (ii), quantitative analysis of that image (iii), and interpretation of the results (iv) (Sutherland and Gottlieb, 1991).

The automatic mineral identification is achieved by comparing the EDX spectrum and BSE intensity to a database containing the spectra and intensities of known minerals (Pascoe *et al.*, 2007). This database is known as a species identification protocol (SIP) list. The SIP list can include several thousand entries. These entries are a collection of protocols for the identification of minerals, but also include protocols for the identification of mixed spectra, resulting from the analysis of boundaries between adjacent mineral phases. A single mineral could therefore have numerous SIP entries, to allow for the identification of the pure mineral, as well as the most common mixed spectra.

Due to the large number of SIP entries, it is impractical to handle the data on the SIP level. For this reason the SIP entries are summarised by grouping related entries to form the Primary List. The iDiscover software used for processing QEMSCAN data allows for a certain amount of pre-processing which operates on the Primary level. The aim of pre-processing is to handle data collection artefacts

for example mixed spectra and touching particles (particles that occur in physical contact with each other, but are not part of a single particle).

However, the Primary List is typically still too large to be practical to use in mineral and particle characterisation. The Primary List is therefore summarised into one or more Secondary Lists. These lists contain actual mineral entries, and it is from these that the data is typically extracted.

The QEMSCAN can operate using point, line, or area mode (Sutherland and Gottlieb, 1991). However, line and area analyses are most commonly used. Gottlieb *et al.* (2000) and Goodall *et al.* (2005) described the QEMSCAN analyses modes as follows:

Bulk mineralogical analysis (BMA) is a line scan method that records the number and length of mineral intercepts. This method can be used to determine mineral abundances, grain size and association data as well as mineral grain or particle surface area. BMAs are a rapid analysis method and produce data much more quickly than the other analysis modes.

Particle mineralogical analysis (PMA) is an area analysis method applied to particles up to 1 mm in size. Textural characteristics are determined from a BSE image. After elimination of grains that do not fit the selection criteria (due to size or contact with other particles), the grains are mapped using a series of closely spaced points. The spacing of the points is determined by the amount of detail needed in the maps. For finer detail a closer spacing is used, but this also increases the amount of time required for the analysis. PMAs are slower than BMAs. Therefore, given equal amounts of time, PMAs do not determine mineral abundances as accurately as BMAs (due to the analysis of fewer particles). However, the textural data is vastly more detailed and ideal for liberation analysis.

Specific mineral search (SMS) is similar to the PMA except that only particles that contain minerals with a preselected BSE intensity are mapped. This selective mapping method makes it possible to gather information about phases that are present in concentrations below 0.5 vol% (which is not practical by PMA).

Trace mineral search (TMS) is used when the phase (or phases) of interest are present in trace amounts. These low concentrations would require excessive amounts of time to analyse by SMS. Therefore, specialised hardware is used to accelerate the data collection for TMS analysis. During the analysis, the BSE intensity is constantly monitored, this makes possible the immediate rejection of fields that do not contain grains within sufficiently high BSE intensity. Because selection is based on high BSE, this method lends itself to the analysis of mineral grains with high average atomic number. Gold analysis is a common application, but because U minerals also have high BSE intensities they are also readily detected in the TMS analysis.

Stereology

There is no bias when determining mineral abundances from point counting, line scans or area maps. Therefore, assuming the statistical requirements are satisfied (Sutherland and Gottlieb, 1991), point fractions, line fractions, area fractions and volume fractions are all equal (Russ, 1986). However this is not the case with all mineral properties.

QEMSCAN data are collected from the surface of polished ore blocks or polished thin sections. These surfaces are two dimensional representations of the three dimensional structure of minerals. Therefore area measurements are two dimensional representations of three dimensional structures, while line scans are one dimensional representations of three dimensional structures. The use of lower dimensional data results in a systematic bias in the measurement of certain mineral properties. These include particle or grain size (King, 1982).

Figure 34 illustrates the sources of stereological bias in QEMSCAN analyses. The first type of bias is introduced when the particles are mounted in a resin block and the block is ground and polished to expose the particles. This grinding produces a two dimensional representation of the original particle. Only one possible cut through a particle will reproduce the original diameter. All others result in systematic underestimation of size.

In area based scans such as QEMSCAN TMS, this sectioning bias is the only stereological effect that must be considered. However in line based analyses (such as the BMA) there is an additional source of bias. Only one possible line will reproduce the true diameter of the two dimensional representation of the particle. All other lines will underestimate even the two dimensional representation. For this reason the BMA data include two sources of stereological bias.

Due to the systematic nature of the bias, it is possible to mathematically correct for stereological effects (King and Schneider, 1998). Such corrections rely on probability theory and can produce either mean particle (or grain sizes) or even size distributions (Higgins, 2000).

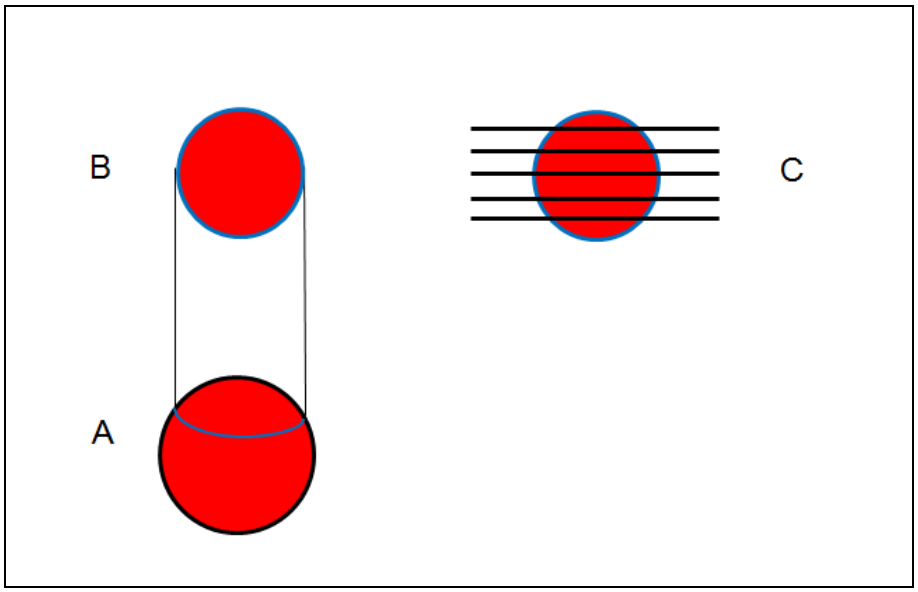

Figure 34: Stereological bias in QEMSCAN analyses. (A) Represents a spherical mineral grain which has been included into a polished section. Grinding of the polished section exposes a two dimensional (circular) representation of the original spherical particle (B). It is this two dimensional representation that is mapped in the area scans described above. There is only one possible section (along the "equator" of the grain) which will reproduce the original diameter of the sphere. All other cuts will under estimate the size of the particle. Further bias is introduced in the use of line scans. Rather than mapping the entire area of the circle, the BMA produces line scans (C) which intersect the circular representation. Only one line would measure the diameter of the circle, all others would underestimate the size of the circle.

5.2. Methodology

Each sample (after undergoing comminution) was micro-rotary split to produce 2 g aliquots. These aliquots were used to prepare 30 mm polished sections. In order to reduce the potential for bias, which could result from density-based segregation (Pirrie and Rollinson, 2011), two transverse polished sections were produced per sample. These transverse sections were produced by first resin mounting a 2 g aliquot in a 10 ml plastic tablet vial. The tablet vials were then cut longitudinally to produce a section which would sample across any density based segregation. The sections were mounted in 30 mm moulds and used to produce the transverse polished blocks. These blocks were used for the BMA analysis. An additional 7 normal, 30 mm polished blocks were prepared for the TMS analyses.

The samples were carbon coated and loaded for analysis using one of the two QEMSCANS at SGS South Africa's Johannesburg Advanced Mineralogical Facility. These QEMSCANs are based on Carl Zeiss Evo 50 scanning electron microscopes (Figure 35) with four SiLi EDX detectors.

The instrument BSE was calibrated using a three point calibration with quartz, Cu and Au standards. The BSE standard intensities are quartz: 42, Cu: 130, and Au: 242. The X-ray detectors were calibrated using the Cu Lα and Kα peaks, and the spectral engine was calibrated using the Cu and quartz standards.

The QEMSCANs are also able to perform manual scanning electron microscopy, including semi-quantitative EDX analysis of mineral grains. These were used to augment the automated QEMSAN analyses.

The BMA and TMS analyses were conducted according the methods described by Gottlieb *et al.* (2000) and Coetzee *et al.* (2011). A point spacing (the gap between individual analysis points within the line) of 2.5 µm was used with a line spacing (the gap between individual lines) of 150 µm for the BMAs. One thousand count X-ray spectra were collected at each point for most samples, however these standard spectra were found to be inadequate for analysis of the Mooi blocks. Due to the presence of laumontite in the Mooi sample it was necessary to use 3000 count spectra in the BMA analysis of this sample.



Figure 35: One of the QEMSCANS at SGS South Africa, showing the electron gun and column (1), the chamber into which the samples are loaded (2), the energy dispersive X-ray detectors (3), the standard Evo 50 computer (4) with its two monitors (5), the additional computer providing QEMSCAN capacity (6), with its monitor (7) and the pulse processors (8) which convert the signal from the X-ray detectors into a signal that the computer can process.

The use of higher (3000) count spectra made it possible to distinguish between laumontite and high Ca plagioclase, by detecting the Na in the plagioclase. These small amounts of Na were not detected in the 1000 count spectra.

The TMS analyses were run using a field size of 800 μm and a point spacing of 0.7 μm. The numbers of counts in the spectra collected in the TMS particle maps were adjusted depending on the BSE of the mineral being mapped. One thousand count spectra were used for minerals in the gangue silicate BSE range (except in Mooi blocks where 3000 count spectra were used), and 5000 count specta were used for any phase with a higher BSE. The higher counts on the higher BSE phases allowed for the production of very high quality patterns for the U minerals.

Grain Size and Surface Area

The BMA results were used to produce size and surface area data for the various gangue phases. The surface areas for most minerals were calculated using the method discussed in Chapter 4 (based on the work of Tester *et al.* (1994)). Due to the surface area dependence of this model, it was necessary to stereologically correct the grain size and corresponding surface area data. The stereological correction function built into the QEMSCAN software was used for this purpose. This function produces corrected average sizes for the various mineral phases.

The method for estimating surface area from grain size data (discussed in Chapter 4) assumes that the grains are spherical. However, this spherical assumption was considered too simple to reliably model the phyllosilicates. Based on the work of Hodson (2006), the phyllosilicates were modelled as cuboids with equal lengths and breadths. Hodson used a two 2 μm for smaller grains and 4 μm for grains larger grains. In this study the thickness was taken as a linear function of the grain size, rather than using the Hodson's two classes. Hodson, ignored the basal surface areas of the grains, while the entire phyllosilicate surface area was considered in the present study. This was done to maintain the similarity with BET surface areas.

The surface areas calculated using either Tester *et al.* (1994) or Hodson's (2006) method tend to under estimate the true surface area of the mineral as they do not consider the effect of fractures and other surface roughness. This surface roughness can be calculated using Equation 30.

Using published dissolution studies that included both grain size and BET surface area data, the surface roughness of each mineral was calculated. It was found, based on the published data, that the roughness of many minerals is a function of the grain size. Therefore based on the data from several studies, linear relationships between grain size and surface roughness were established.

Equation 54 gives the surface roughness of calcite and was based on the work of Anderson (1968), Oleg *et al.* (2005) and Oelkers *et al.* (2011). Equation 55 gives the surface roughness of chlorite and was based on Brandt *et al.* (2003), Lowson *et al.* (2005) and Henn *et al.* (2007). Equation 56 gives the surface roughness of muscovite and was based on Nickel (1973), Knauss and Wolery (1989) and Kalendova *et al.* (2010). Equation 57 gives the surface roughness of feldspar and was based on Knauss and Wolery (1986), Casey and Westrich (1991), Stillings and Brantley (1995) and Chen and Brantley (1997). Using these functions also corrects for any deviation between the geometric model and the actual shape of the grains. This is the reason that the surface roughness of calcite is not a function of grain size, that of chlorite increases with increasing grain size and those of muscovite and feldspar decrease with increasing grain size.

$$\mathbf{R_s = 2.451}$$

Equation 54

$$\mathbf{R_s = 0.012\phi + 6.087}$$

Equation 55

$$\mathbf{R_s = -0.058\phi + 14.21}$$

Equation 56

$$\mathbf{R_s = -0.076\phi + 12.33}$$

Equation 57

Where R_s is the surface roughness and Φ is the mean diameter.

Such detailed surface area data was not available for zeolite and so a simple geometric surface area was used for laumontite.

Because the QEMSCAN does not readily distinguish grain boundaries of very fine adjacent grains of the same mineral, it was not possible to determine surface areas for illite and smectite. A surface area of 42 m^2/g was used for illite (Bibi *et al.*, 2011). No attempt was made to estimate the surface area of smectite because, the relationship between total surface areas and reactive surface areas are too complex to allow for surface area normalisation of smectite (Metz *et al.*, 2005).

The TMS results are not subject to the same degree of bias as the BMA data. It was also desirable to retain the grain size distribution of the U minerals which would have been lost if corrected using the same method as the BMA data. More sophisticated methods (not included in the software) are available which can produce corrected size distributions, rather than average sizes (Higgins, 2000). However, because the TMS results were not used in assessing reaction kinetics, they were not stereologically corrected.

Species Identification Protocol (SIP) Development

The original data was collected using the AuU5 SIP file, but then reprocessed using the more recent AuU7 SIP. The AuU series are a collection of standard Au and U SIPs developed by Louis Coetzee and are the standard SGS South Africa SIPs for the analysis of Witwatersrand Au-U ores.

While AuU7 is a very powerful SIP file, certain modifications were necessary to ensure that the SIP file could be used on Karoo ores. The mapping of C-rich phases such as coal and organic C has traditionally been problematic by QEMSCAN. Van Alphen (2007) describes some of these challenges. The main complication is that the minimum BSE which is mapped by the system is 25. This allows the system to map mineral grains without mapping the mounting resin. However, the C-rich phases have a BSE lower than 25. It is also difficult to

distinguish the resin and a C-rich phase based on composition, because both are dominated by C. This problem was not addressed in the AuU7 SIP.

It was not necessary to determine the absolute amount of organic C contained in each sample. This was already determined by Leco (Appendix B). However, the determination of the surface exposure of a U mineral grain is based on its association with background (resin). If it was not possible to distinguish between resin and organic C, the QEMSCAN TMS data could cause the U minerals to appear erroneously exposed.

Since the organic C was only of particular interest when it was associated with a U mineral grain, it was possible to overcome this challenge by modifying the SIP file. It was unnecessary to use the exotic mounting media described by Van Alphen (2007). Due to the high atomic number of U, minerals of this element have a very high BSE. This BSE increase can even be seen in spectra collected from the resin surrounding the U mineral (due to the effect illustrated in Figure 33).

The AuU7 SIP classified these high BSE resin analyses using a C>200 SIP entry. This entry was then included in the background on the Primary level. A new SIP entry was created to exploit the brightening effect of the U on organic C. It was observed that the mounting resin contains measurable amounts of Cl and the organic C contains measurable S. The new entry (Org. Carbon) included S as a “must have” element and did not permit the inclusion of spectra containing Cl.

The resulting Org. Carbon SIP entry was unable to identify organic C that is not associated with a bright phase, but was successful in identifying instances of organic C associated with U minerals.

It was also necessary to include SIP entries for laumontite and uranocircite, which were both present in the Karoo samples, but not considered in AuU7. One

million count spectra were collected from both of these mineral phases. These spectra were used to produce one thousand simulated spectra, each with a thousand counts using the iDiscover software. The ranges defined by these spectra were used to generate several SIP entries for each of laumontite and uranocircite.

5.3. Results

Scanning Electron Microscopy

The manual scanning electron microscope analyses were used to augment the QEMSCAN analyses by identifying phases that are not included in the SIP file. The manual analyses were also used to assess the compositions of the various minerals. Although the EDS analyses are semi-quantitative, they are sufficiently accurate to make it possible to determine the approximate end-members present in the various solid solution series (for example plagioclase and chlorite). These compositional data were used in the data validation of the mineral quantification both by XRD and QEMSCAN.

The compositions of plagioclase, laumontite and chlorite were of interest in the Mooi sample (Figure 36). It was found that the plagioclase ranges from albite through to more calcic varieties, however anorthite was not present. The only calcic aluminosilicate present, that did not contain Na, was laumontite. The laumontite spectra suggest that the composition of this phase is close to ideal, while the average plagioclase composition was estimated to be approximately $Na_{0.93}Ca_{0.07}Al_{1.07}Si_{2.93}O_8$.

Analysis of chlorite grains indicated that the chlorite is enriched in Fe relative to Mg and the average composition was estimated to be approximately $(Mg_{3.75}Fe_{6.25}Al_2)(Si_6Al_2O_{20})(OH)_{16}$.

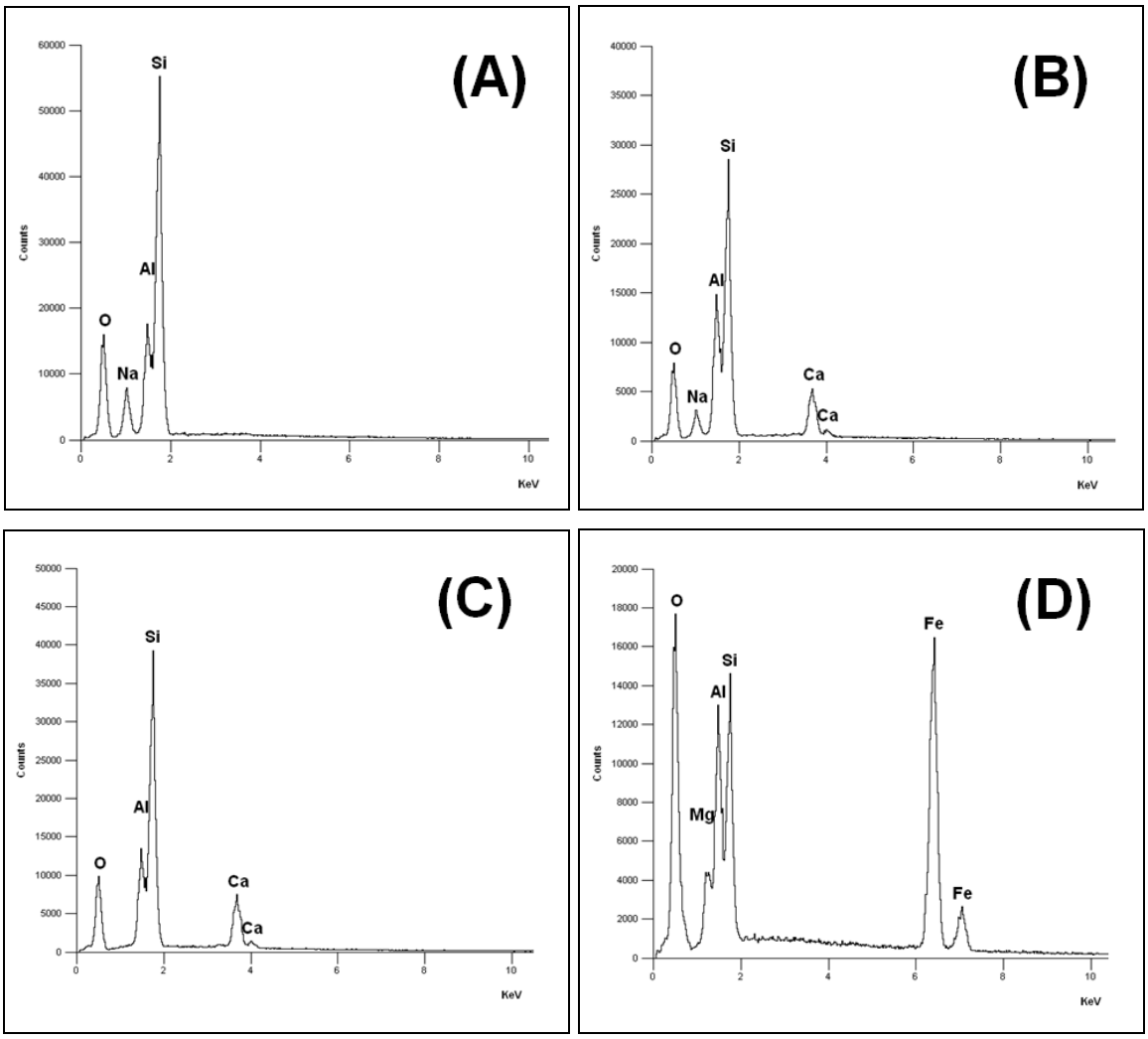

Figure 36: EDX spectra showing the compositional range of plagioclase grains within Mooi (A and B), as well as the composition of laumontite (C) and chlorite (D).

All of the U minerals in the Mooi sample had corresponding SIP entries in both AuU5 and AuU7. The most abundant U mineral was coffinite (Figure 37). Other U minerals were also observed and several thorite grains (Figure 38) were found to contain minor amounts of U (estimated as averaging 0.5% contained U).

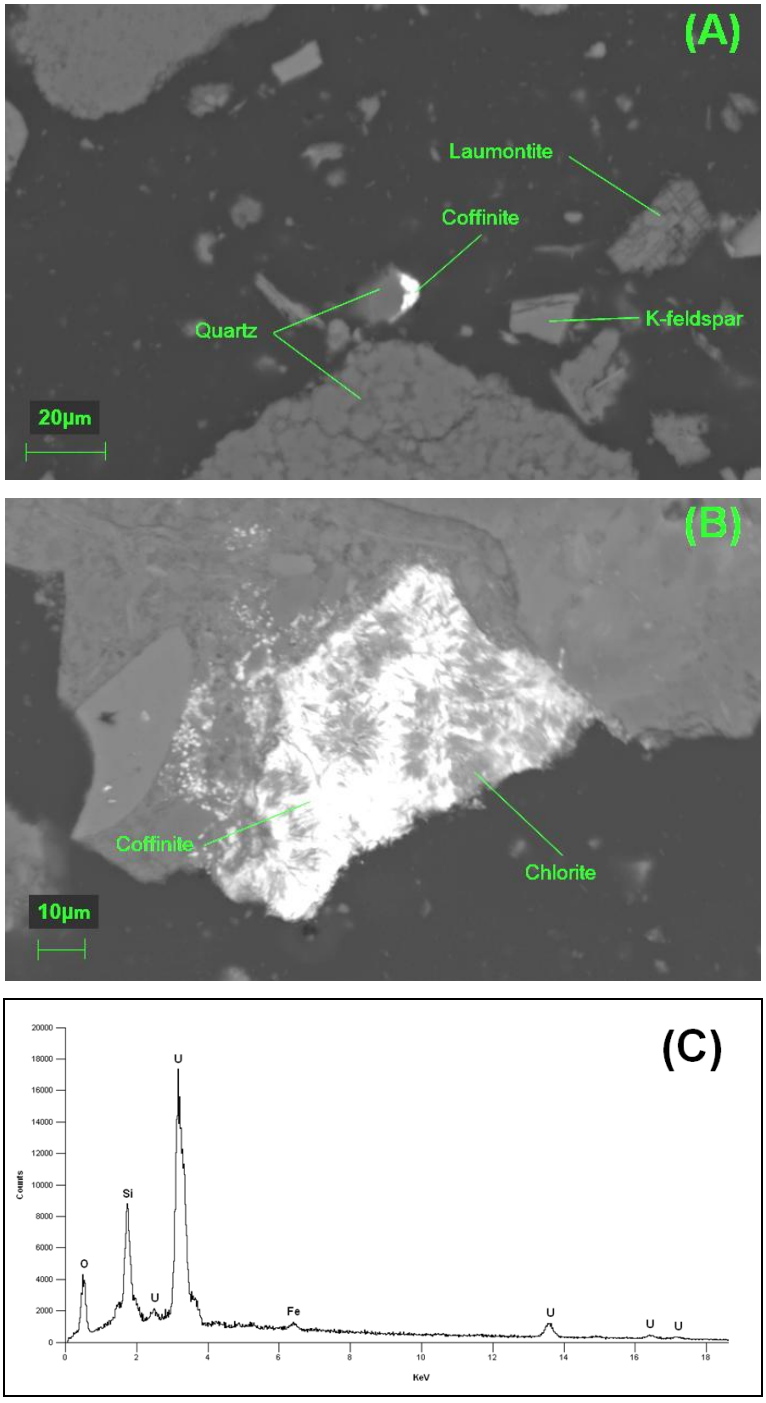

Figure 37: BSE micrographs and an EDX spectrum collected from Mooi showing coffinite associate with quartz (A) and finely intergrown with chlorite (B) as well as an EDX spectrum collected from the coffinite (C). The small Fe peak in the spectrum is from the surrounding chlorite.

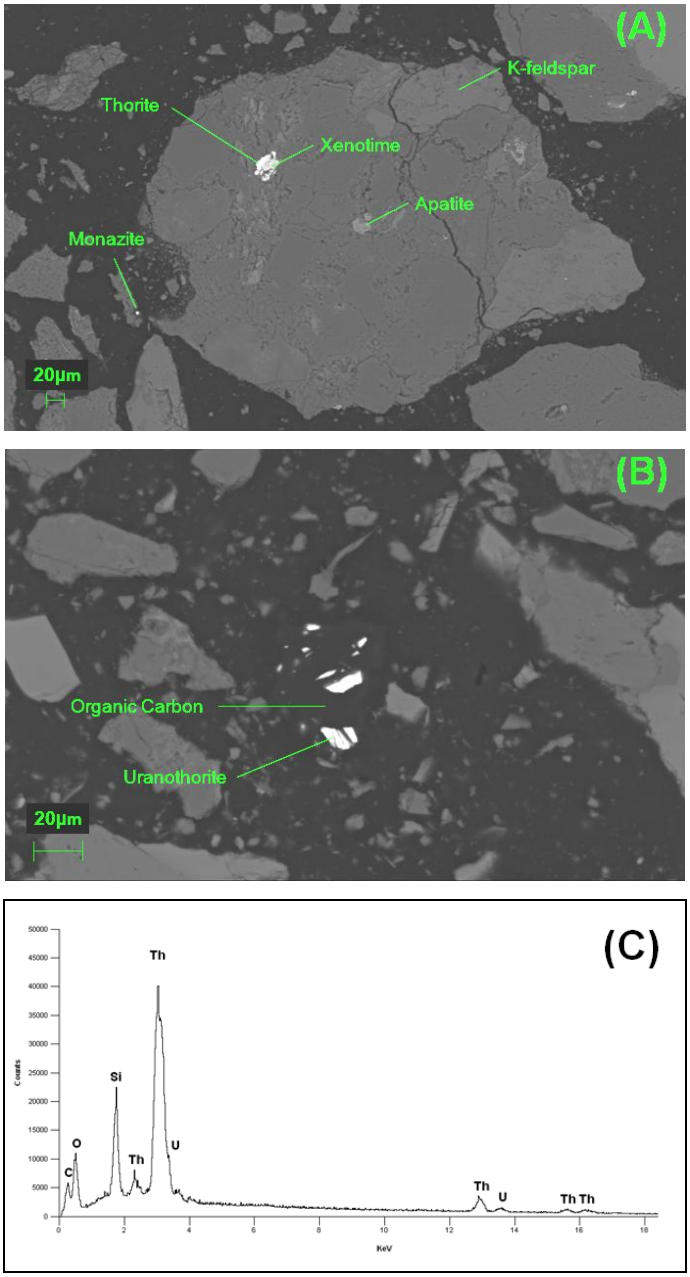

Figure 38: BSE micrographs and an EDX spectrum collected from Mooi showing thorite occurring with xenotime (A) and organic C (B), as well as an EDX spectrum showing that a minor amount of U is present.

The U in RAO occurs in uraninite (Figure 39), coffinite and as fine intergrowths of these minerals with uraniferous leucoxene (Figure 40). In addition to an association with leucoxene, U minerals also occur along grain boundaries of detrital silicates and within fractures, as well as in close association with organic C (Figure 41).

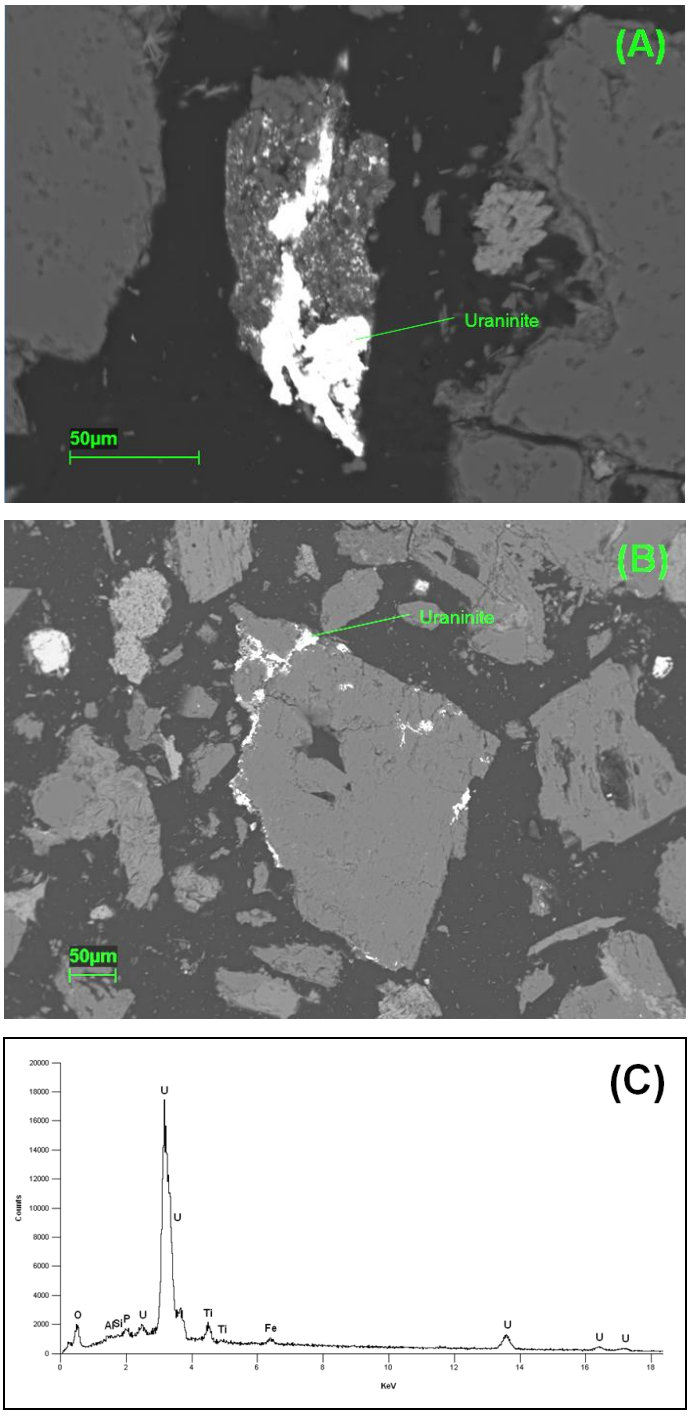

Figure 39: SEM BSE micrographs showing the mode of occurrence of uraninite (A and B) in RAO. The composition of the grain in (A) is shown in the EDX spectrum in (C).

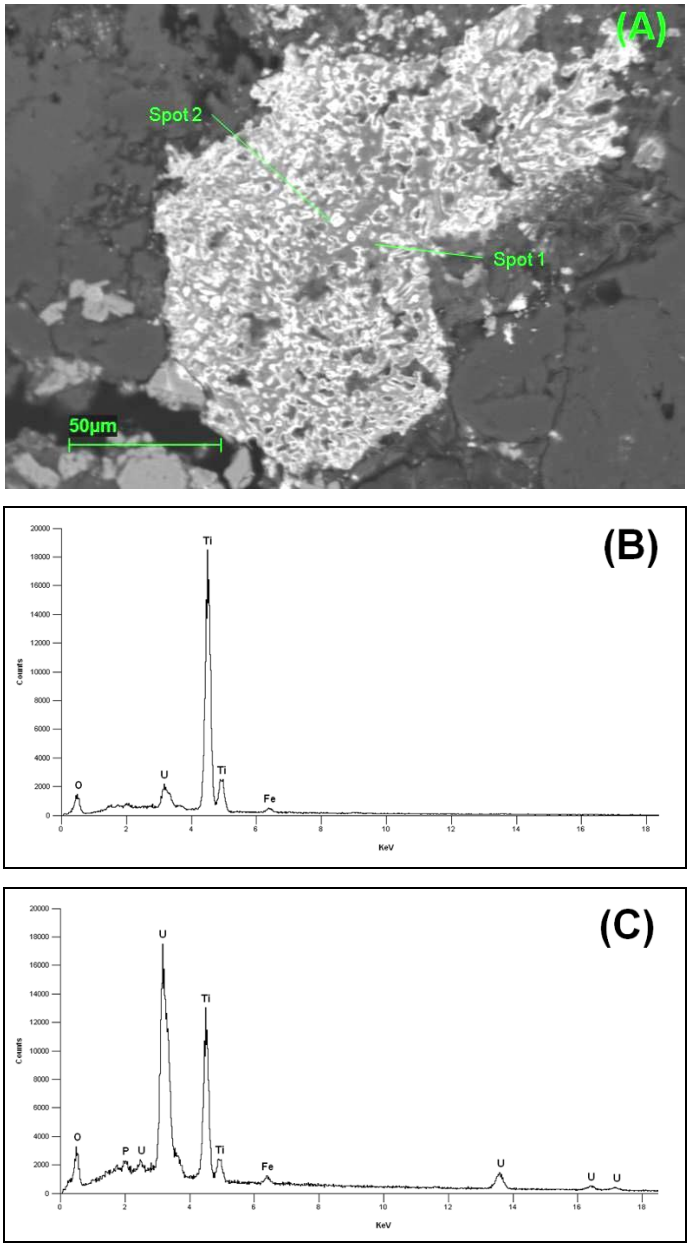

Figure 40: Intergrowths between uraninite and uraniferous leucoxene in RAO (A) and EDX spectra showing the variation in the relative abundances of U and Ti within this intergrowth. (B) and (C) indicate the compositions of Spots 1 and 2 respectively.

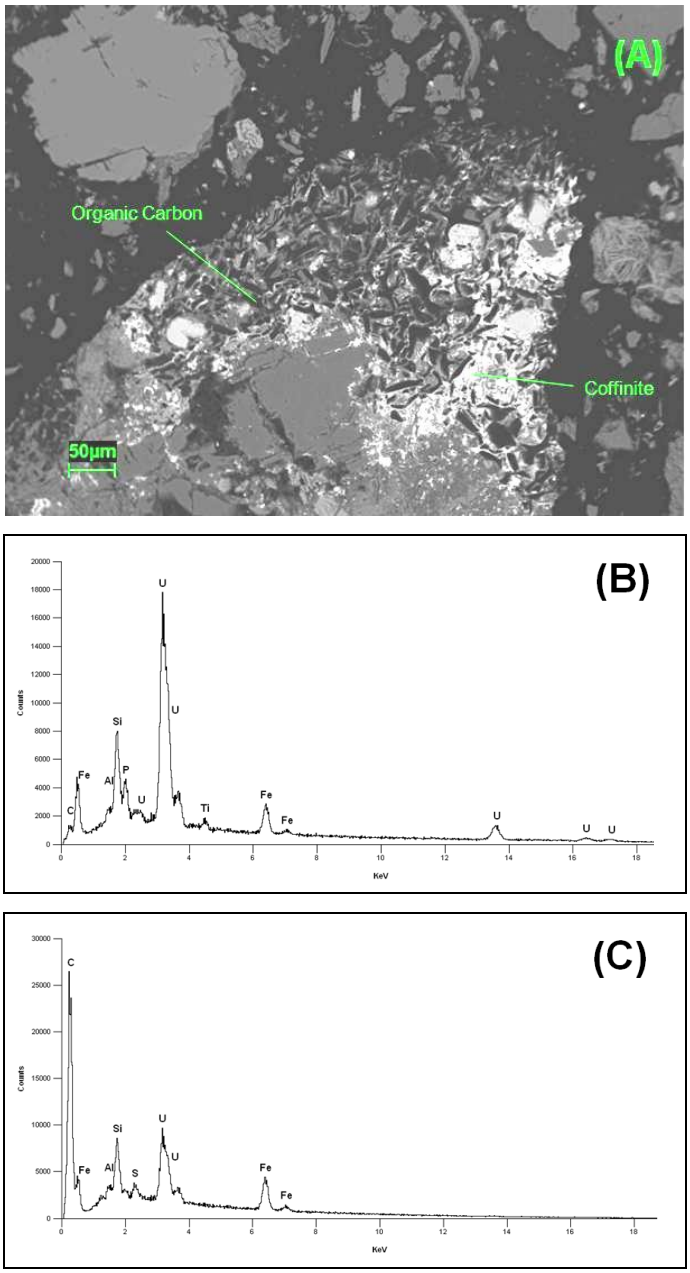

Figure 41: Coffinite associated with organic C in RAO (A) and EDX spectra collected from the coffinite (B) and organic C (C).

Uraninite and coffinite host the U in OAO. These grains tend to be coarser and more liberated than those in RAO. For this reason the original mode of occurrence of uraninite and coffinite (prior to comminution) was not as apparent in this sample as in RAO. However, grains of uraninite were observed in association with smectite (Figure 42) and filling cavities (Figure 43). Coarse liberated coffinite grains were also observed (Figure 44).

The EDX spectrum in Figure 42 shows that some smectite grains contain minor amounts of K. However, the estimated average smectite composition is considered to be $(Ca_{0.22}Mg_{2.18})(Mg_{0.7}Fe_{2.3}Al)(Al_{1.8}Si_{6.2})(OH)_4$.

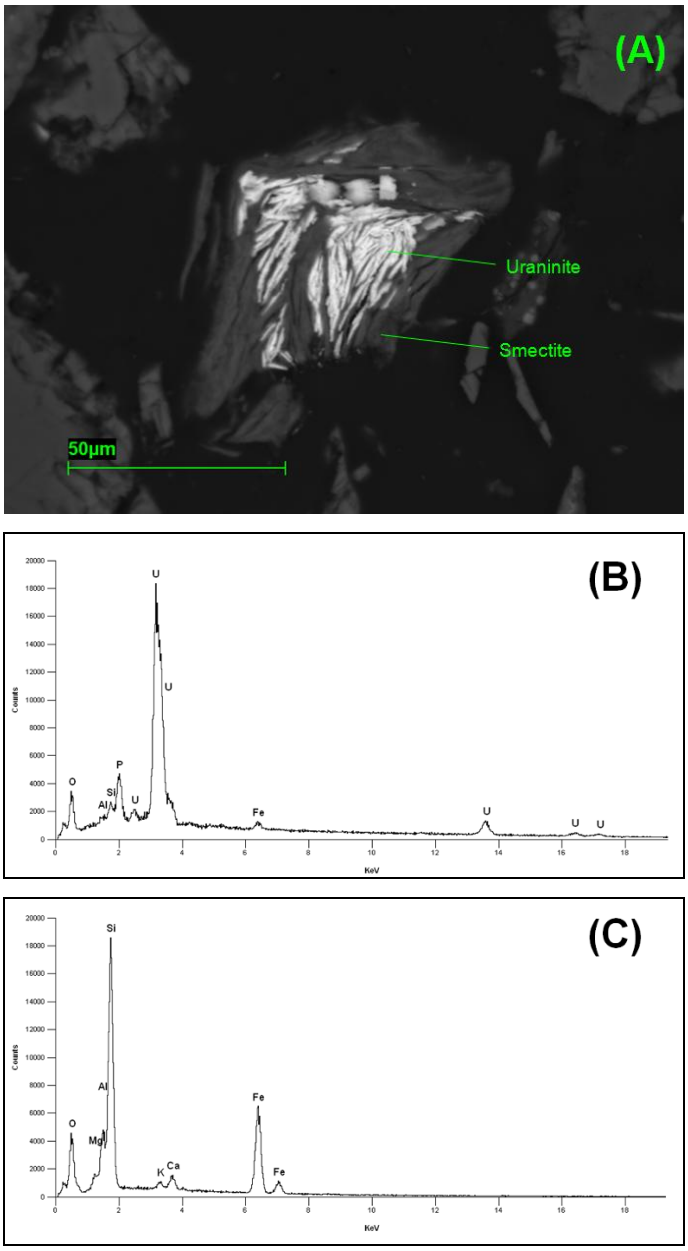

Figure 42: Uraninite occurring with smectite in OAO (A) and EDX spectra from the uraninite (B) and smectite (C). Xenotime was detected elsewhere in the sample and it appears that the small P peak in (B) may be due to the presence of fine grains of xenotime associated with the uraninite.

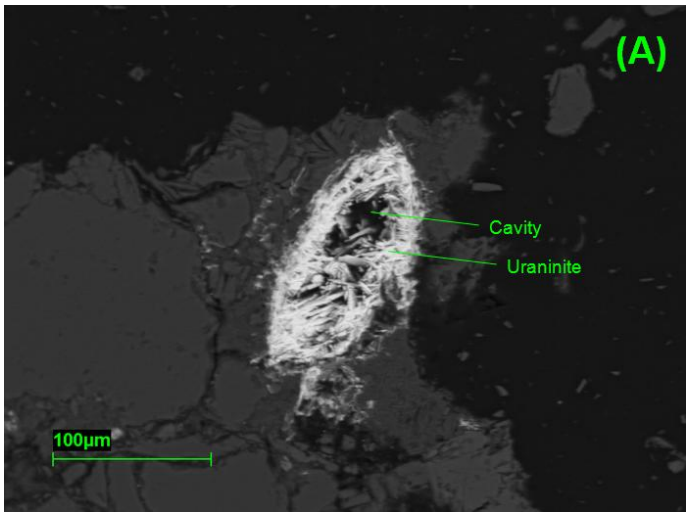

Figure 43: Uraninite partially filling a cavity in OAO. This effect may also be due to plucking of the uraninite, however, the absence of topography suggests that the cavity was a part of the original rock and is resin-filled rather than the result of plucking.

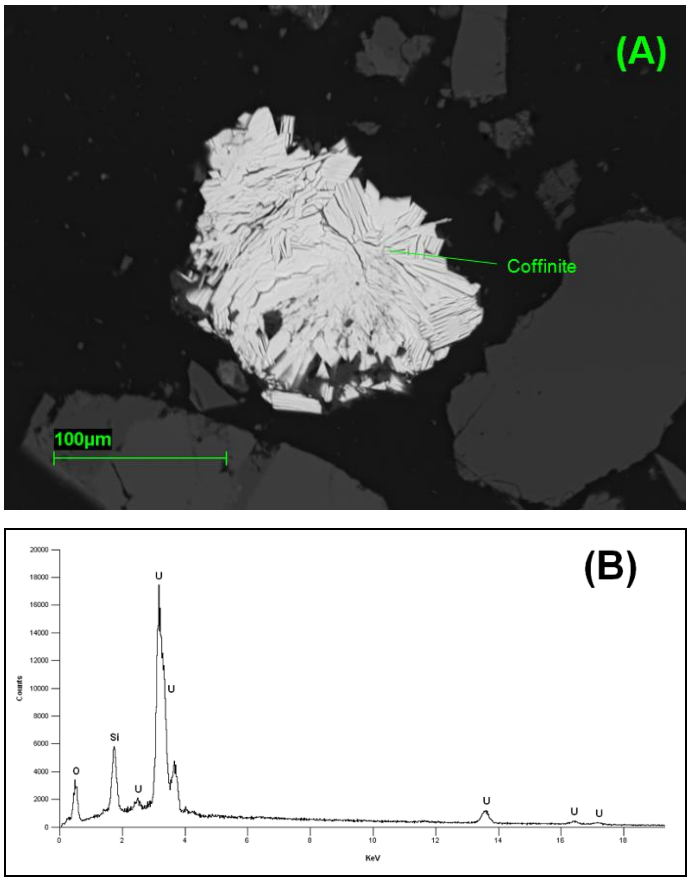

Figure 44: Coarse liberated coffinite in OAO (A) and an EDX spectrum collected from the coffinite (B).

In MSO the U is hosted by meta-uranocircite (Figure 45) and meta-autunite (Figure 46). These minerals have very similar compositions, differing mainly in that meta-uranocircite contains Ba, with a chemical formula of $Ba(UO_2)_2(PO_4)_2.6H_2O$ (Vochten *et al.*, 1992), while meta-autunite contains Ca, with a chemical formula of $Ca(UO_2)_2(PO_4)_2.2.5H_2O$ (Elevatorski, 1978). Both U phases occur as coarse, liberated grains, typically with well developed cleavage.

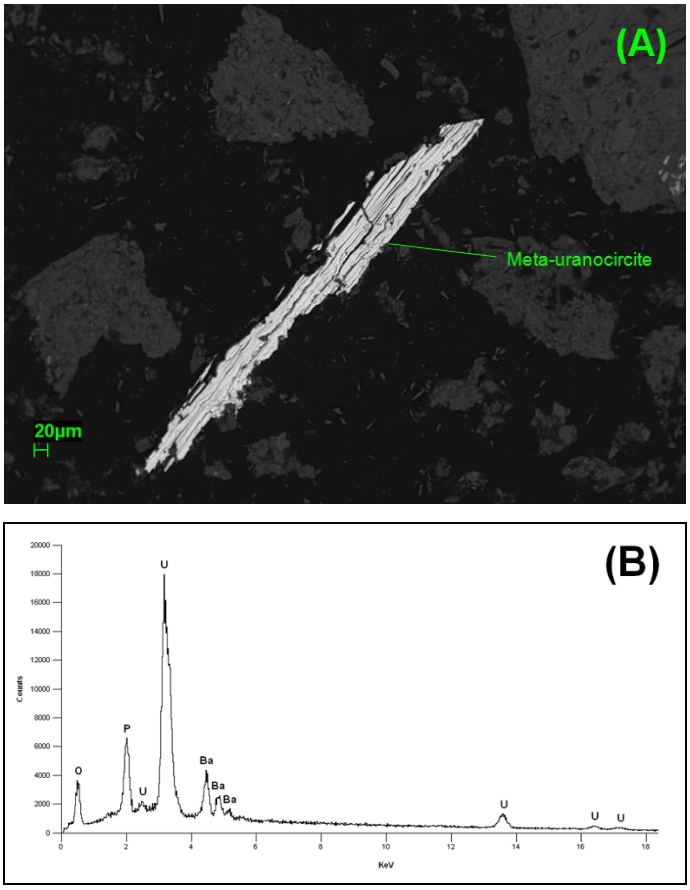

Figure 45: A grain of meta-uranocircite with well developed cleavage in MSO (A) and an EDX spectrum collected from this grain (B).

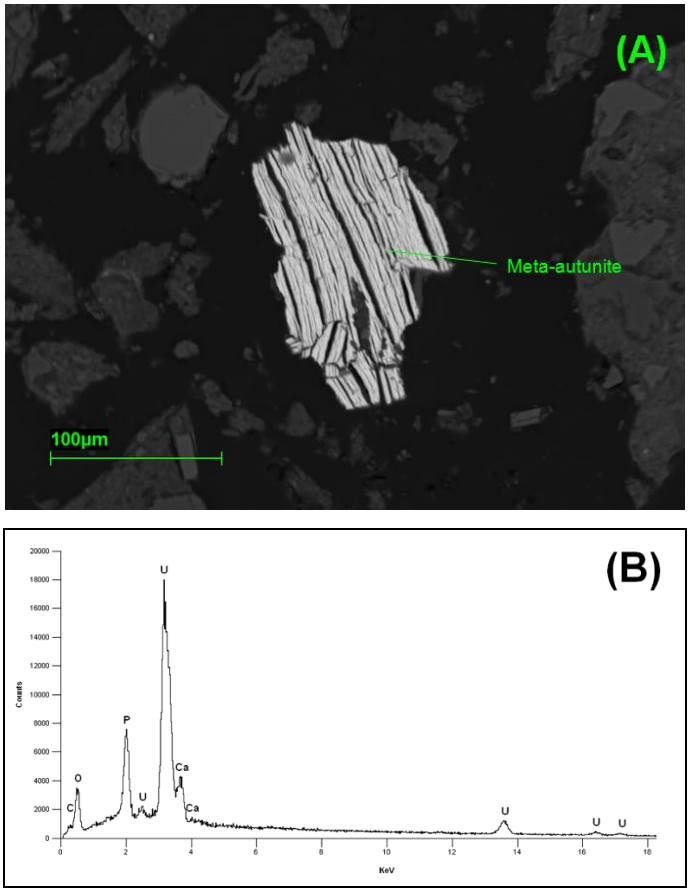

Figure 46: A grain of meta-autunite with well developed cleavage in MSO (A) and an EDX spectrum collected from this grain (B).

QEMSCAN Analyses

The QEMSCAN analyses were used to characterise both gangue (by BMA) and ore minerals (by TMS) present in the four samples. The results of the gangue characterisation were used to validate the XRD gangue mineral identification (and quantification) and to obtain textural data. The ore mineral characterisation was used to extend the qualitative data produced by manual scanning electron microscopy.

Validation of XRD Data by QEMSCAN BMA

The results of the QEMSCAN analyses confirmed the mineral identification and quantification by XRD, with only two exceptions. While the XRD did not detect muscovite in RAO and OAO, the QEMCAN data show that this phase is present in these samples in concentrations of 0.53 and 0.91% respectively. The other exception is that the samples contain minor amounts of Fe-Ti oxide/hydroxide which were not detected by XRD. The concentrations of these phases vary from 0.56% in MSO to 4.25% in RAO.

Stereologically Corrected Average Grain Size Data

The stereologically corrected average grain size data are given in Table 34. In each sample quartz is the coarsest phase, followed by plagioclase and then K-feldspar in the Kayelekera samples. In the Mooi sample calcite is the second coarsest phase (at both grinds).

Table 34: Stereologically Corrected Average Grain Size Data

Sample	**Mooi -212**	**Mooi -75**	**RAO**	**OAO**	**MSO**
Units	**µm**	**µm**	**µm**	**µm**	**µm**
Quartz	22.09	15.16	56.32	45.63	12.09
Plagioclase	15.74	13.40	16.87	25.81	5.78
K-feldspar	13.35	12.74	8.03	10.23	4.79
Laumontite	13.87	10.93	-	-	-
Muscovite	7.66	7.40	5.84	5.49	-
Chlorite	6.58	5.63	5.62	-	-
Smectite	-	-	6.74	5.86	5.11
Illite	-	-	-	-	8.19
Calcite	18.73	13.56	-	-	-
Fe-Oxide/Hydroxide	4.08	4.13	4.96	4.75	7.46
Pyrite	-	-	15.01	-	-

A comparison of the Mooi grain sizes, at the two grinds, shows that although the one sample is significantly finer than the other (80% passing 212 µm versus 80%

passing 75 µm), there was only a modest reduction in grain size. Surprisingly the Fe oxide/hydroxide is coarser grained at the finer grind.

Gangue Exposure and Association Characteristics

Gangue mineral associations were determined from the BMA data (Table 35 to Table 39). These associations were calculated from the transitions from one phase to another along the BMA line scans. The higher the association percentage, the more two phases occur in direct contact with each other.

Because the dissolution rates of minerals are typically normalised to the surface area of the mineral (Lüttge and Arvidson, 2008), it was necessary to calculate the surface area of each of the gangue phases. These were calculated from the average size of each mineral (Table 34). However, only the portion of the surface of the grain which is in contact with the leach solution will be available to react. The main reason for producing these results (Table 35 to Table 39) was to determine what proportion of the surface of each mineral occurs in contact with the mounting resin (background). This is the proportion that would be in direct contact with the leach liquor and therefore able to react. The proportion of the surface of each mineral that is in contact with other minerals would (at least in part) be protected from the leach liquor.

A comparison of the background association data for the Mooi sample, at the two different grinds, shows that there is a significant increase in the exposure (background association) of gangue phases at the finer grind.

Table 35: Mooi -212 gangue mineral associations showing the average proportion of the surface of each mineral that is in contact with each other phase and the mounting resin (background)

Mineral	Quartz	K-Feldspar	Plagioclase	Laumontite	Muscovite	Chlorite	Fe-oxide/hydroxide	Calcite
Units	**%**	**%**	**%**	**%**	**%**	**%**	**%**	**%**
Background*	58.57	31.79	41.55	56.83	21.08	53.00	71.33	74.52
Pyrite	0.02	0.00	0.01	0.00	0.00	0.00	0.00	0.00
Other sulphides	0.02	0.00	0.00	0.00	0.03	0.14	0.34	0.30
Quartz	0.00	10.61	14.57	10.21	5.63	7.33	7.17	1.41
K-Feldspar	9.35	0.00	14.57	1.47	41.13	2.39	2.05	1.29
Plagioclase	19.43	24.16	0.00	24.05	22.98	18.23	10.24	9.87
Laumontite	3.91	0.84	8.10	0.00	1.27	2.45	0.68	2.48
Muscovite	2.99	29.91	10.78	1.84	0.00	7.67	2.39	0.00
Chlorite	4.44	1.71	6.63	3.08	7.57	0.00	5.46	9.58
Fe-oxide/hydroxide	0.46	0.09	0.26	0.18	0.18	1.07	0.00	0.04
Zircon	0.08	0.00	0.02	0.00	0.00	0.03	0.00	0.00
Monazite	0.02	0.00	0.01	0.00	0.03	0.06	0.00	0.18
Apatite	0.03	0.00	0.01	0.00	0.00	0.20	0.00	0.15
Calcite	0.66	0.66	3.34	2.28	0.00	6.72	0.00	0.00
Other	0.05	0.23	0.14	0.07	0.10	0.69	0.34	0.18
Total	100.00	100.00	100.00	100.00	100.00	100.00	100.00	100.00

*The percentage of the surface of the mineral which is associated with background represents the proportion that would be in contact with the leach solution.

Table 36: Mooi -75 gangue mineral associations showing the average proportion of the surface of each mineral that is in contact with each other phase and the mounting resin (background)

Minerals	Quartz	K-Feldspar	Plagioclase	Laumontite	Muscovite	Chlorite	Fe-oxide/hydroxide	Calcite
Units	**%**	**%**	**%**	**%**	**%**	**%**	**%**	**%**
Background*	76.68	49.85	61.03	68.83	36.28	66.28	81.43	81.51
Pyrite	0.01	0.00	0.01	0.00	0.00	0.00	0.00	0.00
Other sulphides	0.00	0.00	0.00	0.00	0.00	0.06	0.48	0.11
Quartz	0.00	8.15	10.77	6.43	4.14	5.74	4.52	0.72
K-Feldspar	4.98	0.00	9.27	1.46	30.99	1.81	1.19	1.15
Plagioclase	11.39	19.63	0.00	18.12	19.44	11.44	5.48	7.02
Laumontite	2.00	0.51	5.78	0.00	1.77	1.39	0.24	1.50
Muscovite	1.61	19.80	5.63	0.88	0.00	6.03	1.19	0.07
Chlorite	2.55	1.31	4.38	2.73	6.59	0.00	5.24	7.70
Zircon	0.05	0.00	0.05	0.00	0.00	0.00	0.00	0.00
Fe-oxide/hydroxide	0.41	0.15	0.55	0.08	0.63	1.10	0.00	0.04
Monazite	0.00	0.02	0.00	0.00	0.00	0.03	0.24	0.11
Apatite	0.00	0.00	0.04	0.04	0.00	0.16	0.00	0.04
Calcite	0.29	0.39	2.33	1.39	0.12	5.35	0.00	0.00
Other	0.03	0.19	0.16	0.04	0.04	0.61	0.00	0.04
Total	100.00	100.00	100.00	100.00	100.00	100.00	100.00	100.00

*The percentage of the surface of the mineral which is associated with background represents the proportion that would be in contact with the leach solution.

Table 37: RAO gangue mineral associations showing the average proportion of the surface of each mineral that is in contact with each other phase and the mounting resin (background)

Minerals	Quartz	K-Feldspar	Plagioclase	Muscovite	Chlorite	Fe-oxide/hydroxide	Smectite	Pyrite
Units	**%**	**%**	**%**	**%**	**%**	**%**	**%**	**%**
Background*	77.04	29.19	67.97	9.97	36.81	48.77	35.70	46.15
Pyrite	0.28	0.45	0.50	0.00	0.17	0.32	0.29	0.00
Other sulphides	0.00	0.00	0.02	0.00	0.02	0.16	0.04	0.00
Quartz	0.00	0.30	2.21	0.56	1.37	3.42	0.92	0.77
K-Feldspar	0.96	0.00	9.29	77.23	0.75	1.89	2.54	8.85
Plagioclase	11.70	21.72	0.00	8.44	9.56	9.72	19.72	20.38
Muscovite	0.56	40.80	1.81	0.00	0.30	0.26	0.90	0.00
Chlorite	3.71	1.18	4.01	0.67	0.00	13.14	34.48	4.23
Smectite	2.84	3.92	11.49	2.08	45.24	11.14	0.00	10.00
Zircon	0.04	0.04	0.11	0.00	0.07	0.00	0.03	0.00
Fe-oxide/hydroxide	2.64	0.95	1.68	0.48	4.67	0.00	3.34	2.69
Monazite	0.00	0.02	0.19	0.00	0.28	10.25	0.31	0.00
Apatite	0.00	0.08	0.22	0.00	0.43	0.11	0.14	1.15
Org Carbon	0.00	0.06	0.02	0.00	0.00	0.16	0.00	3.08
Other	0.24	1.30	0.48	0.56	0.33	0.68	1.57	2.69
Total	100.00	100.00	100.00	100.00	100.00	100.00	100.00	100.00

*The percentage of the surface of the mineral which is associated with background represents the proportion that would be in contact with the leach solution.

Table 38: OAO gangue mineral associations showing the average proportion of the surface of each mineral that is in contact with each other phase and the mounting resin (background)

Minerals	Quartz	K-Feldspar	Plagioclase	Muscovite	Chlorite	Fe-oxide/hydroxide	Smectite	Jarosite
Units	**%**	**%**	**%**	**%**	**%**	**%**	**%**	**%**
Background*	91.32	25.31	70.34	27.32	27.61	67.65	52.60	79.31
Pyrite	0.00	0.15	0.06	0.14	0.00	1.12	0.00	6.90
Other sulphides	0.00	0.00	0.00	0.00	0.00	0.00	0.09	0.00
Quartz	0.00	1.51	6.49	1.18	3.70	6.72	0.44	0.00
K-Feldspar	0.41	0.00	15.38	58.78	0.67	1.12	3.88	0.00
Plagioclase	6.25	39.16	0.00	11.41	9.09	12.18	20.92	3.45
Muscovite	0.47	31.46	2.50	0.00	0.34	0.42	1.41	3.45
Smectite	0.12	1.78	3.43	0.76	52.53	9.52	0.00	0.00
Zircon	0.00	0.00	0.00	0.00	0.00	0.00	0.00	0.00
Fe-oxide/hydroxide	1.14	0.43	1.17	0.14	4.71	0.00	8.21	6.90
Monazite	0.00	0.00	0.00	0.00	0.00	0.00	0.00	0.00
Apatite	0.00	0.00	0.01	0.00	0.00	0.00	0.00	0.00
Jarosite	0.02	0.04	0.06	0.07	0.00	0.00	0.09	0.00
Other	0.27	0.15	0.57	0.21	1.35	1.26	12.36	0.00
Total	100.00	100.00	100.00	100.00	100.00	100.00	100.00	100.00

*The percentage of the surface of the mineral which is associated with background represents the proportion that would be in contact with the leach solution.

Table 39: MSO gangue mineral associations showing the average proportion of the surface of each mineral that is in contact with each other phase and the mounting resin (background)

Minerals	Quartz	K-Feldspar	Plagioclase	Fe-oxide/hydroxide	Smectite	Illite
Units	**%**	**%**	**%**	**%**	**%**	**%**
Background*	26.82	42.51	8.20	46.15	46.62	36.77
Pyrite	0.00	0.01	0.00	0.00	0.00	0.00
Other sulphides	0.00	0.00	0.00	0.96	0.01	0.00
Quartz	0.00	0.80	1.78	3.85	3.34	2.73
K-Feldspar	3.01	0.00	5.08	0.96	3.70	13.08
Plagioclase	7.04	6.29	0.00	0.00	12.68	24.85
Illite	31.57	42.34	58.81	5.77	33.18	0.00
Smectite	31.21	7.85	26.06	38.46	0.00	22.44
Zircon	0.00	0.01	0.00	0.00	0.01	0.00
Fe-oxide/hydroxide	0.32	0.02	0.01	0.00	0.19	0.01
Monazite	0.00	0.01	0.02	1.92	0.02	0.00
Apatite	0.00	0.00	0.01	0.00	0.00	0.00
Other	0.04	0.16	0.03	1.92	0.25	0.11
Total	100.00	100.00	100.00	100.00	100.00	100.00

*The percentage of the surface of the mineral which is associated with background represents the proportion that would be in contact with the leach solution.

Specific Surface Area

Using the stereologically corrected grain sizes (Table 34) and the mineral association data (Table 35 to Table 39) the specific surface areas of the various gangue mineral phases (except illite and smectite) were estimated (Table 40). These results were used to normalise the dissolution data obtained in the leach tests (Chapter 6) as suggested by Lüttge and Arvidson (2008).

Table 40: Specific surface areas estimated from QEMSCAN BMA data

Sample	Mooi -212	Mooi -75	RAO	OAO	MSO
Units	m^2/g	m^2/g	m^2/g	m^2/g	m^2/g
Plagioclase	0.67	1.18	1.02	0.65	0.39
K-feldspar	0.63	1.04	0.99	0.67	2.48
Laumontite	0.11	0.17			
Muscovite	1.96	3.43	1.04	2.91	-
Chlorite	2.18	2.89	1.61	-	-
Calcite	0.22	0.33	-	-	-
Pyrite	-	-	0.78	-	-

Uranium Deportment by QEMSCAN TMS

The QEMSCAN TMS mapped 134 U-containing particles from Mooi -212, 113 from Mooi -75, 3063 from RAO, 3802 from OAO and 3355 from MSO. The marked difference in the total number of particles mapped for Mooi when compared to the Kayelekera samples is due to the differences in U grade. The low grade of Mooi limited the number of U-containing particles that could practically be analysed.

The U deportment was determined from the TMS particle maps (Table 41 and Figure 47). The deportments in the Mooi and OAO samples are similar. In these samples the majority of the U is present in coffinite with lesser amounts occurring

in uraninite. RAO differs from these samples in that uraniferous leucoxene, rather than uraninite is the second most important U mineral.

The U deportment of MSO is completely different from any of the arkose samples, with subequal amounts of U occurring in meta-uranocircite and meta-autunite.

The results were fairly similar for Mooi at the two different grinds. This suggests that although a low number of particles were mapped, these were sufficient to produce reasonably consistent results. The average of these two data sets would produce the most reliable estimate of the true Mooi deportment.

Table 41: Uranium deportment, expressing the percentage of the uranium contained in each sample, hosted by each uranium mineral

Sample	**Mooi -212**	**Mooi -75**	**Mooi (Ave)**	**RAO**	**OAO**	**MSO**
Units	**%**	**%**	**%**	**%**	**%**	**%**
Uraninite	23.92	19.30	21.61	4.87	24.79	-
Coffinite	74.60	77.95	76.28	65.18	74.03	-
Uraniferous Leucoxene	0.44	1.16	0.80	29.95	1.17	-
Thorite	1.04	1.59	1.31	-	-	-
Meta-uranocircite	-	-	-	-	-	54.65
Meta-autunite	-	-	-	-	-	45.35
Total	100.00	100.00	100.00	100.00	100.00	100.00

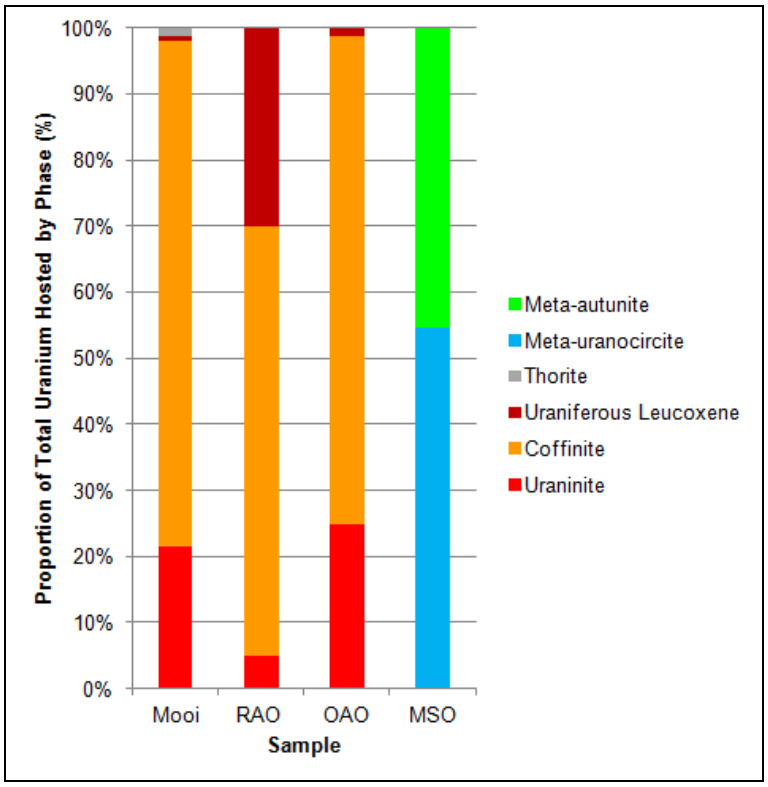

Figure 47: Uranium deportment of the four samples.

Uncorrected Uranium Mineral Grain Size Distributions

The TMS data were also used to determine the U mineral grain size distributions in each sample (Table 42 and Figure 48). The size distributions of OAO and RAO were remarkably similar, while MSO was significantly coarser than the other samples.

Mooi was the finest of the samples at both grinds. However, the comparison between the two grinds produced surprising results. At the finer grind, the U minerals appear coarser. This is not the result of a sample swap, since the gangue mineral sizes were determined from the sample blocks, and the gangue minerals were typically finer at the finer grind.

Table 42: Discrete (Disc.) and cumulative (Cum.) uranium mineral grain size distributions, where the discrete data shows the percentage of the uranium mineral in each class and the cumulative data shows the percentage that is within a particular class or smaller

Sample	Mooi -212		Mooi -75		RAO		OAO		MSO	
Size Class (µm)	Disc. %	Cum. %	Disc. %	Cum. %	Disc. %	Cum. %	Disc. %	Cum. %	Disc. %	Cum. %
< 5	17.77	17.77	9.23	9.23	19.83	19.83	13.31	13.31	1.18	1.18
5-10	28.00	45.76	27.17	36.40	20.43	40.26	27.41	40.72	6.05	7.23
10-15	21.56	67.32	24.05	60.45	16.00	56.26	15.92	56.64	6.80	14.03
15-20	19.60	86.92	5.94	66.39	10.49	66.75	10.61	67.26	6.43	20.46
20-25	13.08	100.00	10.82	77.20	7.90	74.65	8.10	75.35	5.65	26.11
25-30	0.00	100.00	6.71	83.91	5.70	80.35	3.58	78.93	5.41	31.52
30-35	0.00	100.00	0.00	83.91	4.30	84.65	5.31	84.25	5.45	36.97
35-40	0.00	100.00	16.09	100.00	2.73	87.38	2.23	86.47	5.53	42.50
40-45	0.00	100.00	0.00	100.00	0.42	87.80	0.00	86.47	4.28	46.78
45-50	0.00	100.00	0.00	100.00	1.51	89.31	1.75	88.23	3.24	50.02
50-55	0.00	100.00	0.00	100.00	1.87	91.18	1.23	89.46	4.95	54.96
55-60	0.00	100.00	0.00	100.00	0.00	91.18	1.66	91.11	3.39	58.35
60-65	0.00	100.00	0.00	100.00	1.76	92.93	3.29	94.41	4.07	62.41
65-70	0.00	100.00	0.00	100.00	0.96	93.89	0.00	94.41	4.51	66.92
70-75	0.00	100.00	0.00	100.00	1.20	95.09	0.00	94.41	2.59	69.51
75-80	0.00	100.00	0.00	100.00	0.00	95.09	0.00	94.41	2.58	72.09
80-85	0.00	100.00	0.00	100.00	1.60	96.69	2.48	96.89	1.27	73.35
85-90	0.00	100.00	0.00	100.00	3.31	100.00	0.00	96.89	3.73	77.08
90-95	0.00	100.00	0.00	100.00	0.00	100.00	3.11	100.00	2.50	79.59
95-100	0.00	100.00	0.00	100.00	0.00	100.00	0.00	100.00	2.27	81.86
100-150	0.00	100.00	0.00	100.00	0.00	100.00	0.00	100.00	14.73	96.58
150-200	0.00	100.00	0.00	100.00	0.00	100.00	0.00	100.00	3.42	100.00
Total	100.00	-	100.00	-	100.00	-	100.00	-	100.00	-

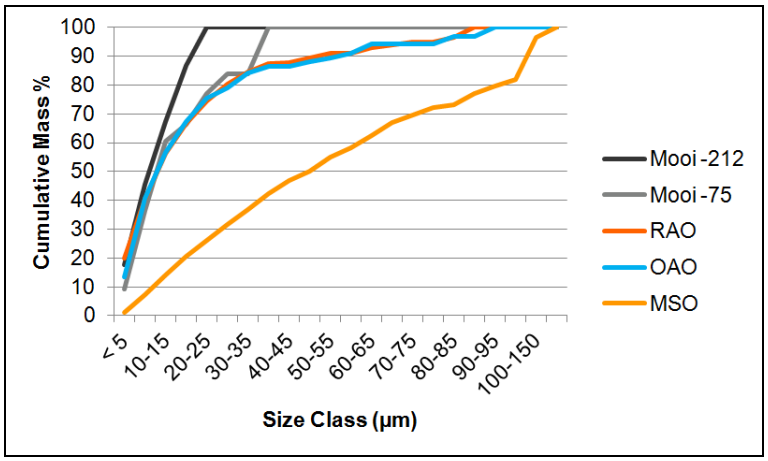

Figure 48: Cumulative uranium mineral grain size distributions showing the mass percent of uranium minerals that fall within the specified size range added to those of the finer classes. This makes it possible to determine what proportion of uranium minerals are finer than a particular size.

Uranium Mineral Exposure and Association Characteristics

The exposure and association characteristics of each sample were determined from the TMS particle maps. These results are given in Table 43 to Table 47. The value N in the tables is the number of U mineral grains in each class. This number may be significantly larger than the number of U-containing particles as a single particle can contain multiple grains. The exposed classes represent U mineral grains that are in contact with background. The percentages are the proportions of the grains perimeter that are in contact with background. These are grains that are exposed to the leach liquor and therefore available for dissolution. The rate of dissolution of a mineral is proportional to the surface area which is in contact with the leach liquor (see the section on modelling of mineral dissolution in Chapter 4 for more detail). Therefore a grain in the ≥80% liberated class would be expected to leach more rapidly than one that is less than 10% liberated.

The reactive mineral classes represent U mineral grains that occur within minerals that have a higher dissolution rate than quartz and the feldspars. These

grains may therefore become exposed as a result of acid dissolution of the surrounding gangue.

The low reactivity class represent U mineral grains that are locked in gangue minerals that have similar dissolution rates to quartz and the feldspars. These grains are either locked within a single mineral grain or on the boundary between two or more unreactive mineral grains.

Mooi exposure was not particularly high at 80% passing 212 μm and ~24% of U mineral grains are locked in low reactivity gangue. Figure 50 shows particle maps collected from the Mooi sample. The degree of U mineral exposure varies from completely locked in silicates in Figure 50 (A) to grains with very high degrees of exposure, associated with organic carbon Figure 50 (C).

There was a significant improvement in the exposure of the Mooi sample U minerals at 80% passing 75 μm, where only ~7% of U mineral grains occur in low reactivity gangue. Figure 51 also shows particle maps of U minerals at this finer grind size and shows a higher degree of exposure than those at the coarser grind (Figure 51).

The proposition of exposed grains in RAO was also low (~64%), however a significant amount of the locked grains occur within reactive gangue. Figure 52 shows U minerals from RAO. These grains are associated with silicates or organic carbon and at least part of the perimeter of these grains is either exposed, or associated with a reactive silicate.

The exposures of U phases in the OAO and MSO samples were both high, with ~92% of grains in OAO and ~94% in MSO showing some degree of exposure (Figure 53 and Figure 54). The meta-autunite and uranocircite grains have a well developed cleavage. This cleavage would cause grains of these minerals to have a higher reactive surface area than grains of another U mineral of a similar size.

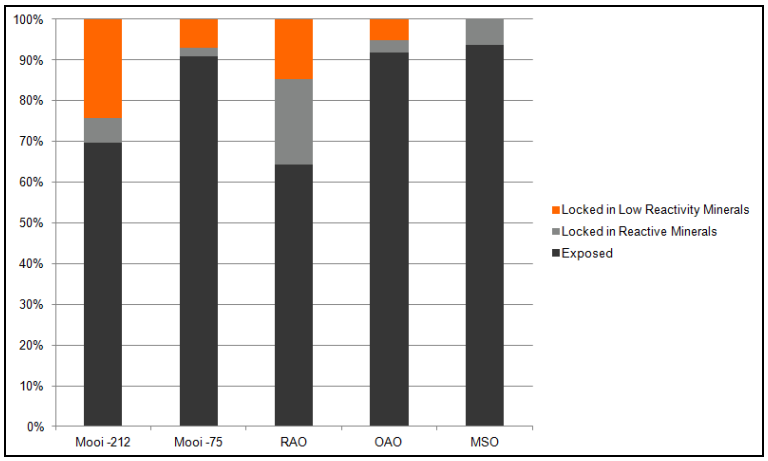

Figure 49: Uranium mineral exposure and association characteristics. Liberated grains are those that have some portion of their perimeter in contact with the mounting resin. These would be accessible to the leach liquor and would be expected to dissolve. Locked grains are those that are enclosed in gangue and would therefore not be accessible to the leach liquor; however those locked in reactive gangue may become exposed due to gangue dissolution.

Table 43: Mooi -212 uranium mineral exposure and association characteristics

Class	**N***	**Mass %****
Exposed (≥80%)	4	3.55
Exposed (10%-80%)	102	53.68
Exposed (<10%)	11	12.48
Total exposed+	**117**	**69.71**
Locked in calcite	1	0.32
Locked in laumontite	0	0.00
Locked in chlorite	3	0.33
Locked on polymineral boundary (including calcite)	10	0.97
Locked on polymineral boundary (including laumontite)	10	3.67
Locked on polymineral boundary (including chlorite)	14	0.66
Total locked in reactive minerals++	**38**	**5.94**
Locked on low reactivity polymineral boundary	128	11.84
Locked in other silicates	184	12.50
Total locked in low reactivity minerals	**312**	**24.34**
Total	**467**	**100.00**

*N represents the number of uranium mineral grains in each class.
**Refers to the mass percentage of the total uranium occurring in each class.
+These are grains that have some portion of their perimeter in contact with the mounting resin. These would be accessible to the leach liquor and would be expected to dissolve.
++These grains may become exposed to the leach liquor if the surrounding gangue minerals are dissolved during the leach.

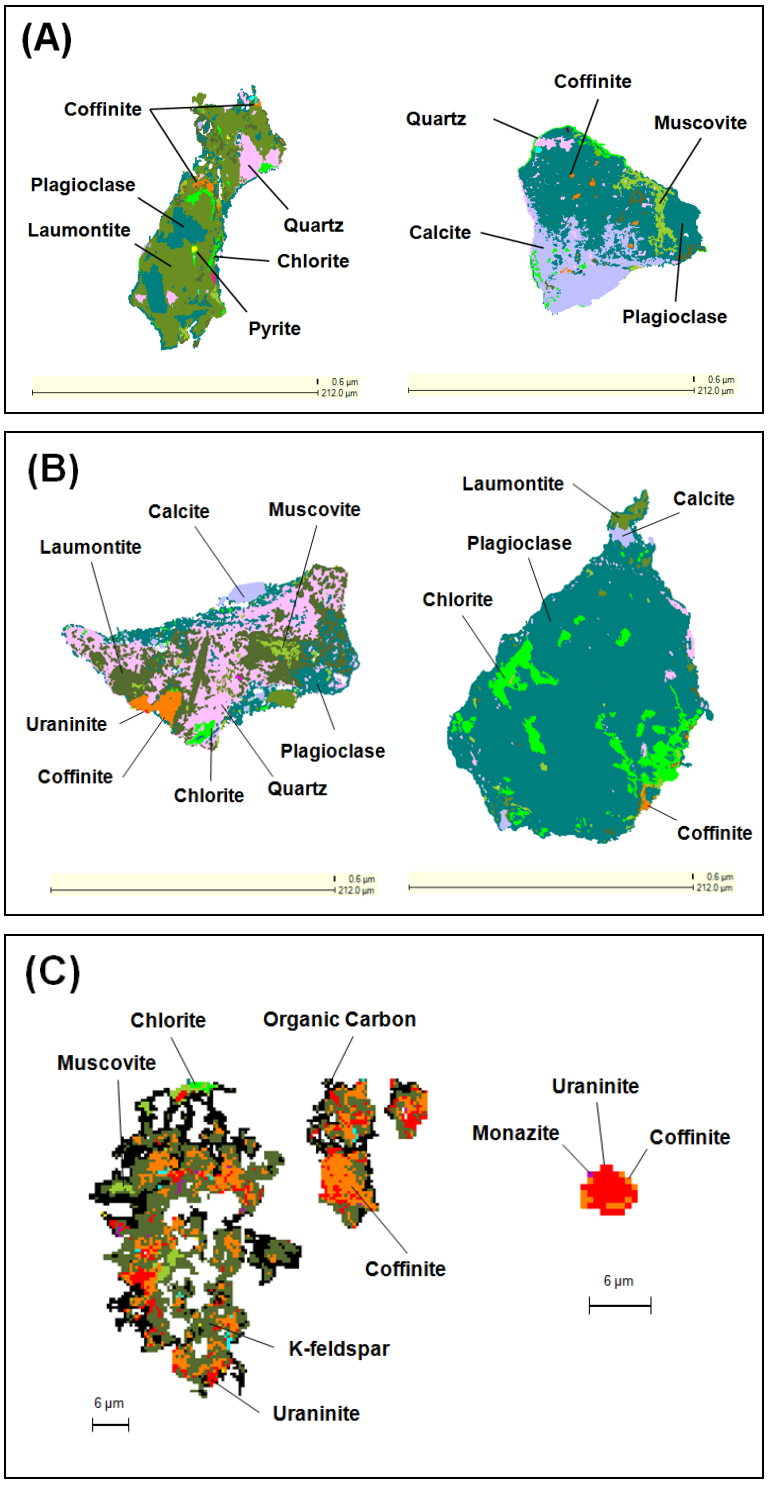

Figure 50: Uranium minerals from Mooi -212 with varying levels of exposure. (A) Most of the coffinite is locked within gangue. (B) The coffinite is exposed at the edge of the particle and (C) a much higher proportion of the perimeter of the coffinite and uraninite grains are in contact with background.

Table 44: Mooi -75 uranium mineral exposure and association characteristics

Class	N*	Mass %**
Exposed (≥80%)	6	11.72
Exposed (10%-80%)	60	64.94
Exposed (<10%)	11	14.20
Total exposed+	**77**	**90.86**
Locked in calcite	0	0.00
Locked in laumontite	0	0.00
Locked in chlorite	1	0.03
Locked on polymineral boundary (including calcite)	2	0.12
Locked on polymineral boundary (including laumontite)	9	0.95
Locked on polymineral boundary (including chlorite)	18	0.92
Total locked in reactive minerals++	**30**	**2.02**
Locked on low reactivity polymineral boundary	106	5.40
Locked in other silicates	40	1.72
Total locked in low reactivity minerals	**146**	**7.12**
Total	**253**	**100.00**

*N represents the number of uranium mineral grains in each class.
**Refers to the mass percentage of the total uranium occurring in each class.
+These are grains that have some portion of their perimeter in contact with the mounting resin. These would be accessible to the leach liquor and would be expected to dissolve.
++These grains may become exposed to the leach liquor if the surrounding gangue minerals are dissolved during the leach.

Table 45: RAO uranium mineral exposure and association characteristics

Class	N	Mass %
Exposed (≥80%)	83	0.11
Exposed (10%-80%)	5631	26.76
Exposed (<10%)	1466	37.51
Total exposed	**7180**	**64.38**
Locked in chlorite	247	0.06
Locked in smectite	523	0.14
Locked on polymineral boundary (including chlorite)	4034	12.47
Locked on polymineral boundary (including smectite)	5113	8.23
Total locked in reactive minerals	**9917**	**20.90**
Locked on low reactivity polymineral boundary	5627	5.42
Locked in other silicates	16024	9.29
Total locked in low reactivity minerals	**21651**	**14.71**
Total	**38748**	**100.00**

*N represents the number of uranium mineral grains in each class.
**Refers to the mass percentage of the total uranium occurring in each class.
+These are grains that have some portion of their perimeter in contact with the mounting resin. These would be accessible to the leach liquor and would be expected to dissolve.
++These grains may become exposed to the leach liquor if the surrounding gangue minerals are dissolved during the leach.

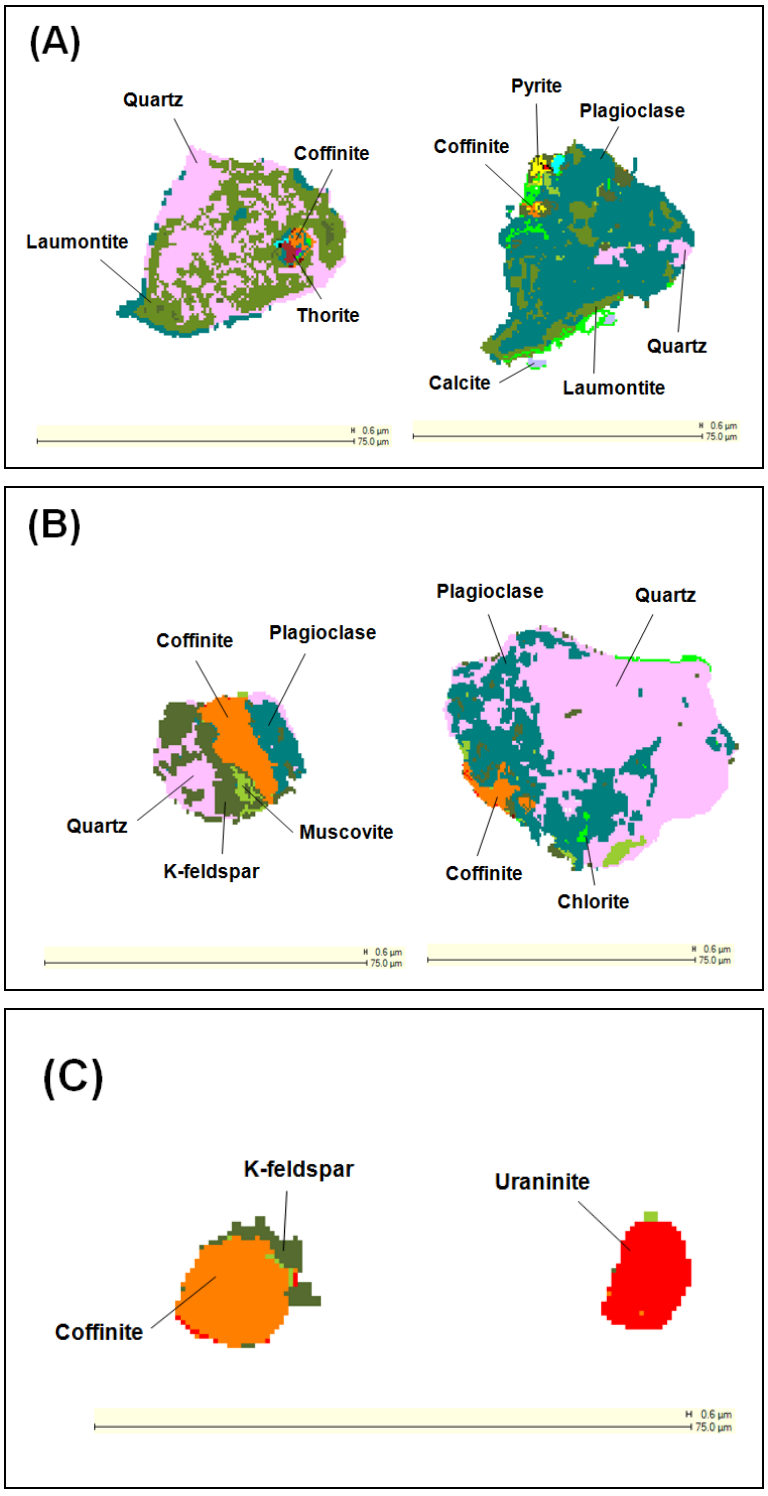

Figure 51: Uranium minerals from Mooi -75 with varying levels of exposure. (A) Most of the coffinite is locked within gangue. (B) The coffinite is exposed at the edge of the particle; (C) a much higher proportion of the perimeter of the coffinite and uraninite grains are in contact with background.

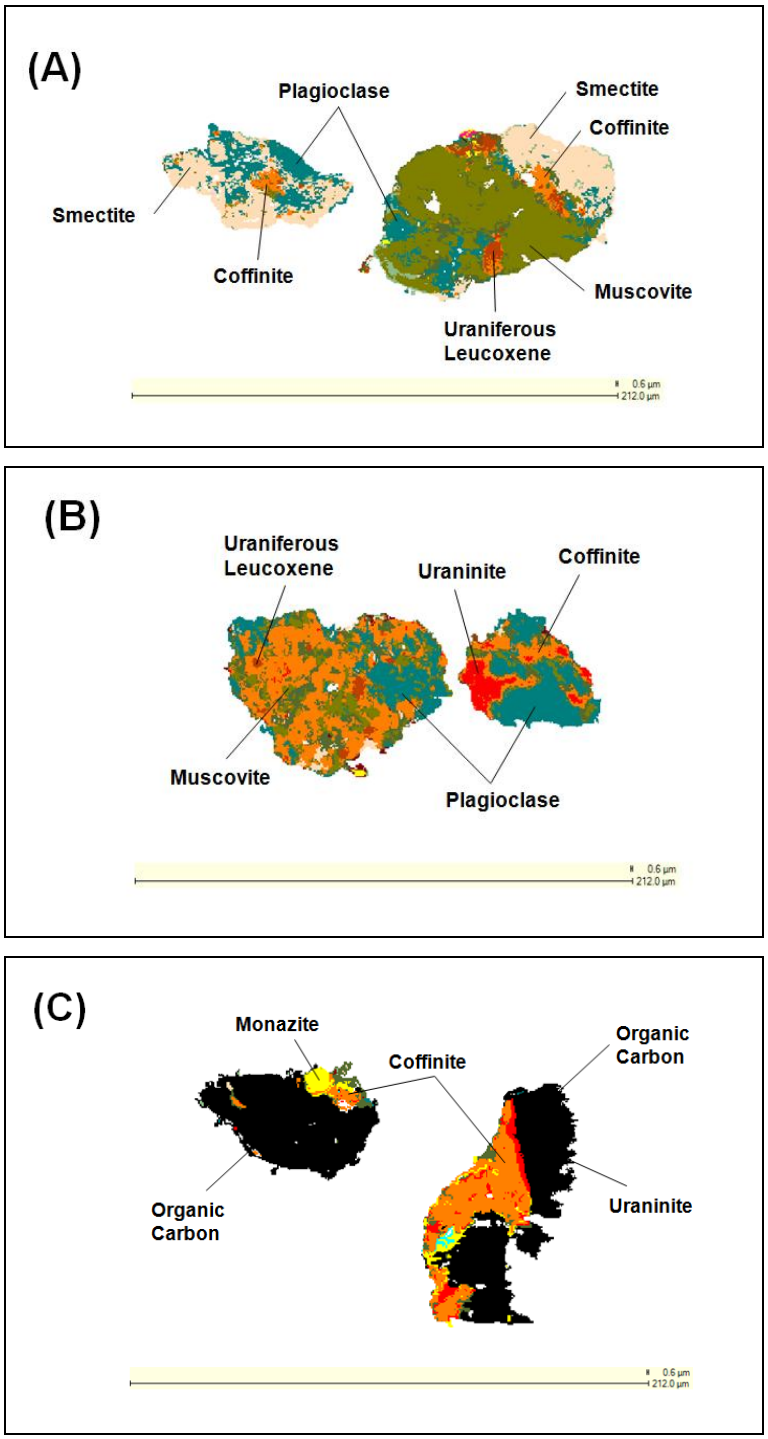

Figure 52: QEMSCAN particle maps from RAO. (A) Coffinite and uraniferous leucoxene locked in silicates. (B) Partially exposed uraninite and coffinite, with the coffinite as an alteration product of uraninite. (C) Coffinite and uraninite occurring with organic carbon (C).

Table 46: OAO uranium mineral exposure and association characteristics

Class	N*	Mass %**
Exposed (≥80%)	127	1.02
Exposed (10%-80%)	5151	80.99
Exposed (<10%)	423	9.78
Total exposed+	**5701**	**91.79**
Locked in chlorite	1	0.00
Locked in smectite	5	0.00
Locked on polymineral boundary (including chlorite)	19	0.06
Locked on polymineral boundary (including smectite)	433	3.05
Total locked in reactive minerals++	**458**	**3.11**
Locked on low reactivity polymineral boundary	819	1.81
Locked in other silicates	2053	3.29
Total locked in low reactivity minerals	**2872**	**5.10**
Total	**9031**	**100.00**

*N represents the number of uranium mineral grains in each class.
**Refers to the mass percentage of the total uranium occurring in each class.
+These are grains that have some portion of their perimeter in contact with the mounting resin. These would be accessible to the leach liquor and would be expected to dissolve.
++These grains may become exposed to the leach liquor if the surrounding gangue minerals are dissolved during the leach.

Table 47: MSO uranium mineral exposure and association characteristics

Class	N*	Mass %**
Exposed (≥80%)	58	0.01
Exposed (10%-80%)	6647	44.69
Exposed (<10%)	2692	48.93
Total exposed+	**9397**	**93.63**
Locked in smectite	22	0.00
Locked in illite	1810	0.15
Locked on polymineral boundary (including smectite)	887	2.03
Locked on polymineral boundary (including illite)	4138	4.14
Total locked in reactive minerals++	**6857**	**6.33**
Locked on low reactivity polymineral boundary	848	0.02
Locked in other silicates	421	0.03
Total locked in low reactivity minerals	**1269**	**0.04**
Total	**17523**	**100.00**

*N represents the number of uranium mineral grains in each class.
**Refers to the mass percentage of the total uranium occurring in each class.
+These are grains that have some portion of their perimeter in contact with the mounting resin. These would be accessible to the leach liquor and would be expected to dissolve.
++These grains may become exposed to the leach liquor if the surrounding gangue minerals are dissolved during the leach.

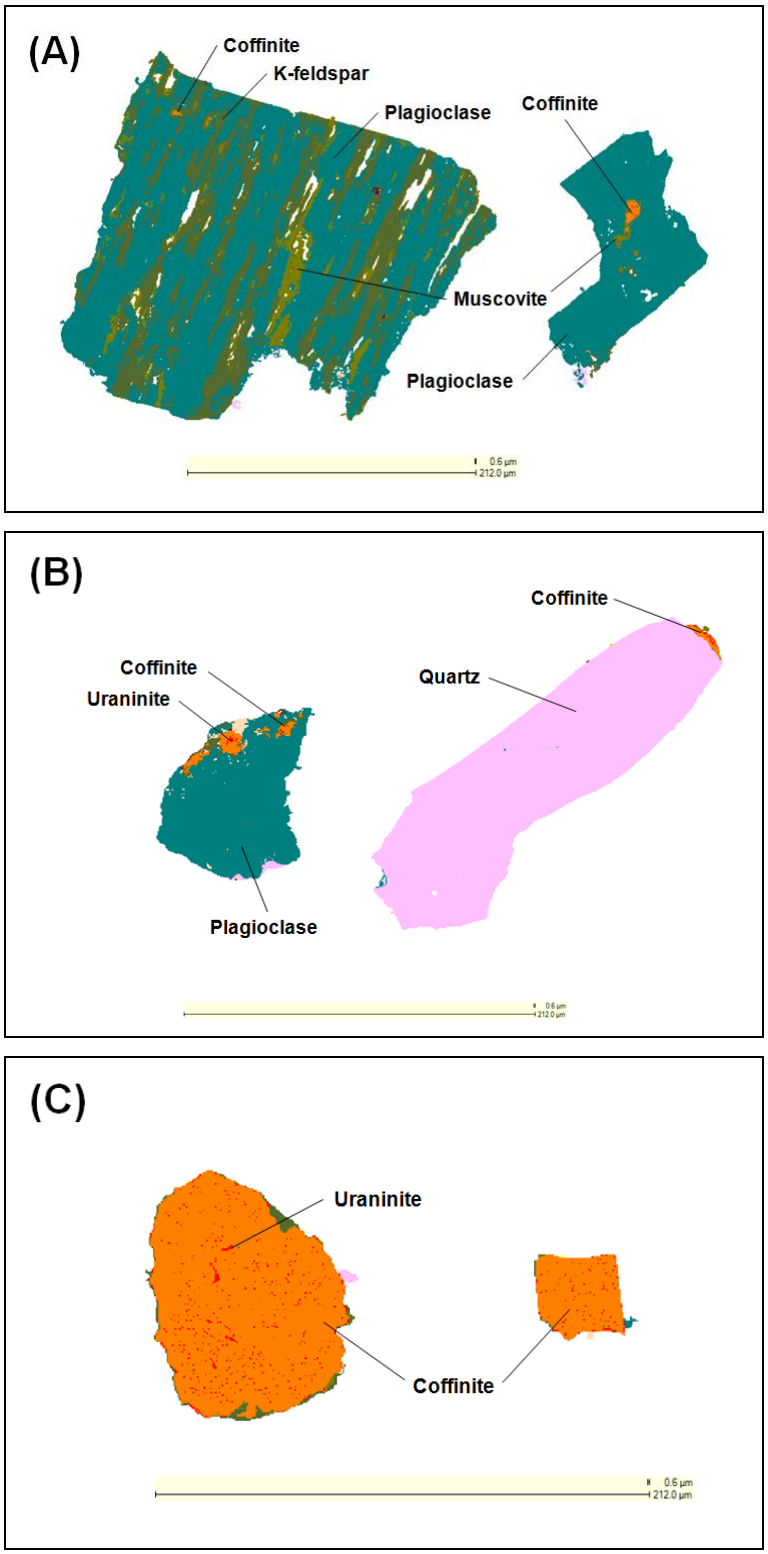

Figure 53: QEMSCAN particle maps from OAO. (A) Coffinite locked in anti-perthite and plagioclase. (B) Partially exposed coffinite and uraninite (B). (C) Coffinite and uraninite with very high surface exposure.

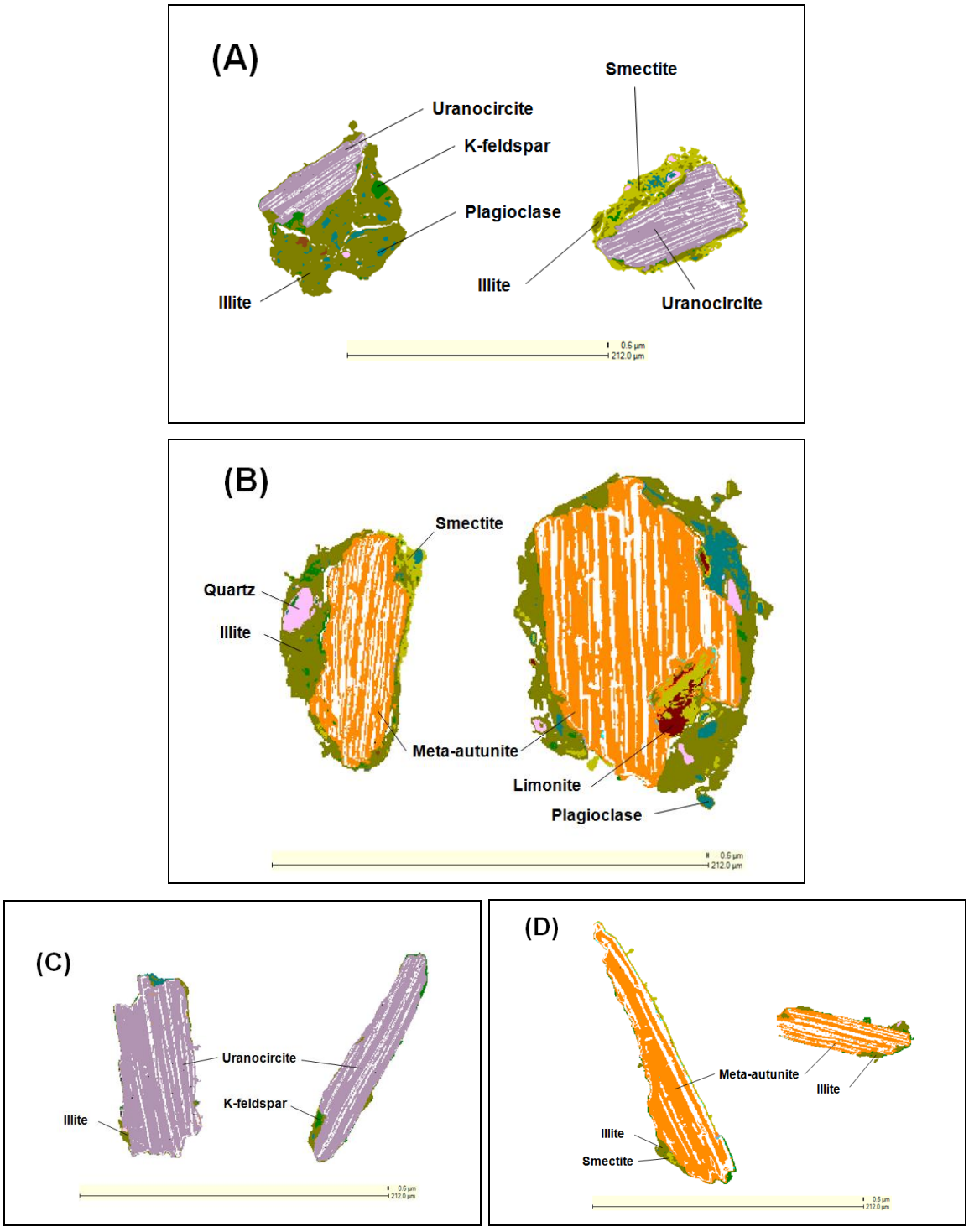

Figure 54: QEMSCAN particle maps for the MSO sample. (A) Uranocircite and meta-autunite in complex particles associated with silicates. (B) Meta-autunite with silicate rims. (C) Well liberated uranocircite with illite and K-feldspar. (D) Well liberated meta-autunite with illite and smectite.

5.4. Discussion

Gangue Mineralogy

BMA analyses of the samples in general support the results of the XRD analyses. However, the muscovite in RAO and OAO was not detected by XRD. Various oxides/hydroxides of Fe and Ti were also not detected. The muscovite was not detected because its concentration in RAO and OAO was below the detection limit of 0.98% (see Chapter 4). It appears that the Fe-Ti oxide/hydroxide was not detected because they are not well crystalline.

With the exception of these two discrepancies, the BMA data supports the XRD data and suggests that calcite, laumontite and chlorite will be the most important gangue acid consumers in the Mooi sample, with chlorite and smectite in RAO, smectite in OAO and smectite and illite in MSO as the most important acid consumers.

Stereologically corrected grain sizes were determined from the BMA data. According to these data, quartz is the coarsest phase in the Mooi sample, followed by calcite. Quartz was also the coarsest mineral in the Kayelekera samples, with plagioclase as the second coarsest, followed by K-feldspar.

In the Mooi sample there was only a modest decrease in grain size from the -212 to the -75 µm samples. However, there was a significant increase in the surface exposure. These results suggest that much of the breakage that occurred in the milling from -212 to the -75 µm occur along grain boundaries, with only modest breakage of the detrital sand grains.

The increase in exposure from -212 to the -75 µm, resulted in a significant increase in surface area, in spite of the only modest grain size reduction. Since the rate of mineral dissolution is proportional to exposed surface area (Lüttge and

Arvidson, 2008) it is expected that gangue dissolution rates will be significantly more rapid at the finer grind. This will result in increased acid consumption at the same pH and Eh conditions.

Uranium Deportment

The uranium deportment shows that Mooi and OAO have similar deportments, in both samples most of the U is hosted by coffinite with lesser amounts in uraninite. The U in RAO also occurs in coffinite with lesser amounts in uraniferous leucoxene, and minor amounts in uraninite. The U deportment in the MSO sample was different from those of the arkosic samples. The U in MSO occurs in urano-circite, with a slightly smaller amount occurring in meta-autunite.

The U minerals in MSO had the coarsest grain size distribution, RAO and OAO were intermediate and Mooi contained the finest U minerals. Surprisingly the U minerals in Mooi appear coarser at -75 µm than at -212 µm. This is probably an indication that while between 100 and 150 grains is sufficient to determine the U deportment with reasonable accuracy; it is probably too few to determine accurate grain size distributions.

At 80% -212 µm Mooi had the lowest exposure (background association) of all of the samples. This is the result of the fine grain-size of the U minerals in this sample. However, at 80% 75 µm the exposure is much higher. It is therefore expected that there will be significant improvements in the U dissolution at the finer grind.

RAO had the highest proportion of U locked in reactive gangue. Because the gangue will have to dissolve before the solution can access a significant proportion of the U, it is expected that this sample will have slow leach kinetics. Both OAO and MSO had very high degrees of exposure (both greater than 90%).

These samples are expected to leach rapidly, with greater than 90% U dissolution.

5.5. Summary and Conclusions

Seven normal and 2 transverse polished sections were prepared from each sample, except Mooi. Because blocks from this sample were prepared at two different grinds (at 80% -212 µm and 80% -75 µm), a total of 14 normal and 4 transverse polished sections were prepared from this sample.

The transverse polished sections underwent analysis by QEMSCAN BMA in order to characterise the gangue minerals in each sample with respect to composition, grain size, exposure and surface area. The normal polished sections were analysed by QEMSCAN TMS to determine the U deportment, grain size distribution and exposure and association characteristics.

Bulk Mineralogical Analyses

The BMA analysis confirmed the quantitative XRD analyses, with the exception that Fe-Ti oxide/hydroxide phases were not detected, due to their low crystallinity. Muscovite was also not detected in RAO and OAO, because the concentration of this phase was below the detection limit of XRD for the conditions used (see Chapter 4). Based on these results the most important gangue acid consumers will be calcite, then laumontite and chlorite in Mooi, chlorite and smectite in RAO, smectite in OAO and smectite and illite in MSO.

Quartz and feldspar were the coarsest phases in most of the sample. The stereologically corrected mean quartz grain size was between ~12 µm (MSO) and ~56 µm RAO while plagioclase grains were between ~6 µm MSO and ~26 µm (OAO). Determination of the size of smectite and illite was subject to

potential error as the QEMSCAN experiences difficulties distinguishing very fine adjacent grains of the same mineral. However it appears that illite in MSO was ~8 µm in size and smectite ranged from ~5 µm (MSO) to 7 µm (RAO). The remaining phyllosilicates (muscovite and chlorite) were between ~5 µm (muscovite in OAO) and ~8 µm (muscovite in Mooi -212).

Using these grain sizes, geometric surface areas were calculated. These were corrected for exposure (as determined from the BMA data) and surface roughness. Published data (which included both grain size and BET surface area data) were used to determine the relationship between grain size and surface roughness for the various minerals. This was then used to estimate the surface roughness in these samples.

Calcite surface areas were between 0.22 (Mooi -212) and 0.33 (Mooi -75) m^2/g. Laumontite surface areas were between 0.11 (Mooi -212) and 0.17 (Mooi -75) m^2/g. In practice the laumontite specific surface area is probably higher than that of calcite, but because of a lack of published surface area data, it was not possible to correct the laumontite for surface roughness. Therefore the results are not directly comparable.

The specific surface area of chlorite ranged from 1.61 to 2.89 m^2/g and that of muscovite was between 1.04 and 3.49 m^2/g. In both cases the lower specific surface area was seen in RAO and the highest in Mooi -75. Due to the differences in specific surface area, it is expected that the rate of phyllosilicate dissolution will be significantly more rapid in Mooi -75 than in RAO.

The surface areas of quartz, smectite and illite were not estimated. Since the dissolution of quartz is not acid consuming (Blum *et al.*, 1990), there was no need to calculate the rate of dissolution of this phase. Smectite and illite could not be accurately calculated because the QEMSCAN does not readily distinguish between very fine adjacent grains of the same mineral. However, since the rate

of smectite dissolution is not surface area normalised (Metz *et al.*, 2005), the lack of a surface area is not a major limitation for this mineral.

Trace Mineral Search

The normal polished sections were examined by QEMSCAN TMS to characterise the U phases. In the arkosic samples coffinite hosted the majority of the U, with this phase accounting for ~76% of the U in Mooi, ~74% in OAO and ~65% in RAO. Subordinate amounts of U occur in uraninite in Mooi (~22%) and OAO (~25%), while in RAO uraniferous leucoxene was the second most important U phase (~30%). The ore mineralogy of MSO was unlike any of the arkosic samples. Uranocircite was the dominant U mineral (hosting ~55% of the U), with a slightly smaller proportion of the U (~45%) occurring in meta-autunite.

The grain size distributions of the U minerals in each sample were also determined from the TMS data. The Mooi sample (at both grinds) had the finest U minerals. Mooi -75 shows a slightly coarser size distribution than Mooi -212. This counter intuitive result suggests that too few grains were mapped to get truly accurate grain size distributions. This is supported by the jagged shape of the Mooi -75 cumulative grain size distribution curve. Provided the grain size distribution is unimodal, these curves are typically smoother (as is the case with the other samples).

RAO and OAO have very similar grain size distributions, while that of MSO is significantly coarser. Assuming identical U mineralogy and exposure characteristics, the Mooi sample would have the most rapid U dissolution kinetics, while MSO would be the slowest, with RAO and OAO showing intermediate kinetics. However, the differences in U mineralogy prevent a comparison of this sort.

The finer grain size also typically results in lower exposure at the same grind. This is because the finer the grain, relative to the size of the host particle, the more likely it is to be locked within that particle. This results in a reduction in the specific surface area and can be seen in the low exposure of Mooi -212 (of ~70%) when compared with MSO (of ~94%), which contained significantly coarser-grained U minerals. OAO also had very high proportions of liberated U minerals, with ~92% exposed to some degree. The exposure of RAO was low (~64%), however a further ~21% occurs locked within reactive gangue and could potentially be recovered depending on the dissolution of the gangue. However, the need to first dissolve the gangue will result in slow dissolution kinetics for this sample.

Chapter 6. Leach Testwork

6.1. Introduction Aims and Objectives

The batch acid leach tests were conducted using the guidelines given by the IAEA (1980 and 1999). The purpose of the leach tests was to provide data to test and refine the predictions made from the results of the mineralogical investigation. There were three main objectives:

1. Assess the effects of changes in pH and Eh on reagent consumption, U dissolution rate and percentage dissolution. This will be achieved by conducting a number of leach tests at different pH and Eh conditions.
2. Assess the effects of particle size by leaching the same sample at different grinds.
3. Assess the effect of variation in composition by leaching different samples at the same conditions.

6.2. Methodology

Leach tests were conducted on 2 kg split aliquots of each sample. Due to the large amount of Mooi material, it was possible to leach this sample at a number of different pH and Eh conditions and at two different grinds (80% passing 212 and 75 μm). The limited amount of material in the Kayelekera samples limited these leach tests to one test per sample.

The pH was controlled using concentrated sulphuric acid and the redox potential was controlled using manganese dioxide (both Associated Chemical Enterprises Platinum Line analytical reagent grade). Eh and pH conditions were monitored

using two Metrohm 826 mobile pH units (one for pH and the other for redox potential). The pH meter was calibrated using fresh commercially available pH 1 and 2 buffers and the Eh measurements were corrected based on the results of measurements against a 475 mV standard solution.

The leaches were performed at a solid to liquid ratio of 1:1 (by mass), in 5 L plastic beakers. Agitation was achieved by overhead stirrers driven by 0.37 kW motors. These motors rotated stainless steel impellors at a speed of ~350 rpm. The impellors had four blades, with each blade approximately 50 mm long and 20 mm wide, and angled at ~30° to the horizontal. Figure 55 shows one of the batch reactors used in this study.

Temperature control was achieved by means of a stainless steel loop submerged in the slurry. Warm water (heated and controlled in a separate sump) was circulated through the loop to raise the temperature to between 35 and 40° C.



Figure 55: Batch reactor used in the leach tests. The tests were conducted in 5 L plastic beakers (1), with Perspex covers to limit evaporation (2). Temperature was controlled by circulating warm water through a stainless steel loop (3). The reactor had the facility (not used in the present study) to introduce gas into the reaction through a stainless steel tube (4). Agitation was achieved by a four blade impellor (5) rotated by an electric motor (6).

The initial liquid added to the ore was tap water. Tap water was used in preference to distilled water because it has a composition more similar to the water used on processing plants (Maria Klaas, pers. comm.). Once the water had been added, and an acceptable degree of agitation achieved, the sulphuric acid was added using a plastic pipette. The quantity of acid used was determined gravimetrically (by weighing of the sulphuric acid bottle).

After an hour of pre-conditioning, at as close as possible to the desired pH, the manganese dioxide was added. The pH and Eh were then monitored throughout the remainder of the leach and adjusted as needed.

Samples of slurry were collected 1, 3, 8 and 24 hours after adding the manganese dioxide, with the 24 hour sample representing the end of the leach. The slurries were filtered to separate the solid and liquid fractions. After filtration and recovery of the pregnant solution, the solids were washed using dilute sulphuric acid solution (pH ~1.5), followed by distilled water, to remove any remaining pregnant solution from the solid residue. The masses of the original slurry, wet residue and dry residue were determined gravimetrically, with the solution mass determined from the difference between the original slurry mass and that of the dry residue.

The dry residues were split into two aliquots. One was kept and the other was pulverised. Approximately 3 g of the pulverised material was miconised in ethanol, using a Mcrone micronising mill, for a period of three minutes in order to achieve the crystallite size recommended by McCusker *et al.* (1999). The resulting micronised material was analysed by XRD using the settings described in Chapter 4. However, while the analyses, instrument and settings were kept the same, the tube of the diffractometer had been replaced between collection of the initial diffractograms (Chapter 4), and analysis of the residues. For this reason the head samples were also reanalysed in order to keep the diffractograms as comparable as possible.

In addition to the XRD analyses, the 3 hour and 24 hour residues were analysed by XRF for major elements by borate fusion and U and Th by pressed pellet.

The solutions were analysed by inductively coupled plasma-mass spectrometry (ICP-MS) to determine U and Th concentrations and inductively coupled plasma optical emission spectrometry (ICP-OES) to determine Si, Al, Mg, Fe, Mn, Na and K concentrations.

The results of the U analyses were used to determine the U recovery and the ICP-OES analyses were used to understand gangue mineral dissolution (and by extension gangue acid consumption).

6.3. Results

X-ray Diffraction of Leach Residues

X-ray diffractograms are shown for each of the four samples. The Mooi and RAO samples are shown in Figure 56 and those of OAO and MSO are shown in Figure 57. Only one of the Mooi leaches has been shown. This leach was at a P_{80} of 212 and an average pH of 1.52 (the raw leach data is included in Appendix B). The other leaches show similar trends, except that the leaches at lower pH or finer grind show more rapid gangue dissolution, while the leach at higher pH showed slower dissolution.

The most noticeable changes in the mineralogy of the Mooi sample (Figure 56 A) is the disappearance of calcite and laumontite, the depletion of chlorite and the formation of gypsum. Trace amounts of gypsum also formed in the residues of RAO (Figure 56 A). The RAO sample also showed depletion of chlorite and changes in the shape and position of the smectite peak (Figure 56 B).

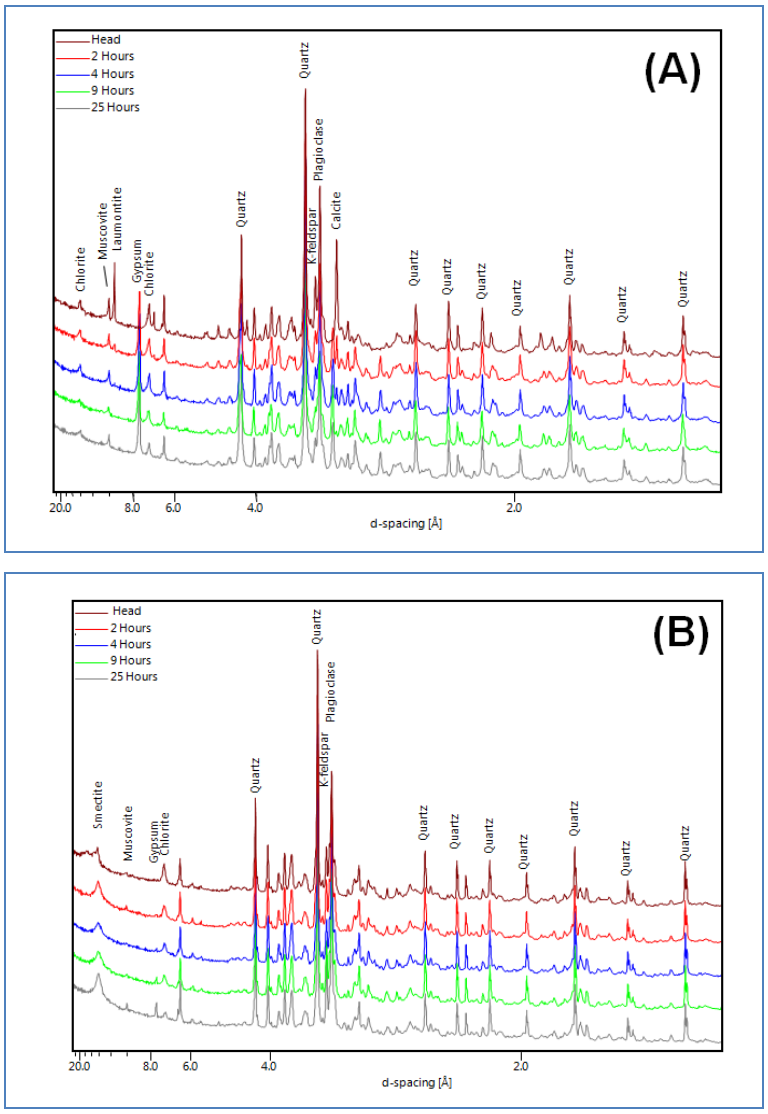

Figure 56: X-ray diffractograms of the Mooi (A) and RAO (B) samples showing the change in gangue mineralogy with time. (A) The peaks of calcite and laumontite decrease with time and gypsum forms. (B) Chlorite is depleted and the shape and position of the smectite peak changes with time.

Variation in the smectite peak shape and position were the only changes seen in the residues of OAO (Figure 57 A). However, these changes are more clearly seen in MSO (Figure 57 B) where the higher smectite concentration made the changes more obvious. These samples were glycolated prior to analysis to ensure that any variation in peak position was the result of changes in the mineral and not varying degrees of hydration. It can be seen that the interlayer spacing of the smectite progressively collapses from 17.1 Å in the head sample

to 14.4 Å in the 9 hour residue. This is accompanied by a marked broadening of the peak. However, in the 25 hour residue, the interlayer spacing increases to 16.7 Å, with a significantly narrower peak than in the 9 hour residue.

The intensities of the main calcite (3.03 Å) and laumontite (9.44 Å) peaks were used to determine the extent of the dissolution of these minerals in each of the Mooi residues. It was necessary to correct these intensities for changes in the mass absorption coefficient, for mass losses due to the acid dissolution and sampling. It was also necessary to correct the laumontite peak intensity data for preferred orientation (detailed descriptions of the method used are given in Chapter 4). Table 48 shows that calcite was completely dissolved in all of the Mooi leaches and that calcite dissolution was most rapid at the finer grind. Table 48 also shows that laumontite completely dissolves, in some cases within the first hour. However, the leach solutions contain significantly lower Al concentrations than would be expected for complete laumontite dissolution. It is therefore likely that either some of the Al precipitated as a new phase, or that the incongruent dissolution of laumontite left an amorphous Si-Al-enriched residue.

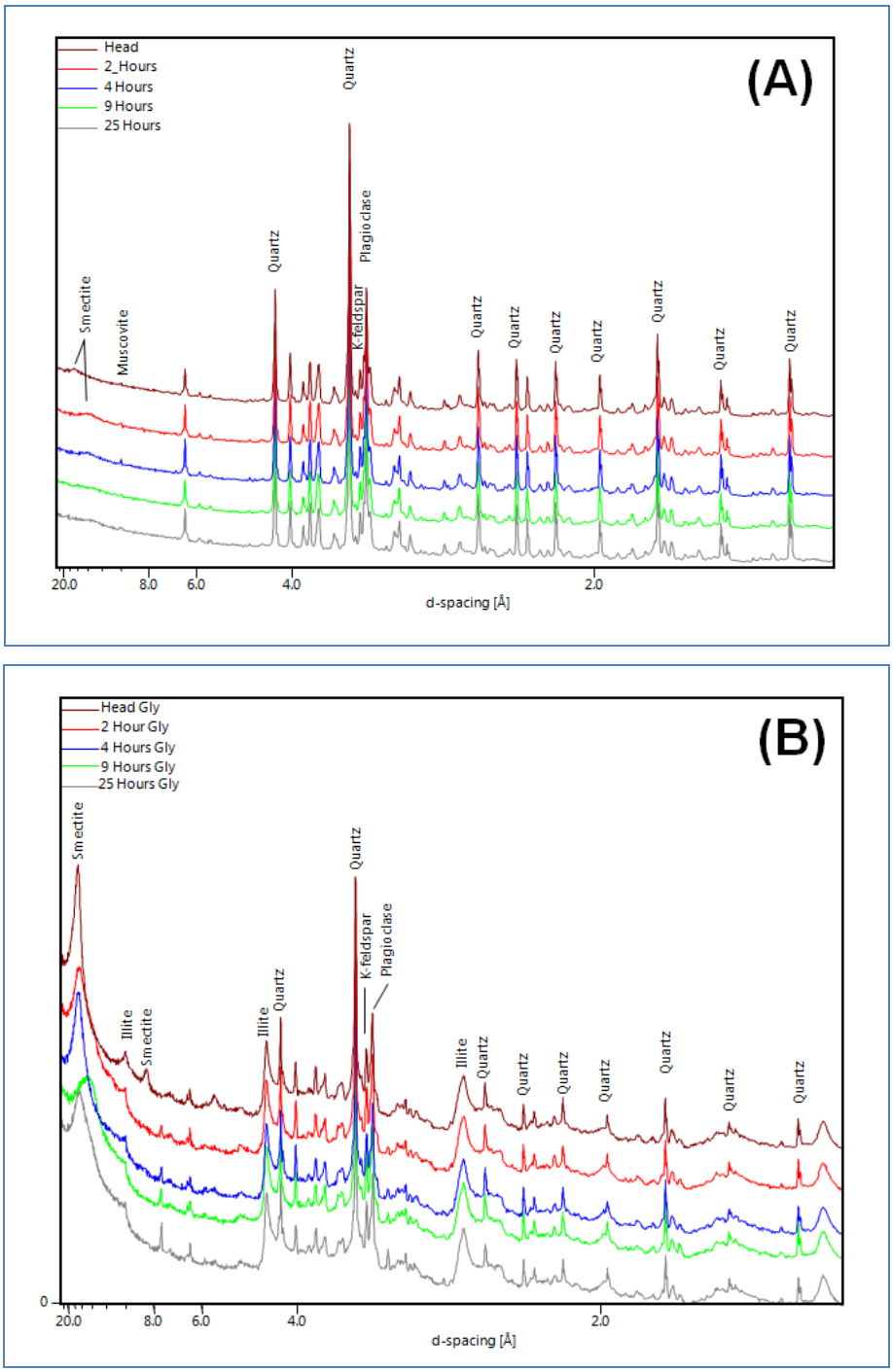

Figure 57: X-ray diffractograms of OAO (A) and MSO (B) showing the change in gangue mineralogy with time. (A) The only change seen in the gangue mineralogy of the OAO sample was the change in shape and position of the smectite peak. (B) This change was also seen in the MSO sample, but due to the higher concentration of smectite in the sample, the changes are more distinct.

Table 48: Changes in the proportion of calcite and laumontite remaining in the leach residues after specific time intervals showing the dissolution rates of these minerals under different pH conditions and at two different grind sizes

Calcite				
Sample	**Mooi**	**Mooi**	**Mooi**	**Mooi**
pH	**0.97**	**1.52**	**1.51**	**2.02**
P_{80}	**-212**	**-212**	**-75**	**-212**
Time (Hours)	**% Remaining**	**% Remaining**	**% Remaining**	**% Remaining**
0.00	100.0	100.0	100.0	100.0
2.02	15.1	21.9	2.2	13.6
4.03	9.3	9.8	0.0	10.5
9.00	2.1	2.5	0.0	11.2
25.00	0.0	0.0	0.0	0.0
Laumontite				
Sample	**Mooi**	**Mooi**	**Mooi**	**Mooi**
pH	**0.97**	**1.52**	**1.51**	**2.02**
P_{80}	**-212**	**-212**	**-75**	**-212**
Time (Hours)	**% Remaining**	**% Remaining**	**% Remaining**	**% Remaining**
0.00	100.0	100.0	100.0	100.0
2.02	0.0	18.8	0.0	79.2
4.03	0.0	5.5	0.0	40.2
9.00	0.0	0.0	0.0	18.2
25.00	0.0	0.0	0.0	0.0

The chlorite dissolution was calculated from Mg concentrations in the head sample and leach solutions (Appendix B includes the solution assay data). The values in Table 49 have been corrected for mass losses due to sampling and increases in Mg concentrations resulting from evaporation of water during the leach. Depending on the pH and the grind, between ~7 and 47% of the chlorite dissolved. Unlike calcite, which was more sensitive to grind, chlorite appears to be more sensitive to pH in these tests. After 25 hours at a ~pH 2 only 6.5% of the chlorite dissolved, while at ~pH 1 approximately 47% of the chlorite dissolved. However, at the finer grind only about 23% chlorite dissolution occurred.

Table 49: Changes in the proportion of chlorite remaining in the Mooi sample residues after specific leaching intervals, showing the rate of chlorite dissolution under various pH conditions and at two different grind sizes

Sample	**Mooi**	**Mooi**	**Mooi**	**Mooi**
pH	**0.97**	**1.52**	**1.51**	**2.02**
P_{80}	**-212**	**-212**	**-75**	**-212**
Time (Hours)	**% Remaining**	**% Remaining**	**% Remaining**	**% Remaining**
0.00	100.0	100.0	100.0	100.0
2.02	87.4	96.2	93.2	96.5
4.03	82.5	92.9	90.4	95.5
9.00	71.3	91.1	82.2	95.2
25.00	53.4	84.1	77.3	93.5

The dissolution of plagioclase was calculated from Na concentrations in the head samples and leach solutions. The values in Table 50 have been corrected for sampling and evaporative concentration. It is important to note that the rate of Na release is slightly slower than that of Ca, and significantly more rapid than Al or Si (Stillings and Brantley, 1995). In each of the tests no more than 2% of the plagioclase dissolved with slightly more rapid dissolution at lower pH or finer grind size.

Table 50: Plagioclase dissolution calculated from sodium concentrations in the head sample, and leach solutions, showing the rate of plagioclase dissolution at various pH conditions and at two different grind sizes

Sample	**Mooi**	**Mooi**	**Mooi**	**Mooi**
pH	**0.97**	**1.52**	**1.51**	**2.02**
P_{80}	**-212**	**-212**	**-75**	**-212**
Time (Hours)	**% Remaining**	**% Remaining**	**% Remaining**	**% Remaining**
0.00	100.00	100.00	100.00	100.00
2.02	98.61	99.19	98.96	99.50
4.03	98.58	98.42	98.34	99.08
9.00	98.43	98.54	98.18	99.12
25.00	98.00	98.96	98.21	98.91

Determining the rate of K-feldspar dissolution was particularly complex, as K also occurs in muscovite and illite. The dissolution data at pH 1.47 (Table 51) was

determined from the K concentrations in the OAO head sample and leach solutions. The OAO sample was selected because the concentration of muscovite was very low in this sample, while K-feldspar was a major phase. The data has been corrected for sampling and evaporative concentration, and shows that K-feldspar dissolution is almost negligible. This is especially true when considering that K is released 5 times faster than Al and 20 faster than Si in the initial stages of acid dissolution (Stillings and Brantley, 1995).

Table 51: K-feldspar dissolution calculated from potassium concentrations in the head sample and leach solutions showing negligible K-feldspar dissolution within 25 hours

Sample	**OAO**
pH	**1.47**
P_{80}	**-212**
Time (Hours)	**% Remaining**
0.00	100.0
2.05	99.7
4.00	99.6
9.00	99.6
25.00	99.6

Table 51 shows that the extent of K-feldspar dissolution is very small within the duration of a typical U leach. However, in order to accurately determine the extent of muscovite dissolution it was necessary to correct for K-feldspar dissolution. Since K-feldspar dissolution data was not readily available at all of the pH conditions used, these were estimated from the data in Table 51 and the pH dependence seen in plagioclase. The resulting data was used to correct the muscovite dissolution data. These data (Table 52) have also been corrected for sampling and evaporative concentration. Between ~9 and 17% of the contained muscovite dissolved, depending on pH and grind, with the highest dissolution at the finer grind size and significantly slower dissolution at the coarser grind and higher pH.

Smectite and illite dissolution data were calculated from the results of leaching the MSO sample. Smectite dissolution was calculated from Mg concentrations

and illite from K. Corrections for sampling and evaporation have been applied. Approximately 7% of the smectite dissolved, while illite dissolution was negligible (Table 53).

Table 52: Muscovite dissolution calculated from K-feldspar-corrected potassium concentrations in the head sample and leach solutions showing increased rates of dissolution at lower pH or finer grind size

Sample	**Mooi**	**Mooi**	**Mooi**	**Mooi**
pH	**0.97**	**1.52**	**1.51**	**2.02**
P_{80}	**-212**	**-212**	**-75**	**-212**
Time (Hours)	**% Remaining**	**% Remaining**	**% Remaining**	**% Remaining**
0.00	100.0	100.0	100.0	100.0
2.02	89.0	94.5	91.9	96.6
4.03	88.7	87.6	86.2	92.8
9.00	88.5	88.7	87.3	93.1
25.00	87.6	89.9	83.0	90.8

Table 53: Smectite and illite dissolution calculated from magnesium and K-feldspar-corrected potassium concentrations in the head sample and leach solutions; smectite dissolution was significantly more rapid than illite

Mineral	**Smectite**	**Illite**
Sample	**MSO**	**MSO**
pH	**1.33**	**1.33**
P_{80}	**-212**	**-212**
Time (Hours)	**% Remaining**	**% Remaining**
0.00	100.0	100.0
2.08	95.8	99.9
4.05	93.7	99.8
9.03	93.0	99.7
25.07	93.2	99.7

Uranium Dissolution

The degree of U dissolution was determined from the results of the ICP-MS analyses of the leach solution and was checked against the XRF analyses of the residues. The results of the leaches (corrected for sampling and evaporation) are

given in Table 54; the leach conditions are also shown.Figure 58 shows the U dissolution curves for the four Mooi and three Kayelekera leaches.

In the Mooi leaches, the low pH (Test A) and finer grind (Test C) showed very similar dissolutions, with progressively lower dissolution in B and D (intermediate and high pH respectively). The Kayelekera dissolutions were all above 80%, with dissolutions increasing from OAO through RAO to MSO. However, examination of the dissolution curves show that OAO reached maximum dissolution (of 91.21%) at four hours and MSO reached maximum dissolution (of 97.31%) at nine hours. Thereafter, both samples show a decrease in the percentage U dissolution.

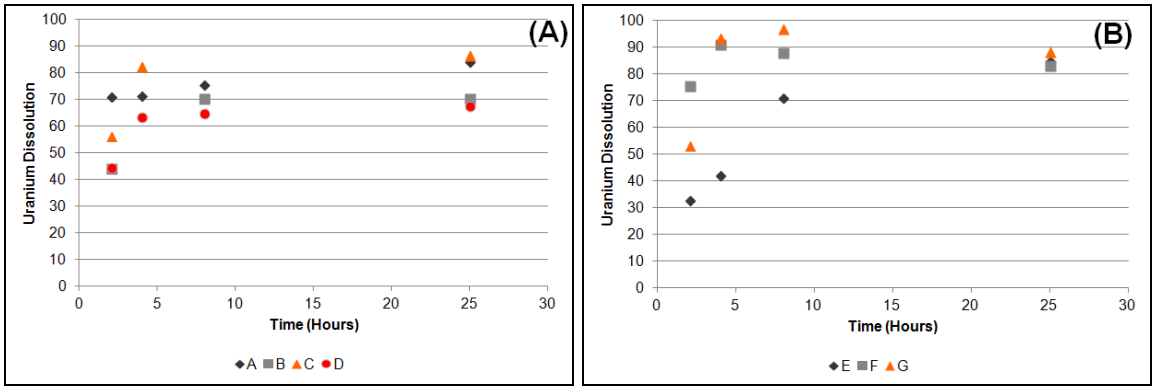

Figure 58: Uranium dissolution as a function of time. (A) The four Mooi sample leaches. Leach A was at a pH of 0.97, B at 1.52, C at 1.51 (but a finer grind size) and D at pH 2.02. (B) The Kayelekera sample leaches all at ~pH1.5. Leach E was of the RAO sample, F of the OAO sample and G of the MSO sample.

Table 54: Leach conditions and uranium dissolution as a function of time and pH

Test	A	B	C	D	E	F	G
Sample	**Mooi**	**Mooi**	**Mooi**	**Mooi**	**RAO**	**OAO**	**MSO**
pH	**0.97**	**1.52**	**1.51**	**2.02**	**1.56**	**1.47**	**1.33**
Eh (SCE)*	**499**	**449**	**457**	**413**	**428**	**485**	**471**
P_{80} (µm)	**212**	**212**	**75**	**212**	**212**	**212**	**212**
Time (Hours)	**U Dissoln (%)**	**U Dissoln (%)**	**U Dissoln (%)**	**U Dissoln (%)**	**U Dissoln (%)**	**U Dissoln (%)**	**U Dissoln (%)**
2	71.21	43.99	56.31	44.44	32.64	75.44	53.17
4	71.46	-	82.48	63.39	42.13	91.21	93.33
8	75.77	70.42	-	64.66	71.10	87.91	97.13
25	84.44	70.36	86.80	67.71	85.13	83.06	88.44

*Saturated calomel electrode

6.4. Discussion

A comparison of the Mooi exposure data obtained by QEMSCAN TMS, with U dissolution in the leach tests found that, in Tests B and D, the amount of exposed U agreed well with the percentage U dissolution. The finer grind used in Test C allowed for significantly higher U dissolution and again there was agreement between the exposure and dissolution data. However, the dissolution seen in Test A far exceeds the predicted value based on the U mineral exposure. In order to achieve such high dissolutions, significant amounts of locked U must have been exposed by the aggressive conditions of the leach (at pH 0.97).

As shown in Table 46 and Table 47, the U minerals in the OAO and MSO samples both had very high degrees of exposure (>91%), but the final U dissolution in these samples was less than 89% (Table 54). The maximum dissolution in both of these samples was not achieved at 24 hours, with OAO reaching a maximum dissolution of ~91% at four hours and MSO reaching maximum dissolution (~97%) at nine hours. After these maxima, both leaches showed progressive decreases in U dissolution. This could be the result of U precipitation from solution or may be due to the presence of smectite (as described below.

XRD analyses of the leach residues show a progressive collapse in the interlayer spacing of the smectite from the head sample (at ~17 Å) to the 9 hour residue where it reached ~14 Å). Thereafter the interlayer spacing increased, reaching ~17 Å in the 25 hour residue. It is possible that the interlayer collapse is the result of H^+ replacement of the interlayer cations. Then as the ionic strength of the solutions increased, other larger cations (including U) became available for substitution. The substitution of these cations could have resulted in the increase in the interlayer spacing. This substitution may also be the reason for the decrease in U dissolution in the later stages of the leach.

OAO and MSO were not the only samples to contain smectite. RAO contained more smectite than OAO, but this sample did not show the same decrease in dissolution in the later stages of the leach. There are two likely reasons. The first is that in RAO ~20% of the U occurred in grains locked in reactive gangue. This U was released more slowly as time was required to dissolve the gangue. This prevented this leach from developing an early maximum. The second is that the RAO solution contained very high concentrations of other elements, especially Mn from the oxidiser. These elements may have preferentially substituted into the smectite.

The dissolution characteristics of several common gangue minerals were determined. These results show that gangue dissolution increases with decreasing pH and grain size. The rate of dissolution of most minerals follows an exponential decay function, from an initially rapid rate to a much slower one as the leach progresses.

The dissolution rates of calcite and laumontite are rapid and both phases were completely dissolved, (although laumontite is subject to incongruent dissolution and it is likely that an amorphous Si-Al solid phase is still present in the residues at the end of the leach).

Chlorite dissolution was also rapid, but not as rapid as that of calcite or laumontite. Depending on the pH and specific surface area, between about 7 and 47% of the contained chlorite can dissolve within the duration of an acid leach. Muscovite dissolution was much slower and only about 12% dissolved at pH 0.97.

While the feldspars do dissolve, the rate of this dissolution was very slow. Neither plagioclase nor K-feldspar showed more than 2% dissolution.

6.5. Summary and Conclusions

The aim of the leach tests was to provide a dataset to test and refine the mineralogical predictions. All four samples were leached. Due to the large amount of Mooi material, this sample was leached at three different pH and Eh conditions and at two different grinds. However, it was only possible to do one leach for each of the Kayelekera samples (due to the low sample mass).

The qualitative mineralogical predictions were fairly accurate. It was predicted that the most important gangue acid consumers in the Mooi sample would be calcite, laumontite and chlorite. XRD analyses of the leach residues showed the disappearance of calcite and laumontite, with the depletion of chlorite. The rate of dissolution of the minerals increased with decreasing pH and particle size. It was also predicted that gypsum would form in the residues and this was seen by XRD.

The XRD of the residues show the complete disappearance of the laumontite peak, however, the ICP-OES analyses show that the leach solutions did not contain sufficient Al for complete dissolution of laumontite. It is therefore likely that either Al precipitated as part of a new phase, or that the dissolution of laumontite is highly incongruent. Dissolution of the Ca resulted in an Al-Si enriched, amorphous phase. The second possibility (incongruent dissolution) is considered more likely.

In the RAO sample it was predicted that chlorite and smectite would be the most important acid consumers. The XRD of the residues supports this prediction and show the depletion of chlorite and changes in the position and intensity of the smectite peak. A small amount of gypsum also formed in this sample.

OAO was the only sample which did not form gypsum. The only changes that can be seen in the residue diffractograms is a variation in the position and intensity of the smectite peak.

The changes in the smectite peak were most obvious in the MSO leach residues, where the peak collapsed from a narrow peak at 17.1 Å to a broad peak at 14.4 Å. Thereafter, the peak moved to 16.7 Å and narrowed. It is likely that the changes in the position of the smectite peak is the result of smaller ions (such as H^+) replacing larger ions in the smectite interlayer spaces. This resulted in the collapse of the interlayer spacing. As the leach progressed, other ions became available for exchange. The introduction of larger ions, into the interlayer spacing, resulted in the increase in the peak position to 16.7 Å.

Some of the samples which showed this smectite collapse and recovery phenomenon also had unusual U dissolution characteristics. These samples (OAO and MSO) reached maximum dissolutions (of 91.21 and 97.31%) early in the leach tests. Thereafter, both samples show a decrease in U dissolution (down to 83.06 and 88.44% respectively). It appears that this decrease coincides with the recovery in the smectite interlayer spacing and reflects the uptake of U by smectite.

Although RAO contained smectite and the collapse recovery phenomenon was seen in this sample, the early peak in U dissolution, followed by a decrease, was not seen in this sample. This is likely to be due to two factors. RAO had a very high proportion of U minerals locked in reactive gangue (~21%). The slow

dissolution of these minerals prevented the early peak in dissolution. This leach was also characterised by very high MnO_2 additions. It appears that the abundance of Mn in solution resulted in the preferential uptake of this ion.

A comparison of the exposure characteristics of the U in Mooi at the two grinds, with the percentage U dissolution, provided insight into the relationship between ore-gangue associations, and U mineral dissolution. The TMS data (Chapter 5) indicated that the U minerals in Mooi -212 were ~70% exposed. At moderate conditions (~pH 1.5, Test B), 70.36% of the U dissolved. This agreement suggests a strong textural control on U dissolution. At ~pH 2 (Test C) the U dissolution was 67.71%. It is possible that 70% dissolution was not achieved at this pH due to slower dissolution kinetics.

At ~pH 1 U dissolution reached 89.47%. The increased dissolution at low pH is the result of gangue dissolution. The TMS data suggested that ~6% of the U in Mooi occurs locked in reactive gangue. In order to reach a dissolution of almost 90%, all of the U locked in reactive gangue (and at least some of the U in unreactive gangue) must have dissolved. This shows a clear relationship between ore-gangue textures, leach conditions and final U dissolution.

In the following chapter (Chapter 7) the reagent consumption data, from the leach tests, was used to refine the mineralogical predictions.

Chapter 7. Modelling of Reagent Consumption

In order to make it possible to apply the data produced in the present study to the leaching of other ores, it was desirable to develop a model that allows for the prediction of reagent consumptions from mineralogical data. The results of the mineralogical characterisation of the head samples, and residues, and the chemical analyses of the leach solutions, and residues, were used to develop an Excel-based model to predict acid and MnO_2 consumptions.

7.1. Methodology

The amount of acid consumed in the dissolution of a mineral depends on the composition of the mineral. The acid dissolution reactions are describe by the following equations: calcite (Equation 16), laumontite (Equation 17), chlorite (Equation 19), muscovite (Equation 23), smectite (Equation 24), illite (Equation 26), plagioclase (Equation 27), K-feldspar (Equation 33) and quartz (Equation 37).

These equations represent the simplest case in which complete dissolution occurs. However, as a result of incongruent dissolution, different elements can be released at different rates from the same mineral, resulting in significantly more complicated dissolution reactions. No attempt was made to correct the phyllosilicates for incongruent dissolution. In the case of these minerals, the rate was either calculated from an element with an intermediate release rate, or congruent dissolution was reached fairly early in the leach.

It was not possible to treat the tectosilicates with this simple approach. Feldspar release rates were determined using the relative release ratios of Stillings and Brantley (1995). There was no quantitative data published for laumontite and it was therefore necessary to determine these as part of the present study. Using

these results, the acid consumption characteristics of the tectosilicates were determined. The ideal acid consumption characteristics of selected minerals are given in Table 55. Where necessary, the acid consumption corrected for incongruent dissolution has also been given. Because of the effects of incongruent dissolution, some elements may be leached significantly more rapidly (within the duration of a normal leach test) than others. Because a portion of the structure of the mineral is not dissolved to the same extent, the incongruent acid consumptions of the tectosilicates tend to be lower than those calculated for stoichiometric dissolution.

Table 55: Acid consumption characteristics of selected minerals and MnO_2 showing the amount of acid consumed for congruent dissolution and, where necessary, the acid consumption for incongruent dissolution

Mineral	**Ideal Acid Cons (kg/ton)$^+$**	**Incongruent Acid Cons (kg/ton)$^+$**
Calcite	9.8	-
Laumontite	6.4	3.8**
Chlorite	12.0*	-
Muscovite	12.3	-
Smectite	11.1*	-
Illite	10.7	-
Plagioclase	7.5*	6.1**
K-feldspar	6.8	2.7**
MnO_2	2.3	-

+Calculated assuming that the relevant mineral occurs in the ore in a concentration of 1% and that the rest of the ore is inert.

*These values vary with mineral composition.

**These values are strongly dependant on the element used to calculate the dissolution rate of the mineral.

An exponential decay function was used for modelling the decrease in the rate of dissolution of the various mineral phases with time (Equation 58).

$$R = R_0 e^{(-\lambda t)} + z$$

Equation 58

Where R is the rate at a given time (t), R_0 is the initial rate, λ is the decay constant and z is an approximation of the steady state dissolution rate. In practice the initial rate was usually so much more rapid than the steady state rate that, for most minerals, it was a reasonable approximation to set the steady state rate as zero.

Where this approximation was not valid, it was necessary to develop a function to predict the steady state rate. The relationship between pH and the steady state dissolution of many minerals is approximately parabolic, for example Lowson *et al.* (2005) with chlorite and Kohler *et al.* (2003) for illite (Figure 27 and Figure 29 respectively). Based on these results, parabolic functions were developed for the determination of z. In the same way, parabolic functions were developed to calculate R_0 from the pH of the leach test.

The value of the decay constant was determined from the dissolution data. Again, a parabolic function was used to relate the value of the decay constant to the pH.

Taking the definite integral of Equation 58 with respect to time from 0 to t hours gives Equation 59.

$$\int_0^t R\ dt = R0\ \frac{(e^{(-\lambda t)} - 1)}{-\lambda} + zt$$

Equation 59

Where R is the rate at a given time (t), R_0 is the initial rate, λ is the decay constant and z is an approximation of the steady state dissolution rate. In practice the initial rate was usually so much more rapid then the steady state rate that, for most minerals, it was a reasonable approximation to set the steady state rate as zero.

Because most rates are surface area normalised, multiplying Equation 59 by the surface area gives the percentage dissolution of the mineral. For example, if a mineral occurs in the ore in a concentration of 10%, and Equation 59 gives 20%

dissolution, then the concentration of the mineral in the leach residue would be 8% (ignoring the effect of the minerals dissolution on the total mass of the solids).

Manganese dioxide is the second reagent used in the U leaches. The dissolution of this reagent also consumes acid according to Equation 40. It is therefore necessary to be able to accurately predict the MnO_2 demand of an ore. There was insufficient literature on MnO_2 in U leaching to predict the MnO_2 consumption. It was therefore necessary to produce an equation for this purpose from the results of this study.

Once the gangue acid consumption had been calculated, it was necessary to determine the free acid demand of each of the leach tests. In this case free acid refers to the acid used to maintain the low pH required for the acid leaching of U. The method used is described in detail in Chapter 4. This method involved using the gangue mineral dissolution data to estimate the composition of the leach liquor. The precipitation of gypsum (Messnaoui and Bounahmidi, 2006), the formation of $CaSO_4^0$ ion pairs (Reardon and Langmuir, 1976), the incomplete dissociation of the second acidic proton of H_2SO_4 (Brown *et al.*, 2003) were also considered. Using these calculated solution compositions and the Davies equation (Equation 47) to determine activity coefficients, the free acid demand was calculated. Due to the interdependence of the variables in the model, an iterative approach was used. The first iteration assumed that the activities of the various species equalled their concentration. Later iterations considered the activity coefficients. The model required four iterations to stabilise.

7.2. Results

Using the results of the Fe^{2+} titrations on the head samples (Table 57), the MnO_2 consumptions and the redox potential of the leach tests, Equation 60 was found to predict the MnO_2 consumption with reasonable accuracy (Table 56). However,

as shown in Equation 40 the consumption of MnO_2 involves Fe^{2+} in the leach solution (rather than in the rock) and therefore Equation 60 relies on the assumption that the Fe^{2+} dissolution characteristics of an ore are the same as those in this study. Since Fe dissolution is a function of pH, Equation 60 also assumes a relationship between the pH and Eh conditions used in the leach. The assumption being that when more oxidising conditions are used, then the leaches would also be performed at lower pH.

$$\mathbf{MnO_2 = 38.58 \log [Fe^{2+}] + 0.1069\ Eh - 38.09}$$

Equation 60

Where MnO_2 is the MnO_2 demand (in kg/ton) of the leach test, $[Fe^{2+}]$ is the percentage of Fe^{2+} contained in the ore and Eh is the redox potential relative to a saturated calomel electrode.

Table 56: Ore ferrous iron concentrations, leach conditions, measured and calculated manganese dioxide consumptions

Test	Sample	Fe^{2+}	pH	Eh	MnO_2 Meas (kg/ton)	MnO_2 Calc. (kg/ton)
A	Mooi	0.83	0.97	499	17.88	12.1
B	Mooi	0.83	1.52	449	6.94	6.8
C	Mooi	0.83	1.51	457	11.69	7.6
D	Mooi	0.83	2.02	413	2.93	2.9
E	RAO	4.52	1.56	428	32.93	32.9
F	OAO	0.48	1.47	485	1.45	1.5
G	MSO	0.48	1.33	471	0.00	0.0

The dissolutions of the various gangue phases were modelled using Equation 58 and Equation 59. The variables used in these equations were calculated from the leach results using parabolic functions (Equation 61 to Equation 63). The variables for each mineral are given in Table 57. Based on these variables, the mineral dissolution characteristics were modelled. A comparison of the measured and modelled mineral dissolutions is given in Figure 59 (for calcite, laumontite and chlorite) and Figure 60 (for muscovite, plagioclase and K-feldspar). Because the samples that contained smectite and illite were all leached at approximately pH 1.5, it was not possible to plot the dissolution of these minerals in pH-time space. These were plotted as a function of time at pH 1.5 (Figure 61). The

variables used for smectite were 3.60 for R_0, -0.50 for –λ and 0 for z. Those used for illite were 0.0031 for R_0, -0.40 for –λ and 0 for z.

$$R_0 = a_1\, pH^2 + b_1\, pH + c_1$$

Equation 61

$$-\lambda = a_2\, pH^2 + b_2\, pH + c_2$$

Equation 62

$$z = a_3\, pH^2 + b_3\, pH + c_3$$

Equation 63

Where R_0 is the initial rate, λ is the decay constant, z is an approximation of the steady state dissolution rate and a, b, and c are variables determined from the leach tests.

Table 57: Variables used in modelling the dissolution of specific gangue minerals in Equation 61 to Equation 63

Mineral	Variable	a	b	c
Calcite	R_0	30.48	-155.89	396.53
	-λ	-0.08	0.38	-0.89
	z	0.00	0.00	0.00
Laumontite	R_0	878.27	-3605.07	3870.56
	-λ	-0.79	3.25	-3.50
	z	0.00	0.00	0.00
Chlorite	R_0	6.35	-23.10	21.92
	-λ	0.00	0.00	-0.95
	z	0.42	-1.83	2.04
Muscovite	R_0	-2.93	4.56	4.83
	-λ	0.54	-1.07	-0.57
	z	0.00	0.00	0.00
Plagioclase	R_0	1.75	-7.99	9.61
	-λ	0.43	-0.53	-1.09
	z	0.00	0.00	0.00
K-feldspar	R_0	1.21	-5.08	5.67
	-λ	0.46	-0.17	-2.13
	z	0.00	0.00	0.00

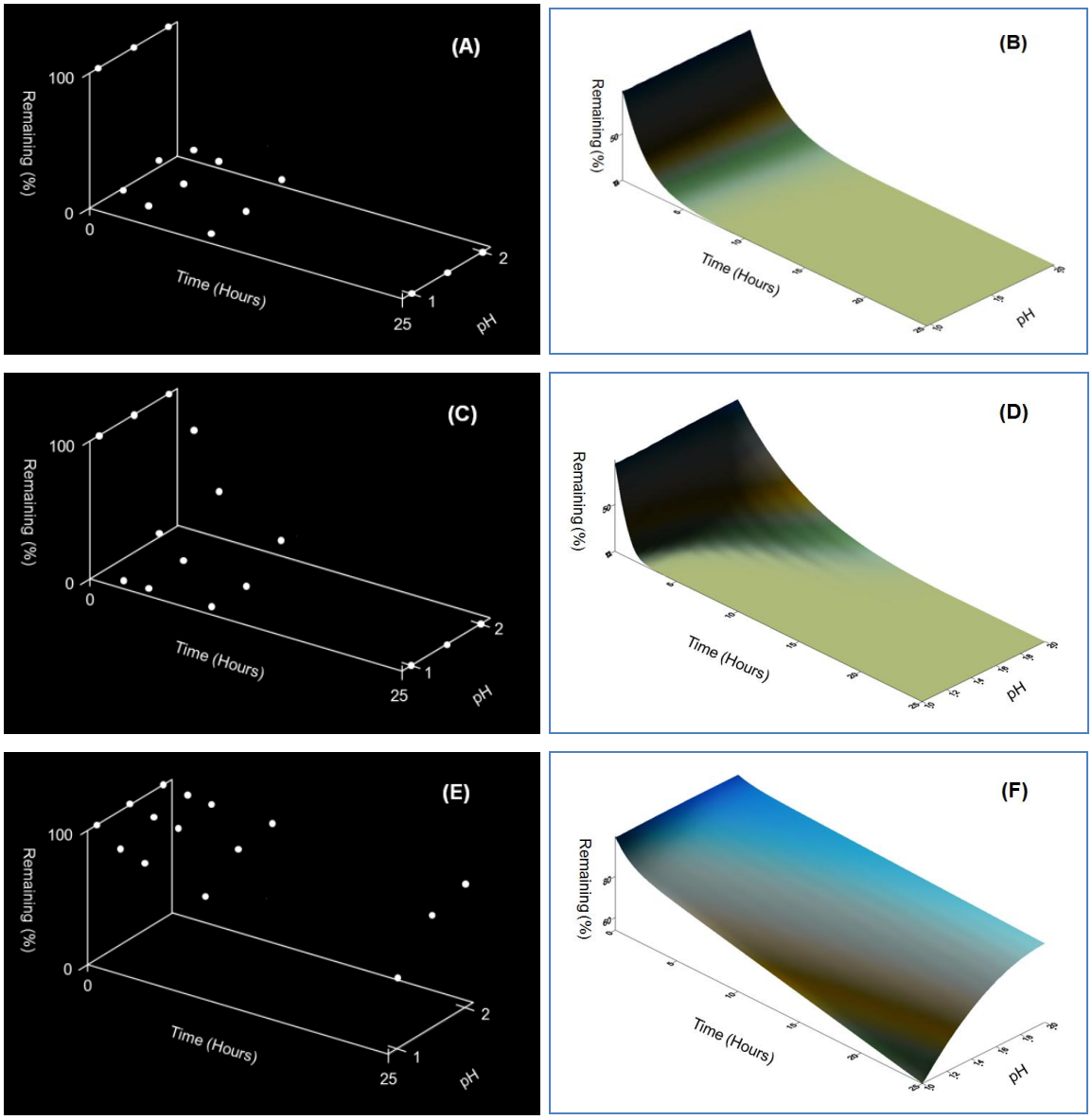

Figure 59: Plots showing the acid dissolution of selected minerals with percentage of the mineral remaining plotted as a function of pH and time. The plots to the left show the measured dissolution data. Those to the right show the modelled dissolution data. (A and B) Measured and modelled acid dissolution of calcite. (C and D) measured and modelled dissolution of laumontite. (E and F) Measured and modelled dissolution of chlorite. Both sets of plots have the same time and pH axes, but the measured data plots all have vertical axes from 0 to 100% while the modelled plots range from 100% to the lowest data point. For this reason, some of the modelled plots show more detail than the measured plots. In spite of this discrepancy, these plots show that the modelled dissolution data follows the measured data with a reasonable high degree of accuracy.

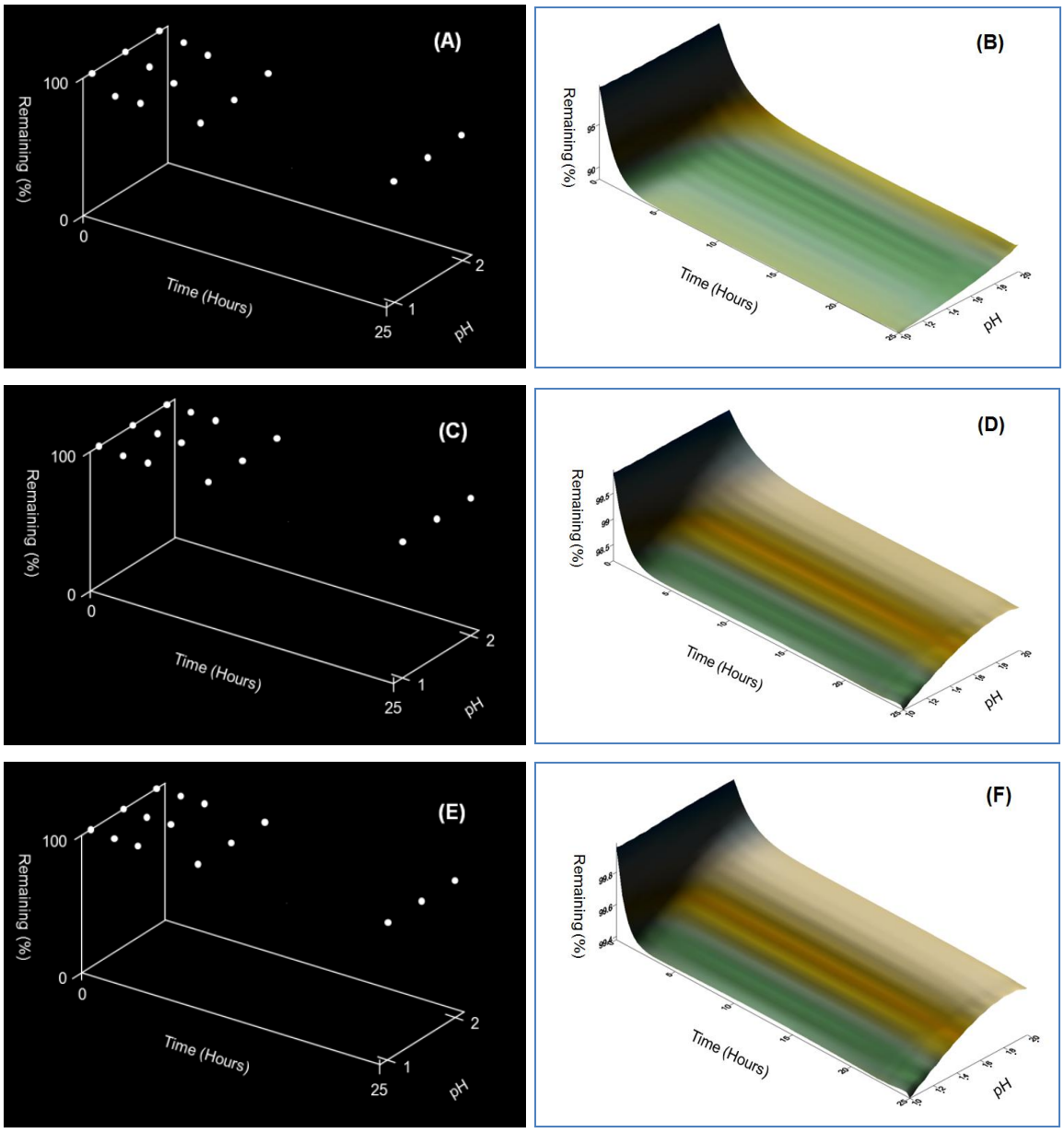

Figure 60: Plots showing the acid dissolution of selected minerals with percentage of the mineral remaining plotted as a function of pH and time. The plots to the left show the measured dissolution data. Those to the right show the modelled dissolution data. (A and B) Measured and modelled acid dissolution of muscovite. (C and D) measured and modelled dissolution of plagioclase. (E and F) Measured and modelled dissolution of K-feldspar. Both sets of plots have the same time and pH axes, but the measured data plots all have vertical axes from 0 to 100% while the modelled plots range from 100% to the lowest data point. For this reason, some of the modelled plots show more detail than the measured plots. In spite of this discrepancy, these plots show that the modelled dissolution data follows the measured data with a reasonable high degree of accuracy.

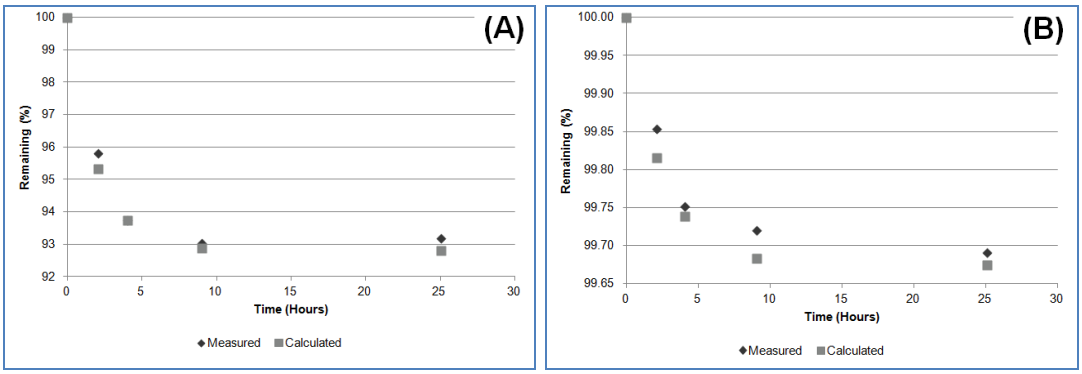

Figure 61: Measured and calculated acid dissolution data for smectite (A) and illite (B) at pH 1.5.

The gangue dissolution data, as well as the free acid calculations were used to model the acid consumption of each of the leach tests (Figure 62). The Eh control was maintained by addition of MnO_2, which is an important acid consumer. However, due to the slow dissolution of MnO_2, it was necessary to add small amounts and then monitor the changes in Eh over time. It was, therefore, not possible to add all of the necessary MnO_2 at the start of the leach. The model assumes that all MnO_2 was added after the hour of preconditioning and for this reason there is a discrepancy between the measured and calculated acid consumptions in the early stages of the leach (especially for Test E). Apart from the MnO_2 discrepancy, the calculated acid consumptions closely approximate the measured consumptions.

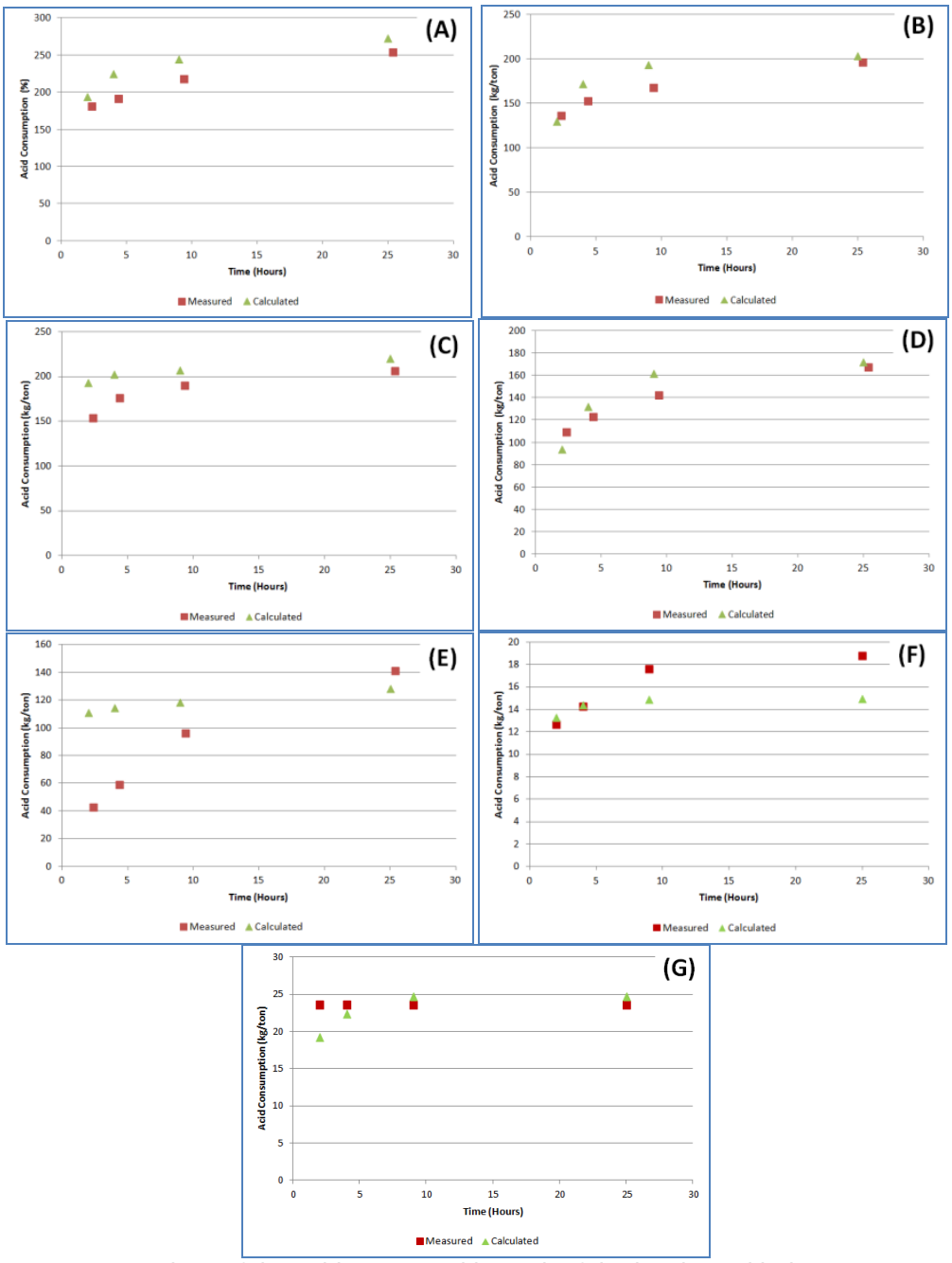

Figure 62: A comparison of the acid consumed in each of the leaches with the amount predicted by the model. Plots (A) to (G) represent leaches A to G respectively (see Table 54 for the conditions of each leach). In several of the plots, especially (E), there is a large discrepancy between the measured and calculated data in the early hours of the leach. This is because the model assumed all the MnO_2 was added at the first hour, while in the leach tests the MnO_2 was added progressively throughout the leach.

In order to assess the improvement in accuracy that was obtained by using the QEMSCAN textural data, the total acid consumptions predicted by XRD, with the textural data estimated from the grind (Chapter 4), was compared with the

refined predictions made using the QEMSCAN textural data, and with the measured acid consumptions. Both data sets compare well with the measured acid consumptions, except in the case of Test E where acid consumption predicted from the XRD data was much too low. The reason for this underestimation is that the published MnO_2 consumptions, (after Lottering *et al.*, 2008) used in the XRD calculations, were significantly lower than the measured MnO_2 consumptions. The use of Equation 60 (p 197) contributed to improving the accuracy of the predicted acid consumption from an error of ~79%, to an error of ~9%.

The mean error in the predictions of all the tests was ~23% for the XRD data. This was improved to an error of ~8% by use of Equation 60 and the QEMSCAN textural data.

Table 58: Measured acid consumptions compared with those predicted from the mineral abundances alone (XRD) and considering mineral abundances and texture (QEMSCAN)

-	H_2SO_4 (kg/ton)		
Test	**Measured**	**XRD**	**QEMSCAN**
A	254	229	272
B	196	200	203
C	168	174	172
D	207	227	221
E	141	29	128
F	19	18	15
G	24	36	25

7.3. Discussion and Conclusions

Development and Limitations of the Model

This chapter aimed to compare the predicted reagent consumption data with the measured data and then to refine the prediction method to allow for its application to other ores. In order to determine the reagent consumption characteristics of the various minerals, it was necessary to determine their rate of dissolution and the amount of acid consumed by each mineral during dissolution.

The rates of dissolution of the various gangue minerals were determined from the XRD and ICP-OES data. Where the ICP-OES data was used, the choice of element is significant. Incongruent dissolution occurs when the release rates of elements from a mineral are non-stoichiometric. If this is the case, and a rapidly released element is used to determine the dissolution rate, then the amount of acid consumed per unit time will be lower than in the case of ideal dissolution. If a slowly released element is used, then the acid consumption could be greater, per unit time, than would be expected in the ideal case. For this reason, adjustments were made to the acid consumption coefficients (Table 55).

The dissolution data was modelled using an exponential decay function. This function (Equation 58) contained three variables. These were the initial dissolution rate (R_0), the decay constant (λ) and the steady state dissolution rate (z), which was typically taken as zero.

It was found that the initial rate changed as a function of pH and parabolic functions were used to model the pH dependence of the initial rate. However, these parabolic functions only produce reliable results within the pH range of a normal U leach (pH 1 to 2), and the use of these functions outside of this range can result in errors.

It was also noticed that the rate of decay of the exponential function typically changed as a function of pH. At lower pH the decay was very rapid, while at higher pH the decay was more gradual. This was handled in the model by varying the decay constant as a parabolic function of pH, with lower values of λ at high pH and higher values at low pH. As with the initial rate calculation, the decay constant equation (Equation 62) only produces accurate results within the pH range of 1 to 2.

No published method was available to use in the prediction of the MnO_2 demand of the samples. This was a major limitation of the reagent consumption predicted by XRD. An equation (Equation 60) was developed to estimate the MnO_2 demand from the Fe^{2+} content of the ore and the desired Eh. The use of this equation significantly improved the accuracy of the predicted reagent consumption. However, Equation 60 relies on a number of assumptions:

1. The MnO_2 demand is not a function of the Fe^{2+} content of the ore, but rather the Fe^{2+} concentration of the leach solution. Therefore, for Equation 60 to produce reliable results, the Fe^{2+} dissolution characteristics must be similar to the samples in this study.
2. The rate of Fe^{2+} dissolution is a function of pH. In this study there was a relationship between the pH and Eh conditions, with higher MnO_2 used in leaches where more acid was added. The relationship, where lower pH correlates with higher Eh, is an implicit assumption in Equation 60.
3. The Eh is within the range used for typical U leaches (ie between 400 and 500 mV).

Even if these assumptions are satisfied, Equation 60 can still return negative MnO_2 demands. This will occur if ores with low Fe^{2+} contents are modelled at low Eh conditions. If Equation 60 returns a negative MnO_2 demand, then it is an indication that the leach will not require an oxidiser. However, if this is the case, it is also important to monitor the Fe content of the leach liquor as it is possible that

the Fe concentration will be too low to achieve U^{4+} oxidation (unless the ore contains high concentrations of Fe^{3+}).

Comparison of Predicted and Measured Reagent Consumption

Both the XRD (guided by the grind) and the refined model with QEMSCAN textural data, predicted the reagent consumption with reasonable accuracy. Without the textural data and a means of predicting the MnO_2 demand, the use of the XRD data alone resulted in an average error of ~23%. The addition of textural data, and development of a means of predicting MnO_2 demand, reduced the average error to only ~8%.

These results show that XRD data could be used in the prediction of reagent consumption (with a reasonable degree of accuracy), and that the major limitation is not the detection limit, but the lack of textural data.

The results of this study also show that although the dissolution characteristics of the various gangue minerals are complex, they are based on factors that can be measured chemically and mineralogically, and are therefore predictable. Because they are predictable, they can be modelled.

Chapter 8. Part I Conclusions

This study focused on improving the accuracy with which mineralogical data could be used to predict the process response of a U ore. There were two main aims:

1. Develop an equation that allowed for the use of XRD data to predict reagent consumption.
2. Contribute to understanding the relationship between ore-gangue associations and their effect on U dissolution.

Previous workers suggested that these aims could not be achieved, because the detection limit of conventional XRD was too high (Reynolds *et al.*, 2010) and the dissolution characteristics of most gangue minerals too complex to model (IAEA, 1980). These contentions were used to formulate the following hypothesis:

The limitations of conventional mineralogical techniques (Reynolds et al, 2010), and the complexity of the mineralogy (IAEA, 1980), are such that it is not possible to use XRD and QEMSCAN to accurately predict the metallurgical response of Southern African U ores.

In order to test this hypothesis, ore samples were secured from two Karoo-aged U occurrences. One sample (Mooi) was from the Mooifontein prospect within the main Karoo basin and the other three samples (RAO, OAO and MSO) were from the Kayelekera mine in Malawi.

These samples underwent petrographic examination, comminution and XRD analysis. Then, using published mineral dissolution data, the reagent consumption characteristics of each sample were predicted.

The petrographic investigation found that all of the samples (except MSO) are arkosic sandstones dominated by quartz with lesser plagioclase and minor K-feldspar. MSO was a mudstone dominated by illite and smectite.

During comminution it was found that the hardness of the arkosic samples was strongly controlled by the size of the detrital sand grains. If the selected grind was coarser than the sand grains, the rock milled rapidly. If the selected grind was finer than the sand grains, then milling was slow and energy intensive. This suggests that careful selection of a grind can significantly reduce the costs associated with comminution.

The XRD analyses indicated that calcite, laumontite and chlorite would be the main gangue acid consumers in Mooi, with chlorite and smectite in RAO, smectite in OAO and smectite and illite in MSO.

Based on the mineral quantities obtained by XRD (and supported by XRF) predictions were made as to the amount of reagent that would be required in the leaching of each sample.

In a sense the statement by the IAEA (1980) was partially true. The dissolution of the various gangue phases is indeed complex as it depends on pH, temperature and the specific surface area of the mineral (which is in turn a function of the mineral grain size and exposure characteristics). Dissolution calculations are further complicated by parabolic kinetics and incongruent dissolution. It was also necessary to develop a method to predict the free acid demand (the acid required to maintain the low pH needed for U dissolution). It was necessary to consider the hydrogen ion activity, the ionic strength, the formation of gypsum, of ion pairs in solution, the build-up of SO_4^{2-} in solution and its effect on the second acid dissociation of sulphuric acid.

On average the predictions made based on the XRD data were accurate to within 23%. The major limitation was not the detection limit of the XRD, but the lack of textural data and a method to predict the MnO_2 demand of the ore. It was however, found to be too complex to use a single equation to predict the reagent consumption, and it was necessary to develop an Excel-based model (which could consider the factors described above).

A method was developed to predict the MnO_2 demand from the Fe^{2+} content of the ore and the desired Eh. This equation (Equation 60) significantly improved the accuracy of the data. When taken in combination with gangue mineral surface area data, it was possible to improve the accuracy of the predictions, and reduce the average error to only ~8%.

These results show that, for Karoo-aged sedimentary ores, it is possible to predict reagent consumptions from XRD data, provided that major element XRF and Fe^{2+} concentrations are available. The accuracy of these predictions can be significantly improved by QEMSCAN textural data. This shows that although the dissolution of gangue minerals is complex, it is based on measurable parameters and can therefore be predicted and modelled. It was therefore possible to disprove the hypothesis stated above.

A comparison of the results of the leach tests and QEMSCAN data was used to understand the relationship between ore-gangue textures and the percentage U dissolution. It was found that provided the ore does not contain high concentrations of refractory U, the ore-gangue textures are the major control on total U dissolution. Under moderate conditions (pH ~1.5 and Eh ~450 mV) the amount of U dissolved is approximately equal to the amount of U occurring in grains with some degree of background exposure. Under very mild conditions (pH ~2 and Eh ~400 mV) the dissolution of U (within a 24 hour leach) will be slightly lower than the amount of exposed U (probably due to slow dissolution kinetics).

Under more aggressive conditions (pH ~1 and Eh ~500) at least some of the U locked in reactive gangue will be dissolved, and even some of the U in unreactive gangue may be recovered.

8.1. Key Findings

The following is a summary of the key findings of this study:

- Careful selection of the grind size can significantly reduce comminution costs.
- In addition to calcite, certain gangue minerals such as laumontite, chlorite and smectite are significant acid consumers.
- Reasonably accurate predictions of reagent consumptions (and by extension reagent costs) can be made based on quick, low cost XRD data.

Part II

Chapter 9. Application to Igneous Ores

9.1. Aims

In Part I of this study it was found that the dissolution characteristics of natural U-bearing material are too complex to allow reagent consumptions to be predicted by a single equation. A method was developed which made use of mineralogical data to model the reagent consumption characteristics of Karoo-aged U ores. This model considered both mineral dissolution kinetics and solution equilibrium chemistry.

The application of the model to XRD data showed that it is possible to use conventional XRD data to predict the acid consumption characteristics of an ore. However, the error was reasonably large (with a mean error of ~23%). This error resulted from the XRD being unable to provide textural data, rather than due to limitations in detection limit, as would be suggested by the data of Reynolds *et al.* (2010). In order to provide the necessary textural data, QEMSCAN analyses were used. These data made it possible to reduce the mean error from ~23% to ~8%.

While Part I of this study only considered sedimentary U ores, Part II will focus on another important southern African U ore type. The ores that will be tested will be igneous, in the form of Namibian leucogranites.

In Part I, the simple nature of the U mineral deportment meant that texture (mineral exposure) was the only important factor in controlling U dissolution.

Because certain of the granite-hosted ores of Namibia contain refractory U minerals (Kinnaird and Nex, 2007), these ores offer an opportunity to investigate the relationship between U mineral speciation and U dissolution.

The aims of the analyses of the igneous ores will be:

1. To better understand the mineralogical controls exerted by the various U minerals on the dissolution of U.
2. To determine if the current model (developed on sedimentary rocks) can be directly applied to igneous U deposits. If the current model cannot be applied to igneous U, then any limitations will be investigated and the model extended to allow for the consideration of igneous lithologies.

In order to achieve these aims, five composite samples were prepared. Two were collected from the Rössing SH area, two from the Rössing SJ area and one from the Valencia deposit. The regional geology of these deposits is discussed below.

9.2. Regional Geology of Namibian Igneous-hosted Uranium Deposits

Namibia is characterised by a large number of U occurrences. These range from anomalously high U concentrations in the basement rocks and Damara metasediments, to economic and sub-economic occurrences in sheeted leucogranites, Karoo-aged sediments and carnotite-bearing calcrete-hosted deposits (Kinnaird and Nex, 2007). Mineralised sheeted leucogranites occur at various locations within the Central Zone. These include Rössing, Valencia, Ida Dome and Goanikontes (Roesener and Schreuder, 1999).

The Damara Orogen represents the product of a Wilson Cycle (Kinnaird and Nex, 2007) and consists of Northern, Central and Southern Zones separated by distinct lineaments (Nex et al., 2001). The Omaruru Lineament occurs between

the Central and Northern Zones and the Okahandja Lineament occurs between the Central and Southern Zones (Jacob et al., 1986). Of the three zones, the Central Zone is of primary interest as it hosts all of the igneous U occurrences of economic importance, as well as several secondary U occurrences (Roesener and Schreuder, 1999).

The stratigraphy of the Central Zone is summarised in Table 59. Rocks of the Abbabis Complex form the basement to the Damara metasediments and consist of granite gneiss (Jacob et al., 1986). The Damara metasedimentary sequence is divided into the lower Nosib and upper Swakop Groups (Nex et al., 2001). The Nosib Group is dominated by quartzites and arkoses, with minor conglomerates, deposited during incipient rifting, while the calcareous and pelitic Swakop Group represents sediments deposited under deeper basin conditions (Kinnaird and Nex, 2007).

Table 59: Stratigraphy of the Damara Metasedimentary Sequence (After Jacob et al., 1986)

Group	Formation	Maximum Thickness (m)	Lithology
Swakop	Kuiseb	>3 000	Pelitic and Semi-pelitic Schist, Gneiss, Migmatite, Calc-silicate, Quartzite
	Karibib	1 000	Marble, Calc-silicate, Pelitic and Semi-pelitic Schist, Gneiss, Biotite Amphibole Schist, Quartz Schist, Migmatite
	Chuos	700	Diamictite, Calc-silicate, Pebbly Schist, Quartzite, Migmatite
	Rössing	200	Marble, Pelitic Schist, Gneiss, Biotite Amphibole Schist, Migmatite, Calc-silicate, Quartzite, Metaconglomerate
Nosib	Khan	1 100	Banded and Mottled Quartzofeldspathic Clinopyroxene Amphibole Gneiss, Migmatite, Pyroxene Garnet Gneiss, Amphibolite, Quartzite, Metaconglomerate
	Etusis	3 000	Quartzite, Metaconglomerate, Pelitic and Semi-pelitic Schist, Gneiss, Migmatite, Quartzofeldspathic Clinopyroxene Amphibole Gneiss, Calc-silicate, Metarhyolite
Unconformity			
Abbabis Complex			Granitic Gneiss, Augen Gneiss, Quartzofeldspathic Gneiss, Pelitic Schist, Gneiss, Migmatite, Quartzite, Marble, Calc-silicate, Amphibolite

Kinnaird and Nex (2007) and Nex et al. (2001) describe the Damara metasedimentary sequence as follows: The base of the Nosib Group is the Etusis formation. This formation was deposited unconformably on the Abbabis basement and typically consists of quartzites and arkoses. The Khan Formation overlies the Etusis Formation and consists of quartzofeldspathic gneiss (which also contain amphibole and pyroxene).

The base of the Swakop Group is the Rössing Formation which consists of marble, quartzite and schist. This is followed by the diamictites, and to a lesser extent, marbles and banded ironstones of the Chuos formation. These are overlain by the Karibib marbles and the Kuiseb pelitic schists.

The Central Zone has undergone medium to high grade metamorphism, characterised by high temperature (in excess of 650° C), and lower pressures (Jacob et al., 1986). These rocks have also undergone several phases of deformation and folding. The earliest deformational event resulted in isoclinal F1 folds, while the second event resulted in less intense F2 folds (Kinnaird and Nex, 2007). These are followed by intense F3 folding, which resulted in the widespread northeast structural grain seen in the Central Zone (Jacob et al., 1986).

This third deformational event is significant as it separates the unmineralised (pre F3) granites from the mineralised (post F3) granites (Kinnaird and Nex, 2007). Nex, et al. (2001), based largely on structural analysis and field relationships at Goanikontes, identified six granite types ranging from A through to F. The type A granites, which are the oldest, tend to be caught up in isoclinal F3 folding, are pink in colour and unmineralised. Type B is also unmineralised, is white in colour, variable in grain size and contains accessory minerals such as garnet, biotite and tourmaline. Type C is pale cream pink, contains clear quartz, accessory magnetite, ilmenite and tourmaline. This type is also unmineralised. Types A to C all predate the F3 event.

Types D to F postdate the F3 event, and of these types D and E are mineralised. Type D is a white, granular granite, with smoky quartz and a medium to coarse grain size. Type E is not as strongly mineralised as Type D, is variable in both colour and grain size and tends to contain oxidation halos. Type F is a red, coarse-grained to pegmatitic granite.

In addition to the control on mineralisation exerted by the F3 event, there appears to be a stratigraphic control on mineralisation, with mineralised granites frequently occurring at or near to the Khan-Rössing boundary (Kinnaird and Nex, 2007). Jacob et al. (1986) considered four factors which may have contributed to this structural control:

1. Structural trapping of the granite by the marble bands
2. Water saturation at the level of the Khan-Rössing boundary
3. Reducing effects resulting from the assimilation of phases such as sulphides and graphite
4. Uranium precipitation, due to boiling of the magma, triggered by contact with the marble of the Rössing Formation

Nex and Kinnaird (2007), based on the results of fluid inclusion studies, considered the release of methane from the Khan formation and carbon dioxide from the Rössing formation to be significant. The release of methane is thought to have contributed to changes in redox potential, while the carbon dioxide triggered the magma boiling described in point 4 above.

9.3. Rössing

Three U occurrences (SH, SJ and SK) are present in the Rössing area (Kinnaird and Nex, 2007). However, only the SH and SJ areas (Figure 63) will be

considered in this study. The main Rössing pit is located in the SJ area, ~70 km northeast of Swakopmund (Roesener and Schreuder, 1999) and is the only producing granite-hosted U deposit in the world (Basson and Greenway, 2004). The pit is 3 km long, 0.5 km wide and 0.35 km deep (Kinnaird and Nex, 2007).

The granite intrusions at Rössing are emplaced into the metasediments of the Khan and Rössing formations (Roesener and Schreuder, 1999). Here the Khan Formation consists of gneisses, while the Rössing Formation is more variable and consists of impure marble (which contains significant amounts of serpentine with minor olivine, diopside and scapolite), coarse graphite-bearing marble and schist (Berning, 1986).

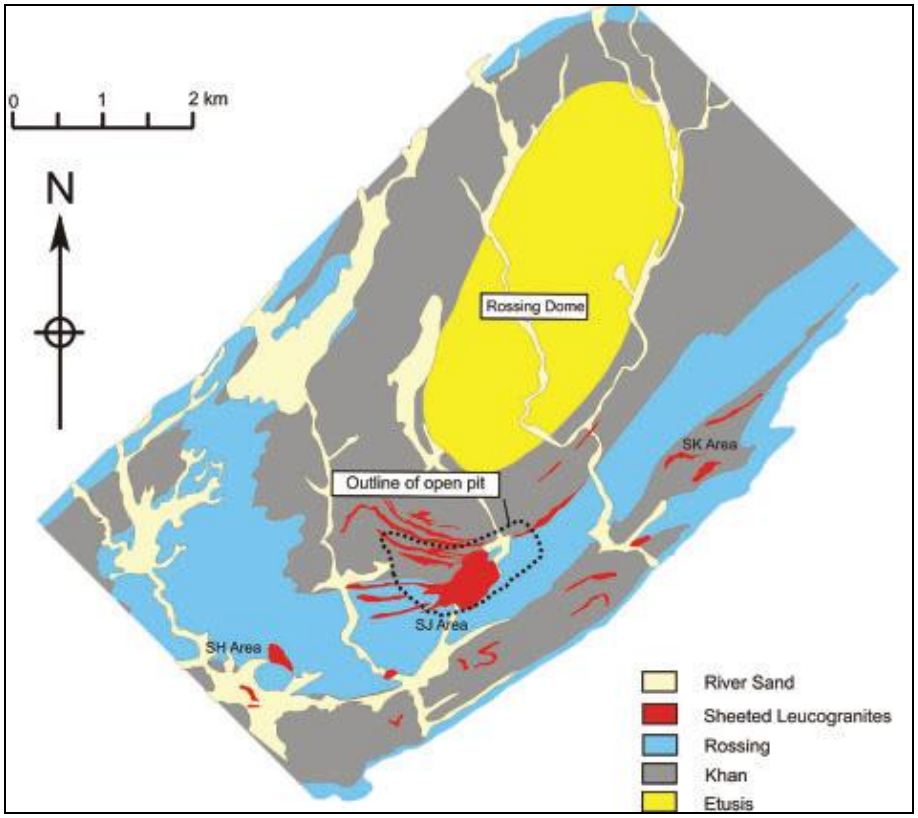

Figure 63: Simplified geological map showing the positioning of the SH, SJ and SK areas at Rössing, as well as the Damaran sediments which host the mineralisation (Kinnaird and Nex, 2007, after Smith, 1965).

In the SJ area uraninite (UO_2) is the dominant primary U mineral and typically occurs as grains of between 50 and 100 µm in size, although grains as small as a few microns and as large as 300 µm are present (Berning, 1986 and Roesener and Schreuder, 1999). Uraninite is often associated with biotite and zircon (Berning, 1986). Thorium is present in the uraninite with a U:Th ratio of 13:1 and partial oxidation of the uraninite has occurred resulting in a U^{4+}:U^{6+} ratio of 2.46:1 (Berning, 1986).

In the SJ area betafite [$(U,Ca,Ce)(Ti,Fe)_2O_6$] hosts minor amounts of U and has a variable colour, ranging from brown to bright yellow (Berning, 1986 and Roesener and Schreuder, 1999).

Secondary U minerals are also present, and of these, beta-uranophane [$Ca(UO_2)Si_2O_7.6H_2O$] is the most abundant (Berning, 1986 and Roesener and Schreuder, 1999). These secondary minerals occur as direct replacement of primary grains, in fractures within the granite and as discrete grains (Berning, 1986).

The SH area occurs ~1.5 km to the southwest of the main Rössing pit (Roesener and Schreuder, 1999). It is a granite body with dimensions of 0.5 by 0.2 km (Kinnaird and Nex, 2007). The most significant difference between the SJ and SH areas is the minerals which host the U. In the SJ area uraninite hosts ~55% of the U, with ~40% in secondary minerals and less than 5% in betafite (Berning, 1986), while in the SH area betafite hosts approximately 90% of the U (Kinnaird and Nex, 2007). These betafite grains may reach 3 mm in size and are frequently surrounded by a thin alteration rim (Roesener and Schreuder, 1999). Secondary minerals are significantly less abundant in the SH area than in the SJ area. This is probably due to the higher fluid availability in the SJ area and the refractory nature of the U minerals in the SH area (Kinnaird and Nex, 2007).

Due to the refractory nature of betafite, the U hosted in this mineral cannot be recovered by the acid leach employed at Rössing (Kinnaird and Nex, 2007). This renders the mining and processing of SH material uneconomic. While the SJ material is mined economically, its mining is complicated by the mixture of barren country rock with mineralised granite, the variability in the size of the granite intrusions (ranging from narrow bodies to large masses), and the variability of the U grade within the granites (Berning, 1986).

Mining of the SJ material is not the only complexity in the beneficiation of Rössing ore. Johnson (1990) listed several difficulties in the extraction of the U. These included:

1. The hardness of the ore, which resulted in extensive wear during comminution
2. A shortage of soluble Fe in the ore, which prevented the oxidiser from acting on the U (this was overcome by adding Fe to the leach)
3. High acid consumptions if marble country rock contaminates the ore
4. A small proportion of refractory U

Due to these and other constrains Johnson (1999), records that U extraction at the plant does not typically exceed 86.9 to 90.6%.

9.4. Valencia

The Valencia deposit occurs ~75 km to the southeast of Usakos and, like Rössing, the U mineralisation is hosted in granite (Kinnaird and Nex, 2007).There is very little published literature describing Valencia deposit. The following description is based largely on the unpublished results of a field study conducted by the Author in 2007:

The Valencia granites are hosed within the metasedimentary rocks of the Rössing, Chuos, Karibib and Kuiseb Formations (Figure 64). The deposit has a general northeast-southwest trend with the youngest rocks exposed in the Southeast, and progressively older formations to the northwest. In the more eroded areas to the northwest (especially in dry river beds) rocks of the Abbabis Complex, Etusis and Khan Formations are exposed.

The Abbabis rocks consist of grey and pink granite-gneiss (some of which is porphyritic). These rocks typically have an uncalibrated scintillometer count rate of ~57 cps, however some of these rocks are anomalously mineralised, and count rates can reach 400 cps in portions of the deposit. The overlying Etusis rocks are represented by finely banded quartzite which contains abundant magnetite.

The Khan sediments consist mainly of metapelite and schist which in places are distinctly green in colour. This horizon is extensively folded and may show extensive partial melting. The Rössing marble is generally fine-grained (although calcite grains may reach 2 mm in size), white to light grey and may contain forsterite.

The Chuos Formation consists of schist and diamictite, while the Karibib Formation consists of white marble (often containing a thin shale horizon). The Kuiseb rocks are biotite schists which have been intensely folded.

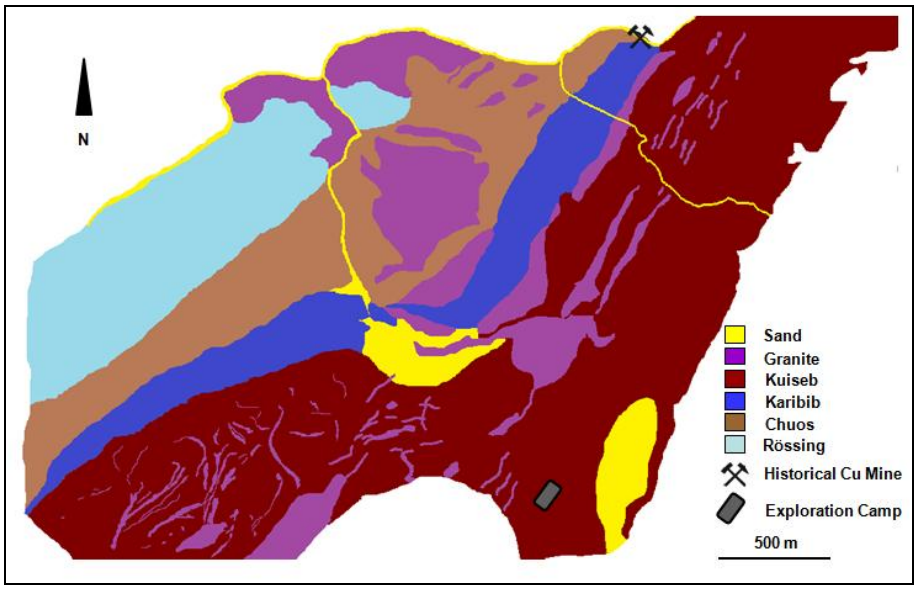

Figure 64: Simplified geological map showing the granites of the Valencia deposit and their metasedimentary host rocks.

Rocks corresponding to each of the granite types described by Nex, et al. (2001) at Goanikontes, are present at Valencia, and as with these described rocks, there is a tendency for the pre-D3 granites to contain low levels of U, while those following the D3 event are mineralised.

Type A granites are rare, pink in colour and intensely folded. Type B granites may also be folded, contain accessory garnet and tourmaline, with scintillometer counts between 52 and 71 cps. Type C granites have similar scintillometer count rates to the Type B granites and may contain accessory magnetite. Types D and E are post-D3, tend to be equigranular, contain smoky to black quartz and have the highest scintillometer count rates at the deposit. Accessory minerals, with the exception of biotite, are not common in these granites. Type F granites tend to be pink and are recognised by a tendency to crosscut earlier granite types.

As the post-D3 granites (types D and E) represent the mineralised lithologies, these rocks were of particular interest in Phase II of this study. This material, as well as samples from the SJ and SH areas at Rossing, were selected for mineralogical and metallurgical investigation.

Chapter 10. Mineralogical Characterisation

10.1. Introduction Aims and Objectives

Five samples were selected for further investigation. These were selected to prepresent typical ore from both Rössing and Valencia. Two samples were collected from each of the Rössing SH and SJ areas and one sample from Valencia. The Rössing samples were diamond borehole core, while the Valencia sample was a surface sample. Drill core would have been preferable (as the risk of weathering-related changes to the mineralogy of the rock is lower), but no core was available from Valencia. In order to reduce the risk of including weathered material, a large sample was taken, and only the core of the material was used.

The aim of the mineralogical analyses was to characterise each of the five samples with respect to those characteristics which would influence the beneficiation of the U. Of these characteristics, the following were of particular importance:

1. Chemical composition
2. Gangue mineralogy
3. Gangue mineral textures prior to milling
4. Comminution characteristics
5. Gangue mineral textures after milling
6. Uranium mineralogy
7. Uranium mineral textures after milling

10.2. Methodology

A combination of optical petrography, comminution, chemical analyses, XRD, QEMSCAN BMA, scanning electron microscopy and QEMSCAN TMS were used

to determine the mineralogical characteristics listed above. In as far as was practical, the methodologies have been kept the same as the analyses performed in Part I of this study. The reasons for selecting these methods and the specific conditions/parameters have been explained in Part I. A brief description of each method and any difference between the Part I methodology and that used in Part II is described below.

10.2.1. Optical Petrography

Polished thin sections were prepared from the samples from each of the SH, SJ and Valencia areas. These were examined by optical microscope to determine the mineralogy of the samples and their textural characteristics. No attempt was made to quantify mineral abundances because the coarse-grained nature of the rock would limit the representivity of the data (unless a very large number of thin sections were examined), and because this quantification would be obtained from the results of the XRD and BMA analyses.

10.2.2. Comminution

Five composites were prepared from the samples. The samples used to produce each composite, and their respective masses, are listed in Table 60.

In Part I of this study the samples were crushed using a two stage closed circuit process, starting with jaw crushing and followed by cone crushing. However, there was too little mass in each composite in Part II to allow for the same methodology to be applied. Therefore, each composite was jaw crushed; the +1.7 mm material was screened off the hand crushed, using a steel mortar and pestle, to 100% passing 1.7 mm and combine with the -1.7 mm material from the jaw crushing.

Table 60: Core samples, and associated masses, used to produce each composite

Sample Number	Mass (g)	Composite
SH06D12-159.29	1750.38	SH1
SH06D12-160.70	2041.10	
SH06D12-N7795	1431.86	
Total	**5223.34**	
SH06D14-234.23	1119.63	SH2
SH06D14-229.88	2091.71	
Total	**3211.34**	
44.6	431.99	SJ1
56.9	426.98	
69.6	455.67	
26911	471.65	
Total	**1786.29**	
103.35	844.11	SJ2
104.75	391.03	
100.5	550.30	
Total	**1785.44**	
Valg 03	**4060.00**	Val

In the Part I study an aliquot of the crushed material was screened into various size fractions to determine the particle size distribution. Each fraction was then assayed for a crude assessment of U mineral grain size and association characteristics (to aid in selecting a grind size for the milling). It was not possible to perform screen analysis on these samples due to the shortage of mass. In order to keep the results of the two parts of this study as comparable as possible, the same grind size (80% passing 212 µm) that was used in the Part I milling was used here.

The same methodology as described in Section 3.2 was used for the milling. However, while the mill casing and grinding media had the same specifications as the Phase I study, the motor had been upgraded, resulting in more rapid milling (when compared to that of Phase I). For this reason it was not possible to compare milling times between the Phase I and II samples.

10.2.3. Chemical Analyses

An aliquot of the material, milled to 80% passing 212 µm, was split off and pulverised for the chemical analyses. A portion of the pulverised material was used to prepare a borate fusion disk. This was analysed by XRF, with the fusion for major elements. A portion of this material was also analysed by ICP-MS for U and Th. This differs from the method used for the sedimentary samples in Part I, but was preferable because of the low masses of the igneous samples (as ICP-MS analyses require less than 1 g, while XRF pressed pellet analyses required 30 g).

Another portion of the pulverised material was analysed by Leco for total S and C and titration for FeO. The remaining pulverised material was used for the XRD analyses.

10.2.4. X-ray Diffraction and QEMSCAN Bulk Mineralogical Analyses

The pulverised material left over from the chemical analyses was miconised and analysed by XRD using a Panalytical X'pert Pro diffractometer, employing Co radiation. The resulting data were processed using HighScore Plus and the PanICSD database. In the Part I study Rietveld refinement was used to quantify mineral abundances, to facilitate a comparison between the performance of the XRD and QEMSCAN BMA. In this part of the study the two methods were used in conjunction with each other.

The BMA analyses were performed on two transverse polished sections per composite sample. These were carbon coated and analysed using a QEMSCAN based on a Carl Zeiss Evo 50. The instrument BSE was calibrated using a three point calibration with quartz, Cu and Au standards. The BSE standard intensities are quartz: 42, Cu: 130, and Au: 242. The X-ray detectors were calibrated using

the Cu Lα and Kα peaks, and the spectral engine was calibrated using the Cu and quartz standards. A line spacing of 150 µm and a point spacing of 2.5 µm were used.

In addition to the major mineral abundances, a limited amount of textural data was obtained for the more important minerals (either due to their abundance or reactivity). This textural data includes stereologically corrected mean grain sizes, mineral exposure and association data and an estimate of the geometric surface area of selected phases.

Where possible, the surface roughness of the minerals was also considered. This makes it possible to use the geometric surface areas to estimate a BET surface area (Helgeson *et al.*, 1984). These roughness factors were calculated from published grain size and BET surface area data. The grain sizes were used to calculate geometric surface areas and the roughness factors were then calculated by dividing the BET surface area by the geometric surface area according to Equation 30.

As the dominant minerals in the granite samples are similar to those in the sedimentary samples (described in Part I) these surface areas were calculated using the method described in Section 4.7 and Chapter 5. However, due to the high reactivity of several of the major and minor phases, it was not generally necessary to consider the dissolution of phases present in concentrations less than 1% during Part I of this study. This simplification was not possible for the granite samples. Phases such as Fe oxides and hydroxides, ilmenite, rutile and apatite which were present in the sedimentary samples were ignored in the Part I modelling, but have been considered in Part II because of the low reactivity of the phases that are present in higher concentrations. However, there was insufficient published BET surface area data for these minerals to calculate surface roughness factors, and therefore only geometric surface areas have been calculated.

Biotite was detected in the samples and unlike phases such as ilmenite and apatite, there was sufficient published BET and grain size data to calculate surface roughness factors. The calculation made use of the data of Malmstrom et al. (1996), and yielded Equation 64.

$$R_s = -0.0153\phi + 13.5$$

Equation 64

Where Rs is the surface roughness and Φ is the stereologically corrected mean diameter.

10.2.5. Scanning Electron Microscopy

The SEM petrography was performed on the same polished sections used for the BMA and TMS analyses. These were examined using the backscattered electron (BSE) and semi-quantitative energy dispersive spectrometry (EDS) capabilities built into the QEMSCAN. The purpose of the SEM petrography was to identify and describe the gangue and ore minerals to ensure that the QEMSCAN mineral identifications were accurate.

10.2.6. QEMSCAN Trace Mineral Search

The TMS analyses were performed on normal polished sections of each sample. The number of polished sections analysed depended on the U grade of the sample (as lower grade sample required more polished sections to reach an acceptable number of grains). Seven blocks were analysed from the SH1 sample, 9 from the SH2 and Val samples and 4 from the SJ1 and SJ2 samples.

A point spacing of 2.5 µm was used, with a field size of 1500 µm. The count limits were set at 1000 counts for the silicates, 3000 counts for the sulphides as well as the Fe and Ti oxides, and 5000 for the U minerals. The higher count limits were necessary for accurately distinguishing the U minerals, particularly beta-uranophane from coffinite (where the Ca is a critical distinguishing element).

10.3. Results

10.3.1. Optical Petrography

The samples are described in Table 61 to Table 65. These tables describe the mineral compositions, textural features and alteration characteristics of each sample. Particular emphasis has been placed on gangue phases (although descriptions of U minerals have been included, if these were observed in thin section).

Table 61: Petrographic description of sample SH1

Lithology: Fine- to Medium-grained Alkali Feldspar Granite
This composite consists of three core samples. All three are alkali feldspar granites. However, while samples D12-160.70 and D12-N7795 are fine- to medium-grained granites with a granular texture, D12-159.29 has undergone significant deformation, resulting in an L-tectonite. Sample D12-159.29 contains a cavity several centimetres in size and also contains a higher proportion of minor and trace minerals than do the other two samples. Chlorite represents an alteration product of biotite, and in many chlorite grains, significant amounts of the original biotite are preserved. Calcite occurs as disseminated grains, in fracture and within the cavity in D12-159.29. Pyrite was the only sulphide observed in thin section and tends to occur as disseminated grains and in a fracture in D12-159.29.
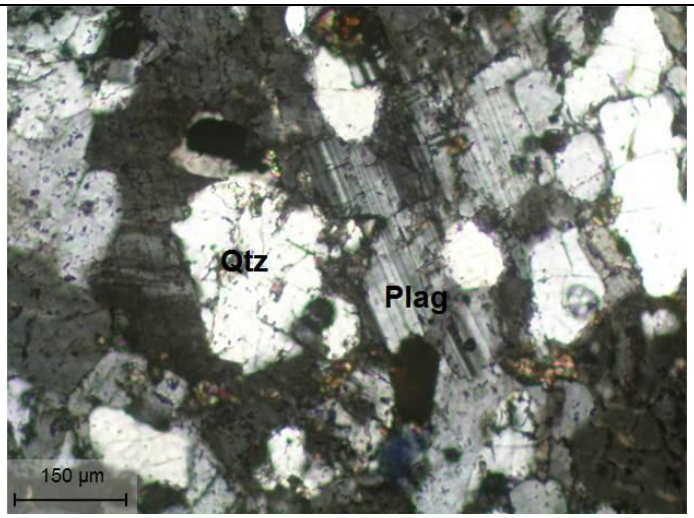 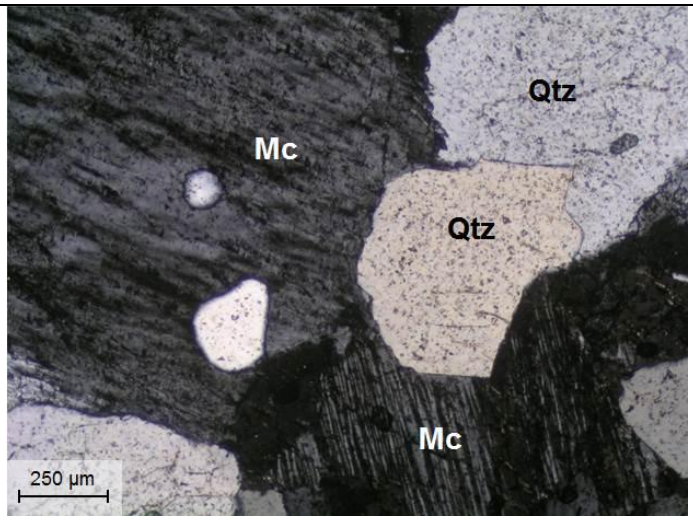
Plagioclase (Plag) and quartz (Qtz) in sample D12-159.29 taken perpendicular to the lineation (left). Microcline (Mc) and quartz (Qtz) in D12-160.70 (right).

Table 61 Cont.: Petrographic description of sample SH1

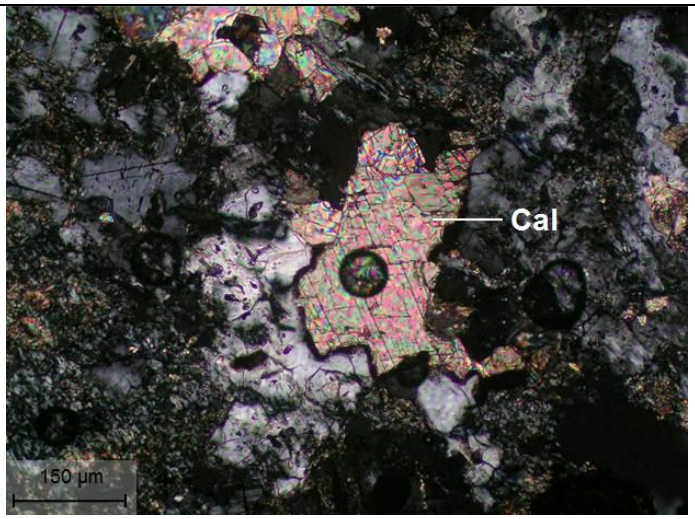

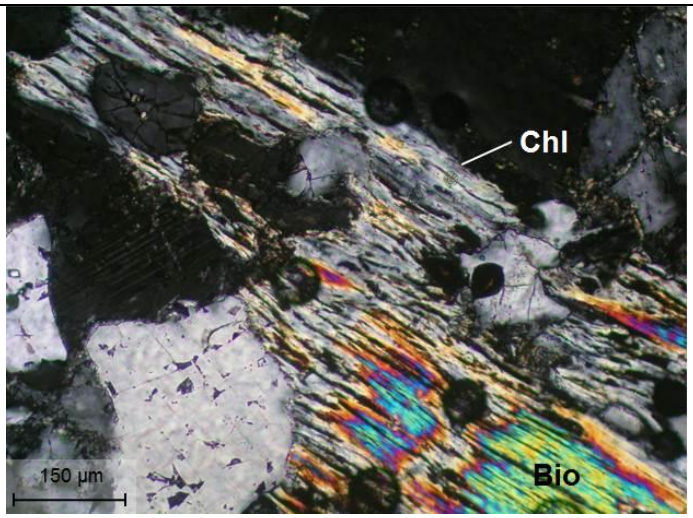

Disseminated calcite (Cal) (left). A biotite (Bio) grain showing partial alteration to chlorite (Chl) (right).

Mineral assemblage and approx. quantity		**Mineral description, alteration and mineralisation**	
Plagioclase (Albitic)	Major	*Between 0.5 and 6 mm in size. Most grains are equant anhedral, except in sample D12-159.29 where the grains are elongate.*	
Microcline	Major	*Between 0.3 and 5 mm in size. Most grains are equant anhedral, except in sample D12-159.29 where the grains are elongate.*	
Quartz	Major	*Dark grey in hand specimen. Grains are between 0.3 and 2 mm in size, except in sample D12-159.29 where the grains are up to 8 mm in size and tend to be elongate.*	
Chlorite	Minor	*Alteration product of biotite. Particularly abundant in sample D12-159.29. Individual grains may reach 3 mm in length.*	
Calcite	Minor	*Particularly abundant in sample D12-159.29 where calcite occurs in a several centimetre wide cavity, as disseminated grains within the granite and within fine fractures. The disseminated grains range from very fine to 0.37 mm in size.*	
Biotite	Minor	*Up to 3 mm grains, particularly in sample D12-159.29. These show significant alteration to chlorite.*	
Sericite	Tr	*Very fine alteration product of feldspars.*	
Pyrite	Tr	*Typically occurs as between 0.01 and 0.2 mm disseminated anhedral grains, however along a fracture in sample D12-159.29 the pyrite grains may reach 1.5 mm.*	
Alt/Met minerals:		*Chlorite, calcite and sericite.*	
Texture and structure:		*Samples D12-160.70 and D12-N7795 are fine- to medium-grained granites dominated by granular plagioclase, microcline and quartz. While sample D12-159.29 has a similar composition to the other two samples, it has undergone significant deformation and is an L-teconite.*	
Veining:		*Fine fractures filled with sericite and calcite.*	

Table 62: Petrographic description of sample SH2

Lithology: Alkali Feldspar Granite and Quartz-Feldspar-Biotite Schist
Two lithologies are present in this composite. The one is an alkali feldspar granite and the other is a quartz-feldspar-biotite schist. The granite consists of interlocking grains of plagioclase, quartz and microcline with trace amounts of biotite. Biotite is also present in the schist and it is the alignment of these biotite grains that forms the fabric of the schist. Minor amounts of chlorite are present and are the result of alteration of the biotite. While the feldspars are generally unaltered, a trace amount of sericite is present. Sericite also occurs in fine fractures (as does calcite). Hematite was the only oxide phase observed and occurs mainly in the schist as anhedral grains.
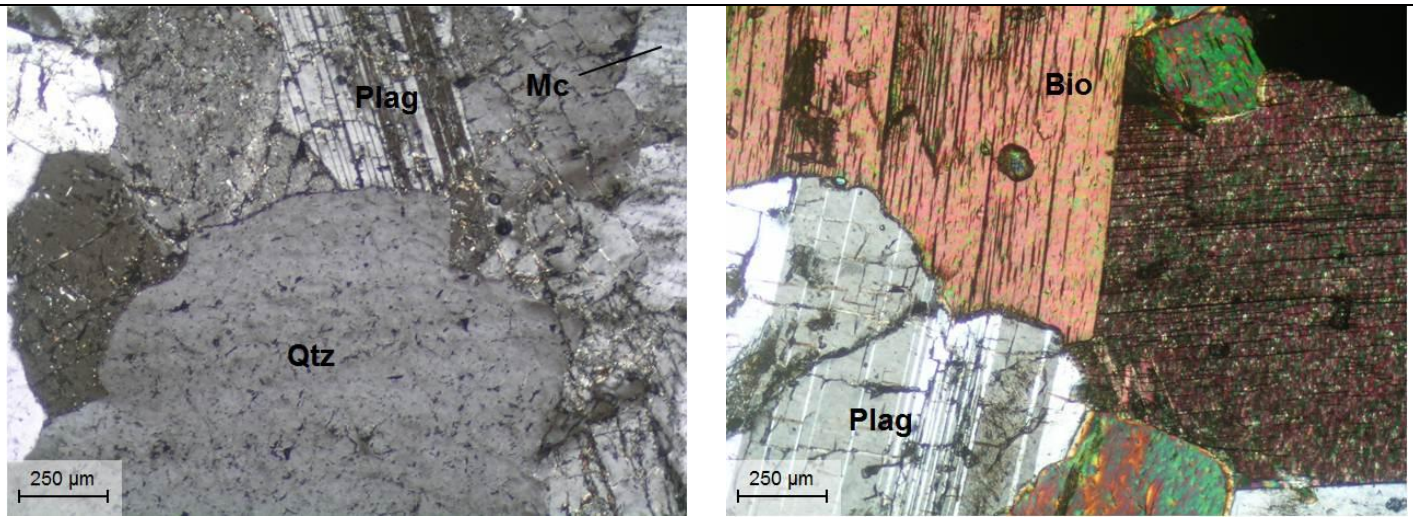 *Plagioclase (Plag), quartz (Qtz) and microcline (Mc) in the granite (left). Plagioclase (Plag) and biotite (bio) grains in the schist (right).*
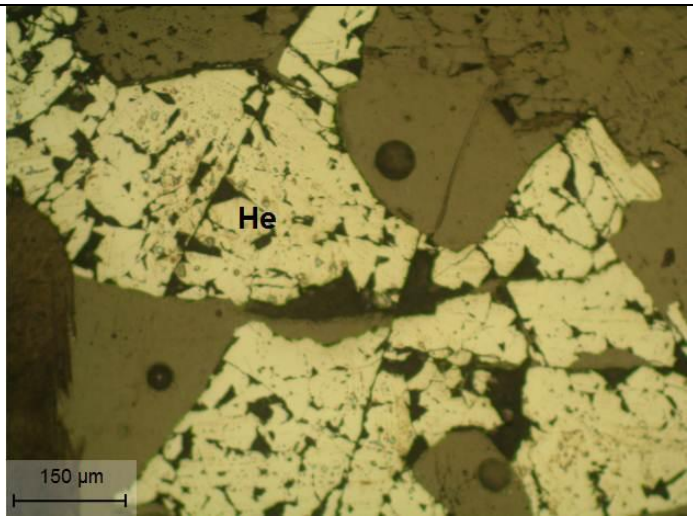 *Hematite (He) grains in the schist (1391 10x).*

Table 62 Cont.: Petrographic description of sample SH2

Mineral assemblage and approx. quantity		Mineral description, alteration and mineralisation	
Plagioclase	Major	*Occurs as equant anhedral grains both in the granite and in the schist and range from 1 to 12 mm in size.*	
Quartz	Major	*Occurs both in the granite and the schist. Grains are anhedral and range from 1 to 11 mm in size. In hand specimen quartz grains are light grey to black.*	
Microcline	Major	*Equant anhedral grains both in the schist and granite. These range from 2 to 20 mm in size.*	
Biotite	Major	*Occurs mainly in the schist. Most grains are 1 mm in size, but may reach 11 mm in length. The alignment of these grains defines the fabric in the schist.*	
Chlorite	Minor	*Alteration product of biotite.*	
Hematite	Trace	*Most common in the schist and occurs mainly as 0.2 to 1.2 mm anhedral grains.*	
Sericite	Trace	*Very fine alteration product of feldspar.*	
Calcite	Trace	*Very fine material occurring in fractures.*	
Zircon	Trace	*Typically 0.08 mm grains, mainly in the granite.*	
Alt/Met minerals:		*Chlorite and sericite.*	
Texture and structure:		*The granite has a granular texture consisting of medium to coarse interlocking grains of plagioclase, quartz and microcline. The schist contains a fabric defined by the alignment of biotite grains. The thin section shown to the right was taken in the incorrect orientation to show the fabric.*	
Veining:		*Fine fractures filled with sericite and calcite.*	

Table 63: Petrographic description of sample SJ1

Lithology: Biotite-bearing Alkali Feldspar Granite
The rock has a granular texture formed by interlocking grains of microcline, quartz and plagioclase. Myrmekitic intergrowths were also observed, however these were rare. Biotite is present in minor amounts. The rock is relatively unaltered, but some feldspars show minor alteration to sericite and less commonly calcite. Calcite also occurs in fine fractures. Sulphides are rare and disseminated. Pyrite and chalcopyrite are the most abundant of the sulphides with chalcocite and covellite seen as alteration on the periphery of some chalcopyrite grains. Uraninite is the dominant U mineral and occurs as euhedral grains which may be coarser than 0.5 mm in size. Where these occur in biotite, the biotite grains show a rim of alteration around the uraninite. In addition to the uraninite, the rock contains rare betafite grains. These tend to have a rounded appearance and have a limonite rim. Limonite is also present as earthy masses, independent of betafite. These may be the result of oxidation of sulphides.
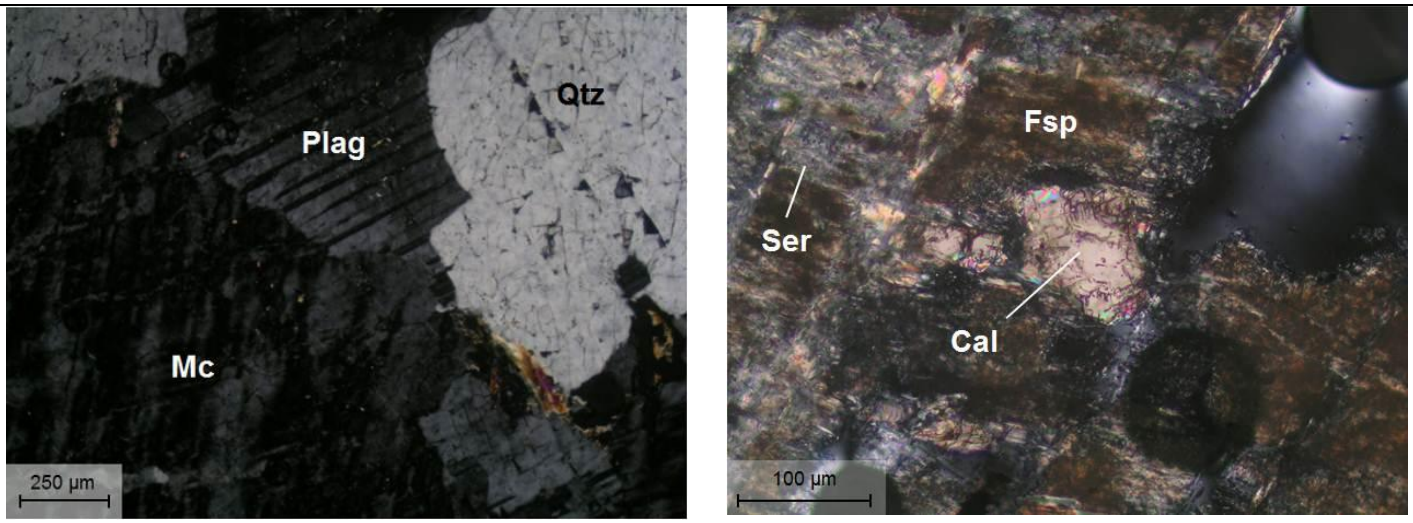 *Microcline (Mc), quartz (Qtz) and plagioclase (Plag) dominate the sample (left). Calcite (Cal) occurring with sericite (Ser) in an altered feldspar (Fsp) grain (right).*
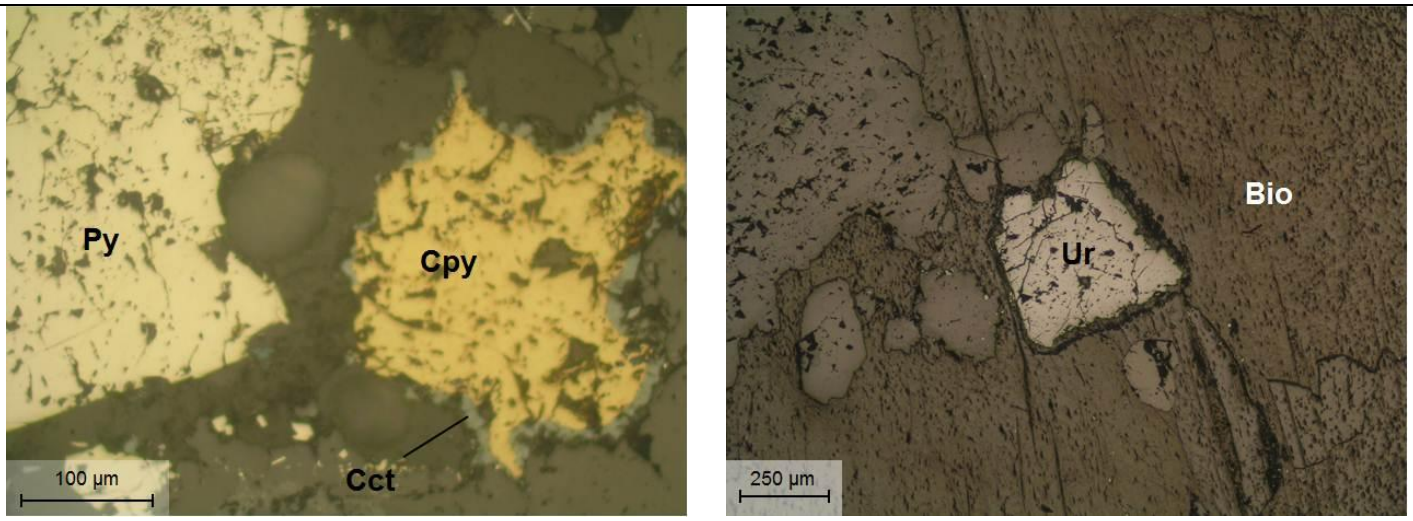 *Pyrite (Py) and chalcopyrite (Cpy) grains. The chalcopyrite has a rim of chalcocite (Cct) alteration (left). Uraninite (Ur) occurring in biotite (Bio). There is a rim of alteration in the biotite surrounding the uraninite grain (right).*

Table 63 Cont.: Petrographic description of sample SJ1

Mineral assemblage and approx. quantity		Mineral description, alteration and mineralisation	
Microcline	Major	*Between 3 and 20 mm grains which interlock with quartz and albite.*	 
Quartz	Major	*Dark grey to black in hand specimen, 2 to 18 mm grains interlocking with microcline and albite. Rare myrmekitic intergrowths with feldspars were also observed.*	
Plagioclase (Albitic)	Major	*Similar in size and to microcline.*	
Biotite	Minor	*Occurs as disseminated masses, typically between 1 and 3 mm in size, but may reach 12 mm.*	
Sericite	Trace	*Very fine alteration product of feldspars.*	
Calcite	Trace	*Typically fine-grained, but may reach 0.1 mm in size. Occurs in fine fractures and as an alteration product of feldspar grains.*	
Pyrite	Trace	*Anhedral to subhedral disseminated grains, averaging ~1 mm in size, but may reach 3 mm. Many pyrite grains are associated with chalcopyrite.*	
Uraninite	Trace	*Euhedral grains typically between 0.215 and 0.525 mm in size. Where these occur in biotite, there is a rim of altered biotite (about 0.03 mm wide) probably due to radiation attack of the biotite.*	
Chalcopyrite	Trace	*Very fine to 590 µm grains anhedral grains occurring as disseminated grains (with pyrite) and in fractures. Chalcopyrite is most abundant in a fracture zone.*	
Betafite	Trace	*Subrounded red-brown grains between 0.112 and 1.51 mm in size. These grains have a (up to 0.025 mm) rim of limonite; similar rims were described by Kinnaird and Nex (2007).*	
Zircon	Trace	*Typically 0.130 mm, zoned euhedral grains.*	
Limonite	Trace	*Approximately 1 mm patches of red massive earthy material and up to 0.025 mm rims around betafite grains. The earthy masses appear to be the result of sulphide oxidation.*	
Chalcocite	Trace	*Alteration along the periphery of chalcopyrite within a fracture zone.*	
Covellite	Trace	*Alteration along the periphery of chalcopyrite within a fracture zone.*	
Alt/Met minerals:		*Sericite, calcite, limonite, chalcocite and covellite.*	
Texture and structure:		*The rock is dominated by a granular texture formed by quartz and feldspar. Within a fine fracture zone, the quartz and feldspar grains have been fractured and granulated.*	
Veining:		*Anatomising healed fractures up to 0.1 mm wide. Fine fractures which contain calcite were also observed.*	

Table 64: Petrographic description of sample SJ2

Lithology: Ilmenite-magnetite-bearing Alkali Feldspar Granite
Plagioclase, quartz and microcline dominate the sample as interlocking grains showing a granular texture. Plagioclase and K-feldspar typically occur as discrete grains, however grains of perthite were observed, as were rare myrmekitic intergrowths between feldspars and quartz. Biotite occurs as up to 4 mm grains, however these have been extensively replaced by chlorite and only fine remnants of biotite remain within grains now dominated by chlorite. Although oxides are not particularly abundant in the composite as a whole, sample 104.75 contains large magnetite grains. These are anhedral to euhedral and may reach 7 mm in size. It appears that the rock has undergone oxidation after crystallisation, and many of the magnetite grains have been, at least partially, altered to hematite. Limonite staining is also particularly abundant in parts of sample 104.75, where it occurs in fractures. Calcite, although not abundant, was also observed in fractures.
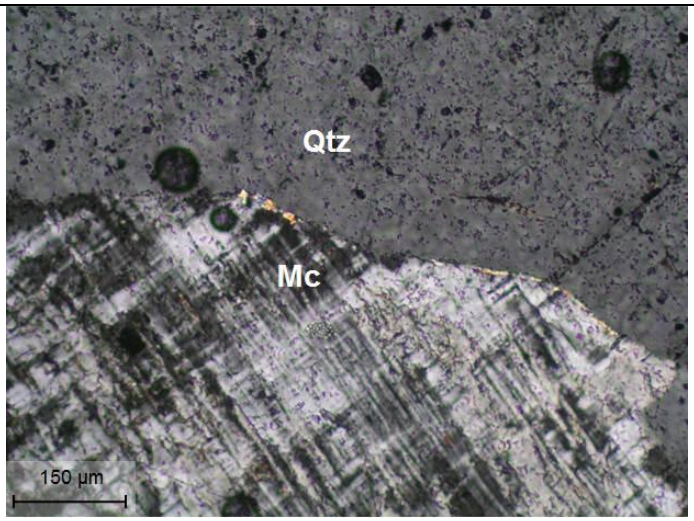 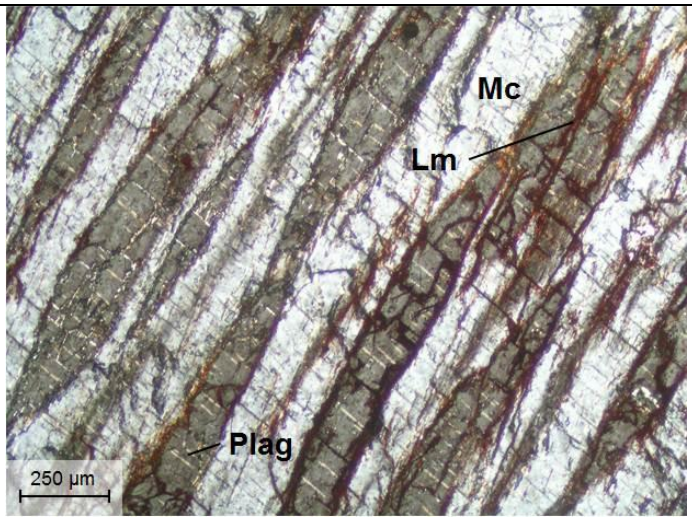
Quartz (Qtz) and microcline (Mc) (left). Perthite consisting of K-feldspar (Kfsp) and plagioclase (Plag). Limonite (Lm) occurs within fractures in the perthite (right).
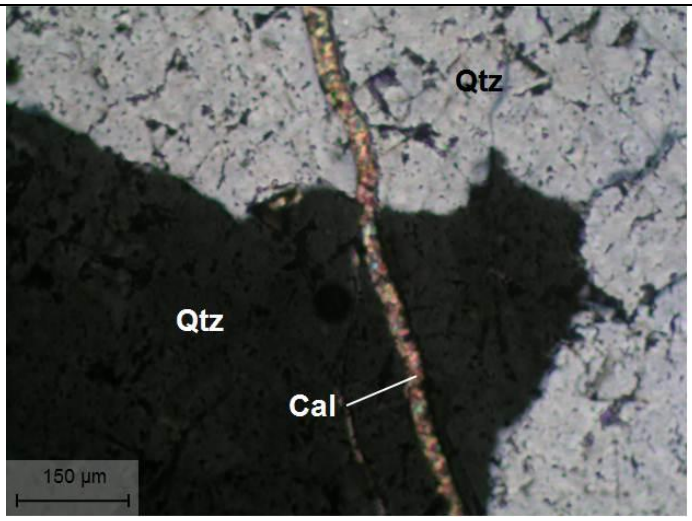 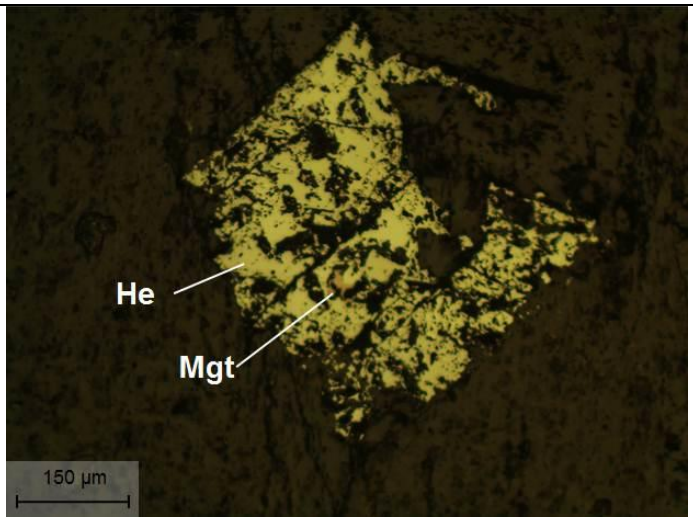
Calcite (Cal) filling a fracture in quartz (Qtz) (left). A hematite (He) grain which appears to contain remnants of original magnetite (Mgt) (right).

Table 64 Cont.: Petrographic description of sample SJ2

Mineral assemblage and approx. quantity		Mineral description, alteration and mineralisation	
Plagioclase (Albitic)	Major	*Anhedral grains interlocking with quartz and microcline. Grains are between 2 and 8 mm in size.*	
Quartz	Major	*Dark grey to black in hand specimen. Grains are between 1 and 13 mm in size (typically ~5 mm) and interlock with surrounding feldspar.*	
Microcline	Major	*Pink to white in hand specimen. Grains are anhedral and between 2 and 16 mm in size. Perthite was also observed.*	
Chlorite	Trace	*Occurs as a replacement of up to 4 mm biotite grains.*	
Biotite	Trace	*Grains were originally up to 4 mm in size, however these have been extensively altered to chlorite, and only small remnants of biotite remain within the chlorite.*	
Ilmenite	Trace	*Anhedral grains, typically 0.2 mm in size.*	
Hematite	Trace	*Oxidation product of magnetite.*	
Magnetite	Trace	*Not abundant in the composite as a whole, but parts of sample 104.75 contain anhedral to euhedral magnetite grains, which may reach 7 mm in size. Many of these grains show partial or complete oxidation to hematite.*	
Limonite	Trace	*Very fine grains occurring in fractures.*	
Calcite	Trace	*Rare fine grains occurring in fractures.*	
Sericite	Trace	*Very fine alteration product of feldspars.*	
Pyrite	Trace	*Disseminated euhedral grains, typically 0.01 mm in size.*	
Alt/Met minerals:		*Chlorite, hematite, limonite, sericite and calcite.*	
Texture and structure:		*The rock shows a granular texture formed by interlocking quartz and feldspar.*	
Veining:		*Up to 0.15 mm wide fractures filled with sericite, calcite and limonite.*	

Table 65: Petrographic description of sample Val

Lithology: Coarse-grained, Biotite-bearing Alkali Feldspar Granite
The rock is dominated by granular microcline and quartz, with lesser amounts of plagioclase. Biotite is present in minor amounts, but has been substantially altered to chlorite. Limonite occurs in masses and within fine fractures. Calcite also tends to occur in fine fractures, or in association with biotite (where it occurs between the cleavage planes). A mass of yellow earthy material observed in hand specimen appears to be beta-uranophane.
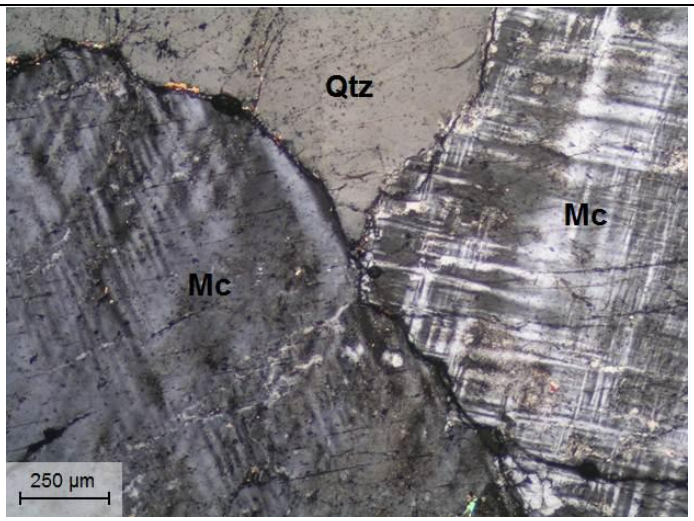 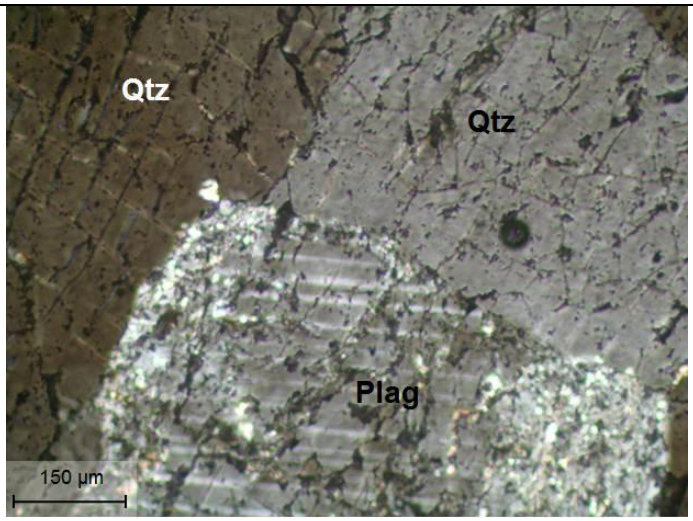
Quartz (Qtz) and microcline (Mc) grains (left). Plagioclase (Plag) occurring with quartz (Qtz) (right).
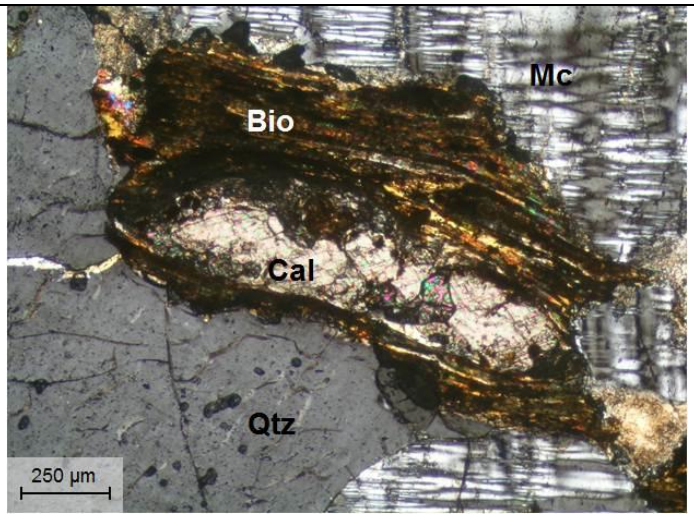 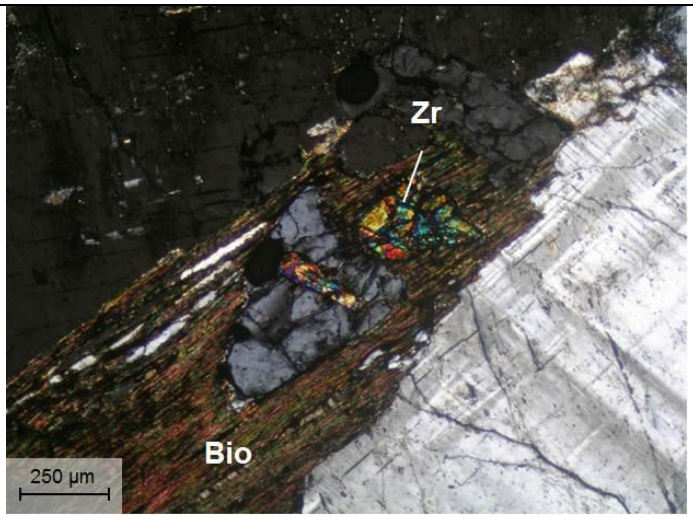
Calcite (Cal) within a partially altered biotite (Bio) grain, surrounded by quartz (Qtz) and microcline (Mc) (left). Zircon (Zr) grains enclosed within biotite (Bio) (right).

Table 65 Cont.: Petrographic description of sample Val

Mineral assemblage and approx. quantity		**Mineral description, alteration and mineralisation**	
Microcline	Major	*Anhedral grains 2 to 18 mm in size, interlocking with quartz grains.*	
Quartz	Major	*Dark grey to black in hand specimen. Grains range from 3 to 22 mm in size.*	
Plagioclase	Minor	*Anhedral grains between 1 and 16 mm in size.*	
Chlorite	Trace	*Alteration product of biotite.*	
Biotite	Trace	*Disseminated grains and masses between 1.2 and 10 mm in length.*	
Limonite	Trace	*Masses of limonite occur throughout the sample. Also occurs in fine fractures.*	
Calcite	Trace	*Occurs mainly within fine fractures. However, calcite may also be associated with biotite and these grains tend to be significantly coarser (and may reach 1.2 mm in size).*	
Sericite	Trace	*Very fine alteration product of feldspars.*	
Beta-uranophane	Trace	*A mass of ~2 mm in size consisting of yellow earthy material.*	
Zircon	Trace	*Zoned grains, typically 0.2 mm in size.*	
Alt/Met minerals:		*Chlorite, limonite, calcite and sericite.*	
Texture and structure:		*Coarse-grained granular texture formed by interlocking grains of microcline, quartz and to a lesser degree, plagioclase.*	
Veining:		*Fine fractures filled with limonite, calcite and sericite.*	

10.3.2. Comminution

The results of the 212 µm milling tests are presented in Table 66 to Table 68 and represented graphically in Figure 65. The shapes of the milling curves for the granitic samples differ from those of the sedimentary sample 212 µm milling tests, described in Section 3.3. While the sedimentary samples showed an initially high milling rate which slowed as the tests progressed (Figure 10), the granitic samples showed linear milling curves, similar to the curve seen in -75 µm milling test conducted on the Mooi sample (Figure 11).

Although they milled at slightly different rates, all of the five samples have very similar milling characteristics. However, the biotite in SH2 was particularly resistant to milling. In order to determine the progress of the milling, the samples were screened at 212 µm, after each milling interval in Table 66 to Table 68. There was a progressive upgrade in the biotite content of the +212 µm fraction of the SH2 sample, to the point where after the final milling interval the +212 µm fraction contained very high levels of biotite.

Table 66: Milling curve data for the Rössing SH samples, showing the proportion of the samples milled to passing 212 µm at various time intervals (the value in bold at the bottom of the table is the calculated milling time to reach the desired grind size)

SH1		SH2	
Time (min)	**Passing 212 µm (%)**	**Time (min)**	**Passing 212 µm (%)**
0.00	22.80	0.00	22.00
2.00	39.72	2.00	34.63
5.00	65.33	5.00	57.62
6.72	80.37	8.00	76.41
6.69	**80.00**	**8.44**	**80.00**

Table 67: Milling curve data for the Rössing SJ samples, showing the proportion of the samples milled to passing 212 µm at various time intervals (the value in bold at the bottom of the table is the calculated milling time to reach the desired grind size)

SJ1		SJ2	
Time (min)	**Passing 212 µm (%)**	**Time (min)**	**Passing 212 µm (%)**
0.00	22.80	0.00	20.22
2.00	33.61	2.00	38.72
5.00	55.64	5.00	69.66
8.00	85.10	-	-
7.68	**80.00**	**6.08**	**80.00**

Table 68: Milling curve data for the Valencia sample, showing the proportion of the samples milled to passing 212 µm at various time intervals (the value in bold at the bottom of the table is the calculated milling time to reach the desired grind size)

Val	
Time (min)	**Passing 212 µm (%)**
0.00	15.95
2.00	29.50
5.00	49.19
8.00	71.00
9.38	**80.00**

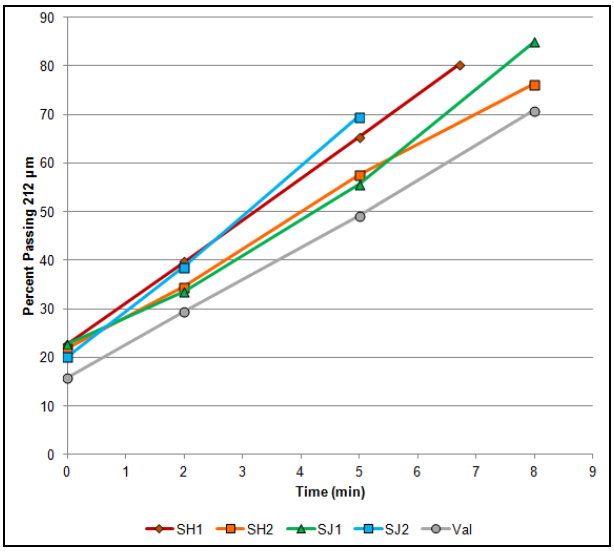

Figure 65: Milling curves showing the rate of change of particle size of each of the granite samples during milling.

Because the milling curves (Figure 65) show very little variation in rate as a function of time, it was possible to fit regression lines to the data. The slopes of the regression lines (Table 69) represent the average rate at which the samples milled. Based on these results sample SJ2 milled the fastest, while SH2 and Val milled the slowest.

Table 69: Gradient and Y intercept data for regression lines fitted to milling curves

Variable	Gradient	Y Intercept
Units	(% passing / min)	(Initial % passing)
SH1	8.564	22.687
SH2	6.900	21.782
SJ1	7.807	20.011
SJ2	9.923	19.714
Val	6.852	15.712

10.3.3. Chemical Analyses

The results of the major element XRF analyses are given in Table 70. As is typical of granites Si is the dominant element with lesser Al and minor amounts of K and Na. Calcium concentrations are low indicating that the samples do not contain high levels of calcic plagioclase.

The Leco data show that neither S nor C is present in high concentrations, with several samples containing less than 0.01% S and none of the samples containing more than 0.2% C. This indicates that sulphides and carbonates are not present in high concentrations.

Table 70: Major elements by XRF, total sulphur and carbon by Leco and FeO by titration

Sample	SH1	SH2	SJ1	SJ2	Val
Units	%	%	%	%	%
SiO_2	75.4	69.1	75.3	76.6	74.6
Al_2O_3	13.5	13.4	12.8	11.9	13.2
CaO	0.90	1.38	0.75	0.81	0.78
MgO	0.29	2.57	0.42	0.21	0.08
Fe_2O_3	0.93	2.32	1.03	2.77	0.63
K_2O	4.89	5.10	7.33	4.24	8.71
MnO	0.02	0.06	0.02	0.02	0.01
Na_2O	4.43	3.68	2.5	3.56	1.43
P_2O_5	0.08	0.07	0.24	0.08	0.23
TiO_2	0.13	0.36	0.08	0.35	0.05
Cr_2O_3	0.05	0.07	0.05	0.06	0.06
V_2O_5	<0.01	0.01	<0.01	<0.01	<0.01
LOI	0.57	0.98	0.31	0.29	0.21
Total	101.19	99.1	100.83	100.89	99.99
S	0.06	<0.01	0.04	<0.01	<0.01
C	0.11	0.16	0.06	0.04	0.07
FeO	0.53	1.18	0.74	0.88	0.51

Uranium concentrations are listed in Table 71. The Val and SH2 samples had the lowest U grades, with intermediate grades in SH1 and high grades in SJ1 and SJ2 samples.

Table 71: Uranium and thorium concentrations as determined by ICP-MS

Samples	SH 1	SH 2	SJ 1	SJ 2	Val
Units	ppm	ppm	ppm	ppm	ppm
U	453	287	2210	957	191
U_3O_8	534	338	2606	1129	225
Th	11.4	22.6	75.6	96.9	30.6
ThO_2	13.0	25.7	86.0	110.3	34.8

10.3.4. Quantitative Gangue Mineralogy

All 5 samples have very similar gangue mineral compositions. The dominant minerals are quartz, K-feldspar and plagioclase which make up more than 95% of most samples (the only exception is SH2 which contains ~11% biotite). Albitic plagioclase it the dominant mineral in all but samples SJ1 and Val (where K-feldspar is enriched at the expense of plagioclase). Quartz concentrations are fairly similar across the samples.

As was suggested by the results of the chemical analyses, carbonates are not abundant. Calcite was the only carbonate present, with SH2 containing the highest levels of calcite at only 0.94%. The high concentrations of quartz, plagioclase and K-feldspar, and generally low levels of phyllosilicates and carbonates indicate that gangue acid consumptions will be significantly lower in these samples, than in the sedimentary samples examined in Part I.

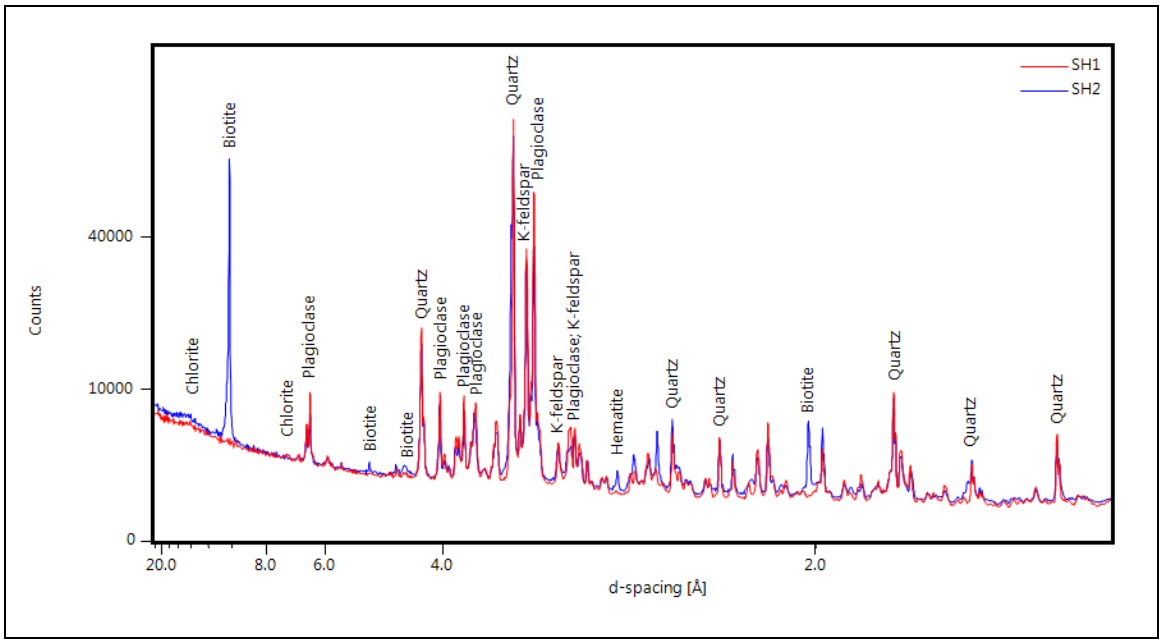

Figure 66: X-ray diffractograms of samples SH1 (red) and SH2 (blue), with certain peaks labelled to facilitate mineral identification. The major difference between the two samples is the significant amounts of biotite in the SH2 sample.

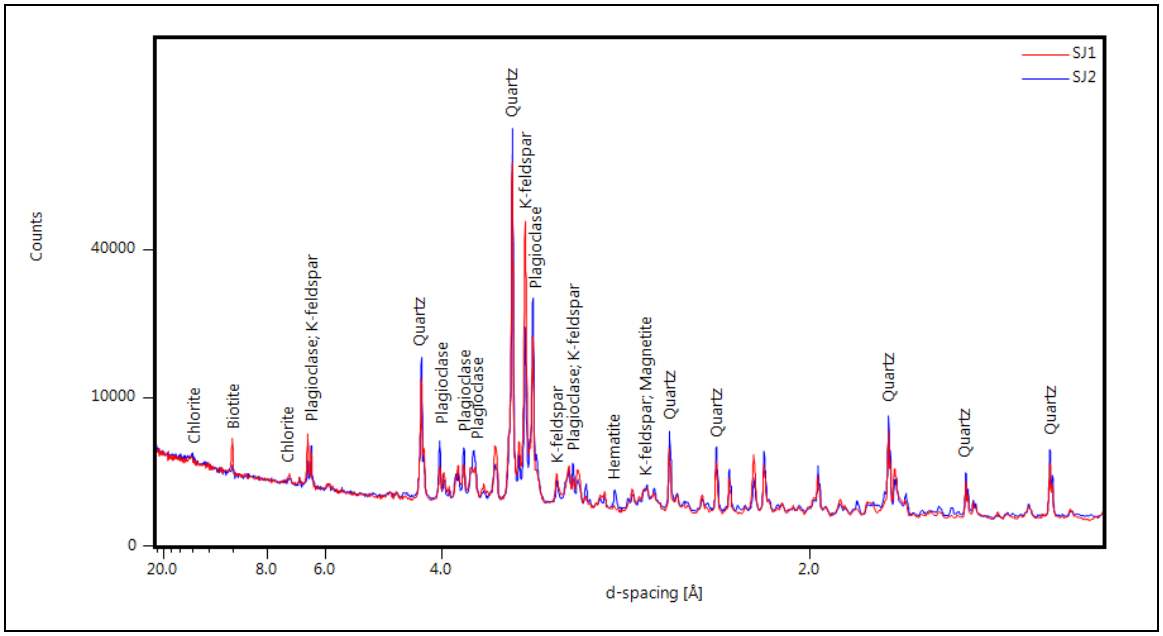

Figure 67: X-ray diffractograms of samples SJ1 (red) and SJ2 (blue). The compositions of these samples are very similar except that SJ1 contains more K-feldspar, while SJ2 contains more plagioclase.

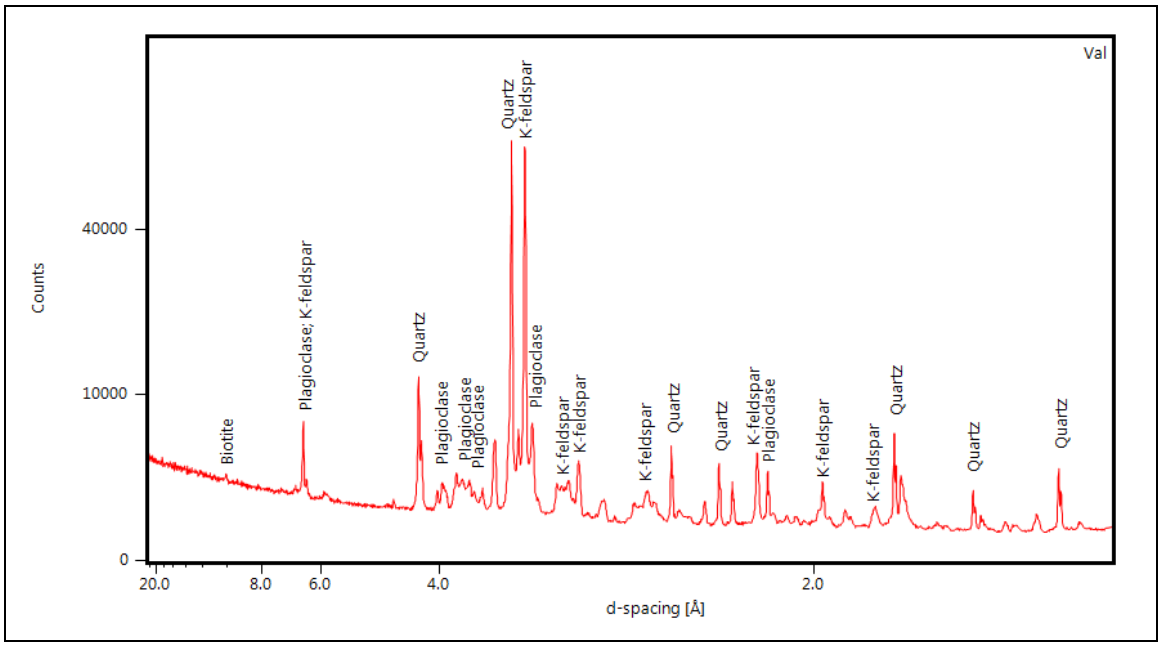

Figure 68: X-ray diffractogram of the Val sample showing a similar composition to SJ1 (Figure 67).

Table 72: Major mineral abundances as determined by QEMSCAN bulk mineralogical analysis

Name	**SH1**	**SH2**	**SJ1**	**SJ2**	**Val**
Units	**%**	**%**	**%**	**%**	**%**
Quartz	28.47	24.30	32.34	35.30	32.43
K-Feldspar	28.99	24.12	44.31	22.94	56.11
Plagioclase	39.78	37.77	18.97	37.93	9.58
Biotite	0.18	11.30	0.62	0.04	0.13
Chlorite	0.80	0.49	1.56	0.95	0.41
Zircon	0.04	0.03	0.09	0.03	0.13
Total Silicates	**98.26**	**98.02**	**97.88**	**97.18**	**98.79**
Fe-oxide/hydroxide	0.45	0.26	0.41	0.79	0.42
Ilmenite/Rutile	0.15	0.49	0.04	1.20	0.04
Total Oxide/Hydroxide	**0.60**	**0.75**	**0.44**	**1.99**	**0.46**
Monazite	0.00	0.00	0.01	0.00	0.00
Apatite	0.09	0.15	0.52	0.09	0.43
Calcite	0.55	0.94	0.48	0.08	0.26
Total Carbonate/Phosphate	**0.65**	**1.10**	**1.00**	**0.17**	**0.69**
Pyrite	0.30	0.00	0.17	0.01	0.00
Other Sulphides	0.01	0.03	0.07	0.02	0.02
Total Sulphide	**0.30**	**0.03**	**0.24**	**0.03**	**0.02**
Other	0.20	0.10	0.43	0.62	0.03
Total	**100.00**	**100.00**	**100.00**	**100.00**	**100.00**

The stereologically corrected mean grain sizes of the more important gangue minerals are presented in Table 73. These minerals were selected either because they are major constituents of the rock, or have the potential to react with sulphuric acid during U leaching.

Although present in reasonably low concentrations, apatite is the coarsest phase in samples SH2 and Val, while quartz is the coarsest phase in the remaining samples. The phyllosilicates are less than 25 µm in size.

Table 73: Stereologically corrected mean grain size data obtained from the results of the QEMSCAN BMA

Name	SH1	SH2	SJ1	SJ2	Val
Units	µm	µm	µm	µm	µm
Quartz	39.85	40.84	31.73	35.37	36.23
K-Feldspar	23.51	25.33	25.69	23.89	30.67
Plagioclase	19.84	25.28	15.50	22.97	14.67
Biotite	9.29	21.19	10.61	4.23	6.26
Chlorite	7.71	3.91	10.48	8.32	5.88
Fe-oxide/hydroxide	8.63	6.83	7.10	5.85	7.50
Ilmenite/Rutile	30.82	49.76	7.50	29.90	6.21
Apatite	25.08	63.48	27.42	15.47	36.61
Calcite	19.59	27.02	14.72	8.81	10.92

The exposure and association characteristics of selected gangue minerals are given in Table 74 to Table 78. These data represent the proportion of the surface of each phase of interest (listed in the top row of each table) in contact with each other phase (listed in the first column). Of particular importance in these tables is the background association, which represents the proportion of the surface of each mineral that would be in contact with the leach solution. Minerals with no background association, and a high degree of association with inert gangue, would not be expected to dissolve, even if these minerals are reactive.

Table 74: SH1 gangue mineral associations showing the average proportion of the surface of each mineral that is in contact with each other phase and the mounting resin (background)

Mineral	Quartz	K-Feldspar	Plagioclase	Biotite	Chlorite	Fe-oxide/hydroxide	Ilmenite/Rutile	Apatite	Calcite
Units	**%**	**%**	**%**	**%**	**%**	**%**	**%**	**%**	**%**
Background	82.39	62.08	61.88	36.99	44.77	63.61	41.46	70.00	71.16
Pyrite	0.00	0.01	0.00	0.00	0.07	0.28	0.00	0.00	0.00
Other sulphides	0.00	0.01	0.01	0.00	0.07	0.28	0.00	0.00	0.27
Quartz	0.00	1.74	4.47	0.91	5.34	5.00	0.00	0.00	0.54
K-Feldspar	3.49	0.00	30.72	32.42	9.24	6.11	4.88	5.00	3.50
Plagioclase	12.92	34.34	0.00	5.02	31.99	16.94	19.51	12.50	15.09
Biotite	0.01	0.40	0.06	0.00	3.47	0.00	0.00	0.00	0.00
Chlorite	0.87	0.97	2.28	23.74	0.00	7.78	24.39	0.00	8.89
Sphene	0.00	0.00	0.01	0.00	0.07	0.00	0.00	0.00	0.00
Zircon	0.02	0.00	0.01	0.00	0.00	0.00	0.00	10.00	0.00
Fe-oxide/hydroxide	0.28	0.11	0.30	0.46	2.45	0.00	0.00	0.00	0.27
Ilmenite/Rutile	0.00	0.02	0.04	0.46	0.58	0.00	0.00	0.00	0.00
Monazite	0.00	0.01	0.00	0.00	0.00	0.00	0.00	0.00	0.00
Apatite	0.00	0.02	0.00	0.00	0.00	0.00	0.00	0.00	0.00
Calcite	0.00	0.07	0.20	0.00	1.88	0.00	0.00	0.00	0.00
Uraninite	0.00	0.01	0.00	0.00	0.00	0.00	0.00	0.00	0.00
U-silicate	0.01	0.13	0.01	0.00	0.00	0.00	0.00	0.00	0.00
Beta-uranophane	0.01	0.02	0.02	0.00	0.00	0.00	0.00	0.00	0.00
Brannerite	0.00	0.03	0.00	0.00	0.00	0.00	4.88	0.00	0.00
Betafite	0.00	0.04	0.01	0.00	0.07	0.00	2.44	0.00	0.00
Other	0.00	0.00	0.01	0.00	0.00	0.00	2.44	2.50	0.27
Total	100.00	100.00	100.00	100.00	100.00	100.00	100.00	100.00	100.00

*The percentage of the surface of the mineral which is associated with background represents the proportion that would be in contact with the leach solution.

Table 75: SH2 gangue mineral associations showing the average proportion of the surface of each mineral that is in contact with each other phase and the mounting resin (background)

Mineral	Quartz	K-Feldspar	Plagioclase	Biotite	Chlorite	Fe-oxide/hydroxide	Ilmenite/Rutile	Apatite	Calcite
Units	**%**	**%**	**%**	**%**	**%**	**%**	**%**	**%**	**%**
Background	85.38	63.85	75.66	55.46	46.69	69.53	46.88	86.96	72.15
Pyrite	0.00	0.00	0.01	0.00	0.07	0.00	0.00	0.00	0.00
Galena	0.00	0.00	0.01	0.00	0.00	0.00	0.00	0.00	0.00
Other sulphides	0.00	0.00	0.00	0.00	0.07	0.86	7.81	0.00	2.78
Quartz	0.00	1.79	4.11	0.46	3.25	3.00	0.00	0.00	0.00
K-Feldspar	3.35	0.00	17.24	30.20	9.25	3.86	3.13	0.00	3.80
Plagioclase	10.03	19.28	0.00	3.61	7.87	9.44	3.13	4.35	11.90
Biotite	0.26	13.52	1.24	0.00	30.80	0.86	0.00	0.00	0.00
Chlorite	0.89	1.31	1.12	10.19	0.00	3.43	6.25	0.00	2.78
Sphene	0.00	0.00	0.01	0.00	0.00	0.00	3.13	0.00	1.01
Zircon	0.00	0.01	0.02	0.00	0.00	0.00	0.00	0.00	0.00
Fe-oxide/hydroxide	0.08	0.09	0.21	0.06	0.48	0.00	28.13	0.00	0.00
Ilmenite/Rutile	0.00	0.00	0.01	0.02	0.35	8.15	0.00	0.00	0.00
Apatite	0.00	0.01	0.00	0.00	0.00	0.00	0.00	0.00	0.25
Calcite	0.00	0.06	0.35	0.00	0.97	0.00	0.00	4.35	0.00
Uraninite	0.00	0.00	0.00	0.00	0.00	0.00	0.00	0.00	0.00
U-silicate	0.00	0.07	0.01	0.00	0.00	0.00	0.00	0.00	0.00
Beta-uranophane	0.00	0.03	0.00	0.00	0.00	0.00	0.00	0.00	0.25
Uranothorite	0.00	0.00	0.00	0.00	0.00	0.00	0.00	0.00	0.00
Other	0.00	0.00	0.02	0.00	0.21	0.86	1.56	4.35	5.06
Total	100.00	100.00	100.00	100.00	100.00	100.00	100.00	100.00	100.00

*The percentage of the surface of the mineral which is associated with background represents the proportion that would be in contact with the leach solution.

Table 76: SJ1 gangue mineral associations showing the average proportion of the surface of each mineral that is in contact with each other phase and the mounting resin (background)

Mineral	Quartz	K-Feldspar	Plagioclase	Biotite	Chlorite	Fe-oxide/hydroxide	Ilmenite/Rutile	Apatite	Calcite
Units	**%**	**%**	**%**	**%**	**%**	**%**	**%**	**%**	**%**
Background	90.98	81.07	62.97	50.71	67.91	82.32	30.00	91.03	76.11
Pyrite	0.02	0.02	0.02	0.00	0.00	0.00	0.00	0.00	0.00
Chalcopyrite	0.00	0.00	0.00	0.00	0.00	0.00	0.00	0.00	0.00
Other sulphides	0.00	0.01	0.02	0.00	0.11	3.05	0.00	0.00	0.56
Quartz	0.00	1.39	4.01	0.57	3.38	2.44	0.00	0.00	0.00
K-Feldspar	2.46	0.00	30.58	28.21	10.47	3.05	0.00	1.28	7.22
Plagioclase	5.44	15.22	0.00	2.28	8.78	6.71	10.00	1.28	5.56
Biotite	0.02	0.86	0.12	0.00	6.76	0.00	0.00	0.00	0.00
Chlorite	0.81	0.88	1.45	17.38	0.00	1.83	20.00	1.28	5.56
Sphene	0.00	0.00	0.12	0.00	1.13	0.00	40.00	0.00	1.11
Zircon	0.00	0.01	0.00	0.00	0.00	0.00	0.00	3.85	0.00
Fe-oxide/hydroxide	0.22	0.10	0.29	0.00	0.34	0.00	0.00	0.00	0.56
Ilmenite/Rutile	0.00	0.01	0.02	0.00	0.23	0.00	0.00	0.00	0.00
Monazite	0.00	0.00	0.00	0.00	0.00	0.00	0.00	0.00	0.00
Apatite	0.00	0.03	0.04	0.00	0.00	0.00	0.00	0.00	0.00
Calcite	0.00	0.11	0.33	0.00	0.79	0.00	0.00	1.28	0.00
Uraninite	0.00	0.03	0.00	0.00	0.00	0.00	0.00	0.00	0.00
U-silicate	0.04	0.18	0.00	0.28	0.11	0.00	0.00	0.00	0.00
Beta-uranophane	0.00	0.04	0.00	0.57	0.00	0.00	0.00	0.00	0.56
Brannerite	0.00	0.00	0.00	0.00	0.00	0.00	0.00	0.00	0.00
Betafite	0.00	0.01	0.00	0.00	0.00	0.00	0.00	0.00	0.00
Uranothorite	0.00	0.00	0.00	0.00	0.00	0.00	0.00	0.00	0.00
Other	0.00	0.03	0.02	0.00	0.00	0.61	0.00	0.00	2.78
Total	100.00	100.00	100.00	100.00	100.00	100.00	100.00	100.00	100.00

*The percentage of the surface of the mineral which is associated with background represents the proportion that would be in contact with the leach solution.

Table 77: SJ2 gangue mineral associations showing the average proportion of the surface of each mineral that is in contact with each other phase and the mounting resin (background)

Mineral	Quartz	K-Feldspar	Plagioclase	Biotite	Chlorite	Fe-oxide/hydroxide	Ilmenite/Rutile	Apatite	Calcite
Units	**%**	**%**	**%**	**%**	**%**	**%**	**%**	**%**	**%**
Background	86.23	76.41	76.31	40.74	45.28	59.36	65.28	73.33	66.67
Pyrite	0.00	0.00	0.03	0.00	0.00	0.00	0.00	0.00	0.00
Other sulphides	0.00	0.00	0.05	0.00	0.28	0.91	0.00	0.00	3.33
Quartz	0.00	2.91	5.12	0.00	2.22	5.94	0.00	0.00	3.33
K-Feldspar	3.71	0.00	14.95	25.93	10.56	6.39	2.78	6.67	3.33
Plagioclase	9.01	17.93	0.00	14.81	27.50	14.16	5.56	6.67	13.33
Biotite	0.00	0.38	0.08	0.00	1.11	0.00	0.00	0.00	0.00
Chlorite	0.43	1.47	2.68	18.52	0.00	7.76	6.94	0.00	10.00
Sphene	0.00	0.00	0.11	0.00	3.61	0.00	0.00	0.00	0.00
Zircon	0.00	0.00	0.00	0.00	0.00	0.00	0.00	6.67	0.00
Fe-oxide/hydroxide	0.43	0.45	0.50	0.00	7.50	0.00	16.67	0.00	0.00
Ilmenite/Rutile	0.00	0.13	0.03	0.00	1.11	5.02	0.00	0.00	0.00
Monazite	0.00	0.00	0.00	0.00	0.00	0.00	0.00	0.00	0.00
Apatite	0.00	0.00	0.03	0.00	0.00	0.00	0.00	0.00	0.00
Calcite	0.00	0.03	0.11	0.00	0.83	0.00	0.00	0.00	0.00
Uraninite	0.00	0.06	0.00	0.00	0.00	0.00	0.00	0.00	0.00
U-silicate	0.07	0.06	0.00	0.00	0.00	0.00	0.00	0.00	0.00
Beta-uranophane	0.11	0.16	0.03	0.00	0.00	0.00	0.00	0.00	0.00
Uranothorite	0.00	0.00	0.00	0.00	0.00	0.00	0.00	0.00	0.00
Other	0.00	0.00	0.00	0.00	0.00	0.46	2.78	6.67	0.00
Total	100.00	100.00	100.00	100.00	100.00	100.00	100.00	100.00	100.00

*The percentage of the surface of the mineral which is associated with background represents the proportion that would be in contact with the leach solution.

Table 78: Val gangue mineral associations showing the average proportion of the surface of each mineral that is in contact with each other phase and the mounting resin (background)

Mineral	Quartz	K-Feldspar	Plagioclase	Biotite	Chlorite	Fe-oxide/hydroxide	Ilmenite/Rutile	Apatite	Calcite
Units	**%**	**%**	**%**	**%**	**%**	**%**	**%**	**%**	**%**
Background	89.37	87.77	58.83	31.13	40.71	66.85	39.13	83.05	69.57
Pyrite	0.00	0.00	0.00	0.00	0.00	0.00	0.00	0.00	0.00
Other sulphides	0.00	0.03	0.00	0.00	0.00	0.56	0.00	0.00	0.72
Quartz	0.00	1.92	5.02	0.94	2.14	2.81	0.00	0.00	0.00
K-Feldspar	5.31	0.00	32.67	26.42	26.90	12.92	4.35	6.78	9.42
Plagioclase	4.84	8.66	0.00	14.15	16.19	9.55	0.00	1.69	9.42
Biotite	0.04	0.19	0.65	0.00	7.62	0.00	0.00	0.00	0.00
Chlorite	0.19	0.97	1.98	26.42	0.00	6.74	47.83	0.00	8.70
Sphene	0.00	0.00	0.00	0.00	0.00	0.00	4.35	0.00	0.00
Zircon	0.02	0.04	0.00	0.00	0.00	0.00	0.00	8.47	0.00
Fe-oxide/hydroxide	0.23	0.18	0.34	0.94	2.62	0.00	4.35	0.00	0.00
Ilmenite/Rutile	0.00	0.04	0.00	0.00	2.14	0.56	0.00	0.00	0.00
Apatite	0.00	0.03	0.00	0.00	0.24	0.00	0.00	0.00	0.72
Calcite	0.00	0.09	0.48	0.00	1.43	0.00	0.00	0.00	0.00
Uraninite	0.00	0.00	0.00	0.00	0.00	0.00	0.00	0.00	0.00
U-silicate	0.00	0.09	0.00	0.00	0.00	0.00	0.00	0.00	0.00
Beta-uranophane	0.00	0.02	0.00	0.00	0.00	0.00	0.00	0.00	0.00
Other	0.00	0.00	0.03	0.00	0.00	0.00	0.00	0.00	1.45
Total	100.00	100.00	100.00	100.00	100.00	100.00	100.00	100.00	100.00

*The percentage of the surface of the mineral which is associated with background represents the proportion that would be in contact with the leach solution.

The specific surface areas of selected minerals are given in Table 79. All of the specific surface (except those of Fe oxide/hydroxide, ilmenite/rutile and apatite) consider both the geometric surface areas and roughness factors. These surface areas are of importance as they influence the dissolution rate of the mineral (Brantley, 2008).

Table 79: Specific surface areas estimated from QEMSCAN BMA data

Name	**SH1**	**SH2**	**SJ1**	**SJ2**	**Val**
Units	**m^2/g**	**m^2/g**	**m^2/g**	**m^2/g**	**m^2/g**
K-Feldspar	0.86	0.82	0.86	0.89	0.68
Plagioclase	0.78	0.60	1.34	0.81	1.54
Biotite	4.73	4.28	4.59	7.95	5.21
Chlorite	1.44	2.81	1.78	1.55	1.34
Fe-oxide/hydroxide	0.08	0.11	0.15	0.12	0.09
Ilmenite/Rutile	0.03	0.02	0.14	0.03	0.14
Apatite	0.03	0.01	0.02	0.08	0.02
Calcite	0.20	0.18	0.34	0.46	0.42

10.3.5. Scanning Electron Microscopy

The manual SEM analysis serves as an independent check (in a qualitative sense) of the results of the QEMSCAN TMS. Although betafite typically hosts approximately 90% of the U in samples from the SH area (Kinnaird and Nex, 2007), the SH samples in this study contained significant proportions of non-refractory U minerals, and in sample SH2 betafite was very rare.

In sample SH1 betafite and beta-uranophane are the dominant U minerals. EDS analyses show that there is variation in the composition of the betafite as seen in changes in the relative abundance of Nb and Ti in the EDS spectra in Figure 69. There is also U enriched material developed on the side of the grain. In addition to the U enrichment, this material also contained no detectable Pb.

Uraninite was the dominant U mineral detected in sample SH2 (Figure 70). The uraninite contains minor amounts of Y and Pb. Uranium silicates, in the form of beta-uranophane and coffinite were also detected. The beta-uranophane grain shown in Figure 70 is enclosed in calcite. As calcite reacts with sulphuric acid, this grain would be leachable, even though it has no background association.

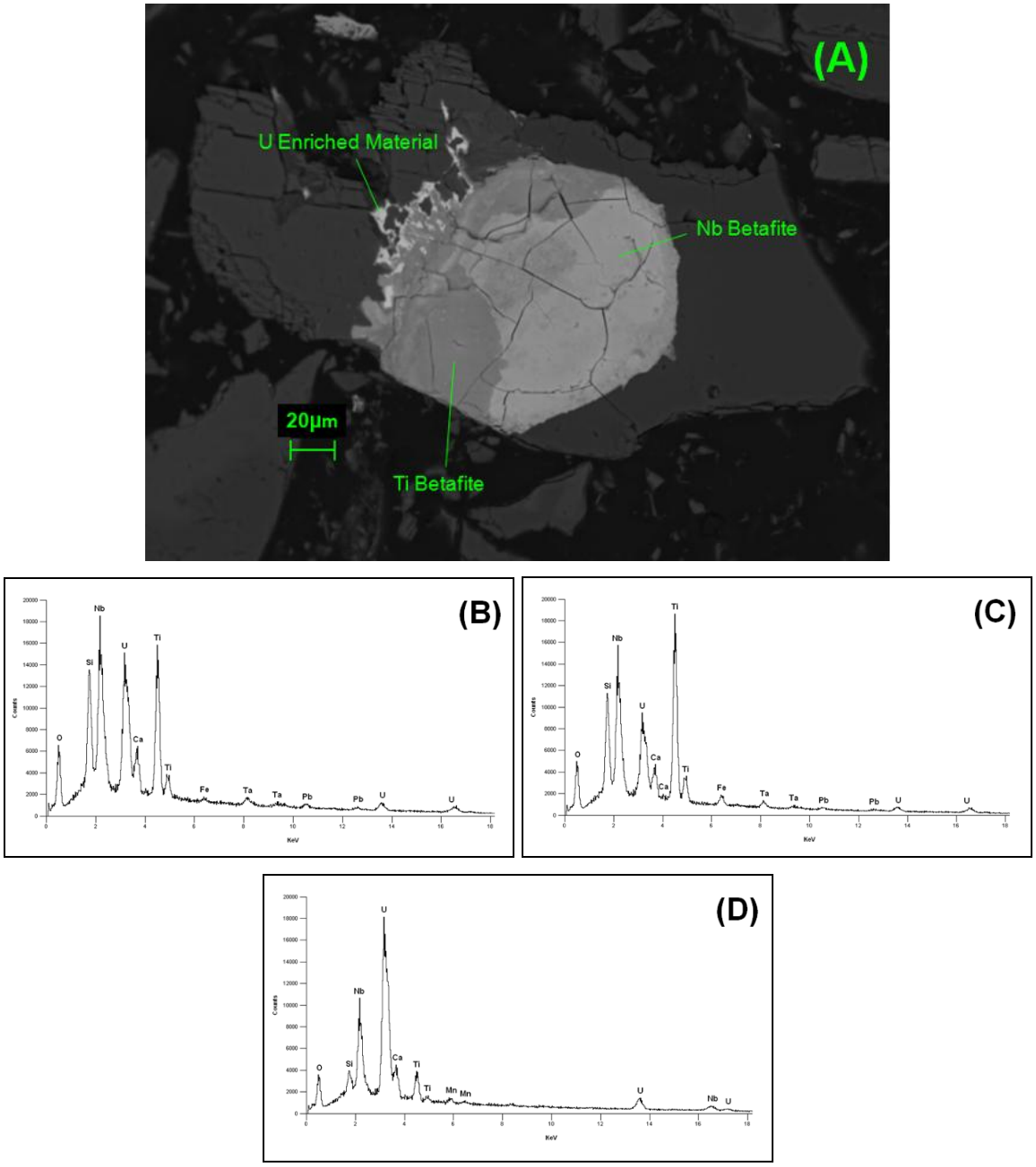

Figure 69: (A) A betafite grain, in sample SH1, consisting of two portions, (B) one in which Nb is more abundant and (C) one in which Ti is more abundant. (D) shows an EDS U enriched area on the periphery of the betafite grain. While the betafite grain contains Pb no Pb was detected in the U enriched material.

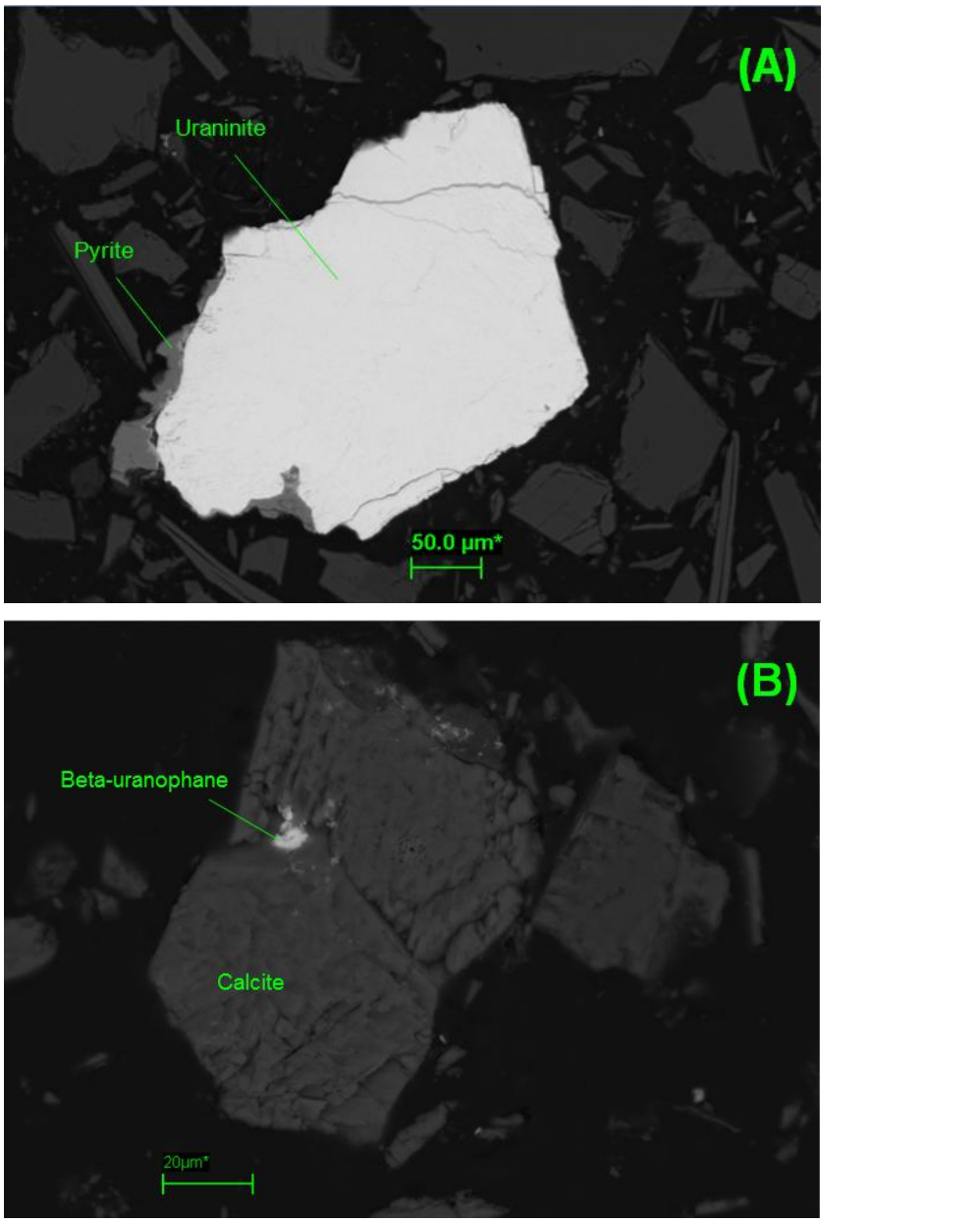

Figure 70: Uranium minerals in sample SH2. (A) Uraninite occurring with pyrite and (B) beta-uranophane in calcite. (C) An EDS spectrum of the uraninite showing the presence of Pb and Y. (D) An EDS spectrum of the beta-uranophane.

The majority of the U in sample SJ1 occurs in uraninite. Uranium silicates are also present occurring as alteration to coffinite along fractures in the uraninite (Figure 71) as well as discrete grains of beta-uranophane grains.

Uraninite is the dominant U mineral in SJ2, however significant amounts of coffinite and beta-uranophane were detected. Traces of U were detected in some thorite grains, however the one shown in Figure 72 contained no U. In addition to thorite, this sample also contained rare earth oxides (in the form of cerianite).

The U in the Val sample occurs mainly in beta-uranophane (Figure 73) and to a lesser extent in brannerite. Many brannerite grains are associated with other Ti minerals.

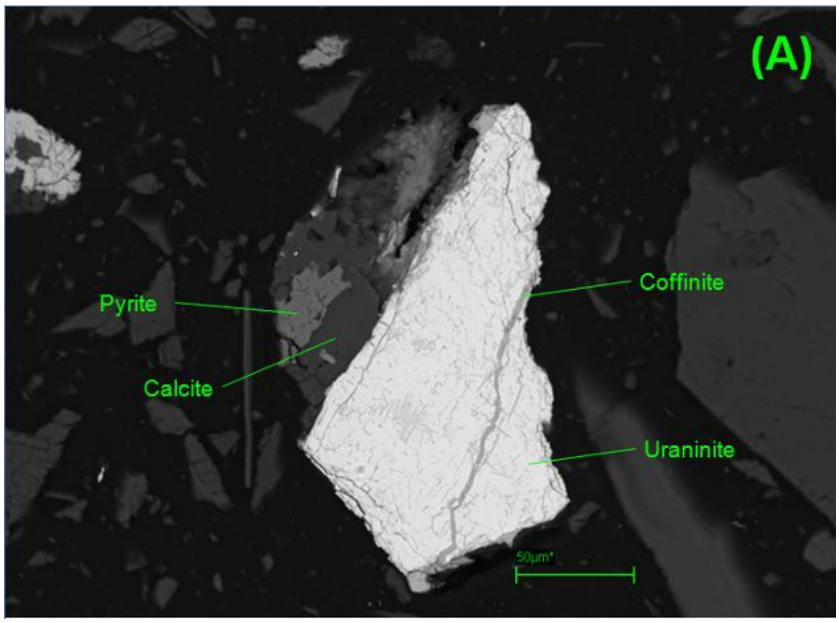

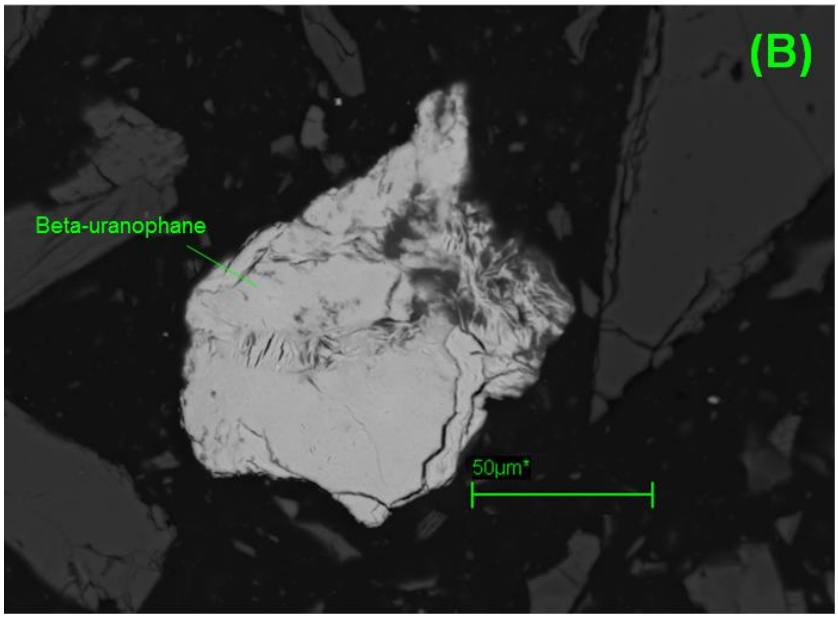

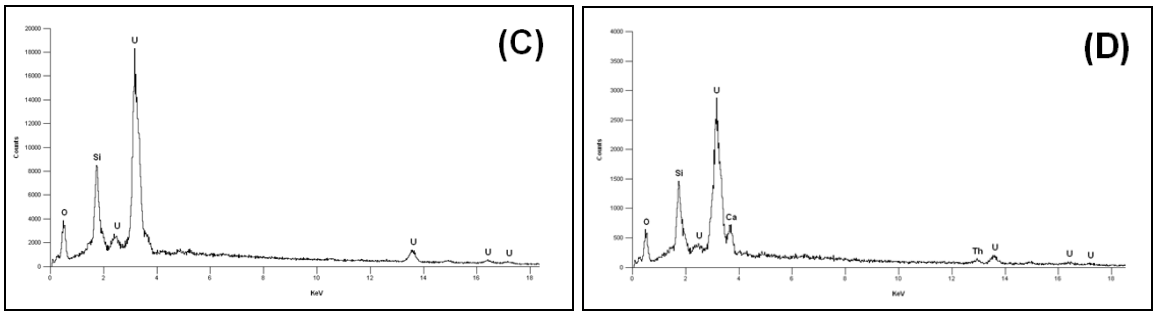

Figure 71: (A) Uraninite, in sample SJ1, with alteration to coffinite along a fracture. (B) A beta-uranophane grain. (C) An EDS spectrum collected from the coffinite within the fracture shown in (A). The absence of Ca in the EDS spectrum distinguishes coffinite from beta-uranophane. (D) An EDS spectrum from the beta-uranophane grains.

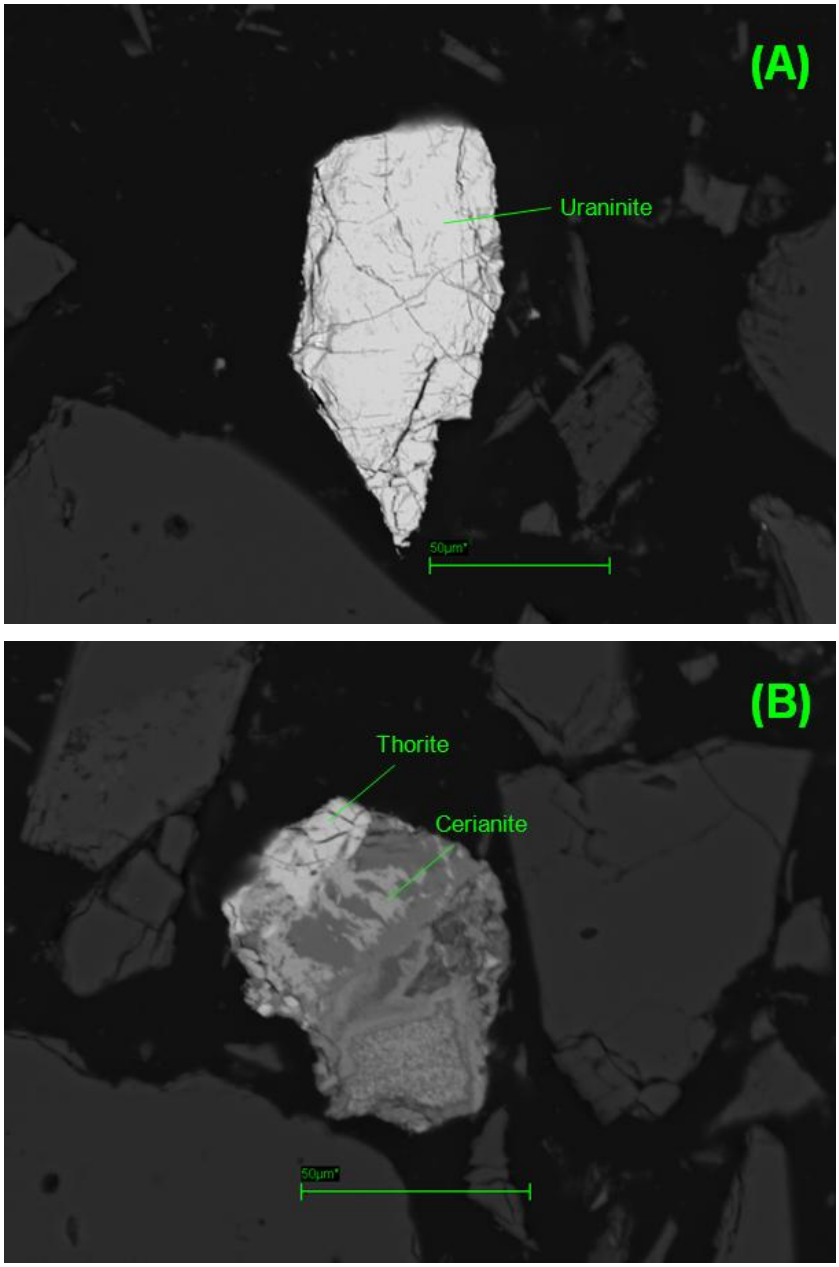

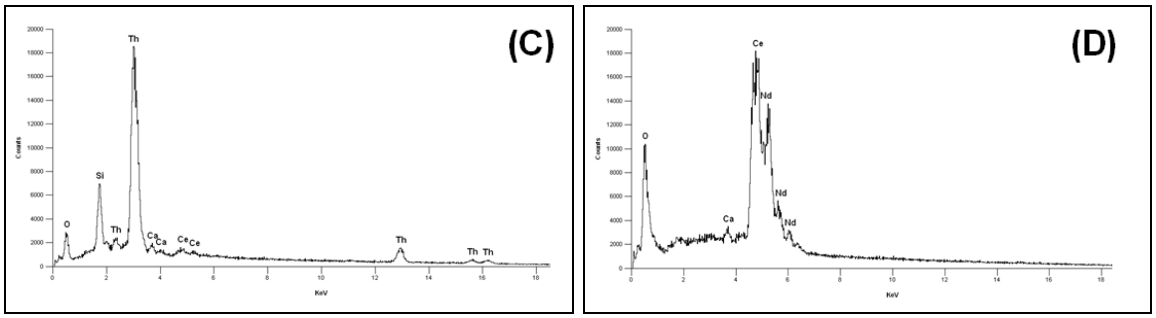

Figure 72: (A) A liberated uraninite grain in sample SJ2. (B) Thorite occurring with cerianite in a composite particle with (C) EDS spectra of the thorite and (D) cerianite.

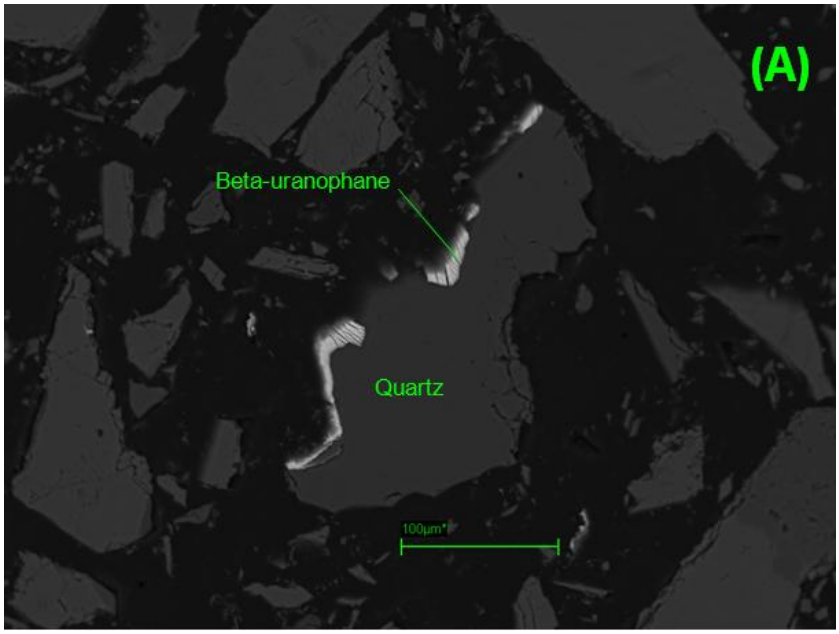

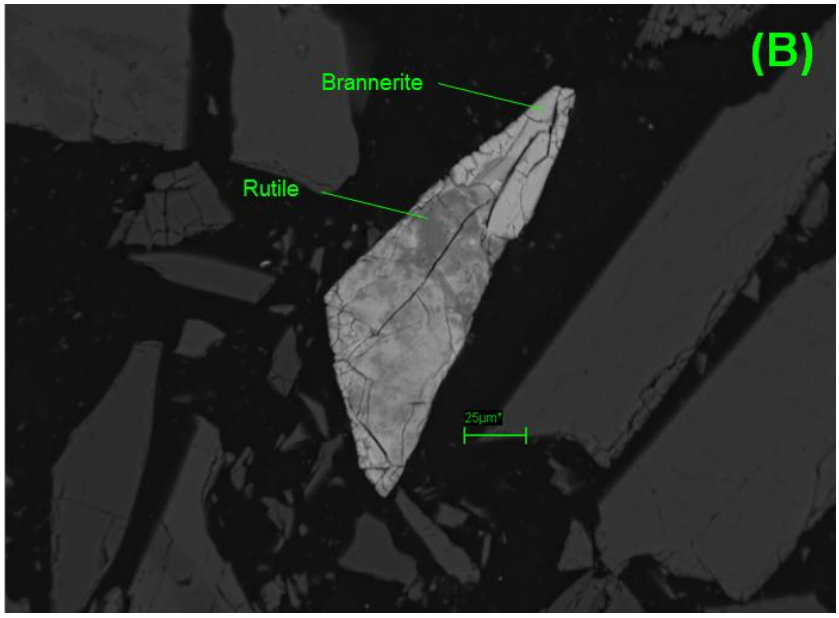

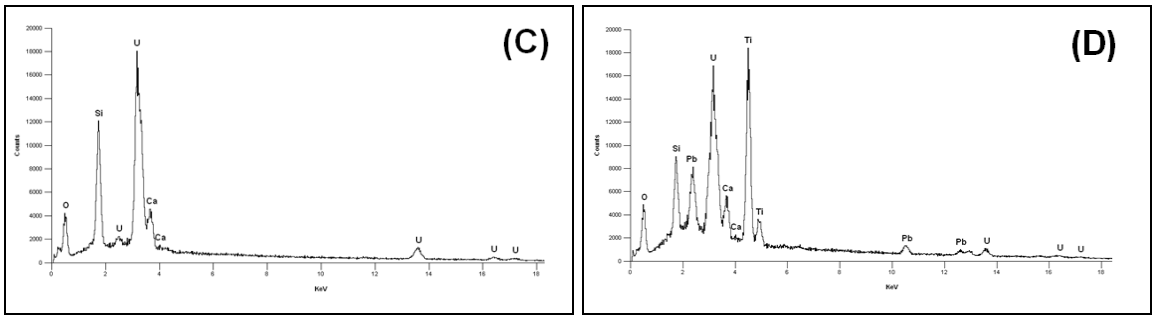

Figure 73: (A) Beta-uranophane on the periphery of a quartz grain from the Val sample. The mode of occurrence suggests that this represents a fracture which was broken apart during milling. (B) A composite particle consisting of brannerite and rutile. (C) An EDS spectrum from the beta-uranophane. (D) An EDS spectrum of the brannerite.

10.3.6. QEMSCAN Trace Mineral Search

The results of the QEMSCAN TMS include the data required for predicting U dissolution for the 5 samples. These data consist of the U deportment (which reflects the proportion of the U contained in each sample that occurs in the various U phases), U mineral grain size distributions and U mineral exposure and association characteristics.

The U deportment is particularly important for determining the proportion of the U occurring in refractory phases and is given in Table 80 and Figure 79. The U elemental deportment agrees well with the qualitative results of the SEM-EDS analyses. The only samples with significant amounts of U occurring in refractory phases were SH1 and Val. In SH1 the dominant U host mineral is betafite, which hosts almost half of the contained U. In Val the dominant U host phase is brannerite, which accounts for more than a third of the contained U.

Surprisingly only minor amounts of the U in sample SH2 occurred in refractory phases. This was also observed during the SEM-EDS analyses. Originally it was suspected that a sample swap occurred during the preparation of the polished blocks. However, the hand specimen descriptions and optical petrography (Section 10.3.1) indicated that this sample was characterised by unusually high levels of biotite (due to the presence of the quartz-biotite schist). These elevated levels of biotite were observed in the polished sections indicating that no sample swap occurred.

In samples SJ1 and 2 the majority of the U occurs in uraninite with minor amounts occurring in coffinite and beta-uranophane.

Figure 74 to Figure 78 show examples of the QEMSCAN TMS particle maps for each sample.

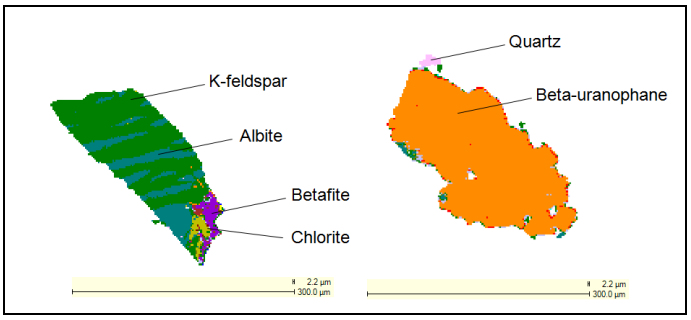

Figure 74: Particle maps from sample SH1 showing betafite occurring with perthite (left) and liberated beta-uranophane (right).

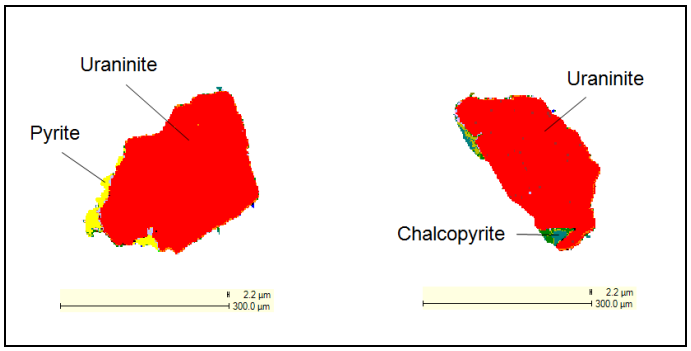

Figure 75: Liberated uraninite from sample SH2 occurring with pyrite (left) and chalcopyrite (right).

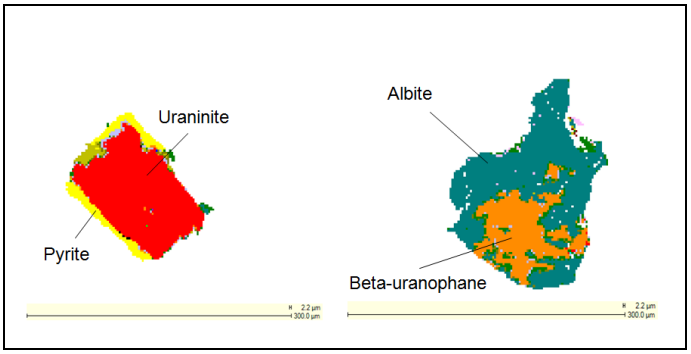

Figure 76: Particle maps from sample SJ1 showing uraninite occurring with pyrite (left) and beta-uranophane occurring with albite (right).

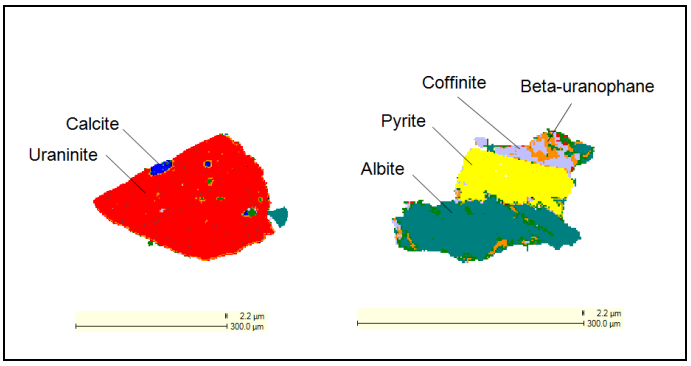

Figure 77: Liberated uraninite associated with calcite (left) and coffinite showing partial alteration to beta-uranophane in a particle that also contains pyrite and albite (right) from sample SH2.

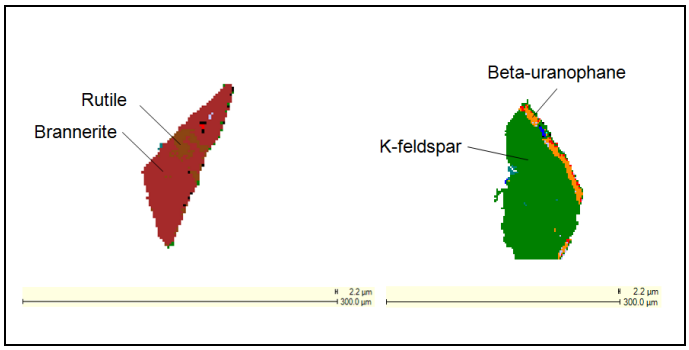

Figure 78: Particle maps from the Val sample showing a composite particle consisting of brannerite and rutile (left) and beta-uranophane occurring along the periphery of a K-feldspar grain (right). The texture in the beta-uranophane suggests that it fills a fracture along which breakage occurred during milling.

Table 80: Uranium deportment expressing the proportion of the total uranium, contained in each sample, hosted by the various uranium minerals

Samples	SH1	SH2	SJ1	SJ2	Val
Units	%	%	%	%	%
Uraninite	6.16	95.24	91.98	84.58	17.09
Coffinite	14.53	1.58	3.09	5.43	16.48
Beta-uranophane	22.45	1.53	3.79	6.18	24.17
Brannerite	7.90	0.22	0.78	0.57	35.16
Betafite	48.23	0.07	0.16	0.05	3.25
Uranothorite	0.73	1.37	0.20	3.19	3.86

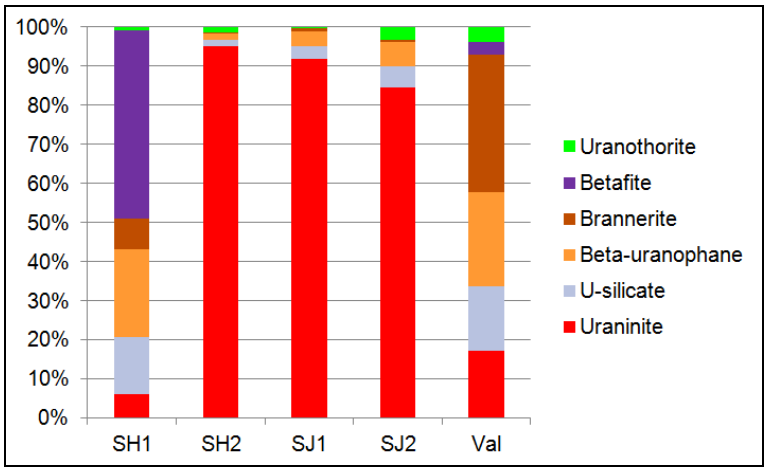

Figure 79: Uranium elemental deportment expressing the proportion of the contained U hosted by each mineral.

While the exact species which hosts the U is critical for the U deportment, this is not the case for grain size and exposure characteristics. For these data sets it is more practical to divide the U minerals into two classes (leachable and refractory). Uraninite and coffinite were shown to be leachable in Part I of this study (Sections 5.3 and 6.3) and, as a secondary hexavalent phase (Nex et al., 2001), beta-uranophane was also considered leachable. While brannerite, betafite and uranothorite were considered refractory (Lottering et al., 2008, Nex and Kinnaird, 2007 and Cuney, 2009 respectively).

The U mineral grain size distributions are given in Table 81 for leachable U minerals and Table 82 for refractory phases. Where refractory minerals make up a significant proportion of U deportment (samples SH1 and Val), the refractory minerals tend to be coarser than the leachable phases. Where refractory minerals are scarce, these tend to be finer than leachable phases. The pronounced steps seen in the curves for the refractory phases in SH2 and SJ1 and 2 are due to the low proportion of refractory U in these samples (Figure 1) as a result too few grains were mapped to produce the smooth distributions seen for the leachable phases.

Table 81: Discrete and cumulative grain size distributions for leachable uranium minerals

Sample	SH1		SH2		SJ1		SJ2		Val	
Size Class (µm)	**Disc (%)**	**Cum (%)**	**Disc (%)**	**Cum (%)**	**Disc (%)**	**Cum (%)**	**Disc (%)**	**Cum (%)**	**Disc (%)**	**Cum (%)**
< 5	11.59	11.59	0.48	0.48	0.72	0.72	0.97	0.97	7.95	7.95
5 - 10	7.00	18.59	1.43	1.91	1.63	2.34	2.60	3.57	12.06	20.01
10 - 15	6.47	25.07	2.17	4.08	2.24	4.58	3.63	7.20	17.07	37.08
15 - 20	6.43	31.50	2.09	6.17	2.41	6.99	3.71	10.90	14.43	51.51
20 - 25	3.00	34.49	1.59	7.76	1.77	8.76	2.90	13.80	8.31	59.81
25 - 30	4.11	38.60	1.41	9.17	2.04	10.80	2.13	15.93	7.89	67.71
30 - 35	3.14	41.74	1.55	10.72	1.42	12.23	1.92	17.85	4.65	72.36
35 - 40	4.00	45.74	1.95	12.67	1.39	13.62	2.61	20.46	1.89	74.25
40 - 45	2.65	48.39	1.21	13.88	1.21	14.83	3.23	23.69	2.47	76.72
45 - 50	3.40	51.79	1.86	15.74	1.39	16.22	1.20	24.89	2.94	79.67
50 - 55	4.31	56.10	1.28	17.01	1.44	17.66	2.71	27.61	1.99	81.66
55 - 60	0.00	56.10	1.55	18.56	1.81	19.46	2.00	29.61	1.89	83.54
60 - 65	2.37	58.47	2.81	21.37	2.11	21.57	2.02	31.64	0.00	83.54
65 - 70	1.44	59.91	4.07	25.44	1.99	23.56	3.36	34.99	4.92	88.46
70 - 75	1.73	61.64	2.01	27.45	1.08	24.64	2.79	37.78	0.00	88.46
75 - 80	0.96	62.60	1.26	28.71	3.07	27.72	1.33	39.10	0.00	88.46
80 - 85	3.09	65.69	3.59	32.30	2.23	29.94	0.00	39.10	0.00	88.46
85 - 90	1.27	66.96	0.83	33.14	3.49	33.43	1.24	40.35	0.00	88.46
90 - 95	2.63	69.59	1.80	34.93	1.57	35.01	1.46	41.80	0.00	88.46
95 - 100	0.00	69.59	1.03	35.96	3.43	38.44	0.77	42.57	0.00	88.46
100 - 150	11.82	81.41	19.04	55.00	24.02	62.46	16.31	58.88	11.54	100.00
150 - 200	18.59	100.00	11.67	66.67	24.74	87.19	18.68	77.56	0.00	100.00
200 - 300	0.00	100.00	21.43	88.10	12.81	100.00	22.44	100.00	0.00	100.00
>300	0.00	100.00	11.90	100.00	0.00	100.00	0.00	100.00	0.00	100.00

Table 82: Discrete and cumulative grain size distributions for refractory uranium minerals

Sample	SH1		SH2		SJ1		SJ2		Val	
Size Class (µm)	**Disc (%)**	**Cum (%)**	**Disc (%)**	**Cum (%)**	**Disc (%)**	**Cum (%)**	**Disc (%)**	**Cum (%)**	**Disc (%)**	**Cum (%)**
< 5	1.61	1.61	39.29	39.29	35.02	35.02	52.72	52.72	9.89	9.89
5 - 10	1.17	2.78	17.86	57.15	16.79	51.80	19.78	72.50	6.04	15.94
10 - 15	1.63	4.41	1.64	58.79	4.41	56.22	6.15	78.65	4.82	20.76
15 - 20	2.12	6.53	5.76	64.56	2.26	58.48	5.34	83.99	1.46	22.22
20 - 25	2.42	8.94	5.06	69.61	1.72	60.20	4.55	88.54	4.78	27.00
25 - 30	3.32	12.26	16.50	86.12	1.81	62.01	0.00	88.54	2.63	29.63
30 - 35	2.83	15.09	0.00	86.12	2.25	64.27	11.46	100.00	2.25	31.87
35 - 40	2.38	17.47	13.88	100.00	3.28	67.55	0.00	100.00	4.93	36.81
40 - 45	4.62	22.09	0.00	100.00	0.00	67.55	0.00	100.00	1.76	38.57
45 - 50	2.09	24.18	0.00	100.00	2.46	70.01	0.00	100.00	9.97	48.54
50 - 55	3.59	27.76	0.00	100.00	0.00	70.01	0.00	100.00	8.76	57.30
55 - 60	6.24	34.00	0.00	100.00	0.00	70.01	0.00	100.00	0.00	57.30
60 - 65	2.37	36.37	0.00	100.00	9.44	79.44	0.00	100.00	8.46	65.76
65 - 70	3.28	39.65	0.00	100.00	0.00	79.44	0.00	100.00	4.64	70.40
70 - 75	3.85	43.50	0.00	100.00	0.00	79.44	0.00	100.00	0.00	70.40
75 - 80	3.06	46.56	0.00	100.00	0.00	79.44	0.00	100.00	0.00	70.40
80 - 85	4.39	50.95	0.00	100.00	0.00	79.44	0.00	100.00	0.00	70.40
85 - 90	1.54	52.49	0.00	100.00	0.00	79.44	0.00	100.00	15.82	86.22
90 - 95	1.80	54.29	0.00	100.00	0.00	79.44	0.00	100.00	0.00	86.22
95 - 100	8.81	63.10	0.00	100.00	0.00	79.44	0.00	100.00	0.00	86.22
100 - 150	17.60	80.69	0.00	100.00	20.56	100.00	0.00	100.00	13.78	100.00
150 - 200	19.31	100.00	0.00	100.00	0.00	100.00	0.00	100.00	0.00	100.00
200 - 300	0.00	100.00	0.00	100.00	0.00	100.00	0.00	100.00	0.00	100.00
>300	0.00	100.00	0.00	100.00	0.00	100.00	0.00	100.00	0.00	100.00

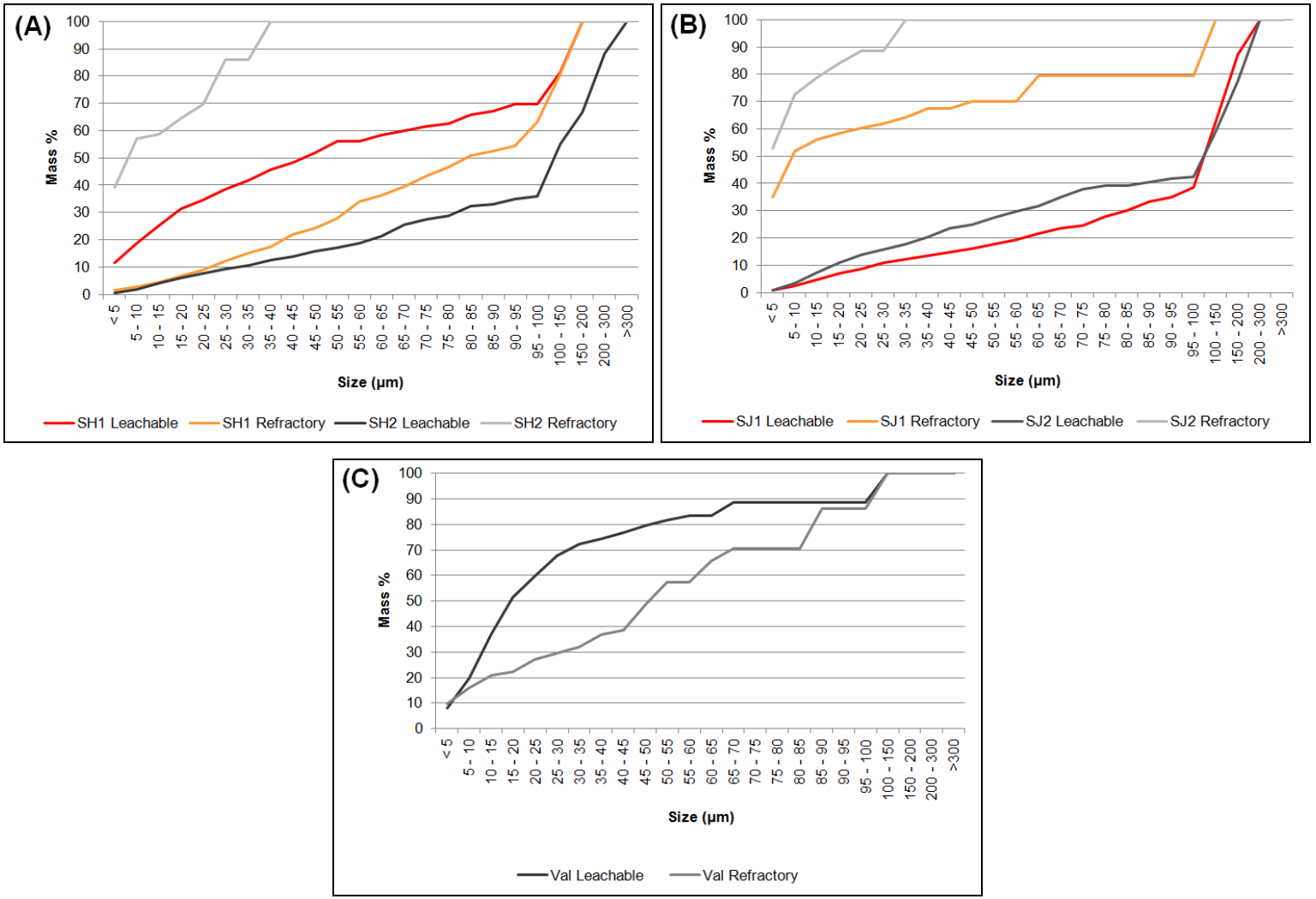

Figure 80: Cumulative grain size distributions for leachable and refractory U minerals in (A) the SH samples, (B) the SJ samples and (C) the Val sample.

The exposure characteristics of the U minerals are important because they exert a strong control on the dissolution of U. In Part I of this study it was found that under moderate leach conditions (pH 1.5 and Eh 450 mV SCE), the U dissolution was proportional to the amount of U that occurs in grains with some degree of exposure.

The U mineral exposure characteristics follow a similar trend to the grain size characteristics with higher levels of exposure associated with coarser grain size distributions (Figure 81). Generally exposure levels were high in all of the samples (for both leachable and refractory phases) except in SH1 and SJ1 and 2 (where less than 42% of the grains are exposed).

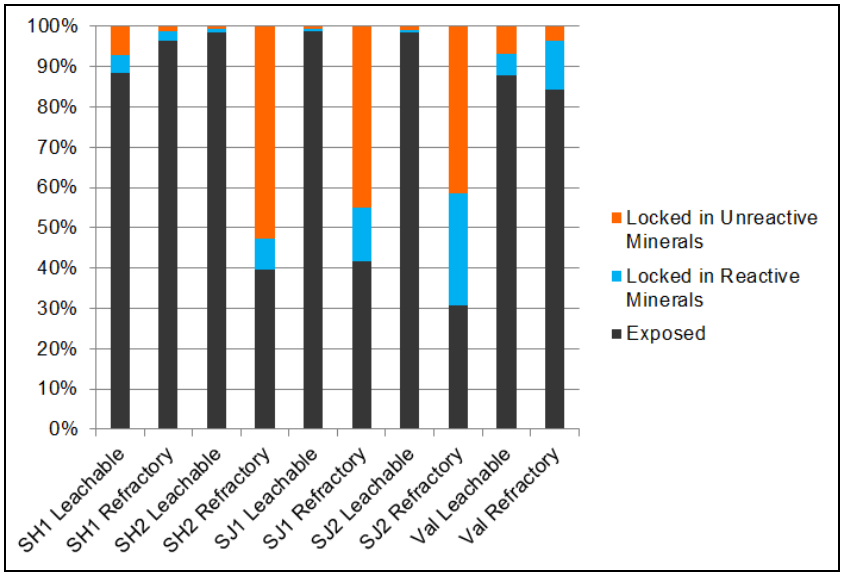

Figure 81: Exposure and association characteristics of the U phases in each sample.

Table 83: Rössing SH samples mineral exposure and association characteristics for leachable and refractory uranium phases

Uranium Mineral Type	**Leachable**			**Refractory**		
Exposure and Association Class	**Total Area (pixels)**	**Number of Grains**	**Mass % U**	**Total Area (pixels)**	**Number of Grains**	**Mass % U**
Sample SH1						
Exposed (>=80%)	13670	180	13.84	43	12	0.03
Exposed (>=10%<80%)	68242	3211	71.37	99789	962	63.87
Exposed (<10%)	2556	80	3.17	51204	110	32.57
Total Exposed	**84468**	**3471**	**88.38**	**151036**	**1084**	**96.47**
Locked in Biotite/Chlorite	32	26	0.04	2	1	0.00
Locked in Carbonate/Phosphate	4	4	0.01	0	0	0.00
Locked in Oxide/Hydroxide	0	0	0.00	175	99	0.11
Locked on Polymineral Boundary (Including Biotite/Chlorite)	2898	660	3.50	1335	162	0.90
Locked on Polymineral Boundary (Carbonate/Phosphate)	323	192	0.38	100	47	0.07
Locked on Polymineral Boundary (Including Oxide)	475	175	0.55	1911	196	1.23
Total Locked in Reactive Minerals	**3732**	**1057**	**4.48**	**3523**	**505**	**2.31**
Total Locked in Low Reactivity Minerals	**6270**	**3878**	**7.14**	**1725**	**656**	**1.22**
Sample SH2						
Exposed (>=80%)	63240	321	40.09	2	1	0.15
Exposed (>=10%<80%)	92636	661	57.81	610	17	39.55
Exposed (<10%)	1384	27	0.63	0	0	0.00
Total Exposed	**157260**	**1009**	**98.53**	**612**	**18**	**39.70**
Locked in Biotite/Chlorite	12	5	0.00	0	0	0.00
Locked in Carbonate/Phosphate	21	8	0.01	0	0	0.00
Locked in Oxide/Hydroxide	0	0	0.00	1	1	0.07
Locked on Polymineral Boundary (Including Biotite/Chlorite)	1930	57	0.89	88	24	6.53
Locked on Polymineral Boundary (Carbonate/Phosphate)	81	11	0.03	0	0	0.00
Locked on Polymineral Boundary (Including Oxide)	12	10	0.00	14	6	1.05
Total Locked in Reactive Minerals	**2056**	**91**	**0.94**	**103**	**31**	**7.65**
Total Locked in Low Reactivity Minerals	**1419**	**384**	**0.53**	**710**	**211**	**52.64**

Table 84: Rössing SJ samples mineral exposure and association characteristics for leachable and refractory uranium phases

Uranium Mineral Type	**Leachable**			**Refractory**		
Exposure and Association Class	**Total Area (pixels)**	**Number of Grains**	**Mass % U**	**Total Area (pixels)**	**Number of Grains**	**Mass % U**
Sample SJ1						
Exposed (>=80%)	196225	802	38.97	0	0	0.00
Exposed (>=10%<80%)	307420	3010	57.01	5383	175	36.64
Exposed (<10%)	18481	148	2.72	698	17	4.89
Total Exposed	**522126**	**3960**	**98.70**	**6081**	**192**	**41.53**
Locked in Biotite/Chlorite	98	69	0.01	2	2	0.01
Locked in Carbonate/Phosphate	2	2	0.00	0	0	0.00
Locked in Oxide/Hydroxide	0	0	0.00	2	2	0.01
Locked on Polymineral Boundary (Including Biotite/Chlorite)	5255	990	0.59	1693	325	11.82
Locked on Polymineral Boundary (Carbonate/Phosphate)	707	143	0.07	10	8	0.06
Locked on Polymineral Boundary (Including Oxide)	80	28	0.01	215	47	1.48
Total Locked in Reactive Minerals	**6142**	**1232**	**0.68**	**1922**	**384**	**13.38**
Total Locked in Low Reactivity Minerals	**5444**	**1523**	**0.62**	**6252**	**2112**	**45.09**
Sample SJ2						
Exposed (>=80%)	88260	452	43.10	40	3	1.36
Exposed (>=10%<80%)	119965	1869	54.29	582	100	19.77
Exposed (<10%)	3093	62	0.94	283	13	9.66
Total Exposed	**211318**	**2383**	**98.33**	**905**	**116**	**30.79**
Locked in Biotite/Chlorite	17	13	0.01	0	0	0.00
Locked in Carbonate/Phosphate	13	10	0.00	0	0	0.00
Locked in Oxide/Hydroxide	13	3	0.00	62	53	1.84
Locked on Polymineral Boundary (Including Biotite/Chlorite)	1457	159	0.46	180	78	5.84
Locked on Polymineral Boundary (Carbonate/Phosphate)	418	91	0.14	210	24	7.04
Locked on Polymineral Boundary (Including Oxide)	472	111	0.15	407	202	12.92
Total Locked in Reactive Minerals	**2390**	**387**	**0.77**	**859**	**357**	**27.65**
Total Locked in Low Reactivity Minerals	**3180**	**691**	**0.91**	**1224**	**509**	**41.57**

Table 85: Valencia sample mineral exposure and association characteristics for leachable and refractory uranium phases

Uranium Mineral Type	Leachable			Refractory		
Exposure and Association Class	**Total Area (pixels)**	**Number of Grains**	**Mass % U**	**Total Area (pixels)**	**Number of Grains**	**Mass % U**
Val Sample						
Exposed (>=80%)	1764	62	9.45	375	16	2.44
Exposed (>=10%<80%)	17291	903	70.05	12488	168	80.96
Exposed (<10%)	1997	39	8.24	124	6	0.82
Total Exposed	**21052**	**1004**	**87.73**	**12987**	**190**	**84.21**
Locked in Biotite/Chlorite	9	7	0.04	3	3	0.02
Locked in Carbonate/Phosphate	22	16	0.10	0	0	0.00
Locked in Oxide/Hydroxide	1	1	0.00	708	420	4.25
Locked on Polymineral Boundary (Including Biotite/Chlorite)	275	115	1.20	152	75	0.88
Locked on Polymineral Boundary (Carbonate/Phosphate)	685	132	3.01	28	15	0.17
Locked on Polymineral Boundary (Including Oxide)	213	89	0.98	1158	424	6.96
Total Locked in Reactive Minerals	**1205**	**360**	**5.33**	**2049**	**937**	**12.26**
Total Locked in Low Reactivity Minerals	**1726**	**479**	**6.94**	**539**	**203**	**3.52**

Using the TMS data, the percentage U dissolution was predicted for each sample. This was calculated by assuming that under the conditions that will be used in the U leach tests (pH 1.5, Eh 450 mV SCE and 24 hour duration); only grains of uraninite, coffinite and beta-uranophane that have some degree of exposure (see Table 83 to Table 85 for full exposure data) will leach. Locked grains and grains of betafite, brannerite and uranothorite were assumed to yield no U to solution. Based on these assumptions it is expected that the dissolutions of SH2, SJ1 and SJ2 would be at or in excess of 95%, while those of SH1 and Val would be much lower (Table 86).

Table 86: Predicted uranium dissolution for the five samples, assuming that locked grains and grains of betafite, brannerite and uranothorite do not leach

Samples	**SH1**	**SH2**	**SJ1**	**SJ2**	**Val**
Units	**%**	**%**	**%**	**%**	**%**
Predicted Dissolution	38.13	96.90	97.58	94.58	50.65

10.4. Discussion

10.4.1. Optical Petrography and Gangue Mineralogy

The samples are all alkali feldspar granites with varying amounts of accessory minerals. The only major exception is SH2, which also contained quartz-feldspar-biotite schist.

Calcite was the only carbonate detected in the samples. This carbonate can be a significant gangue acid consumer, and is generally thought to originate from marble country rock that has been mined along with the ore (Johnson, 1990). It was found that the ore itself does contain calcite in trace amounts, between 0.08% (SJ2) and 0.94% (SH2), it would therefore not be possible to completely eliminate calcite from the mill feed material. However, the addition of even very

small amounts of marble would significantly increase the carbonate in the mill feed material.

This calcite occurs within fine fractures and may possibly represent mobilisation of carbonate, from the country rock marble, into the granite. Calcite also occurs as an alteration product. Although the plagioclase is albitic, it appears to contain sufficient Ca for the formation of calcite during alteration (as calcite was observed as an alteration product of plagioclase).

Due to the high proportions of quartz and feldspar (and the generally low levels of phyllosilicates and other gangue acid consumers), gangue phases with much lower concentrations, than those considered in Part I, will significantly influence the gangue acid consumption. Therefore, although the levels of calcite are low, when compared to the sedimentary samples in Part I (Table 19), these low levels of calcite may be significant.

Table 21 list the lower detection and quantification limits for calcite by XRD as 0.17 and 0.5% respectively. For the sedimentary samples this was more than adequate, but for the igneous samples, more than half the samples had calcite contents (Table 72) below the quantification limit of XRD.

In Part I it was found that the limitation on the use of XRD for predicting gangue acid consumptions related more to the lack of textural data than the quantification limit. The results of this phase of the study indicate that both the quantification limit, and lack of textural data, make the XRD unsuitable for accurate prediction of gangue acid consumptions. However, the XRD would still be able to identify the cause of unusually high acid consumptions, if these consumptions are mineralogically controlled.

Gangue mineral concentrations are not the only factors controlling the consumption of acid. Specific surface areas influence dissolution rates (Brantley,

2008) and therefore the degree of acid consumption during the fixed period of time of the leach test. The specific surface areas of the gangue minerals in the igneous samples were very similar to those of the sedimentary samples, which is to be expected as the rocks were milled to the same grind size. The specific surface area of the chlorite was slightly lower than in the sedimentary samples and the calcite slightly higher, but overall the variation was small. The only major exception was biotite which had a specific surface area of between ~4 and 8 m^2/g, which was significantly higher than the phyllosilicates in the sedimentary samples.

10.4.2. Comminution

The milling curves for the igneous samples differed from those of the 212 µm sedimentary samples in Part I. The sedimentary samples showed an initial phase of rapid milling followed by a steady slower milling rate. The change in rate was interpreted as being the result of breakage along grain boundaries in the initial phases of milling to -212 µm, versus breakage of the mineral grains themselves during the later phases of milling to -212 µm. Because 75 µm was finer than most of the grains in the Mooi sample, there was no initial rapid milling phase and only the slower linear behaviour was seen. The milling curves of the igneous samples were also almost linear. This is likely to be because 212 µm is finer than the majority of the grains in all of the samples. In addition, the interlocking nature of the grains would probably result in stronger bonding between adjacent grains than was seen in the sedimentary samples.

The grain sizes of the samples vary, with SH1 having the finest size (0.3 to 6 mm) and SJ1 and Val the coarsest (3 to 20 mm and 1 to 22 mm respectively). In general (for hard rock ores) fine-grained rocks are considered to be harder to mill than coarse-grained rocks, as fracture propagation through crystals tends to terminate at grain boundaries (Wills and Napier-Munn, 2006). However, it was

found that grain size was not the main factor controlling hardness, as the Val sample was the hardest, followed by SH2, while SJ2 and SH1 were the softest.

It appears that the main factors controlling hardness in these rocks are alteration and accessory minerals. Sample SH1 contained a cavity and there was alteration associated with this cavity, similarly sample SJ2 showed extensive oxidation, with limonite developed along many grain boundaries. In both cases it appears that the alteration weakened the rock.

The relationship between hardness and accessory minerals is more complex. In the Val sample it appears that the particularly low levels of accessory minerals is the reason for the hardness of this rock, while in sample SH2, it is the resistance of the biotite to milling which causes the hardness.

Because of the hardness of the biotite, it would be important to know if the U occurs within biotite. If not, then the target grind size could be adjusted to prevent wasted time and power spent on milling biotite.

10.4.3. Chemical Analyses

The key features of the chemical analyses are the U grades and Fe contents of the samples. There was a wide range in the grades of the samples with U_3O_8 contents varying between 225 (Val) and 2606 ppm (SJ1).

The Fe contents of the samples are significant because Fe acts as a catalyst in the oxidation of the U (Lottering *et al.*, 2008). The total Fe (expressed as Fe_2O_3) contents of the samples vary between 0.63 (Val) and 2.77% (SJ2). These values are much lower than those of the sedimentary samples, which varied between 1.87 (OAO) and 6.95% Fe_2O_3. The FeO contents of the samples vary between

0.51 (Val) and 1.18% (SH2). While high total Fe contents are desirable, the Fe^{3+} state is more desirable than the Fe^{2+} state (as in FeO).

For ideal leaching of U, the Fe^{3+} content of the leach liquor should be at least 3.0 g/L (Johnson, 1990). In order to achieve these levels of solution Fe, very significant percentages of the total Fe in each sample would have to be leached. The Fe in these samples occurs in a range of minerals (including biotite, chlorite, pyrite, chalcopyrite, limonite, hematite, ilmenite and magnetite). As many of these are slow leaching, it is unlikely that the ore will provide the necessary Fe and Fe will have to be added as part of the reagent suite.

10.4.4. Scanning Electron Microscopy and QEMSCAN Trace Mineral Search

SH1 and Val were the only samples to contain appreciable levels of refractory U, while in the remaining three samples the vast majority of the U occurs in leachable phases. Considering the percentage refractory U and the degree of exposure of the leachable U, it is expected that samples SH2, SJ1 and SJ2 would all show U dissolutions at or in excess of 95%, while SH1 and Val would have U dissolutions of ~38 and ~51% respectively.

The low proportion of refractory U in sample SH2 was surprising considering that the sample is a composite of material from the SH area. However, due to the unusual composition of the sample (elevated biotite), it was possible to show that no sample swap occurred and that this sample does indeed contain very little refractory U. The unusual U mineralogy of this sample (for material from the SH area) may be a result of the unusual composition of the sample. It is possible that the associated schist played a role in the formation of the U minerals and resulted in the formation of uraninite in preference to betafite.

An unusual phase was detected during the SEM investigation. In sample SH1 a betafite grain was observed to have what appeared to be a U enriched secondary phase occurring along its periphery. This is surprising as the U in betafite is considered refractory (Nex and Kinnaird, 2007), which would generally prevent the leaching and redeposition of the U from this phase. However, the textural appearance of the phase suggests that this is what has occurred. The absence of Pb also suggests that the phase is younger than the associated betafite. While it is possible that the Pb leached from the apparently secondary phase, suggesting a younger age than is true, there is no evidence of Pb loss in any of the older phases, and both uraninite and betafite tend to have distinct Pb peaks in the EDS analyses.

10.5. Summary and Conclusions

Five samples underwent mineralogical and chemical analyses in order to gather the data required to predict their leach response. These analyses consisted of optical petrographic examination, XRD analysis, scanning electron microscopy and QEMSCAN analyses, as well as major element XRF, U and Th by ICP-MS and total S and C by Leco.

The rocks are a suite of alkali feldspar granites, except for sample SH2, which in addition to the alkali feldspar granite, contains quartz-feldspar-biotite schist. With the exception of the high biotite contents of SH2, the samples all have combined quartz and feldspar contents in excess of 95%. The high concentrations of low reactivity minerals suggest that these samples (possibly with the exception of SH2) will have very low gangue acid consumptions. Because the gangue acid consumptions are expected to be much lower than the sedimentary samples, it will be necessary to consider phases that have much lower concentrations during the modelling of the gangue acid consumptions. For this reason, XRD analyses alone are unsuitable for the gangue mineral characterisation of these samples.

While the high quartz and feldspar contents of the samples are an advantage in reducing gangue acid consumptions, they result in significantly harder rocks with higher resistance to milling. The initial rapid phase of milling seen in the -212 µm milling of the sedimentary samples was not seen in the milling curves of the igneous samples. This is because of the grain sizes of the igneous samples are much coarser than those of the sedimentary samples. The interlocking nature of the minerals probably also reduce the weakness along grain boundaries.

It appears that, rather than grain size, the major factors controlling the hardness of these ores are alteration and accessory minerals. Alteration tends to weaken the rock resulting in reduced milling times, while accessory minerals may result in strengthening or weakening of the rock depending on the accessory mineral and its abundance. Very low levels of accessory minerals increase the quartz and feldspar contents of the rocks, which appears to increase hardness, while high levels of biotite increase the hardness of the rock. Because of the resistance of biotite to milling, it would be important to determine if biotite hosts U minerals. If not, then it would be possible to optimise the milling process to limit the milling of biotite. The U minerals in these samples had high levels of exposure and were not strongly associated with biotite. No further milling of biotite would be necessary before leaching.

The chemical analyses show a wide range in U grades extending from 225 (Val) to 2606 ppm (SJ1) U_3O_8.

The results of the major element XRF analyses indicate that the samples have a shortage of Fe and Fe (ideally a source of Fe^{3+}) will be needed as part of the reagent suite.

The only samples with high levels of refractory U are SH1 and Val. In SH1 the dominant refractory mineral was betafite, while in Val the majority of the

refractory U occurs in brannerite. The dominant U host mineral in the remaining samples is uraninite. The degree of exposure is such that U dissolutions of 95% or higher are expected for SH2, SJ1 and SJ2, while the refractory U content of the SH1 and Val samples will be expected to limit dissolution to ~38 and 51% respectively.

Chapter 11. Modelling of Acid Leach Behaviour

11.1. Introduction

The aim of the modelling process was to produce data to test if the modelling methodology developed for the sedimentary samples could be applied to the igneous samples. The results of the mineralogical analyses provided the data to be used in the modelling; however the mineralogical analyses also highlighted several differences between the sedimentary samples and those in this phase of the study. There are three major differences between the two ores:

1. The shortage of Fe in the igneous ores will necessitate the addition of Fe as a reagent.
2. Biotite is present in all of the samples and is particularly abundant in SH2. The levels of biotite in the sedimentary samples were so low (either due to a low initial abundance, or alteration to chlorite), that this phase was not considered in the modelling of the sedimentary samples.
3. The concentrations of gangue acid consumers are significantly lower in the igneous samples. For this reason it will be necessary to consider minerals with much lower concentrations in the ore. These minerals were ignored in the modelling of the sedimentary samples because their contribution to the total acid consumption was less than the error in the carbonate and phyllosilicate acid consumptions.

These three differences would have to be incorporated into the model.

11.2. Methodology

The same model that was used for the sedimentary samples was used here (see Section 7.1). Equation 60 was used to model the MnO_2 demand and Equation 59

the rates of dissolution of the various gangue phases. This was a simple process for most of the phases, as these occurred in the sedimentary samples and the constants needed for Equation 59 had already been obtained. However, it was necessary to consider biotite, Fe oxide, ilmenite and apatite as part of this model, which were not included in the previous modelling process.

Biotite

The absence of data for biotite, made it necessary to make assumptions about the dissolution behaviour of this phase. As a mica, biotite is more structurally similar to muscovite (of the phases for which data is available) (Klein, 2002). However, the presence of Mg and Fe in its structure suggests parallels with chlorite (for which data is also available).

The apparent rate constants of Kalinowski and Schweda (1996) suggest that biotite dissolution rates are almost 200 times those of muscovite (presumably due to the Fe and Mg). For this reason, in the absence of more accurate data, the chlorite constants were used in the biotite calculations. By analogy with the muscovite dissolution reactions given by Knauss and Wolery (1989) and Oelkers *et al.* (2008), the dissolution of biotite is given by
Equation 65.

$$KMg_{2.5}Fe_{0.5}AlSi_3O_{10}(OH)_2 + 5H_2SO_4 \rightarrow K^+ + 2.5Mg^{2+} + 0.5Fe^{2+} + Al^{3+} + 3H_4SiO_4 + 0.25HF + 5SO_4^{2-}$$

Equation 65

Assuming complete dissolution of biotite in an ore that contains 1% biotite, and no other reactive minerals,
Equation **65** gives an acid consumption of 11.32 kg sulphuric acid per ton of ore processed.

Iron

The mineralogical analyses (Section 10.3) show that the Fe oxides in these samples include hematite, magnetite and limonite. Magnetite dissolves according to Equation 66 (Liu, *et al*., 2012). According to this equation the dissolution of 1% magnetite in an ore would result in an acid consumption of 16.9 kg of sulphuric acid per ton of ore processed. However, Equation 66 also shows that the dissolution of magnetite produces both ferrous and ferric Fe. The conversion of ferrous Fe to the ferric state would also consume MnO_2 and in so doing, consumer further acid (according to Equation 40).

$$Fe_3O_4(s) + 4H_2SO_4(aq) \rightarrow Fe_2(SO_4)_3(aq) + H_2O + FeSO_4(aq)$$

Equation 66

The dissolution of hematite only produces ferric Fe in solution and follows Equation 67 (Liu, *et al*., 2012). The dissolution of 1% hematite in an ore would result in an acid consumption of 18.4 kg of sulphuric acid per ton of ore processed.

$$Fe_2O_3(s) + 3H_2SO_4(aq) \rightarrow Fe_2(SO_4)_3(aq) + 3H_2O$$

Equation 67

The dissolution of Fe oxyhydroxide follows Equation 68 (Senanayake and Das, 2004) and for 1% dissolution of Fe oxyhydroxide, 16.56 kg of sulphuric acid would be consumed per ton of ore processed.

$$FeOOH + 3H^+ \rightarrow Fe^{3+} + 2H_2O$$

Equation 68

In order to address the shortage of inherent Fe in the samples, it was assumed (for the purposes of the model) that 3 kg of hematite would be added per ton of ore leached. This would be enough to satisfy the 3.0 g/L recommended by Johnson (1990) even if no Fe was contributed from the ore.

Because a significant proportion of the Fe was being added as a very finely milled reagent, it was assumed that complete dissolution of the Fe oxides (both added hematite and natural Fe oxide in the ore) would occur within the first hour.

Ilmenite

While there is literature on the dissolution behaviour of ilmenite in acid, most of the data refer to more intense conditions than those of a U leach, including higher acid concentrations, elevated temperature and the addition of a reductant, rather than an oxidiser as is used for U leaches (for example Zhang and Nicol, 2010 and Xiong *et al*., 2013). For these intensive conditions the dissolution of ilmenite follows Equation 69, while for less extreme conditions (temperature below 200° C and H_2SO_4 concentrations below 14 M) ilmenite dissolution follows Equation 70 (both equations are after Zhang and Nicol, 2010).

$$\mathbf{FeTiO_3(s) + 2H_2SO_4 \rightarrow TiOSO_4(s) + FeSO_4(s) + 2H_2O(l)}$$

Equation 69

$$\mathbf{FeTiO_3(s) + 4H^+(aq) \rightarrow TiO^{2+}(aq) + Fe^{2+}(aq) + 2H_2O(l)}$$

Equation 70

Using Equation 70, and acid consumption of 12.9 kg/ton would be expected for 1% dissolution of ilmenite. Because no published data was available for the dissolution kinetics of ilmenite (under conditions comparable to those of a U leach), it was necessary to use data from the leach tests conducted in Part I of this study. Not all of the leaches provided data that was suitable for determining leach constants. As the leaches in Part II will all be conducted under moderate

conditions (pH 1.5 and Eh 450 mV SCE), the lower and higher pH leach tests were unsuitable. The Ti dissolution of Test B (Table 54) was considered the most similar to the leaches in Part II and these results were used in the model.

Apatite

As was the case with ilmenite, the conditions used in the literature for the dissolution of apatite are more intense than those of a typical U leach, for example Pandey *et al.* (1980) examined the dissolution of apatite in solutions ranging from 20 to 60% sulphuric acid by mass. Because of the differences in conditions, it was not possible to use the data of Pandey *et al.* (1980) to draw conclusions about the kinetics of apatite dissolution. However, their equation for apatite dissolution in sulphuric acid was still applicable. This equation (Equation 71) shows that the dissolution of apatite generates phosphoric and hydrofluoric acids as well as gypsum, bassanite or anhydrite.

$$Ca_{10}(PO_4)_6F_2 + 10H_2SO_4 + 10nH_2O \rightarrow 10CaSO_4.nH_2O + 6H_3PO_4 + 2HF$$

Equation 71

Where *n* can take values of 0 (anhydrite), 0.5 (bassanite) or 2 (gypsum) depending on the temperature. Previous leach tests (Section 6.3) show that under the temperature used in this study, gypsum is the phase which forms.

Using Equation 71, the dissolution of 1% apatite from an ore would result in an acid consumption of 9.72 kg of sulphuric acid per ton of ore.

Because of the absence of published kinetic data for the dissolution of apatite under conditions similar to those of a U leach, the results of the leach tests in Part I were used. The results of Test E were selected for determining the dissolution parameters because:

1. The leach conditions were similar.

2. The mineralogical data showed that all the phosphate occurred in apatite, which made it possible to determine leach rates from changes in phosphate concentrations. This is not the case for the MSO sample where some of the phosphate occurs in meta-autunite.
3. The phosphate content, of the head sample, was higher than many of the other samples that were leached, resulting in more accurate data (because the concentrations were further from the detection limit).

11.3. Results

The results of the modelling suggest that with the exception of sample SH2, the rate of acid consumption will be very slow after the first two hours of leaching. Sample SH2 is expected to continue to consume acid at a fairly steady rate from the first 2 hours onward (Figure 82). While most of the samples are expected to show low total acid demands, of between ~27 kg/ton (Val) and ~39 kg/ton (SJ1), the model suggests that SH2 will have an acid consumption of ~124 kg/ton (Table 87). Figure 83 shows that the most significant contribution to the total acid demand for SH2 is expected to be due to biotite.

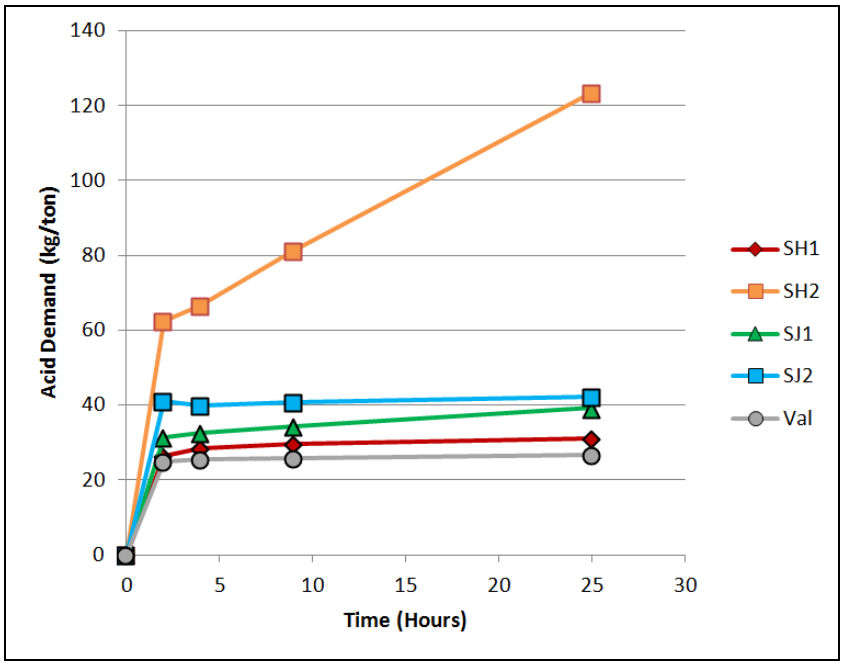

Figure 82: Acid demand curves showing the predicted acid requirements for each sample as a function of time.

Table 87: Predicted acid demand for each mineral, as well as MnO_2 and free acid, for a twenty five hour leach duration

Sample	SH1	SH2	SJ1	SJ2	Val
Units	kg/ton	kg/ton	kg/ton	kg/ton	kg/ton
Plagioclase	3.1	2.3	2.5	3.1	1.5
K-feldspar	0.5	0.4	0.8	0.4	0.8
Biotite	1.0	60.0	4.5	0.4	0.8
Chlorite	1.1	1.3	2.8	1.4	0.5
Ilmenite	0.1	0.5	0.0	1.1	0.0
Fe-Oxide	16.1	12.8	15.3	22.4	15.7
Apatite	0.3	0.5	1.6	0.3	1.5
Calcite	5.0	7.7	4.8	0.8	2.5
MnO_2	0.0	19.3	1.7	8.2	0.0
Free Acid	3.8	18.7	5.1	4.1	3.4
Total	31.1	123.5	39.2	42.4	26.8

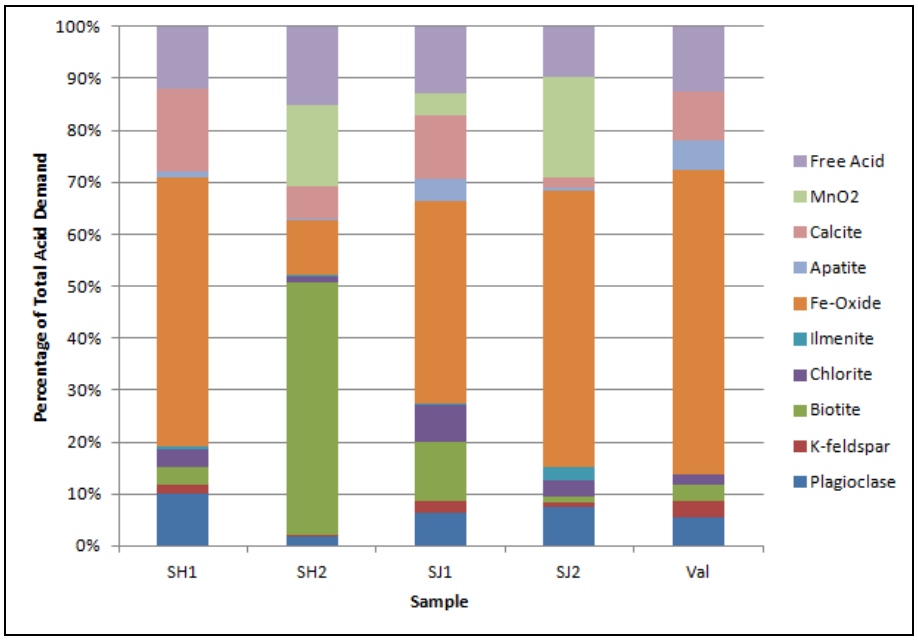

Figure 83: Predicted acid consumption of each mineral, as well as MnO_2 and free acid, expressed as a percentage of the total acid demand. In most samples the Fe-oxides are predicted to be the highest acid consumers. The only exception is SH2 where although the acid consumption by Fe-oxides is still significant, the model predicts that biotite will consume the majority of the acid.

11.4. Summary and Conclusions

The model developed for the sedimentary samples in Part I was applied to the igneous samples. Due to differences in the mineralogy and chemistry of the two groups of rocks, there were a number of problems with the direct application of the model to the igneous samples. These problems included a shortage of contained Fe (necessitating the addition of Fe as a reagent), the presence of biotite (which was not present in significant concentrations in the sedimentary samples), and the low proportion of reactive minerals.

Due to the low proportion of reactive minerals, it was necessary to consider minerals with very low abundances. These minerals (ilmenite and apatite) were not considered in the sedimentary model because the error in the dissolution, of

the more abundant and reactive minerals, accounted for more acid than these trace phases.

Because of these differences, it was necessary to include hematite (as a reagent), biotite, ilmenite and apatite to the model. Information was available in the literature on all of these, and this was used to determine the amount of acid that would be consumed by the total dissolution of each phase. However, kinetic data at the appropriate conditions was not available. In the case of ilmenite and apatite, this was addressed by using Ti and P dissolution data from the sedimentary leach tests. This was not possible for biotite and hematite and it was, therefore, necessary to make certain assumptions. These assumptions were:

1. Because the hematite is being added as a very finely divided reagent, it will undergo complete dissolution in the first hour.
2. Biotite will have similar dissolution properties to chlorite.

The risks associated with these assumptions become apparent when considering the results of the model as given in Figure 83. This shows that in all but one of the samples, Fe-oxide will be expected to be the major acid consumer. The only sample where Fe-oxide is not predicted to be the dominant acid consumer is SH2. In this sample the dominant acid consumer is expected to be biotite. Because these two phases feature so prominently in the predicted acid consumption data, the model will be extremely sensitive to the assumptions stated above.

Chapter 12. Acid Leach Tests

12.1. Introduction Aims and Objectives

The leach tests conducted in Part I were aimed at assessing the effect of sample composition, pH, Eh and grind size on reagent consumption and U dissolution, as well as to provide data for testing and refining the predictions of the model. In order to achieve these aims it was necessary to leach the samples at various conditions of pH, Eh and grind size. However, the low masses of the igneous samples constrained the number of tests that could be performed. Therefore it was only possible to perform one test per sample.

Because of the limitation in the number of tests that could be performed, it was necessary to restrict the aims to only the most important. Thus the aims were:

1. To provide U dissolution data (under typical leach conditions).
2. To provide reagent consumption data (under typical leach conditions).

These would make it possible to test and, if necessary, recalibrate the sedimentary model for its application to igneous ores.

12.2. Methodology

As far as possible the methodology was kept the same as that as described in Section 6.2. However, a brief summary is given below. For a more detailed description, including the reasons for selecting the various leach conditions see Chapter 6.

Approximately 2 kg aliquots of each sample were leached at a 50:50 solid to liquid ratio. The grind size of the samples was 80% passing 212 µm. The pH was controlled at ~1.5 using concentrated sulphuric acid and the redox potential controlled with the addition of MnO_2. The target redox potential was 450 mV SCE. Both the sulphuric acid and MnO_2 were analytical reagent grade.

To address the shortage of Fe in the samples, 3 g/kg of hematite was added (Johnson, 1990). Associated Chemical Enterprises chemically pure Fe_2O_3 was used, as analytical reagent grade hematite was not available. However, the purity of the reagent was tested and found to be acceptable for use in the leach tests.

A preconditioning period of an hour was used where the pH was controlled, but the redox potential was not. After the hour the Fe was added and then the redox potential controlled. This was considered to be the start of the leach for assessing the U dissolution, but when the gangue dissolution is considered, it is important to consider the preconditioning period. As was observed in Part I, the control of the redox potential was complicated by the slow leach kinetics of the MnO_2.

Samples were taken of the slurry at 1, 3, 8 and 24 hours after the addition of the hematite. These were filtered. The solutions were bottled and the residues washed (first with barren, pH 3, sulphuric acid solution and then with distilled water) and dried. The masses of the original slurry sample, the washed residue and dried residues were all recorded.

All of the solution samples were analysed by ICP-OES for Si, Al, Mg, Fe, Na, K and Ca, and by ICP-MS for U and Th. All of the residues were pulverised and analysed by XRF for major mineral composition. The 3 and 24 hour residues were also analysed by XRF for major elements and ICP-MS for U and Th.

12.3. Results

The actual leach conditions (Table 88 and Appendix C) differed slightly from the target leach conditions. In general the pH was fairly close to the target pH of 1.5, while the Eh varied significantly, ranging from 416 mV (SJ2) to 481 mV (SH1). The temperature in all the leaches was close to 42 °C.

Table 88: Actual conditions used in the leaching of each sample (each value represents a time weighted mean)

Sample	SH1	SH2	SJ1	SJ2	Val
pH	1.49	1.48	1.47	1.47	1.40
Eh (mV SCE)	481	441	425	416	421
T (°C)	41.8	41.6	41.4	41.5	42.4

In spite of adding sufficient, very finely divided Fe to the leach as a reagent, Figure 84 shows that the solution Fe concentrations were all below those recommended by Johnson (1990). The Val sample had the highest solution Fe concentration throughout the duration of the leach, while SJ1 had the lowest. The SH2 sample had a very similar solution Fe concentration to SJ1.

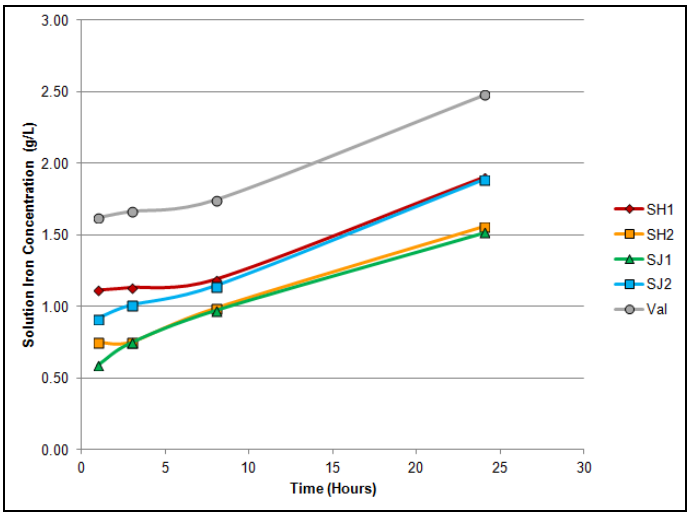

Figure 84: Solution iron concentrations showing progressive increases with time. Due to the very fine nature of the hematite reagent, it appears that some passed through the filter during the filtering of the 1 and 3 hour residues (resulting in the noise seen in these values). Therefore the first two data points for each leach should be treated with caution.

12.3.1. Uranium Dissolution

The U dissolution in each of the five leaches is shown as a function of time in Figure 85 and Table 89 gives the final U dissolution values. For comparison, the predicted U dissolution, based on the mineralogy has also been given.

The predicted and measured U dissolution for the SH1 sample were very similar. This was not the case for the rest of the samples. A number of surprising results were observed. Table 89 suggests that samples SH2 and SJ2 had U dissolutions in excess of 100%. However, the work of Youlton and Kinnaird (2013) indicate that leach tests of this type have an average error of 3.89%. This would suggest that the actual dissolution for samples SH2 and SJ2 could be 97.28 and 99.17% respectively. Both values are slightly higher than those predicted from the mineralogical data.

The Val sample also showed a significantly higher U dissolution that was predicted by the mineralogy, however, unlike samples SH2 and SJ2 where the differences were small, the difference between the measured and predicted U dissolution was ~19%.

There was also a large discrepancy between the predicted and measured U dissolution for sample SJ1, where almost 30% less U was leached than would be expected from the mineralogical data.

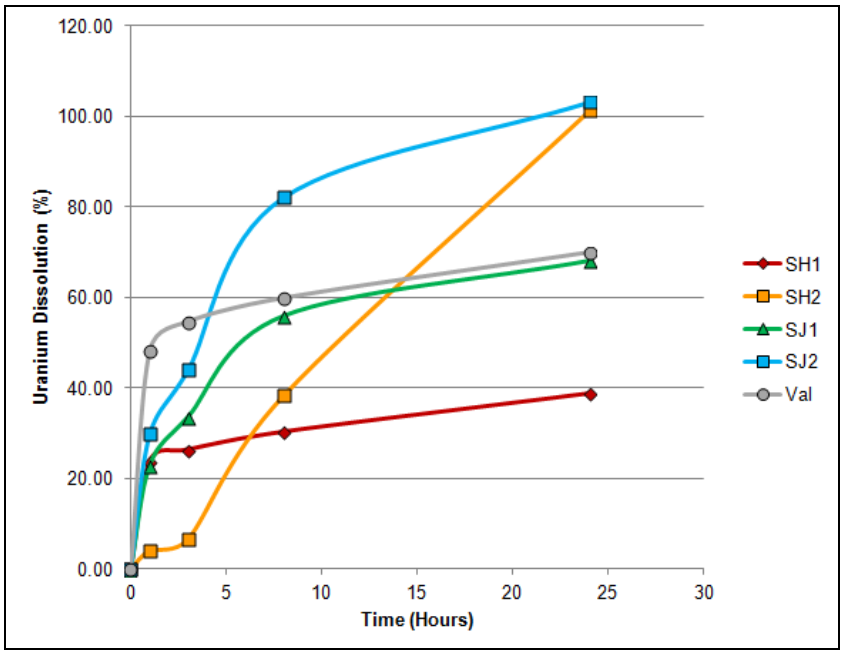

Figure 85: Uranium dissolution curves for each sample, showing the percentage of the uranium dissolved during the leach tests given as a function of time.

Table 89: Percent uranium dissolution at the end of each leach test, as well as the predicted uranium dissolution based on the mineralogy and the difference between the predicted and measured dissolutions

Sample	SH1	SH2	SJ1	SJ2	Val
Units	%	%	%	%	%
Measured	38.67	101.17	68.05	103.06	69.92
Predicted	38.13	96.90	97.58	94.58	50.65
Difference	0.55	4.28	-29.53	8.48	19.27

12.3.2. Gangue Dissolution and Reagent Consumption

The pronounced changes in major mineral composition that were seen in the leach products of the sedimentary samples (Figure 56 and Figure 57), were not seen in the igneous samples. As was predicted from the mineralogical data (Chapter 11), there was very little change in the overall composition of the samples during the leach. The X-ray diffractograms, in Figure 86 to Figure 90, show that the only noticeable changes in the major mineralogy of the samples is

a progressive decrease in the abundance of chlorite and biotite, the dissolution of calcite from sample SH2 (Figure 87), in some cases the formation of gypsum and variations in the amount of hematite. Because hematite occurs in the samples, and was added as a reagent (after the hour of pre-treatment), the abundance of hematite does not follow the simple pattern, of progressive dissolution, seen in the phyllosilicates.

During the modelling of the dissolution behaviour of the samples, it was assumed that complete dissolution of hematite would occur within an hour of being added to the leach. The XRD analyses show that this is not the case and that complete dissolution of hematite did not occur, even by the end of the leach (a dissolution period of 24 hours).

Assumptions were also made regarding the dissolution behaviour of biotite. These assumptions resulted in predicted biotite dissolutions of ~50% for samples SH2 and SJ1. However, Figure 87 and Figure 88 show that the actual dissolution was significantly lower.

The application of Equation 60 in the prediction of the MnO_2 consumption also involved assumptions that proved to be untrue. Because the MnO_2 demand is based on leach solution properties (particularly Fe ion abundances and speciation) and Equation 60 is based on ore properties, the inherent assumption is that the Fe in the rocks has similar dissolution properties. This proved not to be a valid assumption. This is not a surprising result. There were differences in the mode of occurrence and abundance of the Fe in the ore (as compared to the sedimentary samples). Iron was also added to the leach as a reagent. A new equation will be needed for the prediction for the MnO_2 demand for these ores.

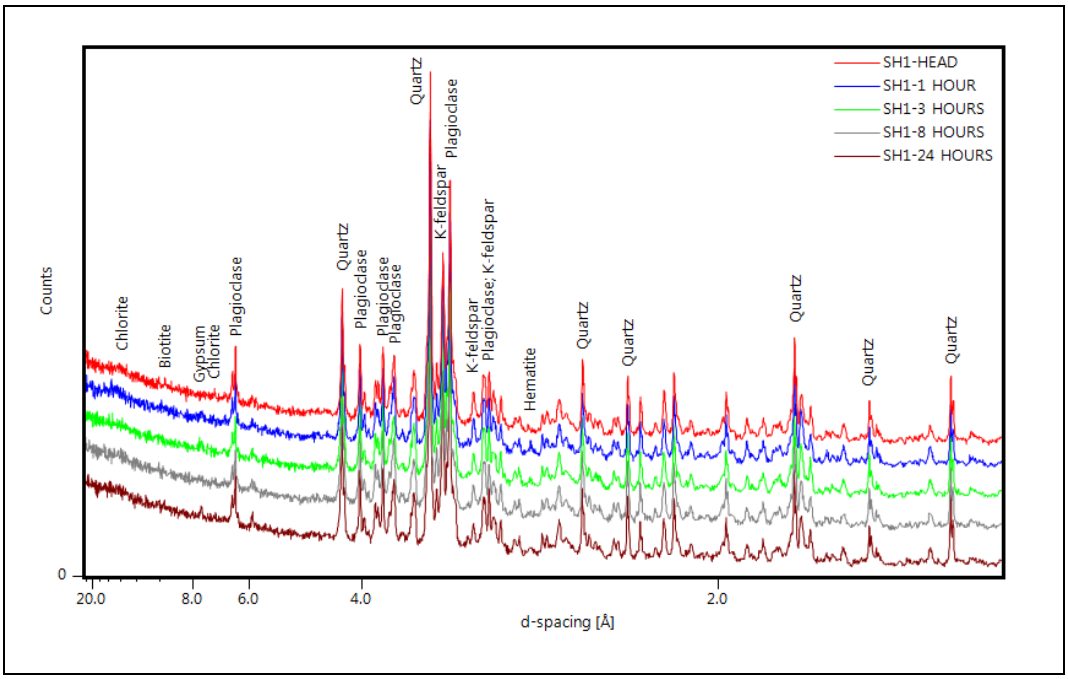

Figure 86: X-ray diffractograms of the SH1 head sample and residues. Besides the appearance of a hematite peak at 2.70 Å a in the 1 hour residue, the progressive disappearance of this peak in later residues, and the appearance of gypsum in the residues, there is little difference between the patterns.

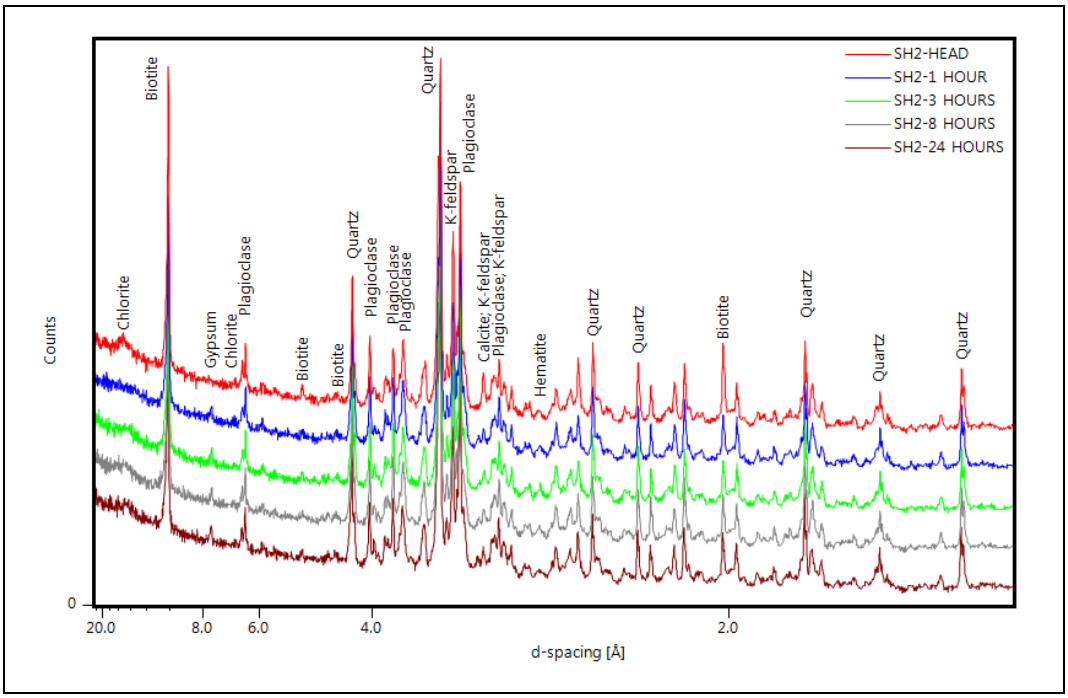

Figure 87: X-ray diffractograms of the SH2 head sample and residues. The overall mineralogy did not change significantly during the leach, however, calcite was dissolved, gypsum formed, chlorite and biotite were partly depleted and variations can be seen in the hematite peak.

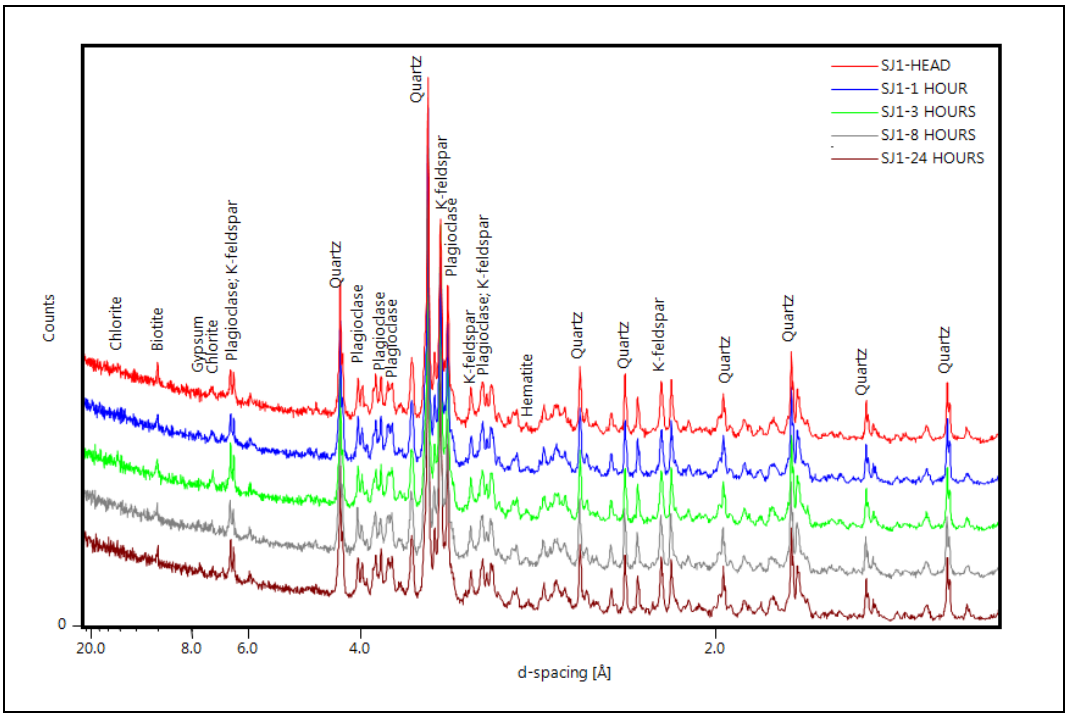

Figure 88: X-ray diffractograms of the SJ1 sample showing little change in the major mineralogy of the sample from the head sample to the residues. Partial depletion of chlorite and biotite occurred, gypsum formed and variations in the amount of hematite were observed.

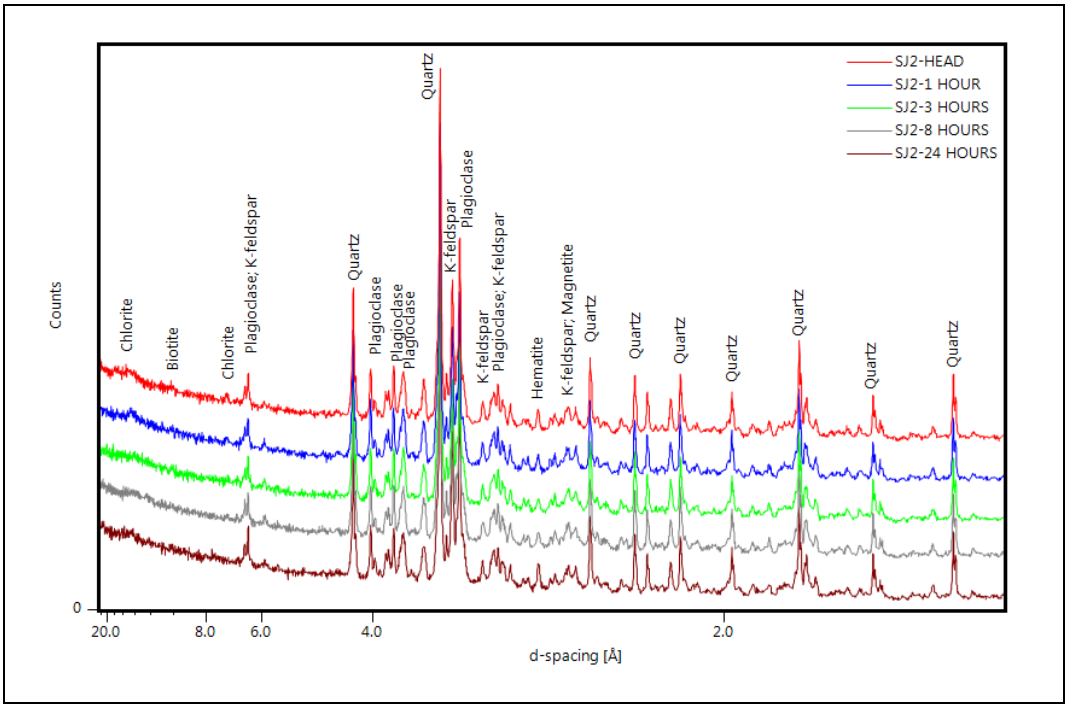

Figure 89: X-ray diffractograms of the SJ2 sample showing little change in the major mineralogy of the sample from the head sample to the residues. Almost complete dissolution of chlorite and biotite occurred, and variations in the amount of hematite were observed.

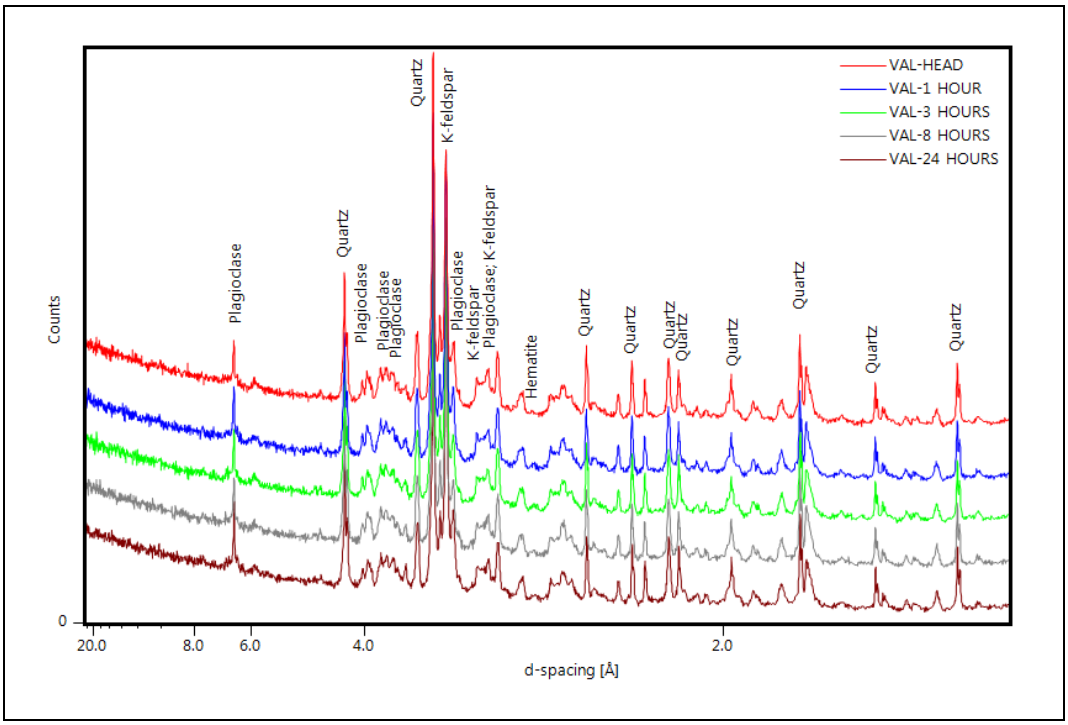

Figure 90: X-ray diffractograms of the Val sample showing very little change in the major mineralogy of the sample from the head sample to the residues. Almost no difference can be seen in the patterns.

For most of the samples Equation 60 underestimated the MnO_2 demand (Table 90), the only exceptions were samples SH2 (where the MnO_2 demand was overestimated) and SJ2 where the predicted and measured values were fairly similar.

Table 90: A comparison between the MnO_2 demand, predicted during the modelling, and the MnO_2 demand of the leach tests

Sample	Predicted kg/ton	Measured kg/ton
SH1	0.00	4.20
SH2	8.57	2.94
SJ1	0.75	3.44
SJ2	3.65	3.34
Val	0.00	3.97

The model correctly predicted that the Val sample would have the lowest acid demand and SH2 the highest (Table 91). However, because of errors in the

predicted dissolution of hematite and biotite, and the incorrect prediction of the MnO_2 demand, large discrepancies were seen between the predicted and measured acid demands. The measured acid demands were between ~18 and 25 kg/ton, while the modelled acid demands were between ~27 and ~124 kg/ton. The largest error (over 400%) was seen in SH2 due to the high biotite content of this sample.

Table 91: A comparison between the acid demand, predicted during the modelling, and the acid demand measured during the leach tests

Sample	Predicted kg/ton	Measured kg/ton	Error %
SH1	31.1	22.87	36.19
SH2	123.5	24.52	403.52
SJ1	39.2	22.29	75.75
SJ2	42.4	18.74	126.01
Val	26.8	18.29	46.79

12.4. Discussion

The prediction of U dissolutions in the sedimentary samples was reasonably simple and proved very accurate. This was not the case for the igneous samples. The reason for the complexity in predicting the behaviour of the igneous samples is that U dissolution in these ores is based on two parameters. In the sedimentary samples almost all the U occurred in readily leachable minerals. For this reason, provided the leach solution could access the mineral grain, it would dissolve. While this textural restriction was also true for the igneous samples, the presence of refractory U minerals, made it necessary to simultaneously consider the U deportment and the texture in predicting the U dissolution.

The U deportment is calculated using the mass percentage and U content of each U mineral. This means that the accuracy of the deportment is dependent on the accuracy of the U content used in the deportment calculations. The results of the EDS analyses (Section 10.3.5) show that the U contents of the various

minerals differ from the ideal U content (calculated from the minerals ideal formula). For example uraninite is not pure U oxide, but contains significant amounts of Pb (Figure 70). For this reason the EDS U content was used in the deportment calculation. The work of Kuisma-Kursula (2000) shows that while SEM-EDS analyses have acceptable levels of accuracy (especially in the analyses of heavy elements present as major components), SEM-EDS analyses are not as accurate as electron microprobe wavelength dispersive analysis. While this error is not large, it is one reason for the discrepancy between the predicted and measured U dissolutions. This is likely to be the reason for the small discrepancies between the predicted and measured U dissolution for samples SH2 and SJ2.

The reason for the discrepancy between the predicted and measured U dissolution in the Val sample was the assumption that brannerite is completely refractory. The U deportment showed that the Val sample had ~58% of the contained U within readily leachable minerals. Factoring in mineral texture, the expected U dissolution was reduced to ~51%. However, the measured U dissolution was ~70%. It would not be possible to leach 70% of the contained U (even ignoring the effect of texture) without leaching some of the U from the refractory phases. The dominant refractory phase in this sample was brannerite (which accounted for 35% of the U in the sample). Other refractory phases accounted for so little of the total U that even if they were completely dissolved, they could not have provided the required amount of U. Therefore, it is clear that some U was leached from the brannerite.

This partial recovery of U from brannerite is unexpected considering that Venter and Boylett (2009) referred to brannerite as being “extremely refractory”. However, not all authors share Venter and Boylett’s (2009) pessimistic view of brannerite. Lottering *et al*. (2008) and Bowell *et al*. (2011) both consider brannerite, with higher levels of U and lower levels of Ti, to be less refractory than low U, high Ti brannerite. The results of this study support their assessment

of brannerite leach properties, and indicate that not all U contained within brannerite, from Namibian granite hosted U is refractory, even under conventional acid leach conditions.

The only sample where the mineralogical data suggested better dissolution than was observed in the leach tests was SJ1. This sample was expected to show ~98% U dissolutions, but only 68% U was leached. It is clear that the poor dissolution was not mineralogically controlled.

Table 88 shows that the leach of sample SJ1 had the second lowest redox potential (425 mV SCE) and Figure 84 shows that it had the lowest solution Fe content. It appears that the combination of low Fe content and low redox potential is the reason for the poor dissolution in this sample. Examination of the leach data for sample SJ2 supports this assessment. While SJ2 leach had the lowest redox potential (416 mV SCE) of all the igneous leach tests, SJ2 showed approximately total U dissolution. This is because this sample had the third highest solution Fe content.

Closer inspection of the dissolution curve for the SJ2 sample (Figure 85), further highlights the importance of solution Fe content at low redox potentials. It is clear that U dissolution was slow in the early stages of the SJ2 leach and was then followed by a period of rapid leaching (until approximately total U dissolution). The rapid change in leach rates appears to be the result of the progressive increase in solution Fe content.

A comparison between the results of the modelling (based on the mineralogical data, and using the sedimentary model) showed major discrepancies between the predicted and measured total acid demands. The modelled acid demands overestimated the leach acid requirements. This overestimation ranged from 36% and to over 400%. Careful analysis of the data suggested that there were two reasons for this overestimation and that both related to phases (hematite and

biotite) that were not considered in the sedimentary model. Therefore the discrepancy does not represent a major failure of the model, but rather that extension of the model is required.

Errors were also seen in the predicted and measured MnO_2 demands. The predicted MnO_2 was generally much lower than the required amounts, except in the SH2 leach, where the predicted MnO_2 was significantly higher than the measured demand. These results suggest that Equation 60 will require recalibration for igneous ores in which Fe is added as a reagent.

12.5. Summary and Conclusions

In order to provide leach data to test the predictions made from the result of the mineralogical analyses, the 5 igneous samples underwent acid leach tests. These tests had target conditions of pH 1.5, Eh 450 mV SCE and a 24 hour duration (with a 1 hour pre-treatment).

It was found that prediction of the U dissolution in the igneous ores was much more complex than the same process for the sedimentary ores. This was because only texture was important in the sedimentary ores, while it was necessary to consider both texture and U deportment in the igneous ores. Small errors in the U deportment contribute to small discrepancies between measured and predicted dissolution data.

Large discrepancies between predicted and measured U dissolutions were observed for the Val sample. This was due to the assumption that brannerite is completely refractory. The results of this study show that Namibian granite-hosted brannerite is partially leachable under the conditions and duration of a conventional U leach.

In general the predicted U dissolution was lower than that observed during the leach tests. The only exception was sample SJ1, where the mineralogy predicted over 95% dissolution and the leach test showed only ~70%. It is clear that problems in the leach test resulted in slow leaching of U and were the reason for the poor dissolution. This highlights the importance of being able to predict U dissolution from mineralogical data, as it makes it possible to detect problems in the leach test that may not be immediately obvious. If the mineralogical data had not been available, it may have been (incorrectly) assumed that the SJ1 sample was refractory. However, because the mineralogical analyses are based on completely different principles to the leach tests, they provide a completely independent data set that can be used for validation.

Iron dissolution was lower than expected and the solution Fe concentrations did not reach the levels recommended by Johnson (1990). These low levels of Fe coupled with a low redox potential were the reason for the low U dissolutions in the SJ1 sample. However, the results of the leach tests on samples SH2 and SJ2 show that provided the redox potential is high, the leaches are not excessively sensitive to solution Fe content, and will tolerate lower levels than the 3 g/L recommended by Johnson (1990).

The SJ2 leach also shows that the slow dissolution of Fe can slow the U leach kinetics at the beginning of the leach. For this reason it is recommended that the hematite be added at the start, rather than the end, of the pre-treatment.

The application of the model, which was developed for the sedimentary ores, to the igneous samples resulted in overestimations of the acid demand of between 36 and over 400%. The overestimation was the result of errors in the prediction of the dissolution of hematite and biotite. As neither of these minerals were specifically considered in the sedimentary model, it is not surprising that the prediction of their leach properties was incorrect. The model will therefore need to be extended to include these phases to allow for application to igneous rocks.

Chapter 13. Model Calibration for Igneous Ores

13.1. Introduction

The aim of the model calibration was to address the discrepancies between the predicted and measured reagent consumption data. As discussed in Chapter 12, the main reasons for the discrepancies were:

1. Overestimation in the dissolution of hematite. The hematite dissolution was assumed to be complete within the first hour (because the hematite was added as a finely divided reagent). The results of the leach test show that complete dissolution of hematite did not occur within the 24 hour duration of the leach tests.
2. Overestimation in the dissolution of biotite. As biotite was not present in significant levels in the sedimentary ores, the sedimentary model did not include biotite. The specific surface areas were estimated using the same methodology as for the phyllosilicates in the sedimentary ores and the constants used in the dissolution calculations were assumed to be the same as those of chlorite.
3. Equation 60 failed to accurately predict the MnO_2 demand for the igneous ores. This was due to differences in the concentration and mode of occurrence of Fe between the sedimentary and igneous samples. This was because the igneous samples contained very low levels of inherent Fe and therefore hematite was added as a reagent.

13.2. Methodology

The calibration of the model for the igneous ores involved detailed comparisons of the results of the mineralogical study and the leach tests. Because the

samples contain low levels of inherent Fe, and the hematite concentrations are so close to the detection limit of XRD, the solution Fe contents were used to assess the hematite dissolution, rather than relying on XRD analyses of the residues (which would be subject to higher degrees of error).

The biotite calibration involved checking the two basic assumptions (that the surface area calculation would be the same as the phyllosilicates in the sedimentary samples, and that biotite had similar dissolution constants to chlorite). The results were then corrected such that it was no longer necessary to make such assumptions. This process involved two phases:

1. Careful assessment of the surface area calculation to determine its applicability to biotite in these samples.
2. Derivation of the dissolution constants for biotite. ICP-OES K concentrations (corrected for K-feldspar dissolution) were used to determine the biotite dissolution rate and dissolution constants.

The MnO_2 demand equation (Equation 60) was also re-derived for the igneous ores.

13.3. Results and Discussion

13.3.1. Iron Oxide Dissolution

Figure 91 shows the Fe dissolution as a function of time (calculated from the solution Fe contents and corrected for the Fe content of the tap water that was used in the leach). For some of the samples the 1 hour data point suggests higher dissolution than the 3 hour data point. This is because the hematite reagent contained a proportion of ultra fine material which did not dissolve in the first hour. This material passes through the filter that was used to separate the

solution from the 1 hour residue. For this reason the 1 hour data was not included in the assessment of the Fe dissolution.

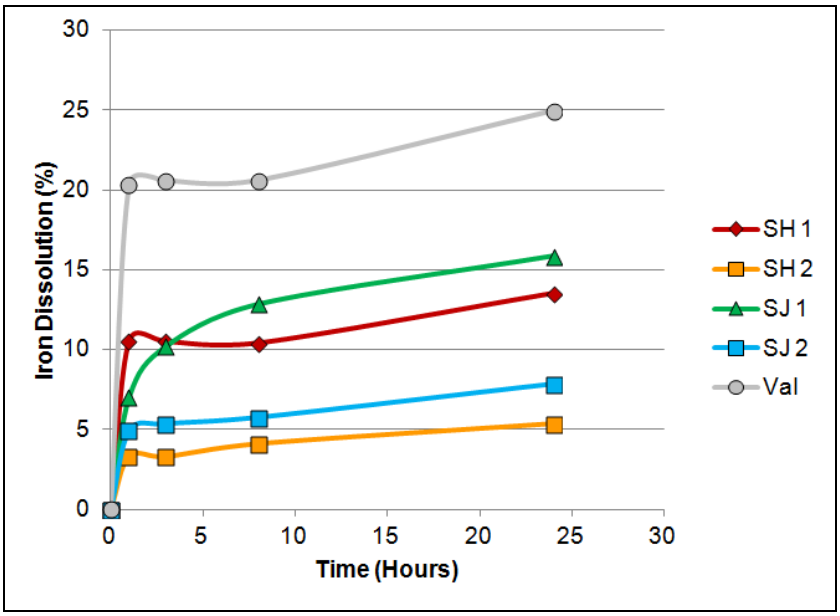

Figure 91: Iron dissolution as a function of time. It can be seen that in some cases the percentage dissolution is higher at 1 hour than at 3. This is because the Fe reagent that was added to the leach contained a portion of ultra fine material which (although it did not dissolve in the first hour) was fine enough to pass through the filter and result in the error in the 1 hour data point. For this reason the 1 hour point was not included in the dissolution calculations.

Analysis of the leach data showed that the percent Fe dissolution is not just a function of time. It is also a function of what proportion of the total Fe in the leach is represented by hematite added as a reagent. The function that was found to best predict the dissolution of Fe is given in Equation 72:

$$FE = (0.00699 \times t + 0.308) \times F$$

Equation 72

Where FE is the percentage Fe dissolved during the leach, t is the leach duration in hours and *F* is the proportion (as a percentage) that the hematite (added as a reagent) makes up of the total Fe in the leach.

Comparing the predictions of Equation 72 with the measured results of the leach tests (Figure 92) shows that there is good agreement between the predicted and

measured Fe dissolutions. There is some scatter evident, which is due to variations in the minerals which host the Fe from one sample to another.

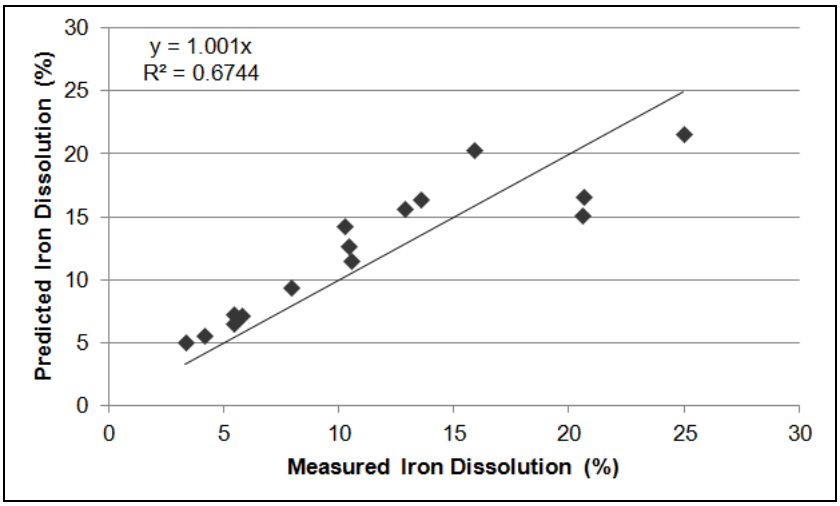

Figure 92: Comparison of the measured iron dissolution with that predicted using Equation 72. The level of agreement is good, with the scatter due to variations, from sample to sample, in the minerals which host the iron.

13.3.2. Biotite Dissolution

A comparison, of the estimated surface areas of the phyllosilicates (at the same grind size) from Part I and Part II is given in Table 92. This table shows that while the estimated chlorite specific surface areas fall into a similar range in both the igneous and sedimentary samples, the biotite surface areas are much higher than those of any of the other phyllosilicates in all of the samples. This over estimation could be due, either to an overestimation of the surface roughness, or an underestimation of the average grain size.

Table 92: Comparison of phyllosilicate estimated specific surface areas from Parts I and II, suggesting that biotite specific surface areas have been overestimated

Name	**Mooi -212**	**RAO**	**OAO**	**SH1**	**SH2**	**SJ1**	**SJ2**	**Val**
Units	**m^2/g**	**m^2/g**	**m^2/g**	**m^2/g**	**m^2/g**	**m^2/g**	**m^2/g**	**m^2/g**
Muscovite	1.96	1.04	2.91	-	-	-	-	-
Biotite	-	-	-	4.73	4.28	4.59	7.95	5.21
Chlorite	2.18	1.61	-	1.44	2.81	1.78	1.55	1.34

During the comminution of the SH2 sample it was observed that biotite was very resistant to milling and made up a major proportion of the +212 µm fraction. As the +212 µm fraction represented 20% of the sample, and the sample only contained 11.3% biotite, a large proportion of the contained biotite must have been coarser than 212 µm. This is not supported by the grain size estimated from the BMA data (which suggest that biotite had an average grain size of 21.19 µm). This discrepancy was found to be a reason for the overestimation of the biotite dissolution and resulted from the coarse, liberated nature of the biotite.

During preparation of the transverse polished section the biotite was preferentially aligned, such that the BMA analysis oversampled the biotite sheet thickness at the expense of the sheet length (Figure 93).

A comparison of the average size measured from the BMA line scans, with average sizes determined from particle maps of normal polished sections (Table 93) highlights this effect (and shows that the BMA data estimate the sheet thickness, while the particle maps estimate the sheet lengths). Using these dimensions and the roughness values calculated using Equation 64 yielded the surface area results in Table 93. These values are significantly lower and correspond well with the other phyllosilicates. It can also be seen that the average sheet length of the biotite in SH2 is coarser than 212 µm, which corresponds with the observations made during the comminution.

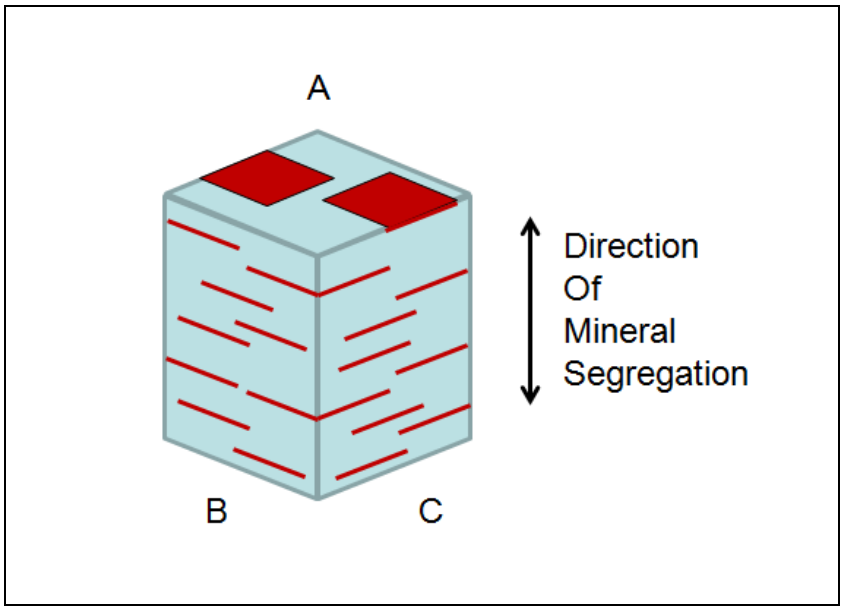

Figure 93: Schematic diagram showing alignment of grains of coarse liberated platy minerals (in this case brown sheets of biotite) when poured into a sample mould (note that moulds are usually cylindrical and surfaces B and C only become flat after cutting and grinding). As milled sample material is poured into the mould for the preparation of the polished blocks, the platy mineral tends to align horizontally. For this reason, if the polished block is prepared to expose either surfaces B or C the sheet thickness will be over sampled, while if the polished block is prepared to expose surface A, the sheet length will be over sampled (the degree of alignment of the grains has been exaggerated for the purposes of illustration). Normal polished sections tend to expose surfaces more similar to surface A, while transverse polished sections expose surfaces B or C in order to facilitate accurate sampling across the direction of mineral segregation. The direction of BMA line scans is typically selected such that the individual lines run in the direction of mineral segregation (again to ensure sampling across the segregation). This further over samples the sheet thickness (at the expense of the sheet length).

Table 93: Average biotite sheet thickness (calculated from the BMA), sheet length (calculated from the particle maps), length to thickness ratio (L/T) and biotite estimated surface areas

Parameter	**Thickness**	**Length**	**L/T**	**SA**
Units	**µm**	**µm**	**-**	**m^2/g**
SH1	7	172	25	0.41
SH2	14	424	30	0.19
SJ1	5	54	12	2.09
SJ2	3	18	7	1.75
Val	6	80	14	0.49

Using the K dissolution data (corrected for K-feldspar) the percentage biotite dissolution was determined. The biotite dissolution constants were found to be 1.16 for the initial rate and -0.15 for the decay constant. Figure 94 shows the measured and calculated biotite dissolution as a function of time.

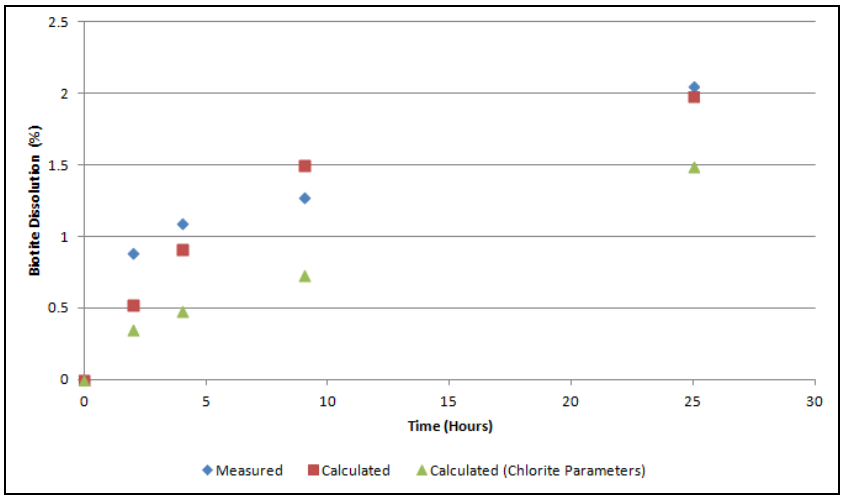

Figure 94: Measured and calculated biotite dissolution expressed as a function of time for sample SH2. For comparison the biotite dissolution data, calculated using the parameters from chlorite, have also been shown. Use of the chlorite parameters would slightly underestimate the biotite dissolution.

Figure 94 also shows the predicted biotite dissolution for sample SH2 calculated from using the constants from chlorite, but with the corrected surface area data. A comparison of the data shows that using chlorite's constants would cause an underestimation of the biotite dissolution, however the error resulting from this assumption was small relative to the error in the surface area (compare Table 92 with Table 93).

13.3.3. Manganese Demand Equation

The calibrated MnO_2 demand equation is given below (Equation 73):

$$\mathbf{MnO_2 = 2.56 \log [Fe^{2+}] + 0.004559\ Eh + 1.02}$$

Equation 73

Where MnO_2 is the manganese dioxide demand in kg/ton, $[Fe^{2+}]$ is the ferrous iron content of the ore in percent and Eh is the redox potential in mV SCE.

A comparison of the measured MnO_2 demands with those calculated using Equation 73 is given in Table 94. These results show that the MnO_2 demand can be predicted to within 7% error.

Table 94: Measured manganese dioxide demands compared with those calculated using Equation 73 (errors are calculated on values using more decimal places than are shown below, therefore although values appear the same to two decimal places, they are not identical)

Parameter	Measured	Predicted	Error
Units	**kg/ton**	**kg/ton**	**%**
SH1	4.20	4.20	-0.07
SH2	2.94	3.12	6.32
SJ1	3.44	3.57	3.70
SJ2	3.34	3.34	-0.16
Val	3.97	3.97	-0.09

13.3.4. Comparison of Measured Acid Demands with those Predicted by the Calibrated Model

The calibrated model was able to predict the acid demand to within 10% and for most samples to within about 5% (Table 95).

Table 95: Comparison of measured acid demands with those predicted from the calibrated model

	Predicted	Measured	Error
Sample	**kg/ton**	**kg/ton**	**%**
SH1	22.96	22.87	0.39
SH2	24.85	24.52	1.35
SJ1	24.36	22.29	9.27
SJ2	17.83	18.74	-4.85
Val	19.25	18.29	5.28

13.4. Summary and Conclusions

The leach testwork highlighted three major factors that contributed to the discrepancy between the actual acid consumptions and those predicted by the uncalibrated model. These related to the dissolution of iron oxides and biotite and the MnO_2 demand of the leach test.

In the uncalibrated model iron oxide dissolutions were assumed to be rapid and to be approximately complete. This was found to be incorrect and that Fe dissolutions did not exceed 25% in any of the leaches. It was found that the extent of Fe dissolution was a function of two factors, time and the proportion that the added hematite represent as a percentage of the total Fe in the leach. As would be expected, Fe dissolution was more complete when the added Fe represented a higher proportion of the total Fe. This is because the hematite reagent was a fine, completely exposed powder, while the Fe in the ore was not completely exposed, nor was it as finely ground.

An equation was developed which allowed for the prediction of the degree of Fe dissolution. This equation not only made it possible to correct the acid consumption predictions, but is also valuable in predicting the amount of Fe that would be available in solution (to catalyse the oxidation of U). As was shown in Chapter 12, solution Fe concentrations play a critical role in ensuring U dissolution. Using Equation 72 is will be possible to predict the amount of finely ground hematite that must be added to achieve a particular solution Fe content within a given time.

The error in the biotite dissolution had two causes, the specific surface area calculations and the lack of dissolution constants. The use of the BMA data collected from transverse polished sections resulted in significant underestimation of the average grain size of the biotite (which in turn increased the specific surface area).

The coarse liberated nature of the biotite resulted in preferred orientation, with sheet edges preferentially exposed in certain orientations and sheet surfaces exposed in others. The use of transverse polished sections resulted in the oversampling of the biotite sheet thickness, at the expense of the sheet length. This was further exacerbated by the use of the line scans and resulted in the underestimation of the biotite grain size.

The ability to preferentially sample sheet thickness by one method, and sheet length by another, was exploited in determining the correct grain size properties of the biotite. It was then possible to calculate accurate grain sizes and shapes, which were used to derive specific surface areas.

There are two reasons for the surface area calculation method (described in Section 5.2) producing acceptable results for muscovite (in Part I) and chlorite (in Parts I and II), but not for biotite. These are both due to textural differences. The biotite is both coarser and better liberated than the muscovite and chlorite. The coarser the grain, the more it deviates from the 1:1 length to thickness ratio assumed in the stereological correction. For the coarsest biotite this ratio was as high as 30:1 (Table 93). The effects of liberation on preferred orientation have already been discussed.

While the use of chlorite dissolution constants in the uncalibrated model was not as precise as using constants specifically developed for biotite, the error introduced was small relative to the error from the surface area determination. If the use of these constants had been the only source of error in the biotite dissolution, it would have resulted in an underestimation of the dissolution of biotite. However, because of the large overestimation in the surface area, the use of the chlorite constants slightly offset the error introduced by the incorrect surface areas.

The incorporation of these corrections, as well as a revised MnO_2 demand equation, made it possible to predict the acid demand characteristics of the material to within 10% accuracy for all samples, and about 5% accuracy for most. The SJ1 predicted acid consumption was less accurate than those of the other samples. The increased error in this sample is probably due to splitting error in the preparation of the polished sections.

Chapter 14. Conclusions

In Part I of this study it was found that XRD data could be used to predict acid consumptions with an average error of 26%. The major limitation was the lack of textural data, rather than the detection limit (as would be expected from the work of Reynolds *et al*. (2010)). It was also found that, in the absence of refractory U, the main mineralogical controls on U dissolution are the exposure and association characteristics of the U minerals. For the sedimentary samples it was possible to make very accurate predictions of the U dissolution.

The prediction of both reagent consumptions and U dissolutions were far more complex in the igneous ores.

14.1. Gangue Dissolution and Reagent Consumptions

The igneous ores contained very high levels of low reactivity minerals in the form of quartz and feldspar. While this is desirable, as it results in very low reagent consumptions, it necessitates very accurate quantification of minerals present in low concentrations to be able to predict the reagent consumptions. Traces of calcite occur in all the samples as vein fill material (probably remobilised carbonate from the country rock) and as an alteration product of plagioclase. While the levels of calcite were low in all of the samples, it was necessary to consider calcite in order to obtain accurate predictions. Phyllosilicates (in the form of chlorite and biotite) were not abundant in most samples; the only exception was sample SH2 which contained unusually high levels of biotite.

Because of the need for very accurate mineral quantification at low levels, the XRD was completely unsuitable for providing that data needed for predicting the reagent consumption. This was not only because of the lack of textural data, but also because of the high detection limit of the XRD when compared to

QEMSCAN BMA analyses. However, a comparison of the results of Parts I and II shows that, while XRD may not be universally applicable in predicting reagent consumptions, the larger the gangue acid consumption of the ore, the more useful the XRD became in predicting the acid consumption.

The need to quantify low levels of mineral was not the only reason for the increased complexity of the igneous ores. In order to model the mineral dissolutions it is necessary to have an estimate of the specific surface areas of the minerals. For all of the minerals in the sedimentary samples (and most minerals in the igneous samples) BMA data were adequate for estimating mineral surface areas. This even included phyllosilicates such as muscovite and chlorite. However, the igneous samples contained coarse liberated biotite. For this phase, even the BMA analyses were not adequate. It was necessary to specifically measure the sheet thickness and sheet lengths in order to obtain a reasonable surface area estimate.

One of the aims of this study was to develop an equation which would allow for the use of XRD data to predict acid consumptions. The IAEA (1980) state that it is not possible to explicitly predict the behaviour of certain gangue phases, especially the silicates and sulphides. This would suggest that developing an equation to predict the acid consumption characteristics of an ore, from mineralogical data, would not be possible. It was found that it is indeed not possible to produce a single universal equation, which could use XRD data to predict the acid consumptions, both because of the limitations of XRD and the complexity of the dissolution of gangue minerals in acid.

Due to the complexity of the ore, it was necessary to develop a model which considered mineral abundances, specific surface areas, parabolic dissolution kinetics, incongruent dissolution, gypsum formation, hydrogen ion activity, ionic strength and the formation of ion pairs in solution, as well as the build up of SO_4^{2-} in solution and its effect on the second acid dissociation of sulphuric acid. This

model was developed for the sedimentary samples and then applied to the igneous samples to determine the potential to extrapolate the model to ores for which it was not specifically calibrated.

The difficulties in directly applying the uncalibrated sedimentary model to the igneous ores (in one case resulting in an error in excess of 400%) highlight the danger of extrapolating the model to ores for which it was not calibrated. There were four phases which needed to be considered in the igneous model that were not considered in the sedimentary model. These were ilmenite, apatite, hematite (added as a reagent to facilitate U oxidation during the leach) and biotite. Once the model had been calibrated for these phases it was possible to predict the acid consumptions of the ore to within 10% for all samples, and in most cases to within about 5%.

These results suggest that while the basic principles of the model are universally applicable (and establish the parameters which control reagent consumption); the application of the model to ores, that include minerals that have not been studied, will require certain assumptions. The accuracy of the predictions of the model will be very dependent on the reliability of these assumptions.

14.2. Uranium Dissolution

For ores with no refractory U content, QEMSCAN TMS textural analyses provide very accurate predictions of the U dissolution and can even facilitate predictions of changes in U dissolution in response to changes in leach conditions. For ores with a refractory component the process is more complex.

Uranium mineral composition data are vital to accurately determine the U deportment, which gives the proportion of the U hosted in refractory phases. Both the U deportment and the U mineral exposure need to be simultaneously

considered in the dissolution prediction. Due to the complexity of this process, these were much larger discrepancies between the predicted and measured U dissolutions of the igneous ores than the sedimentary ores. In some cases it is clear that the analytical error of the leach itself contributed to the discrepancy. It was also found that in one sample ~40% dissolution of brannerite occurred, which suggests that not all refractory phases are completely refractory.

In one of the samples the discrepancy served to highlight the importance of using mineralogical data in addition to leach tests. For sample SJ1, the mineralogical analyses predicted very high U dissolutions, which were not seen in the leach test. Because of the discrepancy, the leach test was carefully scrutinised and it was found that at low redox potentials, the leach tests are very sensitive to solution Fe concentrations. In this leach the poor dissolution was not due to the mineralogy, but the leach test. If it were not for the mineralogical data, this sample may have been erroneously assumed to contain a refractory component. Because the mineralogical analyses have completely different basic principles to the leach tests, they are not subject to the same errors and a comparison of the two data sets serves as valuable validation process.

In conclusion the combination of XRD and QEMSCAN analyses (augmented by XRF data and Fe speciation) is capable of predicting the leach response of the Southern African U ores analysed in this study. However, the process is complex and the most accurate results are only possible if a calibrated model is applied.

Chapter 15. Recommendations for Further Work

This project identified the parameters necessary to use mineralogical data to predict gangue reagent consumption in U leaching. An Excel-based model was developed to make these predictions. This model can be used to predict leach responses of U ores and would result in reduced technical risk when developing new U prospects. It would also aid in mine planning, by making it possible to predict reagent consumption across a deposit, and in so doing make it possible to more accurately predict the costs of beneficiation.

The ability to predict the process characteristics, of various parts of an ore body, would also make it possible to more accurately predict the reagent needs of the processing plant well into the future. This predictability would aid in ensuring the adequate supply of reagent to the plant.

Preliminary results from this study were included in a presentation by the Author at the Alta U conference in Australia in 2011 and published in the conference proceedings (Youlton *et al.*, 2011).

A second paper detailing the results of the mineralogical investigation, leach tests and modelling as applied to the sedimentary samples has been published in the journal Minerals Engineering (Youlton and Kinnaird, 2013).

An abstract, detailing the results of the analysis of the igneous samples, has been accepted for presentation at the 21st Meeting of the International Mineralogical Association (IMA 2014).

The outcomes of this study also suggested three major areas that warrant further investigation:

1. Grind optimisation of the Kayelekera material.
2. Better constraining the detection limits of XRD.
3. Extension of the model to Witwatersrand ores.

15.1. Grind Optimisation

Further work is recommended to improve the understanding of the relationship between grind size and U mineral exposure and in so doing determine the optimal grind for leaching of material from Mooifontein and Kayelekera. Bulk samples could be collected from both U occurrences. The bulk samples could then be crushed and split into a number of aliquots for further analysis. These aliquots could then be milled to various particle sizes and either examined by QEMSCAN, or acid leached, to determine the effect of grind on U exposure. Blending of mudstone and arkosic ore should also be investigated, in order to determine if this would result in a reduction in the time taken to mill the mudstone. The analysis of the results of these tests should also consider the increase in energy and reagent costs associated with using a finer grind.

15.2. Detection Limits of XRD

Further work is also recommended to aid in estimating the detection limits of XRD. The detection limits of various minerals were determined as part of this study and it was found that the detection limit is a function of the d-spacing of the main peak, the calibration constant and the mass absorption coefficient of the sample. The position of the main peak of a mineral is usually readily available from the literature and the mass absorption coefficient can be estimated from the lithology of the host rock. However, the major limitation in estimating the

detection limit of a new mineral is the calibration constant. This work could aim to develop a method which uses a readily available mineral property (possibly the reference intensity ratio) to estimate the calibration constant and therefore aid in estimating the detection limit of a particular mineral in a particular matrix.

It was also noticed in the original XRD work (Chapter 4) that muscovite was not detected in RAO and MSO. However, in the XRD analyses of the leach residues (which were measured on the same instrument, but with a new tube), muscovite was detected in these samples. Therefore the detection limit is also a function of the tube condition. Further work is recommended to understand the effect of tube age on the background noise and peak intensity.

15.3. Extension of the Model to Witwatersrand Ores

The ores of the Witwatersrand represent another important class of Southern African U deposit. The application of the model to these ores would be complicated by the presence of pyrophyllite, chloritoid and elevated levels of pyrite and pyrrhotite (Phillips and Law, 1994 and Robb and Meyer, 1995).

A useful extension of the work in this study would be to quantify the advantages of U leaching in increasing Au recovery in these ores (Lottering et al., 2008), and to determine the gangue mineral dissolution properties which control this phenomenon.

References

Abhilash, S. Singh, K.D. Mehta, V. Kumar, B.D. Pandey, V.M. Pandey, 2009. Dissolution of uranium from silicate-apatite ore by *Acidithiobacillus ferrooxidans. Hydrometallurgy*, **95**, 70-75.

A-Cap Resources, 2009. *Company Projects*. http://www.acap.com.au/companyprojects.htm

Anderson, T.F., 1968. Surface area measurement in calcite grains by isotopic exchange with C^{14} labelled carbon dioxide. *Geochimica et Cosmochimica Acta*, **32**, 1177-1186.

Amram, K. and Ganor J., 2005. The combined effect of pH and temperature on smectite dissolution rate under acidic conditions. *Geochimica et Cosmochimica Acta, **69**, 2535-2546.*

Baron, D. and Palmer, C.D., 1996. Solubility of jarosite at 4-35° C. *Geochimica et Cosmochimica Acta,* **60**, 185-195.

Basson, I.J. and Greenway, G., 2004. The Rossing Uranium Deposit: a product of late-kinematic localization of uraniferous granites in the Central Zone of the Damara Orogen. *Journal of African Earth Sciences*, **38**, 413-435.

Bengtsson, M and Evertsson, C.M, 2006. Measuring characteristics of aggregate material from vertical shaft impact crushers. *Minerals Engineering*, **19**, 1479-1486.

Bengtsson, M. And Evertsson, C.M, 2008. Modelling of output and power consumption in vertical shaft impact crushers. *International Journal of Mineral Processing,* **88**, 18-23.

Berning, J., 1986. The Rossing Uranium Deposit, South West Africa/Namibia. *In*: Anhaeusser, C.R. and Maske, S. (Eds.), *Mineral Deposits of Southern Africa.* The Geological Society of South Africa, Johannesburg, 1819-1832.

Bibi, I., Singh, B. And Silvester, E., 2011. Dissolution of illite in saline-acidic solutions at 25ºC. *Geochimica et Cosmochimica Acta*, **75**, 3237-3249.

Bish, D.L. and Howard, S.A., 1988. Quantitative phase analysis using the Rietveld method. *Journal of Applied Crystallography*, **21**, 86-91.

Blum, A.E., Yund, R.A. and Lasaga, A.C., 1990. The effect of dislocation density on the dissolution rate of quartz. *Geochimica et Cosmochimica Acta*, **54**, 283-297.

Bowden, R.A. Shaw, R.P., 2007. The Kayelekera uranium deposit, Northern Malawi: past exploration activities, economic geology and decay series disequilibrium. *Applied Earth Science (Trans, Inst. Min. Metall. B)*. **116**, 55-67.

Bowell, R.J., Grogan, J., Hutton-Ashkenny, M., Brough, C., Penman, K. and Sapsford, 2011. *Minerals Engineering*, **24**, 1305-1313.

Bradford, L., McInnes, C., Stange, W., de Beer, C., David, D. and Jardin. A, 1998. The development of the proposed milling circuit for the Nkomati Main Concentrator Plant. *Minerals Engineering*, **11**, 1103-1117.

Brandt, C.G. and Kinneging, A.J., 2005. *X-ray Powder Diffraction: A Practical Guide to Quantitative Phase Analysis.* Panalytical, Almelo, 8.

Brandt, F., Bosbach, D., Krawczyk-Bärch, E., Arnold, T. And Bernhard, G, 2003. Chlorite dissolution in the acid pH-range: A combined microscopic and macroscopic approach. *Geochimica et Cosmochimica Act*, **67**, 1451-1461.

Brantley, S.L., 2003. Reaction kinetics of primary rock-forming minerals under ambient conditions. *In: Treatise on Geochemistry*, **5**, 73-117.

Brantley, S.L. and Conrad, C.F., 2008. Analysis of rates of geochemical reactions. *In:* Brantley, S.L., Kubicki, J.D. and White, A.F. (Eds.), *Kinetics of Water-Rock Interactions*. Springer Science, 1-37.

Brantley, S.L., 2008. Kinetics of Mineral Dissolution. *In:* Brantley, S.L., Kubicki, J.D. and White, A.F. (Eds.), *Kinetics of Water-Rock Interactions*. Springer Science, 151-210.

Briggs, C.A. and Bearman, R.A., 1996. An investigation of rock breakage and damage in comminution equipment. *Minerals Engineering*, **9**, 489-497.

Brown, T.L., LeMay, H.E. and Bursten, B.E., 2003. *Chemistry the Central Science* (9th Edition). Prentice Hall, New Jersey, 635 pp.

Brunauer, S., Emmett, P.H. and Teller, E., 1938. Adsorption of gases in multimolecular layers. *Journal of the American Chemical Society*, **60**, 309-319.

Caglioti, G., Paoletti, A. and Ricci, F.P., 1958. Choice of collimators for a crystal spectrometer for neutron diffraction. *Nuclear Instruments and Methods*, **3**, 223-228.

Casey, W.H., Westrich, H.R. and Holdren, G.R., 1991. Dissolution rates of plagioclase at pH = 2 and 3. *American Mineralogist*, **76**, 211-217.

Chen, Y and Brantley, S.L., 1997. Temperature- and pH dependence of albite dissolution rate at acid pH. *Chemical Geology*, **135**, 275-290.

Chipera, S.J. and Bish, D.L., 2002. FULLPAT: a full-pattern quantitative analysis program for X-ray powder diffraction using measured and calculated patterns. *Journal of Applied Crystallography*, **35**, 744-749.

Cilliers, J.J., Austin, L.G., Leger, P. and Deneys, A., 1994. A method of investigating rod motion in a laboratory rod mill. *Minerals Engineering*, **7**, 533-549.

Cleary, P.W., and Morrison, R.D., 2011. Understanding fine ore breakage in a laboratory scale ball mill using DEM. *Minerals Engineering*, **24**, 352-366.

Coetzee, L., Theron, S.J., Martin, G.J., van der Merwe, J. and Stanek, T., 2011. Modern gold deportments and its application to industry. *Minerals Engineering*, **24**, 565-575.

Cole, D.I., 1998. Uranium *in* The Mineral Resources of South Africa (Wilson, M.S.G and Anhaeusser, eds): Handbook, Council for Geoscience, **16**, 642.

Cuney, M., 2009. The extreme diversity of uranium deposits. *Mineralium Deposita*, **44**, 3-9.

Currie, L.A., 1995. Nomenclature in evaluation of analytical methods including detection and quantification capabilities (IUPAC Recommendations). *Pure and Applied Chemistry*, **67**, 1699-1723.

Danielle, M.C., Huminicki, J. and Rimstidt, D., 2008. Neutralization of sulphuric acid solutions by calcite dissolution and the application to anoxic limestone drain design. *Applied Geochemistry*, **23**, 148-165.

Deer, W.A, Howie, R.A. and Zussman, 1993. An Introduction to the Rock Forming Minerals, 2nd Ed. Longman Scientific and Technical, England, 363-373.

Denholm, P., Kulcinski, G.L. and Holloway, T., 2005. Emissions and energy efficiency assessment of baseload wind energy systems. *Environmental Science and Technology*, **39**, 1903-1911.

Dollase, W.A, 1986. Correction of intensities for preferred orientation in powder diffractometry: application of the March model. *Journal of Applied Crystallography*, **19**, 267-272.

Dyer, A., Abdel Gawad, A.S., Mikhail, M., Enamy, H. and Afshang, M., 1991. The natural zeolite, laumontite, as a potential material for the treatment of aqueous nuclear wastes. *Journal of Radioanalytical and Nuclear Chemistry*, **154**, 265-276.

Elevatorski, E.A., 1978. *Uranium Ores and Minerals*. Minobras 45-89.

Ehrmann, W., 2001. Variations in smectite content and crystallinity in sediments from CRP-3, Victoria Land Basin, Antarctica. *Terra Antartica*, **8**, 533-542.

Faurie, J., 2010. *Bateman embarks on engineering, procurement on the world's first alkaline heap-leach uranium mine*. http://www.miningweekly.com/article/trekkopje-pioneers-alkaline-heap-leaching-process-for-uranium-2010-07-02

Fuerstenau, D.W., Lutch, J.J. and De, A., 1999. The effect of ball size on the energy efficiency of hybrid high-pressure roll mill/ball mill grinding. *Powder Technology*, **105**, 199-204.

Fuller, C.C., Bargar, J.R., Davis, J.A. and Paina, M.J., 2002. Mechanisms of uranium interactions with hydroxyapatite: Implications for groundwater remediation. *Environmental Science and Technology*, **36**, 158-165.

Gonzalez, R., Treasure, T., Phillips, R., Jameel, H., Saloni, D., Abt., R. and Wright, J., 2011. Converting Eucalyptus biomass into ethanol: Financial and sensitivity analysis in a co-current dilute acid process. Part II. *Biomass and Bioenergy*, **35**, 767-772.

Goodall, W.R., Scales, P.J. and Butcher, A.R., 2005. The use of QEMSCAN and diagnostic leaching in the characterisation of visible gold in complex ores. *Minerals Engineering*, **18**, 877-886.

Gottlieb, P., Wilkie, G., Sutherland, D., Ho-Tun, E., Suthers, S., Perera, K., Jenkins, B., Spencer, S., Butcher, A. and Rayner, J., 2000. Using quantitative electron microscopy for process mineralogy applications. *Journal of the Minerals, Metals and Materials Society,* **52**, 24-25.

Guettaf, H., Becis, A., Ferhat, K., Hanou, K., Bouchiha, D., Yakoubi, K., Ferrad, F., 2009. Concentration-purification of uranium from an acid leaching solution. *Physics Procedia*¸ **2**, 765-771.

Harding, J., 2007. Economics of nuclear power and proliferation risks in a carbon-constrained world. *Electricity Journal*, **20**, 65-76.

Harris, D.C., 1999. Quantitative Chemical Analysis, 5th Ed. W.H. Freeman and Co., New York, pp 129-212.

Hartleb, J.W.O., 1988. The Langer Heinrich uranium deposit: Southwest Africa/Namibia. *Ore Geology Reviews*, **3**, 277-287.

Higgins, M.D., 2000. Measurement of crystal size distributions. *American Mineralogist*, **85**, 1105-1116.

Helgeson, H.C., Murphy, W.M., Aaraard, P, 1984. Thermodynamic and kinetic constraints on reaction rates among minerals and aqueous solutions. II. Rate constants, effective surface area, and hydrolysis of feldspar. *Geochimica et Cosmochimica Acta*, **48**, 2405-2432.

Henn, F., Durand, C., Cerepi, A., Brosse, E. and Giuntini, J.C., 2007. DC conductivity, cation exchange capacity, and specific surface area related to chemical composition of pore lining chlorites. *Journal of Colloid and Interface Science*, **311**, 571-578.

HO, E.M. and Quan, H., 2007. Iron (II) oxidation by SO_2/O_2 for use in uranium leaching. *Hydrometallurgy*¸ **85**, 183-192.

Hodson, M.E., 2006. Searching for the perfect surface area normalizing term-a comparison of BET surface area-, geometric surface area- and mass normalised dissolution rates of anorthite and biotite. *Journal of Geochemical Exploration*, **88**, 288-291.

Hulthén, E. and Evertsson, M., 2011. Real-time algorithm for cone crusher control with two variables. *Minerals Engineering*, **24**, 987-994.

IAEA, 1980. *Significance of Mineralogy in the Development of Flowsheets for Processing of Uranium Ores.* International Atomic Energy Agency, Vienna, 1-161 pp.

IAEA, 1990. *Manual on Laboratory Testing for Uranium Ore Processing.* International Atomic Energy Agency, Vienna, 1-127 pp.

IAEA, 2009. *World Distribution of Uranium Deposits (UDEPO) with Uranium Deposit Classification.* International Atomic Energy Agency, Vienna, 3 pp.

Jaboyedoff, M., Bussy, F., Kubler, B. and Thelin, P., 2001. Illite “crystallinity” revisited. *Clays and Clay minerals*, **49**, 156-167.

Jacob, R.E., Corner, B. and Brynard, H.J., 1986. The Regional Geological and Structural Setting of the Uraniferous Granitic Provinces of Southern Africa. *In*: Anhaeusser, C.R. and Maske, S. (Eds.), *Mineral Deposits of Southern Africa.* The Geological Society of South Africa, Johannesburg, 1809-1818.

Johnson, C.C., 1990. Economic leaching at Rössing Uranium Limited. *Journal of the South African Institute of Mining and Metallurgy*, **90**, 141-147.

Johnson, G., Hunter, I. and Holle, H., 1994. Quantifying and improving the power efficiency of SAG milling circuits. *Minerals Engineering*, **7**, 141-152.

Jin-yan, L., Xiu-xiang, T. and Pei, C., 2009. Study of formation of jarosite mediated by thiobacillus ferrooxidans in 9K medium. *Procedia Earth and Planetary Science*, **1**, 706-712.

Kalendova, A., Vesely, D. and Kalenda, P., 2010. Properties of paints with hematite coated muscovite and talc particles. *Applied Clay Science*, **48**, 581-588.

Kalinowski, B.E. and Schweda, P, 1996. Kinetics of muscovite, phlogopite and biotite dissolution and alteration at pH 1-4, room temperature. *Geochimica et Cosmochimica Acta*, **60**, 367-385.

Kinnaird, J.A. and Nex, P.A.M., 2007. A review of geological controls on uranium mineralisation in sheeted leucogranites within the Damara Orogen, Namibia. *Applied Earth Science (Trans. Inst. Min. Metall. B)*, **116**, 68-85.

Klein, C., 2002, The Manual of Mineral Science, 22nd Ed. John Wiley and Sons, Inc., New York, pp 475-554 and 619.

King, R.P., 1982. Determination of the distribution of size of irregularly shaped particles from measurements in sections or projected areas. *Powder Technology*, **32**, 87-100.

King, R.P. and Schneider, C.L., 1998. Stereological correction of linear grade distributions for mineral liberation. *Powder Technology*, **98**, 21-37.

Knauss, K.G. and Wolery, T.J., 1986. Dependance of albite dissolution kinetics on pH and time at 25° C and 75° C. *Geochimica et Cosmochimica Acta*, **50**, 2481-2497.

Knauss, K.G. and Wolery, T.J., 1989. Muscovite dissolution kinetics as a function of pH and time at 70°C. *Geochimica et Cosmochimica Acta*, **53**, 1493-1501.

Kohler, S., Bosbach, D. and Oelkers, E.H, 2005. Do clay mineral dissolution rates reach steady state? Geochimica et Cosmochimica Acta, **69**, 1997-2006.

Kohler, S., Dufaud, F. And Oelkers, 2003. An experimental study of illite dissolution kinetics as a function of pH from 1.4 to 12.4 and temperature from 5 to 50ºC. Geochimica et Cosmochimica Acta, **67**, 3583-3594.

Kotake, N., Daibo, K., Yamamoto, T and Kanda, Y., 2004. Experimental investigation on a grinding rate constant of solid materials by a ball mill-effect of ball diameter and feed size. *Powder Technology*, **143-144**, 196-203.

Kübler, B and Jayboyedoff, M., 2000. Illite crystallinity. *Earth and Planetary Sciences*, **331**, 75-89.

Kuisma-Kursula, P., 2000. Accuracy, precision and detection limits of SEM-WDS, SEM-EDS and PIXE in the multi-element analyses of medieval glass. *X-ray Specrometry*, **29**, 111-118.

Le Roux, J.P., 1993. Genesis of stratiform U-Mo deposits in the Karoo Basin of South Africa. *Ore Geology Reviews*, **7**, 485-509.

Le Roux, J.P. and Brynard, H.J., 1994. A strategy for uranium exploration in the Permo-Triassic Beaufort Group of the main Karoo basin, South Africa. *Journal of African Earth Sciences*, **18**, 245-253.

Lindqvist, M. And Evertsson. C.M., 2003. Liner wear in jaw crushers. *Minerals Engineering*, **16**, 1-12.

Lindqvist, M. and Evertsson, C.M., 2006. Development of wear models for cone crushers. *Wear*, **261**, 435-442.

Liu, K., Chen, Q., Yin, Z., Hu, H. and Ding, Z., 2012. Kinetics of leaching of a Chinese laterite containing maghemite and magnetite in sulphuric acid solution. *Hydrometallurgy*, **125-126**, 125-136.

Lottering, M.J., Lorenzen, L., Phala, N.S., Smit, J.T. and Schalkwyk, G.A.C., 2008. Mineralogy and uranium leaching response of low grade South African ores. *Minerals Engineering*, **21**, 16-22.

Lowson, R.T., Comarmond, J.M.C., Rajaratnam, G. and Brown, P.L., 2005. The kinetics of the dissolution of chlorite as a function of pH and at 25˚ C. *Geochimica et Cosmochimica Acta*, **69**, 1687-1699.

Loveday, B.K., 2004. The use of fag and sag batch tests for measurement of abrasion rates of full-size rocks. *Minerals Engineering*, **17**, 1093-1098.

Lui, Y., Gupta, R., Sharma, A., Wall, T., Butcher, A., Miller, G., Gottlieb, P. and French, D., 2005. Mineral matter-organic matter association characterisation by QEMSCAN and applications in coal utilisation. *Fuel*, **84**, 1259-1267.

Lunt, D., Boshoff, P. Boylett, M. and El-Ansary, Z., 2007. Uranium extraction: the key process drivers. *The Journal of the South African Institute of Mining and Metallugy*, **107**, 419-426.

Lüttge A. and Arvidson, R.S., 2008. The Mineral-Water Interface. *In:* Brantley, S.L., Kubicki, J.D. and White, A.F. (Eds.), *Kinetics of Water-Rock Interactions*. Springer Science, 82-83.

Malmstrom, M., Banwart, S., Lewenhagen, J., Duro, L. and Bruno, J., 1996. The dissolution of biotite and chlorite at 25°C in the near-neutral pH region. *Contaminant Hydrology*, **21**

Marcus, G.H., 2008. Innovative nuclear energy systems and the future of nuclear power. *Progress in Nuclear Energy*, **50**, 92-96.

McCarthy, T.S., 2006. The Witwatersrand Supergroup. *In*: Johnson, M.R., Anhaeusser, C.R. and Thomas, R.J. (Eds.), *The Geology of South Africa.* Geological Society of South Africa, Johannesburg/Council for Geoscience, Pretoria, 156.

McCusker, L.B., Von Dreele, R.B., Cox, D.E., Louër, D. and Scardi, P., 1999. Rietveld refinement guidelines. *Journal of Applied Crystallography*, **32**, 36-50.

McFarlane, A., Bremmell, K. and Addai-Mensah, J., 2005. Microstructure, rheology and dewatering behaviour of smectite dispersions during orthokinetic flocculation. *Minerals Engineering*, **18**, 1173-1182.

McKibben, M.A., Tallant, B.A. and del Angel, J.K., 2008. Kinetics of -inorganic arsenopyrite oxidation in acidic aqueous solutions. *Applied Geochemistry*, **23**, 121-135.

McKibben, M.A. and Barnes, H.L., 1986. Oxidation of pyrite in low temperature acidic solutions: Rate laws and surface textures. *Geochimica et Cosmochimica Acta*, **50**, 1509-1520.

MDHS 101 (2005). *Methods for the Determination of Hazardous Substances 101: Crystalline Silica in Respirable Airborne Dusts. Direct-on-filter Analysis by Infrared Spectrometry and X-ray Diffraction*. Health and Safety Laboratory (United Kingdom), pp 1-16.

Merritt, R.C., 1971. *The Extractive Metallurgy of Uranium.* Colorado School of Mines. Under Contract with the United States Atomic Energy Commission, 60-86 pp.

Messnaoui, B and Bounahmidi, T, 2006. On the modelling of calcium sulphate solubility in aqueous solutions. *Fluid Phase Equilibria*, **244**, 117-127.

Metz, V., Amram, K. and Ganor, J., 2005. Stoichiometry of smectite dissolution. *Geochimica et Cosmochimica Acta*, **69**, 1755-1772.

Michaux, S. And Djordjevic, N., 2005. Influence of explosive energy on the strength of the rock fragments and SAG mill throughput. *Minerals Engineering*, **18**, 439-448.

Miki, H. and Nicol, M., 2009. The kinetics of the oxidation of iron(II) by chlorate in the leaching of uranium ores. *Hydrometallurgy*, **100**, 47-49.

Miyashiro, A. and Shido, F., 1970. Progressive metamorphism in zeolite assemblages. *Lithos*, **3**, 251-260.

Moore, D.M. and Reynolds, R.C., 1989. *X-ray Diffraction and Identification and Analysis of Clay Minerals*. Oxford University Press, 199-200.

Nesse, W.D., 2000. *Introduction to Mineralogy*. Oxford University Press. New York, 163.

Nex, P.A.M., Kinnaird, J.A. and Oliver, G.J.H., 2001. Petrology, geochemistry and uranium mineralisation of post-collisional magmatism around Goanikontes, southern Central Zone, Damara Orogen, Namibia. *Journal of African Earth Sciences*, **33**, 481-502.

Nickel, E., 1973. Experimental dissolution of light and heavy minerals in comparison with weathering and intrastratal solution. *Contributions to Sedimentology*, **1**, 1-68.

Njini, F., 2012. Fukushima still haunts uranium producers. *The Southern Times*. http://www.southerntimesafrica.com/news_article.php?id=6510&title=Fukushima%20still%20haunts%20uranium%20producers&type=69

Norlund, K.L.I., Baron, C. And Warren, L.A., 2010. Jarosite formation by an AMD sulphide-oxidising environmental enrichment: Implications for biomarkers on Mars. *Chemical Geology*, **275**, 235-242.

Oelkers, E.H., Schott, J. and Devidal J., 1994. The effect of aluminium, pH, and chemical affinity on the rates of aluminosilicate dissolution reactions. Geochimica et Cosmochimica Acta, **58**, 2011-2024.

Oelkers. E.H., Schott, J., Gauthier, J. And Herrero-Roncal, T., 2008. An experimental study of the dissolution mechanism and rates of muscovite. *Geochimica et Cosmochimica Acta*, **72**, 4948-4961.

Oelkers, E.H., Golubev, S.V., Pokrovsky, O.S. and Benezeth, P, 2011. Do organic ligands affect calcite dissolution rates? *Geochimica et Cosmochimica Acta*, **75**, 1799-1813.

Oleg, S. P., Sergey, V.G. and Schott, 2005. Dissolution kinetics of calcite, dolomite and magnesite at 25° C and 0 to 50 atm pCO_2. *Chemical Geology*, **217**, 239-255.

Olaleye, B.M., 2010. Influence of some rock strength properties on jaw crusher performance in granite quarry. *Mining Science and Technology*, **20**, 204-208.

Olivero, J.J. and Longbothum, R.L., 1977. Empirical fits to the Voigt line width: A brief review. *Journal of Quantitative Spectroscopy and Radiative Transfere*, **17**, 233-236.

Paladin Energy, 2010. *The Kayelekera Mine, Malawi Southern Africa.* http://phx.corporate-ir.net/External.File?item=UGFyZW50SUQ9MTQ0Mjl8Q2hpbGRJRD0tMXxUeXBlPTM=&t=1&bcsi_scan_0271F170321D1D0A=AIY8MCH0S7ZyqThjvsOoFXqDGuE9AAAAEyI9WA==&bcsi_scan_filename=External.File

Pandey, A. D., Mallick, K. K. and Pandey, P. C., 1980. Intensification of the reaction between Udaipur rock phosphate and sulphuric acid by means of ultrasound. *Ultrasonics*, 115-119.

Pascoe, R.D., Power, M.R. and Simpson, B., 2007. QEMSCAN analysis as a tool for improved understanding of gravity separator performance. *Minerals Engineering*, **20**, 487-495.

Petrov, E.P., 2007. Comment on *The exact expression of the Voigt profile function*. *Journal of Quantitative Spectroscopy and Radiative Transfere*, **103**, 272-274.

Phillips, N.G. and Law, J.D.M., 1994. Metamorphism of the Witwatersrand gold fields: A review. *Ore Geology Reviews*, **9**, 1-31.

Pirrie, D. and Rollinson, G.K., 2011. Unlocking the applications of automated mineral analysis. *Geology Today*, **27**, 235-244.

Pollastro, R.M., 1993, Considerations and applications of the illite/smectite geothermometer in hydrocarbon-bearing rocks of Miocene and Mississippian age. *Clays and Clay Minerals*, **41**, 119-133.

Reardon, E.J. and Langmuir, D., 1976. Activity coefficients of $MgCO_3°$ can $CaSO_4°$ ion pairs as a function of ionic strength. *Geochimica et Cosmoshimica Acta*, **40**, 549-554.

Reed, S.J.B., 2005. *Electron Microprobe and Scanning Electron Microscopy in Geology.* Cambridge University Press, 1-16.

Reynolds, H.S., Ram, R., Charalambous, F.A, Antolasic, F., Tardio, J. and Bhargava, S., 2010. Characterisation of a uranium ore using multiple X-ray diffraction based methods. *Minerals Engineering*, **23**, 739-745.

Rietveld, H. M., 1969. A profile refinement method for nuclear and magnetic structures. *Journal of Applied Crystallography*, **2**, 65-71.

Ring, R.J., 1980. Ferric sulphate leaching of some Australian uranium ores. *Hydrometallurgy*, **6**, 89-101.

Robb, L.J. and Meyer, F.M., 1995. The Witwatersrand Basin, South Africa: Geological framework and mineralisation process. *Ore Geology Reviews*, **10**, 67-94.

Roesener, H. and Schreuder, C.P., 1999. Uranium. *In*: The Mineral Resources of Namibia. Ministry of Mines and Energy, Geological Survey Namibia, pp. 7.1-1–7.1-62.

Rogovin, Z., Casali, A. and Herbst, J.A., 1988. Tracer study of mass transport and grinding in a rod mill. *International Journal of Mineral Processing*, **22**, 149-167.

Ross, G.J., 1969. Acid dissolution of chlorites: release of magnesim, iron and aluminium and mode of acid attach. *Clays and Clay Minerals*, **17**, 347-354.

Ruis, J., 1987. A standardless X-ray diffraction method for the quantitative analysis of multiphase mixtures. *Journal of Applied Crystallography*, **20**, 457-460.

Russ, J.C., 1986. *Practical Stereology*. Plenum Press, New York, 35-39.

Samson, E., Lemaire, G., Marchand, J. and Beaudoin, J.J., 1999. Modeling chemical activity effects in strong ionic solutions. *Computational Materials Science*, **15**, 285-294.

Senanayake, G and Das, G. K., 2004. A comparative study of leaching kinetics of limonitic laterite and synthetic iron oxides in sulphuric acid containing sulphur dioxide. *Hydrometallugy*, **72**, 59-72.

Serway, R.A. and Faughn, J.S., 2003. *College Physics*. Sixth Edition. Thomson, 192-193 and 906.

Shaw, S., Peak, D. and Hendry, M.J., 2009. Investigation of acidic dissolution of mixed clays between pH 1.0 and -3.0 using Si and Al X-ray absorption near edge structure. *Geochimica et Cosmochimica Act,* **73**, 4151-4165.

Shiraki, R. and Holmen B.A., 2002. Airborne respirable silica near a sand and gravel facility in Central California: XRD and elemental analysis to distinguish source and background quartz. *Environmental Science and Technology*, **36**, 4956-4961.

Smith, A.M.L., Hudson-Edwards, K.A., Dubbin, W.E. and Wright, K., 2005. Dissolution of jarosite [$KFe_3(SO_4)_2(OH)_6$] at pH 2 and 8: Insights from batch experiments and computational modelling. *Geochimica et Cosmochimica Acta*, **70**, 608-621.

Smith, D. A. M., 1965. The geology of the area around the Khan and Swakop Rivers in Southwest Africa', Southwest Africa Series, Memoir 3, Geological Survey of South Africa, Pretoria, South Africa.

Środoń, J., 1980. Precise Identification of illite/smectite interstratifications by X-ray powder diffraction. *Clays and Clay Minerals*, **6**, 401-411.

Stillings, L.S. and Brantley. S.L., 1995. Feldspar dissolution at 25° C and pH 3: Reaction stoichiometry and the effect of cations. *Geochimica et Cosmochimica Acta,* **59**, 1483-1496.

Streckeisen, A., 1976. To each plutonic rock its proper name. *Earth Science Reviews*, **12**, 1-33.

Sutherland, D. and Gottlieb, P., 1991. Application of automated quantitative mineralogy in mineral processing. *Minerals Engineering*, **4**, 753-762.

Sutherland, D., Gottlieb, P., Jackson, R., Wilkie, G. and Stewart, P., 1988. Measurement in section of particles of known composition. *Minerals Engineering*, **1**, 317-326.

Tester, J.W., Worley, W.G., Robinson, B.A., Grigsby, C.O., Feerer, J.L., 1994. Correlating quartz dissolution kinetics in pure water from 25 to 625°C. *Geochimica et Cosmochimica Acta*, **58**, 2407-2420.

Turner, B.R., 1985. Uranium mineralisation in the Karoo Basin, South Africa. *Economic Geology*, **80**, 256-269.

UxC, 2012. *Uranium Spot Price*.
http://www.uxc.com/review/uxc_Prices.aspx

Valvoda, V., 1987. Correction of X-ray intensities for preferred orientation in quantitative phase analysis. *Journal of Applied Crystallography*, **20**, 453-456.

Van Alphen, C., 2007. Automated mineralogical analysis of coal and ash products – Challenges and requirements. *Minerals Engineering*, **20**, 496-505.

Velletri, P and Weedon, D.M., 2001. Comminution in a non-cylindrical roll crusher. *Minerals Engineering,* **14**, 1459-1468.

Venter, R. and Boylett, M., 2009. The evaluation of various oxidants used in acid leaching of uranium. *Hydrometallurgy Conference 2009,* The South African Institute of Mining and Metallurgy, 445-456.

Verryn, S., 2010. *XRD Course Rietveld Analysis (XRD Course Material Ed 1).* Panalytical, Johannesburg, 3 pp.

Vochten, R.F., Van Haverbeke, L. and Van Springel, K., 1992. Transformation of chernikovite into meta-uranocircite II, $Ba(UO_2)_2(PO_4)_2.6H_2O$ and study of its solubility. *Mineralogical Magazine*, **56**, 367-372.

Warren, B.E., 1990. *X-ray Diffraction*. Dover Publications Inc., New York, pp 1.

Weisenberger, T. And Selbekk, R.S., 2009. Multi-stage zeolite facies mineralisation in the Hvalfjördur area, Iceland. *International Journal of Earth Science*, **98**, 985-999.

Weisser, D., Howells, M. and Rogner, H., 2008. Nuclear power and post-2012 energy and climate change policies. *Environmental Science and Policy II*, **11**, 467-477.

White, W.M., in Press. *Geochemistry*, Wiley-Blackwell, 85-86.

Wiersma, C.L. and Rimstidt, J.D., 1984. Rates of reaction of pyrite and marcasite with ferric iron at pH 2. *Geochimica et Cosmochimica Acta*, **48**, 85-92.

Wiles, D.B. and Young, R.A, 1981. A new computer program for Rietveld analysis of powder diffraction patterns. *Journal of Applied Crystallography*, **14**, 149-151.

Wills, B.A. and Napier-Munn, 2006. *Mineral Processing Technology (7th Edition).* Elsevier, 109-163.

Xiong, X., Wang, Z., Wu, F., Li, X. And Guo, H., 2013. Preparation of TiO_2 from ilmenite using sulphuric acid decomposition of the titania residue combined with

separation of Fe^{3+} with EDTA during hydrolysis. *Advances in Powder Technology*, **24**, 60-67.

Youlton, B.J., 2007. *Controls on Uranium Mineralisation at the Klein Trekkopje Prospect, Namibia*. Hons. Thesis (unpubl). University of the Witwatersrand, .Johannesburg, 1-68.

Youlton, B.J., Coetzee, L.L., Scott, L.M., O' Connell, J., O' Connell, R., Kinnaird, J.A., 2011. Uranium deportment studies: beyond the assay. *Alta Uranium Conference Proceedings*, Alta Metallurgical Services, Melbourne, Australia.

Youlton, B.J. and Kinnaird, J.A, 2013. Gangue-reagent interactions during acid leaching of uranium. *Minerals Engineering*, **52**, 62-73.

Zhang, S. and Nicol, M.J., 2010. Kinetics of the dissolution of ilmenite in sulphuric acid solutions under reducing conditions. *Hydrometallurgy*, **103**, 196-204.

Zhou, J. And Li, X., 2006. Geoplot: an Excel VBA program for geochemical data plotting. *Computers and Geosciences*, **32**, 554-560.

Zhuang, Z., Hearl, F.J., Odencrantz. J., Chen, W., Chen, B.T., Chen, J.Q., McCawley, M.A., Gao, P. and Soderholm, S.C., 2001. Estimating historical respirable silica exposure for Chinese pottery workers and iron/copper, tin, and tungsten miners. *Annals of Occupational Hygiene*, **45**, 631-642.

Zolotoyabko, E, 2009. Determination of the degree of preferred orientation within the March-Dollase approach. *Journal of Applied Crystallography*, **42**, 513-518.

Zysset, M. and Schindler, P.W., 1996. The proton promoted dissolution kinetics of K-montmorillonite. *Geochimica et Cosmochimica Acta*, **60**, 921-931.

APPENDIX A: Additional XRD Data

Table A1: Variation (noise) in the background of the X-ray diffractograms used to determine the limits of detection and quantification

Position	Position 1			Position 2 (Laumontite)			Position 3		
2 theta	5.500			10.8964			19.000		
d-spacing	18.6431			9.42802			5.4197		
Measurement	Peak	B/G	Delta	Peak	B/G	Delta	Peak	B/G	Delta
Units	Counts	Counts	Counts	Counts	Counts	Counts	Counts	Counts	Counts
MHCC1	2493	2569	-76	1547	1603	-56	950	890	60
MHCC2	2377	2514	-137	1537	1620	-83	932	890	42
MHCC3	2572	2545	27	1690	1606	84	857	899	-42
MHCC4	2474	2523	-49	1621	1596	25	904	890	14
MHCC5	2430	2551	-121	1571	1604	-33	879	891	-12
MHCC6	2445	2484	-39	1611	1564	47	926	918	8
MHCC7	2376	2471	-95	1625	1575	50	902	902	0
MHCC8	2575	2443	132	1574	1574	0	895	895	0
MHCC9	2515	2347	168	1586	1586	0	909	873	36
MHCC10	2335	2366	-31	1538	1578	-40	839	861	-22
MHCC11	2336	2355	-19	1580	1548	32	896	868	28
MHCC12	2344	2344	0	1577	1546	31	876	860	16
MHCC13	2347	2390	-43	1597	1535	62	894	858	36
MHCC14	2409	2276	133	1496	1527	-31	846	855	-9
MHCC15	2396	2326	70	1623	1494	129	816	840	-24
MHCC16	2347	2226	121	1470	1507	-37	892	842	50
MHCC17	2285	2113	172	1486	1458	28	831	819	12
MHCC18	2135	2271	-136	1514	1499	15	899	835	64
MHCC19	2254	2171	83	1488	1488	0	888	816	72
MHCC20	2423	2171	252	1432	1484	-52	853	820	33
MHCC21	2172	2214	-42	1443	1443	0	858	837	21
MHCC22	2217	2122	95	1495	1442	53	850	821	29
MHCC23	2153	2061	92	1498	1413	85	796	848	-52
MHCC24	2220	2103	117	1509	1442	67	850	825	25
MHCC25	2196	2246	-50	1405	1466	-61	865	834	31
MHCC26	2136	2100	36	1371	1439	-68	833	809	24
MHCC27	2293	2108	185	1539	1483	56	897	829	68
MHCC28	2338	2098	240	1481	1424	57	842	804	38
MHCC29	2189	2059	130	1475	1418	57	799	788	11
MHCC30	2173	2204	-31	1405	1440	-35	830	782	48
Average	**-**	**-**	**39.47**	**-**	**-**	**12.73**	**-**	**-**	**20.17**
Std Dev	**-**	**-**	**110.96**	**-**	**-**	**53.33**	**-**	**-**	**30.94**

Table A1 Continued: Variation (noise) in the background of the X-ray diffractograms used to determine the limits of detection and quantification

Position	Position 4 (Calcite)			Position 5			Position 6		
2 theta	34.3589			52.185			73.898		
d-spacing	3.03066			2.0338			1.4881		
Measurement	Peak	B/G	Delta	Peak	B/G	Delta	Peak	B/G	Delta
Units	Counts	Counts	Counts	Counts	Counts	Counts	Counts	Counts	Counts
MHCC1	598	565	33	347	332	15	245	237	8
MHCC2	609	600	9	355	338	17	235	241	-6
MHCC3	601	612	-11	343	333	10	253	233	20
MHCC4	635	599	36	340	326	14	253	239	14
MHCC5	588	601	-13	361	350	11	255	238	17
MHCC6	629	612	17	357	331	26	248	240	8
MHCC7	612	622	-10	353	329	24	255	233	22
MHCC8	615	597	18	340	333	7	233	238	-5
MHCC9	590	600	-10	332	338	-6	245	227	18
MHCC10	586	586	0	341	345	-4	239	226	13
MHCC11	584	584	0	343	331	12	231	231	0
MHCC12	577	604	-27	325	327	-2	232	225	7
MHCC13	604	582	22	339	317	22	240	227	13
MHCC14	572	569	3	314	324	-10	250	222	28
MHCC15	562	574	-12	312	318	-6	234	221	13
MHCC16	544	578	-34	320	303	17	227	217	10
MHCC17	558	594	-36	329	309	20	227	231	-4
MHCC18	563	563	0	336	310	26	223	216	7
MHCC19	574	547	27	324	308	16	220	220	0
MHCC20	533	587	-54	323	310	13	228	219	9
MHCC21	569	559	10	318	315	3	226	212	14
MHCC22	545	557	-12	339	337	2	220	207	13
MHCC23	564	568	-4	343	340	3	216	216	0
MHCC24	547	553	-6	330	312	18	226	208	18
MHCC25	535	548	-13	321	318	3	231	212	19
MHCC26	559	548	11	304	295	9	215	210	5
MHCC27	533	604	-71	332	299	33	215	200	15
MHCC28	529	576	-47	337	297	40	232	212	20
MHCC29	564	549	15	300	289	11	226	218	8
MHCC30	544	566	-22	339	321	18	217	206	11
Average	-	-	-6.03	-	-	12.07	-	-	10.50
Std Dev	-	-	25.25	-	-	11.81	-	-	8.40

Table A2: Chlorite decay constants, initial and steady state rates

Determination	**Initial Rate**	**Steady State Rate**	**Decay Constant (λ)**
pH = 1.0	**Mol.m^{-2}.s^{-1}**	**Mol.m^{-2}.s^{-1}**	**-**
Si	1.37 X 10^{-9}	1.50 X 10^{-10}	2.46 X 10^{-5}
Al	9.63 X 10^{-9}	2.41 X 10^{-10}	4.10 X 10^{-5}
Mg	9.58 X 10^{-9}	2.41 X 10^{-10}	4.09 X 10^{-5}
Fe	6.04 X 10^{-9}	2.41 X 10^{-10}	3.58 X 10^{-5}
Determination	**Initial Rate**	**Steady State Rate**	**Decay Constant (λ)**
pH = 1.5	**Mol.m^{-2}.s^{-1}**	**Mol.m^{-2}.s^{-1}**	**-**
Si	9.59 X 10^{-10}	1.05 X 10^{-10}	2.45 X 10^{-5}
Al	6.73 X 10^{-9}	1.68 X 10^{-10}	4.09 X 10^{-5}
Mg	6.70 X 10^{-9}	1.68 X 10^{-10}	4.09 X 10^{-5}
Fe	4.22 X 10^{-9}	1.68 X 10^{-10}	3.58 X 10^{-5}
Determination	**Initial Rate**	**Steady State Rate**	**Decay Constant (λ)**
pH = 2.0	**Mol.m^{-2}.s^{-1}**	**Mol.m^{-2}.s^{-1}**	**-**
Si	5.46 X 10^{-10}	5.99 X 10^{-11}	2.46 X 10^{-5}
Al	3.83 X 10^{-9}	9.58 X 10^{-11}	4.10 X 10^{-5}
Mg	3.81 X 10^{-9}	9.58 X 10^{-11}	4.09 X 10^{-5}
Fe	2.41 X 10^{-9}	9.58 X 10^{-11}	3.58 X 10^{-5}
Mooi -75	**Initial Rate**	**Steady State Rate**	**Decay Constant (λ)**

Table A3: Muscovite decay constants and initial rates

Determination	**Initial Rate**	**Decay Constant (λ)**
pH	**Mol.m^{-2}.s^{-1}**	**-**
1.0	3.91 x 10^{-14}	2.07 x 10^{-5}
1.5	3.16 x 10^{-14}	2.06 x 10^{-5}
2.0	2.41 x 10^{-14}	2.03 x 10^{-5}

Table A4: Smectite decay constants, initial and steady state rates

Determination	**Initial Rate**	**Steady State Rate**	**Decay Constant (λ)**
pH = 1.5	**Mol.g.s^{-1}**	**Mol.g.s^{-1}**	**-**
Exchangeable Cations	4.28 x 10^{-4}	-	1.84 x 10^{-6}
Octahedral Mg	2.69 x 10^{-11}	2.25 x 10^{-12}	1.15 x 10^{-6}
Fe	2.25 x 10^{-11}	2.25 x 10^{-12}	1.07 x 10^{-6}
Al	1.12 x 10^{-12}	2.25 x 10^{-12}	3.21 x 10^{-7}
Si	1.80 x 10^{-11}	2.25 x 10^{-12}	9.63 x 10^{-7}

Table A5: Illite decay constants, initial and steady state rates

Determination		Initial Rate	Steady State Rate	Decay Constant (λ)
pH =	**1.5**	**Mol.m^{-2}.s^{-1}**	**Mol.m^{-2}.s^{-1}**	**-**
Si		4.73 x 10^{-12}	1.35 x 10^{-12}	2.32 x 10^{-7}
Al		1.30 x 10^{-11}	1.69 x 10^{-12}	3.78 x 10^{-7}
Mg		1.36 x 10^{-11}	1.85 x 10^{-12}	3.69 x 10^{-7}
Fe		1.83 x 10^{-11}	3.21 x 10^{-12}	3.23 x 10^{-7}
K		1.89 x 10^{-11}	3.38 x 10^{-12}	3.19 x 10^{-7}

Table A6: Albite decay constants, initial and steady state rates

Determination		Initial Rate	Steady State Rate	Decay Constant (λ)
pH =	**1.0**	**Mol.m^{-2}.s^{-1}**	**Mol.m^{-2}.s^{-1}**	**-**
Si		2.08 x 10^{-13}	2.08 x 10^{-14}	-9.14 x 10^{-7}
Al		2.65 x 10^{-13}	5.67 x 10^{-15}	-1.53 x 10^{-6}
Na		9.88 x 10^{-13}	4.93 x 10^{-15}	-2.10 x 10^{-6}
Ca		4.04 x 10^{-13}	3.71 x 10^{-16}	-2.78 x 10^{-6}
Determination		**Initial Rate**	**Steady State Rate**	**Decay Constant (λ)**
pH =	**1.5**	**Mol.m^{-2}.s^{-1}**	**Mol.m^{-2}.s^{-1}**	**-**
Si		1.17 x 10^{-13}	1.17 x 10^{-14}	-9.14 x 10^{-7}
Al		1.49 x 10^{-13}	3.19 x 10^{-15}	-1.53 x 10^{-6}
Na		5.56 x 10^{-13}	2.77 x 10^{-15}	-2.10 x 10^{-6}
Ca		2.27 x 10^{-13}	2.08 x 10^{-16}	-2.78 x 10^{-6}
Determination		**Initial Rate**	**Steady State Rate**	**Decay Constant (λ)**
pH =	**2.0**	**Mol.m^{-2}.s^{-1}**	**Mol.m^{-2}.s^{-1}**	**-**
Si		6.57 x 10^{-14}	6.57 x 10^{-15}	-9.14 x 10^{-7}
Al		8.39 x 10^{-14}	1.79 x 10^{-15}	-1.53 x 10^{-6}
Na		3.13 x 10^{-13}	1.56 x 10^{-15}	-2.10 x 10^{-6}
Ca		1.28 x 10^{-13}	1.17 x 10^{-16}	-2.78 x 10^{-6}

Table A7: K-feldspar decay constants, initial and steady state rates

Determination		**Initial Rate**	**Steady State Rate**	**Decay Constant (λ)**
pH =	**1.0**	**Mol.m^{-2}.s^{-1}**	**Mol.m^{-2}.s^{-1}**	**-**
Si		4.76×10^{-9}	4.76×10^{-10}	8.53×10^{-7}
Al		6.34×10^{-9}	1.59×10^{-10}	1.37×10^{-6}
K		3.17×10^{-8}	1.59×10^{-10}	1.96×10^{-6}
Determination		**Initial Rate**	**Steady State Rate**	**Decay Constant (λ)**
pH =	**1.5**	**Mol.m^{-2}.s^{-1}**	**Mol.m^{-2}.s^{-1}**	**-**
Si		3.00×10^{-9}	3.00×10^{-10}	8.53×10^{-7}
Al		4.01×10^{-9}	1.00×10^{-10}	1.37×10^{-6}
K		2.00×10^{-8}	1.00×10^{-10}	1.96×10^{-6}
Determination		**Initial Rate**	**Steady State Rate**	**Decay Constant (λ)**
pH =	**2.0**	**Mol.m^{-2}.s^{-1}**	**Mol.m^{-2}.s^{-1}**	**-**
Si		1.90×10^{-9}	1.90×10^{-10}	8.53×10^{-7}
Al		2.53×10^{-9}	6.33×10^{-11}	1.37×10^{-6}
K		1.27×10^{-8}	6.33×10^{-11}	1.96×10^{-6}

Table A8: Mooifontein -212, pH 1.0 iterative free acid calculation

Element	Al	Mg	Fe	Ca	K	Na	Mn	SO_4^{2-}	HSO_4^-	H^+	Ionic Strength
Units	mol/L										
Calcite	-	-	-	1.19900	-	-	-	1.19900	-	-	-
Laumontite	0.25250	-	-	0.17218	-	-	-	0.55093	-	-	-
Chlorite	0.01714	0.01707	0.01212	-	-	-	-	0.05489	-	-	-
Muscovite	0.00239	-	-	-	0.00136	-	-	0.00426	-	-	-
Plagioclase	0.00229	-	-	0.00330	-	0.00831	-	0.01088	-	-	-
K-feldspar	0.00294	-	-	-	0.01431	-	-	0.01156	-	-	-
MnO_2	-	-	-	-	-	-	0.18299	0.36598	-	-	-
Free Acid*	-	-	-	-	-	-	-	0.05000	-	0.10000	-
Total	0.27725	0.01707	0.01212	1.37448	0.01566	0.00831	0.18299	2.24751	-	0.10000	-
Subtract Gyps	-	-	-	-	-	-	-	0.87303	-	-	-
γ = 1	0.27725	0.01707	0.01212	0.00036	0.01566	0.00831	0.18299	0.09354	0.77949	0.10000	2.15883
Iteration 1	0.27725	0.01707	0.01212	0.00050	0.01566	0.00831	0.18299	0.10963	0.76340	0.10617	2.18633
Iteration 2	0.27725	0.01707	0.01212	0.00049	0.01566	0.00831	0.18299	0.10857	0.76446	0.10578	2.18452
Iteration 3	0.27725	0.01707	0.01212	0.00049	0.01566	0.00831	0.18299	0.10864	0.76439	0.10580	2.18464

-	Ionic Strength		Ca		SO_4^{2-}		HSO_4^-		H^+		$CaSO_4°$	
-	I	Root I	log γ	γ	log γ	γ	log γ	γ	log γ	γ	log γ	γ
Iteration 1 γ	2.15883	1.46930	-0.10400	0.78704	-0.10400	0.78704	-0.02600	0.94189	-0.02600	0.94189	-0.95948	0.10978
Iteration 2 γ	2.18633	1.47862	-0.09758	0.79877	-0.09758	0.79877	-0.02439	0.94538	-0.02439	0.94538	-0.97170	0.10673
Iteration 3 γ	2.18452	1.47801	-0.09800	0.79800	-0.09800	0.79800	-0.02450	0.94515	-0.02450	0.94515	-0.97090	0.10693

Values have been reported to five decimal places to facilitate the calculation of the various parameters. These do not reflect the accuracy of each parameter.

Table A9: Mooifontein -212, pH 1.5 iterative free acid calculation

Element	Al	Mg	Fe	Ca	K	Na	Mn	SO_4^{2-}	HSO_4^-	H^+	Ionic Strength
Units	mol/L										
Calcite	-	-	-	1.19900	-	-	-	1.19900	-	-	-
Laumontite	0.25250	-	-	0.17218	-	-	-	0.55093	-	-	-
Chlorite	0.01714	0.01707	0.01212	-	-	-	-	0.05489	-	-	-
Muscovite	0.00239	-	-	-	0.00136	-	-	0.00426	-	-	-
Plagioclase	0.00229	-	-	0.00330	-	0.00831	-	0.01088	-	-	-
K-feldspar	0.00294	-	-	-	0.01431	-	-	0.01156	-	-	-
MnO_2	-	-	-	-	-	-	0.10921	0.21843	-	-	-
Free Acid*	-	-	-	-	-	-	-	0.05000	-	0.10000	-
Total	0.27725	0.01707	0.01212	1.37448	0.01566	0.00831	0.10921	2.09996	-	0.10000	-
Subtract Gyps	-	-	-	-	-	-	-	0.72548	-	-	-
γ = 1	0.27725	0.01707	0.01212	0.00044	0.01566	0.00831	0.10921	0.07773	0.64775	0.10000	1.98772
Iteration 1	0.27725	0.01707	0.01212	0.00068	0.01566	0.00831	0.10921	0.09687	0.62861	0.10869	2.02126
Iteration 2	0.27725	0.01707	0.01212	0.00066	0.01566	0.00831	0.10921	0.09570	0.62978	0.10819	2.01922
Iteration 3	0.27725	0.01707	0.01212	0.00067	0.01566	0.00831	0.10921	0.09577	0.62971	0.10822	2.01934

-	Ionic Strength		Ca		SO_4^{2-}		HSO_4^-		H^+		$CaSO_4°$	
-	I	Root I	log γ	γ	log γ	γ	log γ	γ	log γ	γ	log γ	γ
Iteration 1 γ	1.98772	1.40986	-0.14481	0.71645	-0.14481	0.71645	-0.03620	0.92002	-0.03620	0.92002	-0.88343	0.13079
Iteration 2 γ	2.02126	1.42171	-0.13670	0.72996	-0.13670	0.72996	-0.03417	0.92433	-0.03417	0.92433	-0.89834	0.12638
Iteration 3 γ	2.01922	1.42099	-0.13719	0.72914	-0.13719	0.72914	-0.03430	0.92406	-0.03430	0.92406	-0.89743	0.12664

Values have been reported to five decimal places to facilitate the calculation of the various parameters. These do not reflect the accuracy of each parameter.

Table A10: Mooifontein -212, pH 2.0 iterative free acid calculation

Element	Al	Mg	Fe	Ca	K	Na	Mn	SO_4^{2-}	HSO_4^-	H^+	Ionic Strength
Units	mol/L										
Calcite	-	-	-	1.19900	-	-	-	1.19900	-	-	-
Laumontite	0.20655	-	-	0.17218	-	-	-	0.48200	-	-	-
Chlorite	0.00682	0.00680	0.00483	-	-	-	-	0.02185	-	-	-
Muscovite	0.00149	-	-	-	0.00085	-	-	0.00266	-	-	-
Plagioclase	0.00072	-	-	0.00104	-	0.00263	-	0.00344	-	-	-
K-feldspar	0.00117	-	-	-	0.00571	-	-	0.00461	-	-	-
MnO_2	-	-	-	-	-	-	0.03640	0.07281	-	-	-
Free Acid*	-	-	-	-	-	-	-	0.00500	-	0.01000	-
Total	0.21676	0.00680	0.00483	1.37222	0.00656	0.00263	0.03640	1.79138	-	0.01000	-
Subtract Gyps	-	-	-	-	-	-	-	0.41916	-	-	-
γ = 1	0.21676	0.00680	0.00483	0.00015	0.00656	0.00263	0.03640	0.22863	0.19053	0.01000	1.60953
Iteration 1	0.21676	0.00680	0.00483	0.00038	0.00656	0.00263	0.03640	0.27042	0.14874	0.01149	1.67341
Iteration 2	0.21676	0.00680	0.00483	0.00035	0.00656	0.00263	0.03640	0.26763	0.15153	0.01137	1.66912
Iteration 3	0.21676	0.00680	0.00483	0.00036	0.00656	0.00263	0.03640	0.26781	0.15134	0.01138	1.66941
Iteration 4	0.21676	0.00680	0.00483	0.00036	0.00656	0.00263	0.03640	0.26780	0.15136	0.01138	1.66939

-	Ionic Strength		Ca		SO_4^{2-}		HSO_4^-		H^+		$CaSO_4°$	
-	I	Root I	log γ	γ	log γ	γ	log γ	γ	log γ	γ	log γ	γ
Iteration 1 γ	1.60953	1.26867	-0.24057	0.57469	-0.24057	0.57469	-0.06014	0.87068	-0.06014	0.87068	-0.71535	0.19260
Iteration 2 γ	1.67341	1.29360	-0.22380	0.59731	-0.22380	0.59731	-0.05595	0.87912	-0.05595	0.87912	-0.74374	0.18041
Iteration 3 γ	1.66912	1.29195	-0.22492	0.59577	-0.22492	0.59577	-0.05623	0.87856	-0.05623	0.87856	-0.74183	0.18120
Iteration 4 γ	1.66941	1.29206	-0.22485	0.59587	-0.22485	0.59587	-0.05621	0.87859	-0.05621	0.87859	-0.74196	0.18115

Values have been reported to five decimal places to facilitate the calculation of the various parameters. These do not reflect the accuracy of each parameter.

Table A11: Mooifontein -75, pH 1.5 iterative free acid calculation

Element	Al	Mg	Fe	Ca	K	Na	Mn	SO_4^{2-}	HSO_4^-	H^+	Ionic Strength
Units	mol/L										
Calcite	-	-	-	1.19900	-	-	-	1.19900	-	-	-
Laumontite	0.25250	-	-	0.17218	-	-	-	0.55093	-	-	-
Chlorite	0.03376	0.03363	0.02388	-	-	-	-	0.10814	-	-	-
Muscovite	0.00677	-	-	-	0.00384	-	-	0.01208	-	-	-
Plagioclase	0.01373	-	-	0.01980	-	0.04988	-	0.06534	-	-	-
K-feldspar	0.01980	-	-	-	0.09645	-	-	0.07792	-	-	-
MnO_2	-	-	-	-	-	-	0.07281	0.14562	-	-	-
Free Acid*	-	-	-	-	-	-	-	0.01581	-	0.03162	-
Total	0.32656	0.03363	0.02388	1.39098	0.10029	0.04988	0.07281	2.17484	-	0.03162	-
Subtract Gyps	-	-	-	-	-	-	-	0.78387	-	-	-
γ = 1	0.32656	0.03363	0.02388	0.00016	0.10029	0.04988	0.07281	0.21563	0.56824	0.03162	2.52365
Iteration 1	0.32656	0.03363	0.02388	0.00017	0.10029	0.04988	0.07281	0.22146	0.56240	0.03202	2.53261
Iteration 2	0.32656	0.03363	0.02388	0.00017	0.10029	0.04988	0.07281	0.22093	0.56294	0.03198	2.53179
Iteration 3	0.32656	0.03363	0.02388	0.00017	0.10029	0.04988	0.07281	0.22098	0.56289	0.03198	2.53186

-	Ionic Strength		Ca		SO_4^{2-}		HSO_4^-		H^+		$CaSO_4°$	
-	I	Root I	log γ	γ	log γ	γ	log γ	γ	log γ	γ	log γ	γ
Iteration 1 γ	2.52365	1.58860	-0.02143	0.95185	-0.02143	0.95185	-0.00536	0.98774	-0.00536	0.98774	-1.12162	0.07558
Iteration 2 γ	2.53261	1.59142	-0.01947	0.95616	-0.01947	0.95616	-0.00487	0.98885	-0.00487	0.98885	-1.12561	0.07488
Iteration 3 γ	2.53179	1.59116	-0.01965	0.95576	-0.01965	0.95576	-0.00491	0.98875	-0.00491	0.98875	-1.12524	0.07495

Values have been reported to five decimal places to facilitate the calculation of the various parameters. These do not reflect the accuracy of each parameter.

Table A12: Reduced Arkose Ore, pH 1.5 iterative free acid calculation

Element	Al	Mg	Fe	Ca	K	Na	Mn	SO_4^{2-}	HSO_4^-	H^+	Ionic Strength
Units	mol/L										
Chlorite	0.01533	0.01527	0.01084	-	-	-	-	0.04910	-	-	-
Smectite	0.00001	0.03245	0.00016	0.00326	-	-	-	0.03587	-	-	-
Plagioclase	0.00206	-	-	0.00297	-	0.00749	-	0.00982	-	-	-
K-feldspar	0.00128	-	-	-	0.00624	-	-	0.00504	-	-	-
Pyrite	-	-	0.00003	-	-	-	-	0.00003	-	-	-
	-	-	-	-	-	-	-	-	-	-	-
MnO_2	-	-	-	-	-	-	0.10921	0.21843	-	-	-
Free Acid*	-	-	-	-	-	-	-	0.01581	-	0.03162	-
Total	0.01868	0.04771	0.01103	0.00623	0.00624	0.00749	0.10921	0.33410	-	0.03162	-
Subtract Gyps	-	-	-	-	-	-	-	0.32787	-	-	-
γ = 1	0.01868	0.04771	0.01103	0.00038	0.00624	0.00749	0.10921	0.09019	0.23768	0.03162	0.66098
Iteration 1	0.01868	0.04771	0.01103	0.00240	0.00624	0.00749	0.10921	0.15899	0.16888	0.04281	0.77382
Iteration 2	0.01868	0.04771	0.01103	0.00209	0.00624	0.00749	0.10921	0.15360	0.17427	0.04188	0.76465
Iteration 3	0.01868	0.04771	0.01103	0.00211	0.00624	0.00749	0.10921	0.15403	0.17384	0.04195	0.76538

-	Ionic Strength		Ca		SO_4^{2-}		HSO_4^-		H^+		$CaSO_4°$	
-	I	Root I	log γ	γ	log γ	γ	log γ	γ	log γ	γ	log γ	γ
Iteration 1 γ	0.66098	0.81301	-0.52612	0.29777	-0.52612	0.29777	-0.13153	0.73870	-0.13153	0.73870	-0.29377	0.50843
Iteration 2 γ	0.77382	0.87967	-0.48801	0.32508	-0.48801	0.32508	-0.12200	0.75509	-0.12200	0.75509	-0.34392	0.45298
Iteration 3 γ	0.76465	0.87444	-0.49106	0.32280	-0.49106	0.32280	-0.12277	0.75376	-0.12277	0.75376	-0.33985	0.45725

Values have been reported to five decimal places to facilitate the calculation of the various parameters. These do not reflect the accuracy of each parameter.

Table A13: Oxidised Arkose Ore, pH 1.5 iterative free acid calculation

Element	Al	Mg	Fe	Ca	K	Na	Mn	SO_4^{2-}	HSO_4^-	H^+	Ionic Strength
Units	mol/L										
Smectite	0.00000	0.01345	0.00007	0.00135	-	-	-	0.01487	-	-	-
Plagioclase	0.00201	-	-	0.00290	-	0.00731	-	0.00958	-	-	-
K-feldspar	0.00078	-	-	-	0.00379	-	-	0.00306	-	-	-
MnO_2	-	-	-	-	-	-	0.07281	0.14562	-	-	-
Free Acid*	-	-	-	-	-	-	-	0.01581	-	0.03162	-
Total	0.00279	0.01345	0.00007	0.00425	0.00379	0.00731	0.07281	0.18894	-	0.03162	-
Subtract Gyps	-	-	-	-	-	-	-	0.18469	-	-	-
γ = 1	0.00279	0.01345	0.00007	0.00067	0.00379	0.00731	0.07281	0.05080	0.13388	0.03162	0.30382
Iteration 1	0.00279	0.01345	0.00007	0.00681	0.00379	0.00731	0.07281	0.09944	0.08524	0.04598	0.39625
Iteration 2	0.00279	0.01345	0.00007	0.00604	0.00379	0.00731	0.07281	0.09694	0.08775	0.04515	0.39054
Iteration 3	0.00279	0.01345	0.00007	0.00609	0.00379	0.00731	0.07281	0.09710	0.08759	0.04521	0.39089

-	Ionic Strength		Ca		SO_4^{2-}		HSO_4^-		H^+		$CaSO_4°$	
-	I	Root I	log γ	γ	log γ	γ	log γ	γ	log γ	γ	log γ	γ
Iteration 1 γ	0.30382	0.55120	-0.65032	0.22371	-0.65032	0.22371	-0.16258	0.68773	-0.16258	0.68773	-0.13503	0.73277
Iteration 2 γ	0.39625	0.62948	-0.61877	0.24056	-0.61877	0.24056	-0.15469	0.70034	-0.15469	0.70034	-0.17611	0.66664
Iteration 3 γ	0.39054	0.62493	-0.62076	0.23946	-0.62076	0.23946	-0.15519	0.69953	-0.15519	0.69953	-0.17357	0.67055

Values have been reported to five decimal places to facilitate the calculation of the various parameters. These do not reflect the accuracy of each parameter.

Table A14: Mudstone Ore, pH 1.5 iterative free acid calculation

Element	Al	Mg	Fe	Ca	K	Na	Mn	SO_4^{2-}	HSO_4^-	H^+	Ionic Strength
Units	**mol/L**										
Smectite	0.00002	0.07597	0.00037	0.00762	-	-	-	0.08399	-	-	-
Illite	0.02352	0.02455	0.03327	-	0.03430	-	-	0.11024	-	-	-
Plagioclase	0.00084	-	-	0.00121	-	0.00304	-	0.00398	-	-	-
K-feldspar	0.00108	-	-	-	0.00525	-	-	0.00424	-	-	-
MnO_2	-	-	-	-	-	-	0.00000	0.00000	-	-	-
Free Acid*	-	-	-	-	-	-	-	0.01581	-	0.03162	-
Total	0.02545	0.10051	0.03364	0.00883	0.03954	0.00304	0.00000	0.21827	-	0.03162	-
Subtract Gyps	-	-	-	-	-	-	-	0.20944	-	-	-
γ = 1	0.02545	0.10051	0.03364	0.00059	0.03954	0.00304	0.00000	0.05761	0.15182	0.03162	0.69637
Iteration 1	0.02545	0.10051	0.03364	0.00360	0.03954	0.00304	0.00000	0.10047	0.10897	0.04251	0.77212
Iteration 2	0.02545	0.10051	0.03364	0.00327	0.03954	0.00304	0.00000	0.09817	0.11127	0.04189	0.76771
Iteration 3	0.02545	0.10051	0.03364	0.00329	0.03954	0.00304	0.00000	0.09830	0.11114	0.04193	0.76797

-	Ionic Strength		Ca		SO_4^{2-}		HSO_4^-		H^+		$CaSO_4°$	
-	I	Root I	log γ	γ	log γ	γ	log γ	γ	log γ	γ	log γ	γ
Iteration 1 γ	0.69637	0.83449	-0.51405	0.30616	-0.51405	0.30616	-0.12851	0.74385	-0.12851	0.74385	-0.30950	0.49035
Iteration 2 γ	0.77212	0.87870	-0.48858	0.32465	-0.48858	0.32465	-0.12214	0.75484	-0.12214	0.75484	-0.34316	0.45377
Iteration 3 γ	0.76771	0.87619	-0.49004	0.32356	-0.49004	0.32356	-0.12251	0.75420	-0.12251	0.75420	-0.34121	0.45582

Values have been reported to five decimal places to facilitate the calculation of the various parameters. These do not reflect the accuracy of each parameter.

APPENDIX B: Additional Sedimentary Sample Leach Test Data

Table B1: Test A raw data

Time		Initial			Final			Acid Add	MnO_2
Hours	Min	pH	Eh (Ag/AgCl)	Temp (°C)	pH	Eh (Ag/AgCl)	Temp (°C)	g	g
11	31	8.5	148	20.4	1.52	390	40.9	14.69	74.07
12	11	2.7	307	32.9	0.85	387	40.7	128.24	74.07
12	34	1.66	379	39.3	0.74	457	44.8	42.27	66.89
12	55	0.48	463	40.6	0.45	474	40.7	42.27	61.96
13	35	0.87	472	36.6	0.82	492	39.5	42.27	54.19
14	53	1	494	38.1	0.99	511	39.1	39.46	46.7
15	15	1.2	542	37.2	0.97	551	39	24.05	46.7
15	36	1.04	547	36.9	1	549	38.8	21.6	46.7
16	11	1.02	536	37.2	0.97	539	38.6	205.75	46.7
17	23	1.1	517	37.6	0.89	536	39.2	191.02	41.47
17	55	0.98	565	36.7	0.98	565	36.7	191.02	41.47
18	36	1.05	548	37.3	0.97	551	38.3	185.01	41.47
19	44	1.15	533	37.6	0.88	535	39.4	166.29	40.09
20	34	0.93	535	35.2	0.94	553	37.4	166.29	37.28
20	58	1.02	556	36.9	0.98	558	37.8	163.96	37.28
22	10	1.09	540	36.8	0.89	545	38.3	151.37	37.28
24	17	1.08	520	37.3	0.89	530	38	141.12	33.58
26	34	1.06	535	36.3	0.88	549	37.7	130.59	31.52
27	52	1	548	36.4	0.94	550	36.8	127.65	31.52
31	13	1.11	527	36	0.87	533	36.5	113.26	31.52
32	22	0.85	524	35.2	0.85	534	35.4	113.26	28.57
33	56	0.95	538	29.8	0.95	538	30.4	113.26	28.57
35	49	1.12	538	28.9	1.05	533	26.6	113.26	28.57
36	10	1.06	531	26.5	1	534	27.7	102.6	28.57
36	34	0.97	535	27.8	0.97	535	27.8	102.6	28.57

Values in red mark where slurry samples were taken.

Table B2: Test B raw data

Time		Initial			Final			Acid Add	MnO_2
Hours	Min	pH	Eh (Ag/AgCl)	Temp (°C)	pH	Eh (Ag/AgCl)	Temp (°C)	g	g
8	42	10.7	57	19.2				13.98	
10	2				1.52	373	38.7	179.98	
10	5	1.92	355	37.3	1.5	427	40.6	152.37	71.26
10	30	1.84	421	38.4	1.5	438	40	142.02	70.29
11	5	2.05	422	33.9	1.39	450	39	125.6	70.29
12	0	2.1	426	37.6	1.5	480	39.4	110.73	63.04
12	40	1.92	507	37.3	1.45	526	39.3	99.51	63.04
13	5	1.63	527	38.3	1.42	534	39.2	92.77	63.04
13	57	1.72	522	38	1.42	532	39.3	84.66	63.04
14	32	1.62	527	38.1	1.41	534	39.3	78.8	63.04
15	19	1.52	521	37	1.45	524	38.6	76.69	63.04
16	35	1.72	508	38.2	1.41	517	39.5	68.86	63.04
17	9	1.51	509	38.1	1.46	511	39.2	67.22	63.04
18	5	1.6	499	38.4	1.43	503	39.3	63.28	63.04
19	7	1.65	491	38.4	1.42	498	39.5	55.98	63.04
19	27	1.42	495	38	1.42	495	38	55.98	63.04
20	29	1.55	483	36.6	1.47	486	38.3	53.24	62.64
21	31	1.63	478	38.4	1.42	485	39.1	46.94	62.17
22	39	1.54	476	37.5	1.38	483	39	41.28	61.44
23	37	1.49	475	36.9	1.45	484	38.3	38.56	59.34
24	16	1.51	484	36.8	1.41	488	38.6	35.06	58.69
25	37	1.55	483	35.9	1.45	487	37.8	31.88	57.81
27	10	1.58	483	34.4	1.44	487	37.3	27.59	56.77
28	37	1.59	485	35.3	1.35	490	37.3	19.52	56.1
30	55	1.47	483	35.6	1.49	484	37	133.3	54.44
31	46	1.6	486	35.1	1.4	492	36.8	126.91	54.44
32	40	1.41	488	34.1	1.41	488	34.1	126.91	54.44
34	5	1.6	482	36.6	1.5	485	38	124.39	54.44

Values in red mark where slurry samples were taken.

Table B3: Test C raw data

Time		Initial			Final			Acid Add	MnO_2
Hours	Min	pH	Eh (Ag/AgCl)	Temp (°C)	pH	Eh (Ag/AgCl)	Temp (°C)	g	g
9	2	10.29	16	28.5				15.01	
9	31				1.48	365	39.4	156.59	
10	37	2.13	334	35.4	1.49	412	40.6	132.16	66.96
10	56	1.98	412	36.4	1.47	435	40	118.35	65.5
11	36	1.94	422	36.7	1.49	448	38.8	106.18	62.72
12	17	2.11	443	38.1	1.5	486	39.3	89.24	57.1
12	50	1.84	496	37.4	1.4	510	39	77.64	57.1
13	39	1.8	514	37.9	1.42	525	39	68.25	57.1
14	11	1.59	529	38.1	1.45	534	38.9	63.92	57.1
14	37	1.59	534	37.8	1.42	539	38.8	58.48	57.1
15	24	1.54	535	37.8	1.46	537	38.8	55.64	57.1
16	37	1.65	527	37.9	1.44	532	38.8	49.85	57.1
17	15	1.45	529	38.3	1.45	529	38.3	49.85	57.1
18	37	1.65	515	36.6	1.43	522	38	43.5	57.1
19	14	1.48	518	37.5	1.48	518	37.5	43.5	57.1
19	30	1.49	516	37.4	1.49	516	37.4	43.5	57.1
20	35	1.55	506	36.2	1.46	508	37.4	40.85	57.1
21	40	1.57	500	37.7	1.44	504	38.8	36.64	57.1
22	47	1.49	495	36.9	1.49	495	36.9	36.64	57.1
23	43	1.57	488	37.3	1.45	491	38.2	33.35	57.1
24	23	1.46	487	36.9	1.44	489	37.9	31.96	56.69
25	42	1.5	482	35.6	1.4	487	37	28.87	55.01
27	17	1.54	486	36.2	1.41	491	37.5	24.84	54.28
28	45	1.49	487	35.3	1.43	488	36.3	23.24	54.28
30	58	1.55	479	36	1.46	485	37.5	141.85	51.27
31	56	1.61	491	36.5	1.45	496	37.7	138.13	51.27
32	45	1.46	495	35.3	1.46	495	35.5	138.13	51.27
34	36	1.61	490	35.5	1.5	492	37.1	135.54	51.27

Values in red mark where slurry samples were taken.

Table B4: Test D raw data

Time		Initial			Initial			Acid Add	MnO_2
Hours	Min	pH	Eh (Ag/AgCl)	Temp (°C)	pH	Eh (Ag/AgCl)	Temp (°C)	g	g
8	46	8.32	35	31.7					
8	56				2.02	376	45.1	68.83	106.66
8	58	3.38	270	39.2	1.84	369	42.8	47.22	106.66
9	9	2.9	289	41	1.82	358	42.2	31.68	106.66
9	12	2.36	329	40.4	1.92	347	41	25.13	106.66
9	22	2.22	308	37.1	1.76	329	38.7	21.16	106.66
9	38	2.71	295	37.4	1.8	339	39	201.17	106.66
9	45	1.89	331	37.9	1.83	362	39.1	192	101.76
10	20	2.68	354	37.6	1.82	382	38.3	186.29	101.76
10	46	2.64	366	38.4	1.99	384	39.2	180.75	101.76
11	38	2.78	356	38.8	1.75	389	39.7	170.14	101.76
11	58	2.34	380	38.4	1.73	392	39.2	161.34	101.76
12	22	2.29	382	38.4	1.74	394	39.3	154.68	101.76
12	49	2.32	383	38.2	1.99	390	39.9	151.14	101.76
13	42	2.5	375	37.4	1.61	395	38.4	140.85	101.76
13	58	2.05	391	38.1	1.82	395	38.5	138.2	101.76
15	19	2.46	376	36.4	1.69	393	37.6	130.2	101.76
16	40	2.45	376	38.3	1.7	392	39	122.24	101.76
17	43	2.33	385	38.7	1.93	391	39.3	118.68	101.76
19	13	2.47	377	37.8	1.71	394	38.6	111.04	101.76
20	14	2.21	387	37.7	1.7	396	38.6	105.01	101.76
21	28	2.23	387	37.8	1.73	394	38.3	99.81	101.76
22	36	2.16	388	37.6	1.73	395	38.5	95.06	101.76
23	34	2.04	390	36.3	1.73	395	37.3	91.48	101.76
25	59	2.31	382	38	1.67	393	38.9	84.33	101.76
28	27	2.11	384	36.5	1.58	391	38.1	77.02	101.76
31	5	1.98	383	36.6	1.98	383	36.8	77.02	101.76
32	44	2.12	379	36.2	1.92	383	37.1	75.4	101.76
33	51	2.01	378	36.2	2.01	378	36.2	75.4	101.76

Values in red mark where slurry samples were taken.

Table B5: Test E raw data

Time		Initial			Final			Acid Add	MnO_2
Hours	Min	pH	Eh (Ag/AgCl)	Temp (°C)	pH	Eh (Ag/AgCl)	Temp (°C)	g	g
9	53	6.06	163	37.9	1.49	388	41.3	170.93	51.27
10	7	1.54	384	38.8	1.47	386	39.9	168.22	51.27
10	27	1.89	348	38.8	1.49	378	40	159.31	51.27
10	53	2.02	342	38.8	1.44	385	40.5	143.69	48.16
11	20	1.85	365	38.6	1.45	391	40.2	130.63	43.03
11	50	1.84	379	37.7	1.49	398	40	122.08	38.96
12	48	1.63	379	38.2	1.39	392	39.3	117.02	31.66
13	15	1.97	385	38.2	1.39	415	40.4	101.89	23.6
13	53	1.92	406	37.5	1.49	423	39.8	92.03	16.83
14	46	2.03	411	37	1.43	431	39.6	80.35	13.29
16	3	2	417	36.9	1.42	435	39.9	68.66	10.71
16	24	1.66	432	36.3	1.42	439	38.9	63.3	61.63
17	17	1.93	429	37.2	1.4	448	40.2	49.28	53.59
17	45	1.7	445	37.1	1.43	455	39.6	41	46.28
18	29	1.81	448	37.7	1.42	461	39.8	30.94	44.64
18	53	1.62	459	37.7	1.5	463	39.2	26.92	42.12
19	42	1.76	459	37.7	1.43	472	39.6	16.94	34.84
20	19	1.7	470	37.2	1.4	481	38.8	185.23	30.62
20	52	1.54	481	36.6	1.45	483	38.2	182.76	29.59
22	2	1.73	477	36.7	1.36	490	38.9	171.26	27.17
24	10	1.74	481	37.4	1.35	493	39.5	160.33	27.17
26	26	1.67	480	37.1	1.35	492	38.8	151.39	25.62
27	45	1.51	486	37.2	1.43	489	37.3	147.87	25.62
31	6	1.67	473	36.4	1.37	485	38.4	138.88	22.15
32	17	1.51	481	36.1	1.46	484	37.4	137.11	19.92
33	36	1.61	480	37.4	1.34	489	38.5	129.64	19.92
34	54	1.42	482	36				129.64	19.92

Values in red mark where slurry samples were taken.

Table B6: Test F raw data

Time		Initial			Final			Acid Add	MnO_2
Hours	Min	pH	Eh (Ag/AgCl)	Temp (°C)	pH	Eh (Ag/AgCl)	Temp (°C)	g	g
10	14	7.95	11	38	1.45	386	40.1	189.96	54.44
10	22	1.52	304	39	1.44	330	39.4	188.26	54.44
10	38	1.53	375	38.8	1.47	383	39.2	186.85	54.44
11	14	1.57	406	37.5	1.44	424	39.1	183.44	52.72
11	26	1.46	438	38	1.47	444	38.5	183.44	50.62
12	17	1.65	468	38.3	1.45	477	39.5	179.06	49.9
12	54	1.15	488	38.5	1.15	488	38.5	179.06	49.9
13	22	1.26	492	38.7	1.26	492	38.6	179.06	49.9
14	14	1.69	495	38	1.48	500	39.6	175.96	49.9
14	52	1.42	502	38.4	1.42	502	38.4	175.96	49.9
16	8	1.55	504	38.7	1.44	507	39.3	174.04	49.9
17	24	1.47	510	38.8	1.47	510	38.8	174.04	49.9
17	50	1.59	511	38.7	1.4	515	39	170.8	49.9
18	33	1.44	517	39	1.44	517	39	170.8	49.9
19	14	1.54	518	37.5	1.49	520	38.6	169.84	49.9
19	43	1.5	521	38.3	1.5	521	38.3	169.84	49.9
20	25	1.51	522	38	1.46	523	38.8	168.51	49.9
20	56	1.38	524	37.7	1.38	524	37.7	168.51	49.9
22	8	1.47	525	37.9	1.47	525	37.9	168.51	49.9
24	15	1.49	526	38.4	1.49	527	38.4	168.51	49.9
26	32	1.49	527	37.6	1.49	527	37.6	168.51	49.9
27	49	1.5	526	37.5	1.5	526	37.5	168.51	49.9
31	11	1.51	525	37.5	1.46	526	38	167.74	49.9
32	20	1.42	525	35.5	1.42	525	35.5	167.74	49.9
33	40	1.43	524	37.2	1.43	524	37.2	167.74	49.9
35	14	1.47	522	37.4	1.47	522	37.4	167.74	49.9

Values in red mark where slurry samples were taken.

Table B7: Test G raw data

Time		Initial			Final			Acid Add	MnO_2
Hours	Min	pH	Eh (Ag/AgCl)	Temp (°C)	pH	Eh (Ag/AgCl)	Temp (°C)	g	g
9	15	6.15	331	31.6					
9	20				1.45	404	32.7	167.02	81.92
9	25	1.2	422	32.3	1.22	424	32.2	167.02	81.92
9	43	1.31	420	30.8	1.3	422	30.6	167.02	81.92
9	52	1.21	425	30	1.2	426	29.9	167.02	81.92
10	15	0.98	430	27.3	0.97	423	27.3	167.02	81.92
11	20	1.13	434	21.8	1.12	434	22.2	167.02	81.92
11	45	1.25	429	28.9	1.24	430	28.6	167.02	81.92
12	5	1.2	429	27.1	1.15	434	28.4	167.02	81.92
12	27	1.3	429	34.5	1.3	433	34.5	167.02	81.92
13	18	1.31	441	34.5	1.31	441	34.8	167.02	81.92
13	48	1.21	441	35.3	1.21	441	35.4	167.02	81.92
15	25	1.21	442	35.1	1.21	443	35.5	167.02	81.92
16	45	1.25	444	33.7	1.25	444	33.8	167.02	81.92
17	37	1.24	442	35.5	1.24	443	35.7	167.02	81.92
18	17	1.2	445	34.5	1.2	445	34.5	167.02	81.92
18	23	1.38	440	35.7	1.38	440	35.7	167.02	81.92
19	19	1.35	443	37.1	1.35	443	37.4	167.02	81.92
19	27	1.29	441	36.1	1.35	441	35.9	167.02	81.92
21	34	1.38	440	36	1.38	441	36.5	167.02	81.92
22	41	1.4	443	36.4	1.4	443	36.7	167.02	81.92
23	38	1.37	437	35.6	1.36	440	35.6	167.02	81.92
26	4	1.43	443	37.2	1.43	444	37.2	167.02	81.92
28	32	1.4	442	35.9	1.4	442	36	167.02	81.92
31	9	1.42	446	36.5	1.42	446	36.9	167.02	81.92
32	49	1.45	444	36	1.45	445	36.5	167.02	81.92
34	19	1.35	438	37.1	1.35	438	37.1	167.02	81.92

Values in red mark where slurry samples were taken.

Table B8: Leach solution assays

Element	U	Th	Al	Si	Fe	Mg	Mn	Ca	K	Na
Lower Detection	**0.2**	**0.5**	**0.08**	**0.3**	**0.02**	**0.02**	**0.5**	**0.05**	**0.11**	**0.05**
Upper Detection	**0**	**0**	**0**	**0**	**0**	**0**	**0**	**0**	**0**	**0**
Units	**ppb**	**ppb**	**mg/L**	**mg/L**	**mg/L**	**mg/L**	**mg/L**	**mg/L**	**mg/L**	**mg/L**
BLANK	0.6	<0.5	1.73	11.6	0.96	8.34	1.3	15.3	3.3	11.9
TestB-1 HOUR	106000000	736	4721	10100	876	248	1449	672	175	201
TestB-3 HOUR	201000000	1720	9287	18560	1868	473	3846	726	339	391
TestB-8 HOUR	180000000	1890	8993	18740	2695	620	4496	660	324	373
TestB-24 HOUR	206000000	2390	10029	1458	6454	1327	6787	498	327	297
TestD-1 HOUR	135000000	1240	5686	9496	1953	444	62.2	623	267	253
TestD-3 HOUR	203000000	2140	9515	16060	3168	636	5449	741	406	407
TestD-24 HOUR	257000000	3490	14027	18960	9332	1865	11090	583	565	528
BLANK	2.3	<0.5	<0.08	26	<0.02	7.43	3	17.7	3.2	11.1
TestE-1 HOUR	807000000	2530	1438	580	9383	1593	2226	641	17.1	130
TestE-3 HOUR	1055000000	3450	2014	698	13421	2301	6533	703	18.6	149
TestE-8 HOUR	1890000000	5210	2867	760	21024	3244	15966	780	2.4	156
TestE-24 HOUR	2455000000	8700	4832	626	33805	5799	30570	623	<0.11	175
TestF-1 HOUR	315000000	669	320	214	1280	393	805	677	36.2	144
TestF-3 HOUR	254000000	596	356	250	1322	458	683	656	38.2	187
TestF-8 HOUR	319000000	803	542	313	2094	713	979	782	43.6	170
TestF-24 HOUR	364000000	1220	879	281	2737	925	1278	601	52.3	179
TestA-1 HOUR	162000000	1960	9040	12363	4387	803	4153	702	<0.11	332
TestA-3 HOUR	165000000	2140	9905	12603	6454	1146	6260	672	<0.11	343
TestA-8 HOUR	197000000	2740	12230	13525	11232	1915	9814	629	384	380
TestA-24 HOUR	213000000	3230	14865	3463	17443	3094	13670	686	394	473
BLANK	3.9	<0.5	<0.08	<0.3	<0.02	6.87	<0.5	11	2	11.2
TestC-1 HOUR	105800	531	2405	48180	623	221	1256	488	112	122
TestC-3 HOUR	155200	1128	5551	112600	986	286	1908	482	208	224
TestC-8 HOUR	163600	1340	5808	110400	1000	317	2007	505	210	222
TestC-24 HOUR	196400	1897	7953	15470	1942	509	2566	418	298	314
TestG-1 HOUR	590400	404	116	213	157	380	13.1	665	64.3	1729
TestG-3 HOUR	881200	429	188	361	275	479	18.1	645	80.6	452
TestG-8 HOUR	950000	458	273	369	397	554	20.6	643	88.7	410
TestG-24 HOUR	843800	414	311	329	405	532	20.6	596	93.9	382

APPENDIX C: Additional Igneous Sample Leach Test Data

Table C1: Sample SH1 raw leach data

Time		Initial pH	Initial Eh	Initial T°	Final pH	Final Eh	Final T°	Acid Addition	MnO_2
Hours	Min	-	mV	°C	-	mV	°C	g	g
								211.75	44.84
9	34	7.97	32	52.1	1.44	-113	45.8	180.47	44.84
9	54	1.46	-54	42.7	1.46	-54	42.7	180.47	44.84
10	17	1.59	250	42.9	1.42	260	43	177.09	44.84
10	28	1.48	277	42.9	1.45	290	42.4	177.09	44.84
10	45	1.51	295	43.6	1.45	374	43.7	175.68	42.09
11	17	1.46	397	41.3	1.46	401	41.3	175.68	39.34
11	23	1.51	413	41.3	1.43	421	41.3	173.93	36.52
12	32	1.64	466	42.6	1.41	472	42.7	170.21	36.52
13	33	1.47	493	42.5	1.47	493	42.5	170.21	36.52
14	45	1.54	508	42.1	1.44	509	42.1	168.87	36.52
15	37	1.48	520	42	1.48	520	42	168.87	36.52
16	56	1.5	531	42.2	1.5	531	42.2	168.87	36.52
18	30	1.52	538	41.8	1.47	539	41.9	168.35	36.52
20	21	1.48	543	42	1.48	543	42	168.35	36.52
21	30	1.49	545	41.8	1.41	548	41.9	167.34	36.52
7	07	1.57	549	41.4	1.47	550	41.3	166.02	36.52
10	36	1.49	543	40.9					

Values in red mark where slurry samples were taken.

Table C2: Sample SH2 raw leach data

Time		Initial pH	Initial Eh	Initial T°	Final pH	Final Eh	Final T°	Acid Addition	MnO_2
Hours	Min	-	mV	°C	-	mV	°C	g	g
								213.51	38.29
10	01	7.8	-101	41.7	1.4	-78	44.4	180.47	38.29
10	21	1.62	47	43.9	1.41	74	43.7	176.37	38.29
10	33	1.44	295	42.7	1.44	294	42.7	176.37	38.29
10	51	1.5	319	42	1.49	320	42	176.37	38.29
11	00	1.51	317	41.8	1.38	324	41.2	174.16	38.29
11	15	1.4	324	41.4	1.4	370	41.3	174.16	35.58
12	00	1.56	400	41.9	1.37	415	42.1	170.71	33.86
12	36	1.47	437	42.3	1.46	440	42.2	170.71	33.3
13	27	1.54	449	42.7	1.41	455	42.8	169.35	32.14
14	00	1.53	467	42.9	1.44	470	42.7	168.41	32.14
14	48	1.5	476	41.9	1.5	476	41.9	168.41	32.14
15	38	1.55	479	41.9	1.44	482	41.9	166.7	32.14
17	04	1.49	487	41.8	1.49	487	41.8	166.7	32.14
18	12	1.53	489	41.8	1.46	492	41.9	165.82	32.14
19	00	1.49	490	41.8	1.49	491	41.9	165.82	32.14
20	24	1.5	492	41.8	1.5	492	41.8	165.82	32.14
21	35	1.52	493	41.6	1.37	497	41.8	163.19	32.14
7	10	1.56	493	40.8	1.47	494	40.8	162.23	32.14
10	37	1.52	488	40.4	1.49	489	40.4	161.89	32.14

Values in red mark where slurry samples were taken.

Table C3: Sample SJ1 raw leach data

Time		Initial pH	Initial Eh	Initial T°	Final pH	Final Eh	Final T°	Acid Addition	MnO_2
Hours	Min	-	mV	°C	-	mV	°C	g	g
8	18	8.67	89	36.8	1.47	-150	38.5	149.08	26.14
8	40	1.64	136	41.7	1.48	148	41.8	146.23	26.14
8	56	1.49	242	41.8	1.49	241	42.3	146.23	26.14
9	18	1.5	282	41	1.47	377	41	145.05	26.14
9	41	1.53	404	41.3	1.47	407	41.2	143.9	26.14
10	18	1.49	408	40.3	1.49	410	40.3	143.9	25.75
11	32	1.56	418	41.3	1.42	423	41.4	141.16	25.75
12	16	1.45	421	41.4	1.44	425	41.4	141.16	24.64
13	15	1.53	438	41.7	1.47	440	41.7	140.06	24.64
15	7	1.53	435	41.3	1.46	442	41.3	138.81	23.21
16	58	1.57	457	41.7	1.41	460	41.9	135.77	23.21
17	18	1.41	460	41.6	1.41	460	41.6	135.77	23.21
19	11	1.46	460	41.8	1.46	460	41.8	135.77	23.21
20	32	1.5	459	41.7	1.39	463	41.8	133.87	23.21
7	51	1.53	449	41.2	1.5	451	41.1	133.46	23.21
9	18	1.5	451	40.1	1.5	451	40.1	133.46	23.21

Values in red mark where slurry samples were taken.

Table C4: Sample SJ2 raw leach data

Time		Initial pH	Initial Eh	Initial T°	Final pH	Final Eh	Final T°	Acid Addition	MnO_2
Hours	Min	-	mV	°C	-	mV	°C	g	g
8	35	8.73	46	40.3	1.5	-186	41.5	149.61	25.46
8	57	1.74	-193	43.6	1.48	-171	42.9	145.94	25.46
9	12	1.53	-129	42.8	1.47	-104	43.8	144.54	25.46
9	35	1.47	35	41.6	1.49	345	41.6	144.54	25.46
10	35	1.61	410	41.4	1.44	415	41.5	141.37	24.77
11	36	1.51	430	41.6	1.47	431	41.6	140.82	24.77
12	35	1.51	432	41.9	1.47	435	41.9	140.15	23.93
13	17	1.54	445	42.6	1.47	446	42.7	139.01	23.93
15	10	1.49	447	41.2	1.49	448	41.3	139.01	23.16
17		1.56	456	41.8	1.44	457	41.9	136.94	23.16
17	35	1.45	459	42	1.45	459	42	136.94	23.16
19	19	1.47	458	41.8	1.47	458	41.8	136.94	23.16
20	35	1.47	459	41.6	1.43	460	41.6	136.37	23.16
7	54	1.46	454	41	1.46	454	41	136.37	23.16
9	20	1.44	450	40	1.44	450	40	136.37	23.16
9	36	1.44							

Values in red mark where slurry samples were taken.

Table C5: Sample Val raw leach data

Time		Initial pH	Initial Eh	Initial T°	Final pH	Final Eh	Final T°	Acid Addition	MnO_2
Hours	Min	-	mV	°C	-	mV	°C	g	g
8	51	8.81	-24	41.3	1.49	-180	43.6	177.68	21.51
9	15	1.61	-302	42.3	1.47	-296	42.5	177.68	21.51
9	44	1.53	-297	43.1	1.43	-293	41.6	175.95	21.51
9	51	1.47	-296	41.4	1.47	-222	41.5	175.95	21.51
10	51	1.78	243	41.2	1.44	302	41.5	170.6	20.39
11	38	1.51	344	41.3	1.47	347	41.4	169.78	18.7
12	51	1.54	365	41.5	1.43	374	41.6	167.73	18.7
13	19	1.45	380	41.9	1.45	380	41.9	167.73	18.7
15	18	1.46	386	41	1.46	386	41	167.73	18.7
17	2	1.48	389	41.5	1.48	389	41.5	167.73	18.7
17	51	1.49	388	41.7	1.49	388	41.7	167.73	18.7
19	14	1.49	389	41.6	1.49	389	41.6	167.73	16.61
19	39	1.54	400	41.5	1.38	410	41.7	164.68	15.91
20	4	1.42	419	41.5	1.42	419	41.5	164.68	15.91
20	39	1.42	428	41.3	1.35	432	41.4	163.17	15.91
7	50	1.39	448	40.7	1.39	407	44.9	163.17	15.24
9	21	1.41	457	39.8	1.41	457	39.8	163.17	15.24
9	46								

Values in red mark where slurry samples were taken.